UNIVERSITY OF CALIFORNIA SAN DIEGO

Laboratory Studies of Aerosol Chemistry: pH Titration, Inorganic Sulfur Oxidation and Organosulfur Formation

A dissertation submitted in partial satisfaction of the requirements for the degree of Doctor of Philosophy

in

Chemistry

by

Ellen M. Coddens

Committee in charge:

Professor Vicki H. Grassian, Chair
Professor Stacey Brydges
Professor Robert E. Continetti
Professor Amato T. Evan
Professor Kimberly A. Prather

2019

The Dissertation of Ellen M. Coddens is approved, and it is acceptable in quality and form for publication on microfilm and electronically:

_____

_____

_____

_____

_____

Chair

University of California San Diego

2019

DEDICATION

To my family

TABLE OF CONTENTS

LIST OF FIGURES

LIST OF TABLES

ACKNOWLEDGMENTS

First and foremost, I would like to thank my research advisor Dr. Vicki Grassian. I am truly grateful for all of the opportunities and experiences she has provided for me to learn and grow as a scientist. In addition to the opportunities to teach with her and assist in grant writing, she also gave me the unique experience of moving a lab across the country. No matter if it was while I was still in Iowa or at UCSD, she was always there to support me along every step of this journey. Without her none of this research would have been possible.

I would also like to thank my undergraduate advisor Juan Navea. Thank you for sparking my interest in atmospheric chemistry and giving me the opportunity to do research so early on in my academic career. Working with you at Lawrence University was exciting and insightful and helped pave the way for the rest of my graduate career leading me to Dr. Grassian.

I would also like to thank all my committee members, both at Iowa and UCSD, for their continued support throughout my degree: Dr. Christopher Cheatum, Dr. Edward Gillan, Dr. Elizabeth Stone, Dr. Alexi Tivanski, Dr. Robert Continetti, Dr. Kimberly Prather, Dr. Stacey Brydges, and Dr. Amato Evan.

Moving to California part way through my degree was unexpected and more challenging than expected - I would like to sincerely thank all of those who helped me make the transition from Iowa to UCSD. Chris Cheatum, thank you for always checking in on me while the group was out in California and I was finishing up back in Iowa. To Jeanine Kolinko, Jeff Rances, Amy Tran and Erica Lennard in the student affairs office-

you helped make the transition to UCSD smooth and were always there to answer my many questions along the way- thank you.

Throughout grad school, your fellow group members become your friends and support system and, in a sense, become your second family. I am forever grateful to have been a part of such an amazing group like this one. Thank you to everyone who has been part of the group and supported me over the years. Jon Trueblood, Liora Mael, and Mike Alves- thank you for always helping me, supporting me, encouraging me, and for helping keep me sane on the days I thought I was losing my mind- I can't imagine making it though grad school without you.

Jon, you became one of my close friends back in Iowa and even though we were excited for the move to California, I think it was hard for both of us to leave Iowa City and everyone there, but it was always comforting knowing I wasn't going through that transition alone. Thank you for making the move first and giving me the lowdown of San Diego and introducing me to goldfish races. But most importantly, thank you for always letting me have Peaches to satisfy my need for a puppy and thereby stopping me from adopting seven dogs throughout grad school.

Liora, thank you for always being there for me to talk through ideas, think out loud or just to vent. Whether helping me practice for a talk or look at the million versions of cover art I made or just giving me a break in the day with a crossword you played a big role in helping me through grad school. Also, thank you for always being my partner in crime for anything SWIGS related and helping me with everything we planned, even if it wasn't even a two-person job (we really perfected the flier hanging procedure).

Mike Alves, you quickly became one of my closest friends in San Diego and it has been great having someone like you in my life, both inside and outside of the lab. Also, thank you for always being my thanksgiving family away from home.

Victor Or, thank you for always helping me with my innumerable computer problems and constant questions about Igor (yes, ee-gor) and Inkscape.

Deborah Kim and Stephanie Mora Garcia, thank you for being my workout buddies and helping me keep up with that work-life balance and making our corner of the office fun.

Armando Estillore, from Iowa to UCSD, moving and setting up the new lab and teaching Chem 171- thank you for being a great mentor.

I would like to thank all of the undergraduates that I mentored and worked with me throughout my time at UCSD; Jimmy, Danielle, Riya and Cynthia. But I would especially like to acknowledge Cynthia- seeing you grow and transform from the little sophomore when I first met you to the strong and confident grad student you are today has been one of the most rewarding parts of my time at UCSD. You are always bubbly and full of energy but also so driven and ambitious and I loved every minute working with you; I can't wait to see all of the great things you'll do in your career. Also thank you for always helping me figure out how to register for classes and find my way around campus. And lastly, thank you for taking surfing lessons with me, we were terrible and spent more time trying to not drown than we did actually surfing but it will always be one of my funniest memories from San Diego.

I would also like to thank those in the group who I have collaborated with on projects. First, thank you to Aruni Gankanda for helping me get started with the sulfate

project. Kyle Angle, thank you for your collaboration with the AOT and for being such a great mentee to take over the AOT project, I know how frustrating the instrument can be at times trying to trap something that just doesn't want to stick. Liubin Huang, thank you for your help and collaboration with the organosulfur project, you have really helped me expand my knowledge in this field.

I would also like to thank all of my friends who have supported me along the way - you have all played a huge role is helping me get to this point. Whether a couple minutes away or a couple states away you have all been there for me no matter what I needed- to support me, cheer me on, hold my hand, or just listen.

To my friends from Iowa City, especially Alisa Fairweather and Alex Martin, I don't know how I would have made it through the first two years of grad school without you. The countless movies nights or shenanigans out at Blue Moose or Joe's helped make the stress of grad school manageable.

Shea Davis, you helped make my move across the country exponentially easier. Having a familiar face and wonderful friend like you in San Diego made the adjustment so much easier. Plus, having ½ of Sage 109 back together almost felt like college again.

To all the other friends I've met out in California, especially Johannes Dietzel and Robert Kaderka, you have helped make San Diego feel like home.

To my friends from Lawrence University, Amy Pettigrew, Katie Nelson, Jenny Angeli, and McKenzie Saunders, you have been amazing supports and outlets

Kelsey Block, you have been there for me since the beginning- all the way back to kindergarten, though high school and college to grad school and out to California. I still shake my head and laugh at how we both ended up on out west- who would have ever

thought we'd both be here? You have always been my little piece of home away from home.

Amanda Ollerer and Ellie Galvin, you two have truly been lifesavers for me along this journey. Thank you for always being a shoulder to lean on, for talking me down when I let the stress and anxiety of grad school build up and for always reminding me of the important things in life. You've always been there to celebrate the good times and have helped get me through the tough ones too and for that unwavering support I am forever thankful.

But most importantly, thank you to my family. You all mean the world to me and I could not have made it through any of this journey without your love and support. You have supported me unconditionally throughout every step. From helping me move into my tiny first apartment to helping me move across the country you've always been there. It hasn't always been easy, some of the scariest/hardest moments of my life have happened while I've been in grad school, but you were always there for me, no matter how many miles away I was. Thank you for always believing in me.

The dissertation author was the primary investigator and author of the work in Chapter 2.

The dissertation author was the primary investigator and author of the work in Chapter 3.

Chapter 4 is reproduced with permission from: Coddens, E.M.; Angle, K.J.; Grassian, V. H. Titration of Aerosol pH through Droplet Coalescence. *J. Phys. Chem. Lett., 10 (15),* 4476-4483, 2019. The dissertation author was the primary investigator and author of this paper.

A portion of Chapter 5 is reproduced with permission from the American Chemical Society: Coddens, E. M.; Huang, L.; Wong, C.; Grassian, V. H. (2018). Influence of Glyoxal on the Catalytic Oxidation of S(IV) in Acidic Aqueous Media. *ACS Earth and Space Chemistry*, 3 (1), 142-149, 2018. The dissertation author was the primary investigator and co-first author of this paper.

Chapter 6 is in preparation: Coddens, E. M., Sony, R., Grassian, V. H. Aqueous Phase Catalytic Oxidation of S(IV): Influence of pH, Ionic Strength, and the Presence of Organic Compounds. The dissertation author was the primary investigator and author of this paper.

VITA

2014	Bachelor of Arts, Chemistry, Lawrence University
2014-2016	Teaching Assistant, Department of Chemistry, University of Iowa
2014-2016	Research Assistant, University of Iowa
2016-2019	Research Assistant, University of California San Diego
2016-2017	Teaching Assistant, Department of Chemistry, University of California, San Diego
2019	Doctor of Philosophy, Chemistry, University of California, San Diego

PUBLICATIONS

Huang, L; **Coddens, E. M.**; Grassian, V.H. (2019). Formation of Organosulfur Compounds from Aqueous Phase Reactions of S(IV) with Methacrolein and Methyl Vinyl Keton in the Presence of Transition Metal Ions. *ACS Earth and Space Chemistry, 3*, 1749-1755.

Coddens, E.M.; Angle, K.J.; Grassian, V. H. (2019). Titration of Aerosol pH through Droplet Coalescence. *Journal of Physical Chemistry Letters, 10*, 4476-4483.

Coddens, E. M.; Huang, L.; Wong, C.; Grassian, V. H. (2018). Influence of Glyoxal on the Catalytic Oxidation of S(IV) in Acidic Aqueous Media. *ACS Earth and Space Chemistry*, 3, 142-149.

Huang, L.; Cochran, R. E.; **Coddens, E. M**.; Grassian, V. H. (2018). Formation of Organosulfur Compounds through Transition Metal Ion-Catalyzed Aqueous Phase Reactions. *Environmental Science and Technology Letters, 5*, 315–321.

Gankanda, A.; **Coddens, E. M**.; Zhang, Y.; Cwiertny, D. M.; Grassian, V. H. (2016). Sulfate Formation Catalyzed by Coal Fly Ash, Mineral Dust and Iron (III) Oxide: Variable Influence of Temperature and Light. *Environmental Science Processes and Impacts, 18,* 1484–1491.

Lesko, D. M. B.; **Coddens, E. M.**; Swomley, H. D.; Welch, R. M.; Borgatta, J.; Navea, J. G. (2015). Photochemistry of nitrate chemisorbed on various metal oxide surfaces. *Physical Chemistry Chemical Physics, 17*, 20775-20785.

ABSTRACT OF THE DISSERTATION

Laboratory Studies of Aerosol Chemistry: pH Titration, Inorganic Sulfur Oxidation and Organosulfur Formation

by

Ellen M. Coddens

Doctor of Philosophy in Chemistry

University of California San Diego, 2019

Professor Vicki H. Grassian, Chair

Atmospheric aerosols can impact Earth's climate and the chemistry of the atmosphere through a variety of processes and pathways. For example, atmospheric aerosols affect Earth's climate directly by scattering or absorbing solar radiation or indirectly by interacting with clouds and impacting their physiochemical properties. Aerosols are unique microenvironments, distinct from the bulk, and therefore their physiochemical properties result in differences between bulk and aerosol phase processes, such as reactivity and kinetics, acidity and interaction with light. Despite the fact that the effects of aerosols on atmospheric chemistry have been studied in previous work, there remains considerable uncertainties associated with aerosol chemistry resulting in gaps between atmospheric chemistry models and field observations. By better understanding chemical processes occurring within aerosols, as well as cloud or fog droplets, and the factors that influence them, we can help reduce some of the uncertainties in atmospheric models. This dissertation investigates sulfur oxidation chemistry in the atmosphere to better understand factors influencing the rate of oxidation and the extent of formation of inorganic sulfate. In particular, we investigated the influence of various atmospherically relevant conditions (presence of organic compounds, ionic strength, etc.) in the oxidation of inorganic S(IV), sulfite/bisulfite, to inorganic S(VI), sulfate/bisulfate, compounds in the presence and absence of transition metals. Most importantly, a new role of transition metal catalyzed formation of organosulfur compounds has been found. Furthermore, in this dissertation, the further development of the Aerosol Optical Tweezer system to study the chemistry within individual aerosols is discussed. Utilizing the Aerosol Optical Tweezer coupled with cavity enhanced Raman spectroscopy it is shown that this method can be used to investigate changes within a droplet, such as: (i) pH changes induced by coalescence

with acidic aerosol; (ii) reactions within the droplet, like monitoring oxidation of S(IV) and; (iii) reaction of glyoxal with sulfite to yield organosulfur compounds. The findings presented in this dissertation can improve our understanding of the factors influencing sulfur oxidation chemistry and help to further develop a method to study the chemistry occurring within single aerosols to reduce some of the uncertainty associated with aerosol chemistry to improve atmospheric chemistry models.

Chapter 1 Introduction

1.1 Atmospheric Aerosols

Atmospheric aerosols are generally defined as small, solid or liquid particles suspended in air ranging in size from 0.001 to 10 μm.[1,2] Aerosols can come from natural sources, such as dust storms, volcanoes, sea spray, biomass burning, as well as anthropogenic sources like fossil fuel combustion or land/soil modification. Primary aerosols are those directly emitted into the atmosphere whereas secondary aerosols are formed in the atmosphere, mostly from gas-particle conversion processes.[3] Aerosol size and composition depend greatly on their source. Primary aerosols tend to be larger while secondary aerosols are generally smaller. Aerosols consist mainly of carbonaceous material, sulfate, nitrate, ammonium, sodium, chloride, crustal elements, trace metals, and water.[1,2,4] The average atmospheric lifetime, or residence time, of aerosols varies from hours to weeks depending on aerosol size.[2,3,5] Some particles are removed from the atmosphere close to their source area; however, many aerosols mix into the atmospheric boundary layer and can be carried by winds for long-range transport. For example, dust particles originating from a dust storm in the Saharan region of North Africa have been found in the continental United States.[6,7] Aerosols are removed from the atmosphere through two mechanisms: dry deposition, also known as gravitational settling, or wet

deposition, in which aerosols are incorporated into atmospheric water and deposited through precipitation or cloud/fog contact with Earth's surface.[1]

Aerosols have a variety of impacts on the atmosphere. Aerosols can reduce visibility, impact human health, interact with light, provide active surfaces for heterogeneous or multiphase reactions to occur and provide nucleation bodies for condensation of atmospheric water.[1,2] Aerosol effects on the atmosphere and climate are generally separated into two main categories: direct and indirect effects. Figure 1.1 summarizes the direct and indirect effects of aerosols. In the direct effect, aerosols interact directly with light by either absorbing or scattering radiation. Some aerosols, like black carbon (soot), absorb radiation leading to a positive radiative forcing, or warming effect, whereas other aerosols, such as sulfate, scatter radiation causing a negative radiative forcing or an overall cooling effect. In the indirect effect, aerosols interact with clouds impacting cloud microphysics which can alter a cloud's albedo, height or size, and the amount and lifetime. Altering the properties of clouds thereby alters the radiative balance and precipitation, indirectly effecting the atmosphere and climate. The direct effect is largely dependent on the optical properties of each aerosol whereas the indirect effect is dependent on an aerosols ability to act as a cloud condensation nucleus. Nonetheless, both the direct and indirect effect are dependent on the chemical and physical properties of each aerosol.[3,8] There is a large uncertainty associated with the contribution of aerosols to

radiative forcing in part due to the poor understanding of the complex chemical interactions occurring during cloud processing (Figure 1.2).

Due to the important role of aerosols and the impact they can have on Earth's climate, it is important to understand the chemical processes involving and occurring within aerosols in order to gain a complete understanding of atmospheric chemistry. When aerosols are released into or formed in the atmosphere, their physiochemical properties, including composition, size, or acidity, can change throughout various atmospheric and cloud processes. Aerosols are unique microenvironments, distinct from the bulk, and their changes in physiochemical properties and increased surface-to-volume ratio result in differences between bulk and aerosol phase processes, such as reactivity and kinetics, acidity and interaction with light. Many recent studies have focused on examining reactions and processes in the aerosol phase or at the air-water interface and thereby highlighting the need to differentiate between bulk and aerosol or surface processes.[9–13] Reaction kinetics in microdroplets have been shown to be significantly different than in the bulk phase with enhanced reactions rates observed in the aerosol phase.[14,15] For example, Nissenson et al. showed that the photolysis of molybdenum hexacarbonyl was approximately three orders of magnitude faster in the aerosol phase than in the bulk aqueous phase.[14] Other recent studies have highlighted the differences in acidity within aerosols and at the air-water interface and how this can impact chemical processes. Lin et al. reported that the pH at the aqueous aerosol interface is ~2.2 pH units more acidic than that of the bulk interior of nanoaerosols.[16] Other recent studies have shown that the surface pK_a of various organic acids differs from the bulk; for example Eugene et al. showed that the lower surface pK_a for acetic and pyruvic acid allow interfacial water molecules to accept protons at lower pH

as compared to the bulk.[17,18] Due to the differences aerosols have been shown to exhibit compared to the bulk phase and to the complexity within atmospheric aerosols themselves, there is a need to better understand and characterize the microphysical, chemical and optical properties of these unique microenvironments. By replacing known bulk phase reaction mechanisms and kinetics being used in atmospheric models with specific aerosol chemistry mechanisms and kinetics, atmospheric chemical models will be able to mitigate discrepancies between model predictions and field observations.

1.1.1. Mineral Dust, Fly Ash and Metal Oxides in the Atmosphere

Mineral dust is a major component of atmospheric aerosols originating mainly from the arid and semi-arid regions of the world that account for approximately one-third of the global land area.[1] The Saharan and Gobi desert regions of north Africa and central Asia, respectively, are the largest sources of mineral dust. Mineral dust originates from crustal material (soil, clays, etc.) blown into the atmosphere, therefore, the composition will vary depending on the source region. The main elements, and their oxides, found in crustal material are aluminum, silicon, iron, calcium, sodium, magnesium, potassium, titanium, barium, and manganese.[1,6] Fly ash is produced during the combustion of fossil fuels and directly emitted into the atmosphere. The composition of fly ash depends on the type of fuel but consists mainly of oxides of aluminum, calcium, iron and silicon as well as elemental carbon (soot) and magnesium, sulfur, titanium, phosphorous, potassium and sodium.[2]

Mineral dust, fly ash, and metal oxides are all metal-containing aerosols that can participate in various atmospheric chemical processes by dissolving in atmospheric liquids

or acting as a platform for heterogeneous or multiphase reactions. As a result of the dissolution of mineral dust and other metal-containing aerosols, dissolved transition metals are ubiquitous in atmospheric liquids. Transition metals, such as iron, have several oxidation states that allow them to catalyze chemical reactions. Among those transition metals commonly found in atmospheric liquid phases, iron, copper, and manganese are the major metals involved in chemical processes.[19] As solid particles or dissolved ions, metal-containing aerosols play an important role in atmospheric chemical processes.

1.2. Sulfur oxidation chemistry

Sulfur dioxide is a common atmospheric gas that comes from a variety of natural and anthropogenic sources. Volcanoes are the primary natural source of SO_2 however, the majority of the SO_2 found in the atmosphere comes from anthropogenic sources. Coal burning is the largest anthropogenic source of SO_2 in addition to the combustion of other sulfur-containing fuels from industrial processes, like ore refineries, and transportation sources, such as automobiles and ships.[1,2,4] Once emitted into the atmosphere, SO_2 can further react to produce sulfuric acid, which contributes to acid rain, or to form particulate sulfate which can reduce visibility and influence Earth's radiation balance from the interaction of light with the newly formed aerosols particles. The major sinks for SO_2 include dry deposition, photochemical reactions, reactions on particulate surfaces and

dissolution into atmospheric waters; in fact, the oxidation of aqueous phase SO_2 is considered to be the major sink of atmospheric SO_2.[1]

Due to its high solubility, sulfur dioxide is commonly found in the atmosphere in the aqueous phase rather than gas phase. The dissolution of SO_2 in water occurs via reactions R1.1-R1.3.

$$\boldsymbol{SO_2 + H_2O \rightleftharpoons SO_2 \cdot H_2O} \quad \text{(R1.1)}$$

$$\boldsymbol{SO_2 \cdot H_2O \rightleftharpoons HSO_3^- + H^+} \quad \text{(R1.2)}$$

$$\boldsymbol{HSO_3^- \rightleftharpoons SO_3^{2-} + H^+} \quad \text{(R1.3)}$$

The dissolved SO_2 may be present in the form of $SO_2 \cdot H_2O$, HSO_3^- or SO_3^{2-} based on acidity. Figure 1.3 shows the relative fraction of each species as a function of pH. At atmospherically relevant pH values (~ 2-7) dissolved SO_2 will be present primarily as the bisulfite ion, HSO_3^-.[1] Dissolved SO_2 can then undergo further aqueous phase or multiphase reactions in the atmosphere to produce compounds such as sulfate or various organosulfur compounds.

1.2.1. Inorganic S(IV) oxidation

Sulfate aerosols are produced from the inorganic oxidation of SO_2 via gas phase reactions, heterogeneous oxidation with ozone on mineral dust surfaces, or through aqueous phase chemistry of dissolved SO_2. Several atmospheric sulfate formation pathways are summarized in Figure 1.4. These pathways include oxidation of dissolved SO_2 by various oxidants including H_2O_2, O_3, O_2, etc. Previous studies have shown that sulfate production can be enhanced by the catalytic oxidation of aqueous S(IV) in the

presence of transition metal ions.[20–22] In fact, oxidation catalyzed by transition metal ions is reported as the major in-cloud oxidation pathway of SO_2.[23] Additionally, modeling studies have found that this mechanism contributes 9-17% to the global sulfate budget.[24] Another study found that transition metal ion catalysis is responsible for about 50% of sulfate production in polluted industrial regions in northern Eurasia.[24,25] The main mechanism for the aqueous phase transition metal ion catalyzed S(IV) oxidation is summarized in reactions R1.4-R1.9.[22]

$$\mathbf{SO_3^{2-} + M^{n+} \rightleftharpoons SO_3^{\bullet -} + M^{(n-1)+}} \quad \text{(R1.4)}$$

$$\mathbf{SO_3^{\bullet -} + O_2 \rightleftharpoons SO_5^{\bullet -}} \quad \text{(R1.5)}$$

$$\mathbf{SO_5^{\bullet -} + SO_3^{2-} \rightleftharpoons SO_5^{2-} + SO_3^{\bullet -}} \quad \text{(R1.6)}$$

$$\mathbf{SO_5^{\bullet -} + SO_3^{2-} \rightleftharpoons SO_4^{2-} + SO_4^{\bullet -}} \quad \text{(R1.7)}$$

$$\mathbf{SO_3^{2-} + SO_5^{2-} \rightleftharpoons 2\,SO_4^{2-}} \quad \text{(R1.8)}$$

$$\mathbf{SO_4^{\bullet -} + SO_3^{2-} \rightleftharpoons SO_4^{2-} + SO_3^{\bullet -}} \quad \text{(R1.9)}$$

A similar mechanism can be written for the oxidation of S(IV) in the form of HSO_3^-.

Sulfate aerosols have been well studied to understand their impact on climate. Sulfate has been shown to directly affect the climate by scattering radiation causing an overall cooling effect.[8] Additionally, sulfate aerosols can interact with clouds indirectly thereby affecting climate by altering cloud microphysics and participating in additional

atmospheric chemical processes; the effects of this indirect interaction not well understood contributing to the large uncertainty associated with aerosol effects (Figure 1.2).[1,6,8,20,26]

Although many atmospheric sulfur oxidation pathways and sulfate formation mechanisms have been elucidated, current atmospheric models underestimate sulfate concentrations and therefore do not accurately account for the effects of particulate sulfate.[20,27–29] Recently, some of the highest levels of particulate sulfate have been measured in China, despite the fact that gas-phase SO_2 levels have remained constant, making it difficult to understand the enhanced levels of sulfate based on the reaction mechanisms currently used in atmospheric chemistry models.[29,30] This underestimate of sulfate concentration is attributed to the uncertainty in aerosol chemistry due to a lack of experimental data and poor understanding of the factors that affect these sulfur oxidation processes and sulfate formation pathways.[20,28–33] Gaining a better understanding of sulfate formation pathways and sulfur oxidation processes, and the factors that influence this chemistry, would provide valuable information to be applied to updating current climate models and achieving better agreement between models and field observations.

1.2.2. Organosulfur

In addition to the formation of inorganic sulfate, atmospheric S(IV) and S(VI) can also react with volatile organic compounds (VOCs) to form various organosulfur compounds such as organosulfites and organosulfates. Organosulfates have recently gained focus as an important group of continental secondary organic aerosol accounting for up to 5-10% of total organic aerosol mass in the continental United States.[34–43] Organosulfates, and other organosulfur compounds, can be formed through a variety of mechanisms

including aqueous phase reactions, photochemical and heterogeneous reactions at the gas-liquid interface or on mineral dust.[44–50] Some recent studies have reported the formation of organosulfur compounds from reactions of SO_2 with unsaturated fatty acids and long-chain alkenes as well as mineral-mediated photochemical reactions of aqueous sulfate with methacrolein or aqueous phase reactions of sulfite/bisulfite with methyl vinyl ketone and methacrolein.[44,49,50] Results from these studies suggest that the reaction rates and mechanisms can be affected by numerous factors including physical state of the reactants, nature of the double bonds (cis, trans, terminal), use of irradiation, the presence of an acid group, and the presence of transition metal ions.

The formation of organosulfate can be categorized by two primary mechanisms: epoxide mechanism and radical mechanism. In the epoxide mechanisms, organosulfates are formed from acid-catalyzed ring opening reactions of epoxide-monoterpene oxides and isoprene-derived epoxydiol.[35,51–53] In the radical mechanism, organosulfates are formed from sulfate and bisulfate radicals, formed in the aqueous phase, interacting with C=C bonds or other radical species.[50,54–56] A major source of uncertainty associated with organosulfate and other organosulfur compounds stems from the lack of understanding of these various formation mechanisms. Information for elucidating formation mechanisms, in conjunction with identification and quantification of products, is imperative to accurately modeling the atmosphere.

1.3. Thesis Objectives

The main objective of this thesis is to obtain a better understanding of the various factors influencing the oxidation of S(IV) to S(VI) in the atmosphere and to further develop

the Aerosol Optical Tweezer system to study the chemistry within individual aerosols. Focusing on laboratory experiments using a spectroscopic and analytical techniques, the influence of various atmospherically relevant conditions on sulfur oxidation chemistry involving transition metal catalysts present in authentic dust samples and metal oxides has been investigated. Additionally, changes within individual droplets were investigated using the Aerosol Optical Tweezer. Some of the main questions this thesis aims to answer are: how is the catalytic oxidation of S(IV) to S(VI) influenced by pH, ionic strength, and presence of organics, what organosulfur products are formed from the oxidation of S(IV) in the presence of atmospherically relevant organic compounds, and how can an Aerosol Optical Tweezer be used to examine aqueous phase or multiphase chemistry of individual aerosols droplets?

A variety of spectroscopic and analytical methods were used to investigate sulfur oxidation chemistry. These methods include attenuated total reflectance-Fourier transform infrared spectroscopy and confocal Raman spectroscopy. Additional experimental details, such as batch reactor design, are also presented.

In addition to the spectroscopic and analytical techniques aforementioned, the Aerosol Optical Tweezer system is an experimental method developed to study the chemistry occurring within individual optically levitated micron-sized droplets and is described in detail in Chapter 3. Details of the theoretical background of the Aerosol Optical Tweezer system are provided, including the physics of trapping a particle and an introduction to cavity enhanced Raman scattering and whispering gallery modes. The apparatus itself and general methods for trapping a particle are also described. Various

experiments conducted to characterize the Aerosol Optical Tweezer are also discussed in this chapter.

In Chapter 4, changes in aerosol pH upon droplet coalescence in an Aerosol Optical Tweezer are investigated. In particular, we show that the pH within individual aqueous aerosol droplets, ~8 μm in diameter, can be titrated via droplet coalescence. Using conjugate acid/base pairs to infer pH changes, the pH of trapped droplets is determined before and after introduction of smaller droplets containing a strong acid. The pH change upon coalescence of the acid within the trapped droplet is calculated using Specific Ion Interaction Theory (SIT).

In Chapter 5, the role of glyoxal on the oxidation of S(IV) in acidic aqueous solutions catalyzed by iron in the form of aqueous Fe^{3+} ions and solid iron oxide was investigated under different experimental conditions. Results from these studies show that the presence of glyoxal inhibits the catalytic oxidation of S(IV) with both iron ions and solid iron oxide particles. As will be discussed, the effects of glyoxal on the catalytic oxidation of S(IV) are highly dependent on the mechanism, form of iron (dissolved versus solid), and the ambient conditions, such as pH and concentration.

In Chapter 6, the influence of a range of variables, including pH, ionic strength, and presence of organic compounds, on the aqueous phase oxidation of S(IV) in the presence and absence of transition metals are investigated. As will be discussed in more detail, the effect of ionic strength on sulfur oxidation varies depending on the pH and type of transition metal ion present at low ionic strength but at high ionic strength S(IV) oxidation to S(VI) is greatly inhibited. The presence of atmospherically relevant organic compounds,

glyoxal and methacrolein, also inhibit the transition metal catalyzed oxidation of inorganic S(IV) to inorganic S(VI).

1.4. Figures

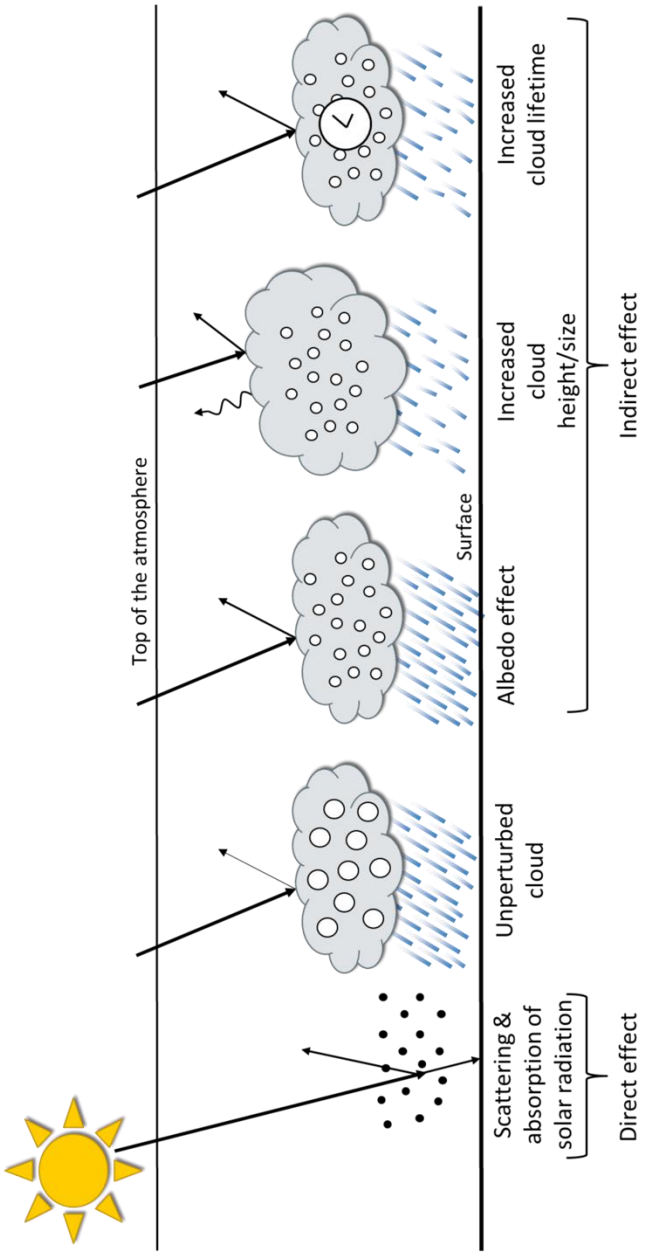

Figure 1.1: Schematic of the direct and indirect effects of aerosols on the atmosphere and climate. Aerosols directly affect the environment by scattering and absorbing radiation. Indirectly, aerosols impact cloud microphysics therefore influencing cloud albedo, height/size, and lifetime all of which alter Earth's radiation balance. Adapted from IPCC 4th assessment report (reference 7).

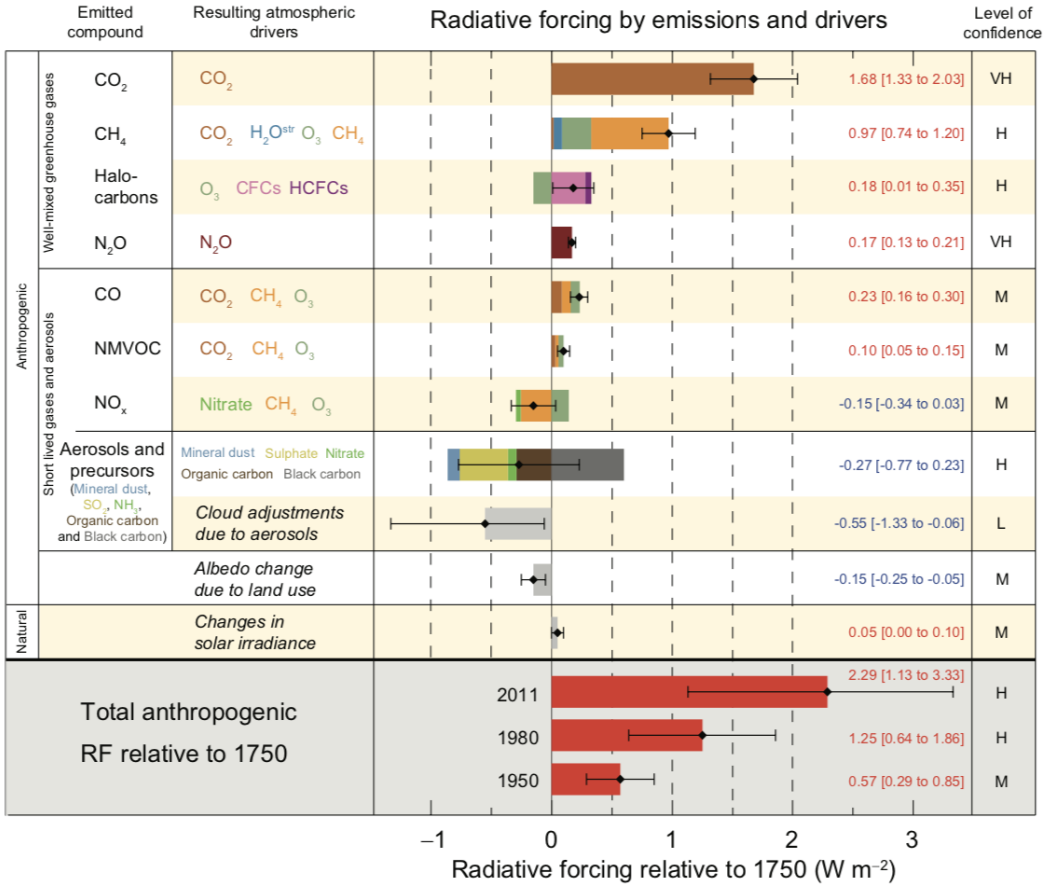

Figure 1.2: Radiative forcing estimates by emissions and drivers from 2011 relative to 1750, associated uncertainty intervals and levels of confidence associated with each estimate. Aerosols and precursors are separated into two categories based on their direct effect with radiation and the cloud adjustments due to aerosols (i.e. indirect effect). Image from IPCC 4th assessment report (reference 7).

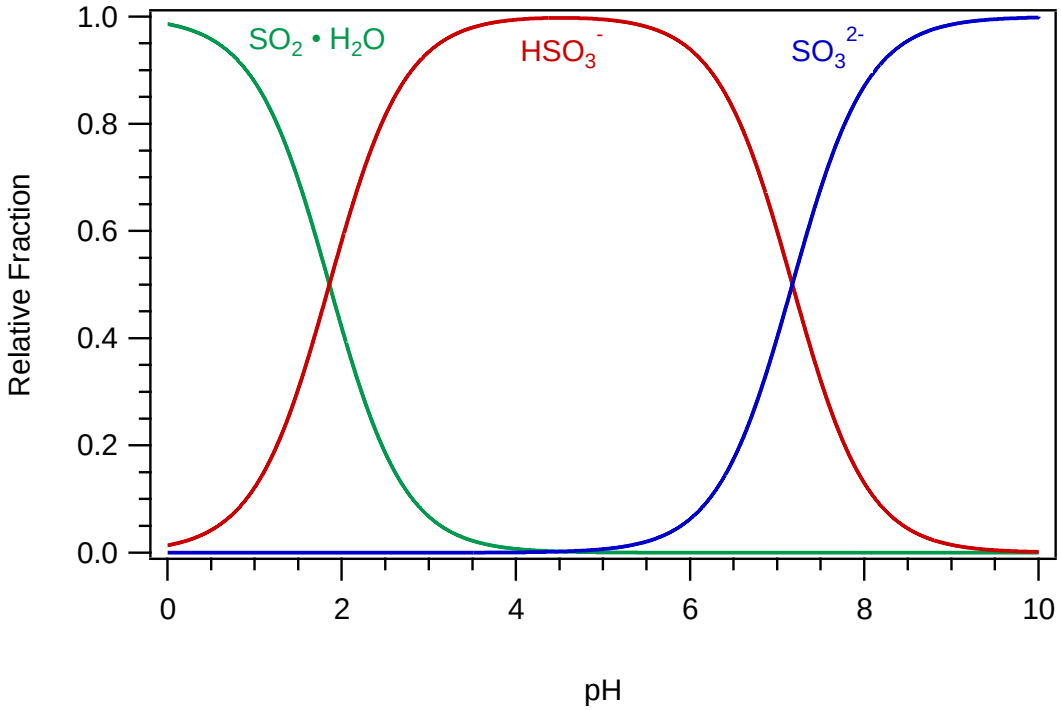

Figure 1.3: Relative abundance of dissolved S(IV) species as a function of pH. At atmospherically relevant pH values (~2-7), dissolved S(IV) is predominately present in the form of the bisulfite ion, HSO_3^- (red).

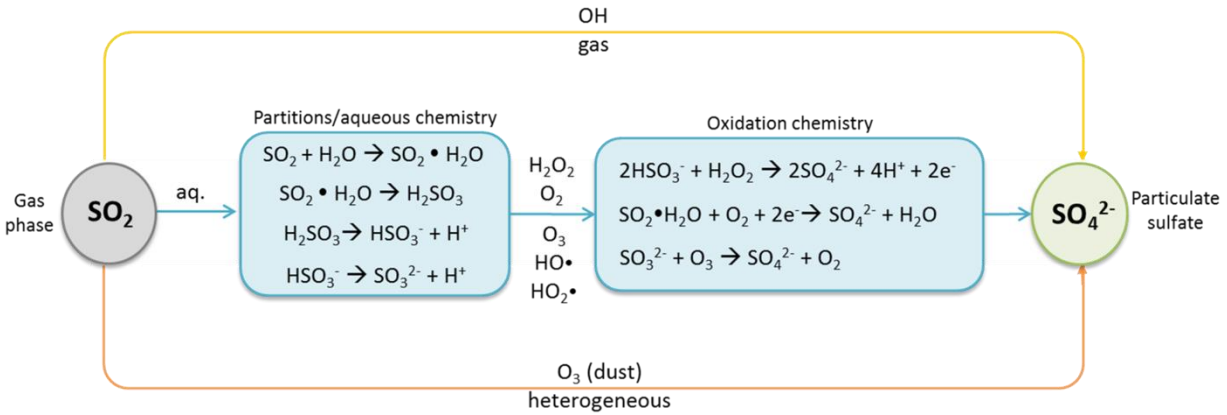

Figure 1.4: Summary of sulfate production pathways from the oxidation of sulfur dioxide. Formation pathways include gas phase and heterogeneous reaction with dust particles in addition to aqueous phase reactions with various oxidants.

1.5. References

(1) Seinfeld, J. H.; Pandis, S. N. *Atmospheric Chemistry and Physics : From Air Pollution to Climate Change*, 2nd ed.; John Wiley & Sons, Inc.: Hoboken, 2006.

(2) Manahan, S. E. *Environmental Chemistry*, 7th ed.; Lewis : Boca Raton, 1999.

(3) Pöschl, U. Atmospheric Aerosols: Composition, Transformation, Climate and Health Effects. *Angew. Chemie Int. Ed.* **2005**, *44*, 7520–7540.

(4) Baird, C.; Cann, M. *Environmental Chemistry*, 5th ed.; W. F. Freeman: New York, 2012.

(5) Mahowald, N.; Ward, D. S.; Kloster, S.; Flanner, M. G.; Heald, C. L.; Heavens, N. G.; Hess, P. G.; Lamarque, J.-F.; Chuang, P. Y. Aerosol Impacts on Climate and Biogeochemistry. *Annu. Rev. Environ. Resour.* **2011**, *36*, 45–74.

(6) Usher, C. R.; Michel, A. E.; Grassian, V. H. Reactions on Mineral Dust. *Chem. Rev.* **2003**, *103*, 4883–4939.

(7) Toon, O. B. African Dust in Florida Clouds. *Nature*. August 7, 2003, pp 623–624.

(8) IPCC. *Climate Change 2007: The Physical Science Basis. Contribution of Working Group I to the Fourth Assessment Report of the Intergovernmental Panel on Climate ChangeNo Title*; Cambridge University Press: Cambridge, United Kingdom and New York, NY, USA, 2007.

(9) Huang, Y.; Barraza, K. M.; Kenseth, C. M.; Zhao, R.; Wang, C.; Beauchamp, J. L.; Seinfeld, J. H. Probing the OH Oxidation of Pinonic Acid at the Air-Water Interface Using Field-Induced Droplet Ionization Mass Spectrometry (FIDI-MS). *J. Phys. Chem. A* **2018**, *122*, 6445–6456.

(10) Al-Abadleh, H. A. Review of the Bulk and Surface Chemistry of Iron in Atmospherically Relevant Systems Containing Humic-like Substances. *RSC Advances*. Royal Society of Chemistry 2015, pp 45785–45811.

(11) Fan, H.; Wenyika Masaya, T.; Goulay, F. Effect of Surface-Bulk Partitioning on the Heterogeneous Oxidation of Aqueous Saccharide Aerosols. *Phys. Chem. Chem. Phys.* **2019**, *21*, 2992–3001.

(12) Finlayson-Pitts, B. J. Reactions at Surfaces in the Atmosphere: Integration of Experiments and Theory as Necessary (but Not Necessarily Sufficient) for Predicting the Physical Chemistry of Aerosols. *Physical Chemistry Chemical Physics*. **2009**, pp 7760–7779.

(13) Pipal, A. S.; Singh, S.; Satsangi, G. P. Study on Bulk to Single Particle Analysis of Atmospheric Aerosols at Urban Region. *Urban Clim.* **2019**, *27*, 243–258.

(14) Nissenson, P.; Knox, C. J. H.; Finlayson-Pitts, B. J.; Phillips, L. F.; Dabdub, D. Enhanced Photolysis in Aerosols: Evidence for Important Surface Effects. *Phys. Chem. Chem. Phys.* **2006**, *8*, 4700–4710.

(15) Lee, J. K.; Banerjee, S.; Nam, H. G.; Zare, R. N. Acceleration of Reaction in Charged Microdroplets. *Q. Rev. Biophys.* **2015**, *48*, 437–444.

(16) Lin, P.; Wu, Z.; Chen, M.; Li, Y.; Chen, W.; Huang, T.; Lee, Y.; Wang, C. C. Interfacial Solvation and Surface pH of Phenol and Dihydroxybenzene Aqueous Nanoaerosols Unveiled by Aerosol VUV Photoelectron Spectroscopy. *J. Phys. Chem. B* **2017**, *121*, 1054–1067.

(17) Eugene, A. J.; Pillar, E. A.; Colussi, A. J.; Guzman, M. I. Enhanced Acidity of Acetic and Pyruvic Acids on the Surface of Water. *Langmuir* **2018**, *34*, 9307–9313.

(18) Wellen, B. A.; Lach, E. A.; Heather C Allen. Surface pKa of Octanoic, Nonanoic, and Decanoic Fatty Acids at the Air-Water Interface: Applications to Atmospheric Aerosol Chemistry. *Phys. Chem. Chem. Phys* **2017**, *19*, 26551–26558.

(19) Deguillaume, L.; Leriche, M.; Desboeufs, K.; Mailhot, G.; George, C.; Chaumerliac, N. Transition Metals in Atmospheric Liquid Phases: Sources, Reactivity, and Sensitive Parameters. *Chem. Rev.* **2005**, *105*, 3388–3431.

(20) Huang, X.; Song, Y.; Zhao, C.; Li, M.; Zhu, T.; Zhang, Q.; Zhang, X. Pathways of Sulfate Enhancement by Natural and Anthropogenic Mineral Aerosols in China. *J. Geophys. Res. Atmos.* **2014**, *119*, 14165–14179.

(21) Sullivan, R. C.; Guazzotti, S. A.; Sodeman, D. A.; Prather, K. A. Direct Observations of the Atmospheric Processing of Asian Mineral Dust. *Atmos. Chem. Phys.* **2007**, *7*, 1213–1236.

(22) Brandt, C.; van Eldik, R. Transition Metal-Catalyzed Oxidation of Sulfur(IV) Oxides. Atmospheric-Relevant Processes and Mechanisms. *Chem. Rev.* **1995**, *95*, 119–190.

(23) Harris, E.; Sinha, B.; Van Pinxteren, D.; Tilgner, A.; Fomba, K. W.; Schneider, J.; Roth, A.; Gnauk, T.; Fahlbusch, B.; Mertes, S.; Taehyoung, L.; Collett, J.; Foley, S.; Borrmann, S.; Hoppe, P.; Herrmann, H. Enhanced Role of Transition Metal Ion Catalysis During In-Cloud Oxidation of SO 2. *Science (80-.).* **2013**, *340*, 727–730.

(24) Alexander, B.; Park, R. J.; Jacob, D. J.; Gong, S. Transition Metal-Catalyzed Oxidation of Atmospheric Sulfur: Global Implications for the Sulfur Budget. *J. Geophys. Res.* **2009**, *114*, D02309.

(25) Li, J.; Wang, Z.; Zhuang, G.; Luo, G.; Sun, Y.; Wang, Q. Mixing of Asian Mineral Dust with Anthropogenic Pollutants over East Asia: A Model Case Study of a Super-Duststorm in March 2010. *Atmos. Chem. Phys.* **2012**, *12*, 7591–7607.

(26) Kiehl, J. T.; Briegleb, B. P. The Relative Roles of Sulfate Aerosols and Greenhouse Gases in Climate Forcing. *Science (80-.).* **1993**, *260*, 311–314.

(27) Ervens, B. Modeling the Processing of Aerosol and Trace Gases in Clouds and Fogs. *Chem. Rev.* **2015**, *115*, 4157–4198.

(28) Luo, C.; Wang, Y.; Mueller, S.; Knipping, E. Diagnosis of an Underestimation of

Summertime Sulfate Using the Community Multiscale Air Quality Model. *Atmos. Environ.* **2011**, *45*, 5119–5130.

(29) He, H.; Wang, Y.; Ma, Q.; Ma, J.; Chu, B.; Ji, D.; Tang, G.; Liu, C.; Zhang, H.; Hao, J. Mineral Dust and NOx Promote the Conversion of SO2 to Sulfate in Heavy Pollution Days. *Sci. Rep.* **2014**, *4*.

(30) Wang, Y.; Zhang, Q.; Jiang, J.; Zhou, W.; Wang, B.; He, K.; Duan, F.; Zhang, Q.; Philip, S.; Xie, Y. Enhanced Sulfate Formation during China's Severe Winter Haze Episode in January 2013 Missing from Current Models. *J. Geophys. Res.* **2014**, *119*, 10,425-10,440.

(31) Zhang, X. Y.; Wang, Y. Q.; Niu, T.; Zhang, X. C.; Gong, S. L.; Zhang, Y. M.; Sun, J. Y. Atmospheric Aerosol Compositions in China: Spatial/Temporal Variability, Chemical Signature, Regional Haze Distribution and Comparisons with Global Aerosols. *Atmos. Chem. Phys.* **2012**, *12*, 779–799.

(32) Zheng, B.; Zhang, Q.; Zhang, Y.; He, K. B.; Wang, K.; Zheng, G. J.; Duan, F. K.; Ma, Y. L.; Kimoto, T. Heterogeneous Chemistry: A Mechanism Missing in Current Models to Explain Secondary Inorganic Aerosol Formation during the January 2013 Haze Episode in North China. *Atmos. Chem. Phys.* **2015**, *15*, 2031–2049.

(33) Zheng, G. J.; Duan, F. K.; Su, H.; Ma, Y. L.; Cheng, Y.; Zheng, B.; Zhang, Q.; Huang, T.; Kimoto, T.; Chang, D.; Poschl, U.; Cheng, Y. F.; He, K. B. Exploring the Severe Winter Haze in Beijing: The Impact of Synoptic Weather, Regional Transport and Heterogeneous Reactions. *Atmos. Chem. Phys.* **2015**, *15*, 2969–2983.

(34) Chan, M. N.; Surratt, J. D.; Claeys, M.; Edgerton, E. S.; Tanner, R. L.; Shaw, S. L.; Zheng, M.; Knipping, E. M.; Eddingsaas, N. C.; Wennberg, P. O.; Seinfeld, J. H. Characterization and Quantification of Isoprene-Derived Epoxydiols in Ambient Aerosol in the Southeastern United States. *Environ. Sci. Technol.* **2010**, *44*, 4590–4596.

(35) Froyd, K. D.; Murphy, S. M.; Murphy, D. M.; de Gouw, J. A.; Eddingsaas, N. C.; Wennberg, P. O. Contribution of Isoprene-Derived Organosulfates to Free Tropospheric Aerosol Mass. *Proc. Natl. Acad. Sci. U. S. A.* **2010**, *107*, 21360–21365.

(36) Gao, S.; Surratt, J. D.; Knipping, E. M.; Edgerton, E. S.; Shahgholi, M.; Seinfeld, J. H. Characterization of Polar Organic Components in Fine Aerosols in the Southeastern United States: Identity, Origin, and Evolution. *J. Geophys. Res.* **2006**, *111*, D14314.

(37) Hatch, L. E.; Creamean, J. M.; Ault, A. P.; Surratt, J. D.; Chan, M. N.; Seinfeld, J. H.; Edgerton, E. S.; Su, Y.; Prather, K. A. Measurements of Isoprene-Derived Organosulfates in Ambient Aerosols by Aerosol Time-of-Flight Mass Spectrometry - Part 1: Single Particle Atmospheric Observations in Atlanta. *Environ. Sci. Technol.* **2011**, *45*, 5105–5111.

(38) Iinuma, Y.; Müller, C.; Berndt, B. ; Böge, O.; Claeys, M.; Herrmann, H. Evidence for the Existence of Organosulfates from β-Pinene Ozonolysis in Ambient Secondary Organic Aerosol. *Environ. Sci. Technol.* **2007**, *41*, 6678–6683.

(39) Lukács, H.; Gelencsér, A.; Hoffer, A.; Kiss, G.; Horváth, K.; Hartyáni, Z. Quantitative Assessment of Organosulfates in Size-Segregated Rural Fine Aerosol. *Atmos. Chem. Phys.* **2009**, *9*, 231–238.

(40) Surratt, J. D.; Gómez-González, Y.; Chan, A. W. H.; Vermeylen, R.; Shahgholi, M.; Kleindienst, T. E.; Edney, E. O.; Offenberg, J. H.; Lewandowski, M.; Jaoui, M.; Maenhaut, W.; Claeys, M.; Flagan, R. C.; Seinfeld, J. H. Organosulfate Formation in Biogenic Secondary Organic Aerosol. *J. Phys. Chem. A* **2008**, *112*, 8345–8378.

(41) Surratt, J. D.; Kroll, J. H.; Kleindienst, T. E.; Edney, E. O.; Claeys, M.; Sorooshian, A.; Ng, N. L.; Offenberg, J. H.; Lewandowski, M.; Jaoui, M; Flagan, R. C.; Seinfeld, J. H. Evidence for Organosulfates in Secondary Organic Aerosol. *Environ. Sci. Technol.* **2007**, *41*, 517–527.

(42) Hettiyadura, A. P. S.; Jayarathne, T.; Baumann, K.; Goldstein, A. H.; de Gouw, J. A.; Koss, A.; Keutsch, F. N.; Skog, K.; Stone, E. A. Qualitative and Quantitative Analysis of Atmospheric Organosulfates in Centreville, Alabama. *Atmos. Chem. Phys.* **2017**, *17*, 1343–1359.

(43) Tolocka, M. P.; Turpin, B. Contribution of Organosulfur Compounds to Organic Aerosol Mass. *Environ. Sci. Technol.* **2012**, *46*, 7978–7983.

(44) Huang, L.; Cochran, R. E.; Coddens, E. M.; Grassian, V. H. Formation of Organosulfur Compounds through Transition Metal Ion-Catalyzed Aqueous Phase Reactions. *Environ. Sci. Technol. Lett.* **2018**, *5*, 315–321.

(45) Coddens, E. M.; Huang, L.; Wong, C.; Grassian, V. H. Influence of Glyoxal on the Catalytic Oxidation of S(IV) in Acidic Aqueous Media. *ACS Earth Sp. Chem.* **2019**, *3*, 142–149.

(46) Rudziński, K. J.; Gmachowski, L.; Kuznietsova, I. Reactions of Isoprene and Sulphoxy Radical-Anions – a Possible Source of Atmospheric Organosulphites and Organosulphates. *Atmos. Chem. Phys.* **2009**, *9*, 2129–2140.

(47) Shang, J.; Passananti, M.; Dupart, Y.; Ciuraru, R.; Tinel, L.; Rossignol, S.; Perrier, S.; Zhu, T.; George, C. SO2 Uptake on Oleic Acid: A New Formation Pathway of Organosulfur Compounds in the Atmosphere. *Environ. Sci. Technol. Lett.* **2016**, *3*, 67–72.

(48) Shen, X.; Wu, H.; Zhao, Y.; Huang, D.; Huang, L.; Chen, Z. Heterogeneous Reactions of Glyoxal on Mineral Particles: A New Avenue for Oligomers and Organosulfate Formation. *Atmos. Environ.* **2016**, *131*, 133–140.

(49) Schmidt, M.; Jansen van Beek, S. M.; Abou-Ghanem, M.; Oliynyk, A. O.; Locock, A. J.; Styler, S. A. Production of Atmospheric Organosulfates via Mineral-Mediated Photochemistry. *ACS Earth Sp. Chem.* **2019**, *3*, 424–431.

(50) Passananti, M.; Kong, L.; Shang, J.; Dupart, Y.; Perrier, S.; Chen, J.; Donaldson, D. J.; George, C. Organosulfate Formation through the Heterogeneous Reaction of Sulfur Dioxide with Unsaturated Fatty Acids and Long-Chain Alkenes. *Angew. Chemie Int. Ed.* **2016**, *55*, 10336–10339.

(51) Darer, A. I.; Cole-Filipiak, N. C.; O'Connor, A. E.; Elrod, M. J. Formation and Stability of Atmospherically Relevant Isoprene-Derived Organosulfates and Organonitrates. *Environ. Sci. Technol.* **2011**, *45*, 1895–1902.

(52) Eddingsaas, N. C.; VanderVelde, D. G.; Wennberg, P. O. Kinetics and Products of the Acid-Catalyzed Ring-Opening of Atmospherically Relevant Butyl Epoxy Alcohols. *J. Phys. Chem. A* **2010**, *114*, 8106–8113.

(53) Surratt, J. D.; Chan, A. W. H.; Eddingsaas, N. C.; Chan, M.; Loza, C. L.; Kwan, A. J.; Hersey, S. P.; Flagan, R. C.; Wennberg, P. O.; Seinfeld, J. H. Reactive Intermediates Revealed in Secondary Organic Aerosol Formation from Isoprene. *Proc. Natl. Acad. Sci. U. S. A.* **2010**, *107*, 6640–6645.

(54) Nozière, B.; Ekström, S.; Alsberg, T.; Holmström, S. Radical-Initiated Formation of Organosulfates and Surfactants in Atmospheric Aerosols. *Geophys. Res. Lett.* **2010**, *37*, L05806.

(55) Tang, Y.; Thorn, R. P.; Mauldin, R. L.; Wine, P. H. Kinetics and Spectroscopy of the SO4− Radical in Aqueous Solution. *J. Photochem. Photobiol. A Chem.* **1988**, *44*, 243–258.

(56) Wang, Y.; Hu, M.; Guo, S.; Wang, Y.; Zheng, J.; Yang, Y.; Zhu, W.; Tang, R.; Li, X.; Liu, Y.; Le Breton, M.; Du, Z.; Shang, D.; Wu, Y.; Wu, Z.; Song, Y.; Luo, S.; Hallquist, M.; Yu, J. The Secondary Formation of Organosulfates under Interactions between Biogenic Emissions and Anthropogenic Pollutants in Summer in Beijing. *Atmos. Chem. Phys.* **2018**, *18*, 10693–10713.

Chapter 2 Experimental Methods

2.1. Attenuated Total Reflectance-Fourier Transform Infrared Spectroscopy

Infrared (IR) spectroscopy is a well-established vibrational spectroscopy method used to ascertain information on molecular structure and molecular interactions of a wide variety of sample types. Due to its ability to analyze a wide range of molecules/samples in a non-destructive manner, IR spectroscopy has a variety of applications across many scientific disciplines including pharmaceuticals, forensics, and environmental sciences such as atmospheric chemistry or water chemistry. IR spectroscopy measures transitions in vibrational energy levels at resonant frequencies. Resonant frequencies are the specific frequencies at which the frequency of the incident radiation matches the frequency of the vibration within the molecule.[1] At these frequencies, excitation from the ground vibrational level to a higher energy level occurs due to the absorption of a photon and this change in energy is detected. Resonant frequencies are characteristic of the molecule's structure and provide a "fingerprint" of the molecule. Based on the selection rule for IR absorption, in order for a molecule to be IR active, there must be a change in the electric dipole moment of the molecule upon absorption of the incident IR radiation.

Attenuated total reflectance-Fourier transform infrared spectroscopy (ATR-FTIR) is based on the total internal reflection of an infrared beam at the boundary between two media. Therefore, ATR-FTIR spectroscopy can be used to study the interface between two phases, such as at the solid-liquid interface.[2] For example, ATR-FTIR has been used to

study adsorption from solution onto solid particles, such as protein adsorption onto nanoparticles or acid or ion adsorption onto metal oxide or mineral surfaces.[3–9]

A pictorial representation of total internal reflection in ATR spectroscopy is shown in Figure 2.1. An ATR accessory operates by measuring changes that occur in a totally internally reflected IR beam when that beam propagates between an optically dense medium (with refractive index n_1) and approaches an optically rare medium (with refractive index n_2).[10–12] At each reflection an evanescent wave is formed in the optically rare medium if the infrared beam totally internally reflects at an angle of incidence (θ) that is greater than the critical angle (θ_c). The critical angle is dependent on the refractive indices of both media as shown by equation 2.1.

$$\boldsymbol{\theta_c = \sin^{-1}\left(\frac{n_2}{n_1}\right)} \qquad \text{(Eq. 2.1)}$$

The depth of penetration (d_p) into the optically rare medium, or sample, is determined by equation 2.2;

$$d_p = \frac{\lambda}{2\pi n_1\sqrt{[\sin^2\theta - (n_2/n_1)^2]}} \qquad \text{(Eq. 2.2)}$$

where λ is the wavelength of light.[11,13] In regions of the IR spectrum where the sample absorbs energy, the IR beam will be attenuated resulting in characteristic absorptions by the IR active species present in the interfacial region. ATR-FTIR can also be quantitative

where the concentration of absorbed species (c) can be calculated from the absorbance (A) using the Beer's law equation 2.3;

$$\boldsymbol{A = \varepsilon l c} \qquad \text{(Eq. 2.3)}$$

where ε is the molar absorptivity and l is the effective path length.[14] The effective path length is dependent on the number of reflections of the IR beam and the penetration depth as defined by equation 2.4;

$$\boldsymbol{l = N d_p} \qquad \text{(Eq. 2.4)}$$

where N is the number of reflections.[11]

ATR-FTIR spectroscopy measurements were taken with a Thermo-Nicolet spectrometer equipped with an MCT/A detector. For experiments with a metal oxide or mineral dust surfaces, an evenly coated thin film was deposited onto a Ge crystal element in a horizontal ATR cell (Pike Technologies, Inc.). The thin film was prepared by pipetting a uniform colloidal suspension of the metal oxide/mineral dust (5 mg in 1 mL of methanol) onto the crystal and drying for at least 30 minutes. Once dry, 1 mL of Optima/Milli-Q water was pipetted onto the thin film and a background water spectrum was collected. The water was then pipetted off and 1 mL of the sample solution (e.g. Na_2SO_3) was added to the surface. For experiments without a thin film, the water and sample solution were pipetted directly onto the crystal surface. To prevent evaporation a glass slide was placed on the Ge

crystal. A total of 200 scans were acquired for each spectrum over the spectral range from 500 to 4000 cm^{-1}.

2.2. Confocal Raman spectroscopy

Raman spectroscopy is a well-established spectroscopic technique used to obtain chemical and physical information of bulk as well as single particle samples. Raman spectroscopy is often used to complement IR spectroscopy and give a complete picture of the vibrational modes of a molecule. For example, Raman and IR spectroscopy have been used together to obtain complete characterization of the vibrational modes of solid or aqueous sulfur oxides.[15–17] While IR spectroscopy measures the absolute frequency at which a molecule absorbs radiation, Raman spectroscopy measures the relative frequencies at which a molecule scatters radiation. Additionally, Raman spectroscopy can be combined with microscopy to conduct single particle analyses. For example, Raman spectroscopy, equipped with confocal microscopy, has been used to study the complex chemical composition of individual sea spray aerosol.[18–20]

In Raman spectroscopy, incident light interacts with a molecule distorting, or polarizing, the electron cloud around the nuclei forming a short-lived virtual state. This virtual state is not stable however, and the photon is quickly re-radiated (i.e. scattered). The photon can be scattered in two ways: elastically or inelastically. Figure 2.2 depicts these scattering processes. Elastic scattering, also referred to as Rayleigh scattering, occurs when the frequency of the scattered photon is the same as the frequency of the incident light; no transfer of energy. Elastic scattering is the dominant scattering process, however, one in every 10^6-10^8 photons that scatter do so inelastically.[1] In inelastic scattering, also known

as Raman scattering, the energy of the scattered photon is different than that of the incident radiation due to energy being transferred to the molecule (Stokes) or energy being transferred to the scattered photon (anti-Stokes).[21] This change in energy with respect to the incident radiation is one vibrational unit different ($\pm$ 1) and what is detected in Raman spectroscopy.

A classical description of the Raman phenomena follows.[1,14,22] The incident electric field, *E*, of a wave of electromagnetic radiation interacts with a molecule and is described by equation 2.5;

$$E = E_0 \cos(2\pi v_0 t) \qquad \text{(Eq. 2.5)}$$

where E_0 is the amplitude of the wave, v_0 is the frequency of the incident radiation and *t* is time. This interaction with the electric cloud of the molecule induces a diploe moment, μ_{ind},

$$\mu_{ind} = \alpha E = \alpha E_0 \cos(2\pi v_0 t) \qquad \text{(Eq. 2.6)}$$

that is proportional to the electric field of the incident radiation and the polarizability of the bond, α. The polarizability is dependent on the distance between nuclei as described by equation 2.7;

$$\alpha = \alpha_0 + (r - r_{eq})\left(\frac{\partial \alpha}{\partial r}\right) \qquad \text{(Eq. 2.7)}$$

where α_0 is the polarizability of the bond at the equilibrium internuclear distance, r_{eq}, and r is the internuclear distance at any time. The change in the internuclear distance is dependent on the frequency of the vibration, v_v, given by equation 2.8;

$$r - r_{eq} = r_m \cos(2\pi v_v t) \qquad \text{(Eq. 2.8)}$$

where r_m is the maximum internuclear distance. Substituting equation 2.8 into equation 2.7 gives a more descriptive expression for the induced dipole:

$$\mu_{ind} = \alpha_0 E_0 \cos(2\pi v_0 t) + E_0 r_m \left(\frac{\partial \alpha}{\partial r}\right) \cos(2\pi v_v t) \cos(2\pi v_0 t) \qquad \text{(Eq. 2.9)}$$

Through the use of the trigonometric identity for the product of two cosines, equation 2.9 can be further simplified to obtain the following expression for the induced dipole of a vibrating molecule:

$$\mu_{ind} = \alpha_0 E_0 \cos(2\pi v_0 t) + \frac{E_0}{2} r_m \left(\frac{\partial \alpha}{\partial r}\right) \cos[2\pi (v_0 - v_v) t] + \frac{E_0}{2} r_m \left(\frac{\partial \alpha}{\partial r}\right) \cos[2\pi (v_0 + v_v) t] \qquad \text{(Eq. 2.10)}$$

In this expression for the induced dipole, the first component describes Rayleigh scattering while the second and third terms describe Stokes and anti-Stokes scattering, respectively. Further, it shows that the induced dipole oscillates at three frequencies: the frequency of the incident radiation (Rayleigh component) and two frequencies where the frequency of the incident radiation has been modulated by vibrational frequency of the bond. Based on the selection rule for Raman scattering, in order for a molecule to be Raman active there

must be a change in the polarizability during the vibration, meaning $\partial\alpha/\partial r$ must be greater than zero.

Bulk aqueous phase Raman spectroscopy measurements were preformed using a LabRam HR Evolution Raman Spectrometer (Horiba). A diagram of the spectrometer is shown in Figure 2.3. The spectrometer is equipped with a 532nm laser and an Olympus BX41 optical microscope with 10x, 50x, and 100X magnification lenses. Additionally, the spectrometer was augmented with a lens attachment for analyzing liquid samples. The attachment allows for analysis of liquid samples held in a cuvette, a clear bottle/jar, or on a microscope slide; these three arrangements are shown in Figure 2.4.

2.3. Aerosol Optical Tweezer (AOT)

The aerosol optical tweezer (AOT-100, Biral) is an instrument that involves the contactless levitation of a single micron sized droplet and is coupled with cavity enhanced Raman spectroscopy. Cavity enhanced Raman spectra contain the vibrational modes as well as whispering gallery modes allowing for the measurement of physiochemical properties, such as size and refractive index, in addition to the chemical composition of the trapped droplet. A more detailed description of the AOT apparatus and experimental methods can be found in Chapter 3.

2.4. Batch reactor studies

Custom water-jacketed glass reactors, shown in Figure 2.5, were used for all dissolution studies. Each glass reactor is equipped with two sampling ports to extract aqueous samples. The reactors are sealed with a cap containing a quartz window for irradiation in photochemical experiments. Each reactor is water-jacketed in order to control

the temperature of the reaction using a refrigerated water circulator (Julabo). During each batch reactor experiment, temperature is held constant, the solutions are continuously stirred, and the reactors remain fully sealed to exclude any additional air from taking part in the reaction. After extraction from the batch reactors, all samples were filtered with a 0.2 μm PTFE filter (Millex) before additional analysis. Additional analysis techniques for product analysis or metal dissolution include ATR-FTIR, UHPLC-ESI- Orbitrap MS, IC and ICP-MS.

2.5. Reagents and materials

2.5.1. Solid Reagents

To study the influence of solid metals on the oxidation of S, commercially available metal oxides and authentic dust samples were used as is, without further purification. The metal oxide and authentic dust samples include: γ-Fe_2O_3 (Alfa Aesar), Mn_2O_3 (99.2%, US Research Nanomaterials Inc.), Arizona test dust (ISO 12103-1 A2 test dust, Powder Technology Inc.), fly ash (SRM 2690, National Institute of Standards and Technology).

2.5.2. Aqueous Reagents

For all aqueous solutions, ultra-pure water was used (Thermo, Barnsted EasyPure-II; ≥18.2 MΩ cm resistivity). Sulfur (IV) and sulfur (VI) sources include: Na_2SO_3 (LabChem), $Na_2S_2O_5$ (>97%, Alfa Aesar) and Na_2SO_4 (Fisher). Organic sources include: glyoxal (40 wt%, Acros), methyl vinyl ketone (MVK, 99%, Sigma-Aldrich) and methacrolein (MACR, 96%, Alfa Aesar). Solution pH was adjusted with hydrochloric acid (HCl, Fisher) or sulfuric acid (H_2SO_4, Fluka). Formaldehyde (HCHO, Fisher) was used to

quench S oxidation reactions. Aqueous iron (III) was prepared from iron chloride ($FeCl_3$, 98%, Alfa Aesar) or iron (III) sulfate hydrate ($Fe_2(SO_4)_3$, Sigma-Aldrich).

2.6. Additional Analysis Techniques

In addition to ATR-FTIR, confocal Raman, and cavity enhanced Raman spectroscopy, a variety of additional analytical techniques were used for product analysis and sample characterization. Such techniques include ion chromatography (IC), inductively coupled plasma- mass spectrometry (ICP-MS) and heated electrospray ionization- high resolution hybrid linear ion trap mass spectrometry (HESI-HRMS) among others. These additional techniques are described in the appropriate chapters.

2.7. Figures

Figure 2.1: Graphical representation of total internal reflection and an evanescent wave involved in ATR-FTIR spectroscopy. As the IR beam reflects at an angle, Θ, that is less than the critical angle, Θ_c, an evanescent wave is produced that penetrates the sample at a specific penetration depth, d_p.

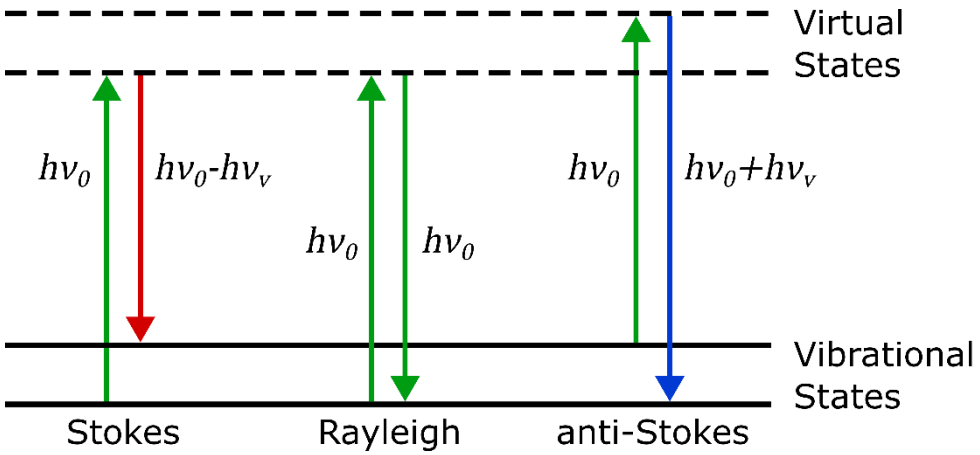

Figure 2.2: Diagram of the Rayleigh and Raman scattering processes. In Rayleigh scattering, incident radiation, with energy $h\nu_0$, polarizes the molecule forming a short-lived virtual state before scattering a photon with the same energy. In Raman scattering, the incident radiation polarizes the molecule forming the virtual state, however, the energy of the scattered photon is different than that of the incident photon giving rise to either Stokes or anti-Stokes scattering.

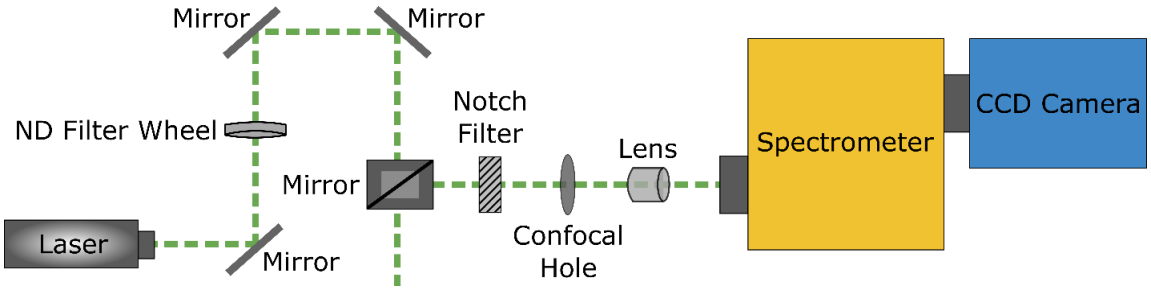

Figure 2.3: Diagram of the confocal Raman spectrometer apparatus used for bulk aqueous studies. The spectrometer is equipped with a 532nm laser.

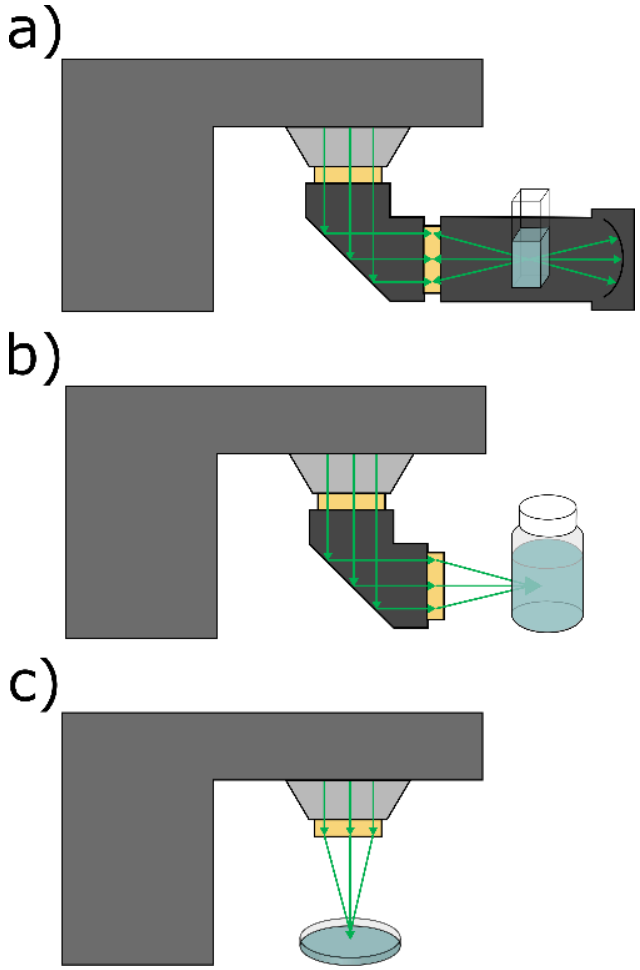

Figure 2.4: Schematic of the lens attachment used to analyze liquid samples with confocal Raman spectroscopy. Aqueous samples, of varying volumes, can be analyzed using a (a) cuvette, (b) glass vial/bottle or (c) microscope slide/small petri dish. Adapted from Horiba, Ltd.

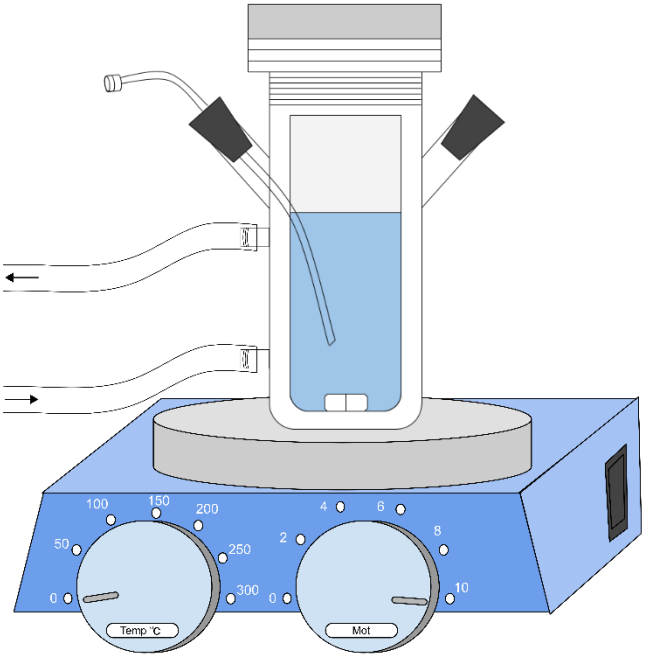

Figure 2.5: A pictorial representation of the batch reactor design. Each reactor is equipped with a cap containing a quartz window for photochemical reactions and two sampling ports. During experiments the sampling ports sealed with rubber stoppers, one of which is fitted with syringe tubbing for sample extraction. The reactor is mounted on a stir plate and continuously stirred throughout the duration of the experiment.

2.8. References

(1) Smith, E.; Dent, G. *Modern Raman Spectroscopy : A Practical Approach*, 2nd ed.; Wiley: West Sussex, England, 2005.

(2) Kolasinski, K. W. *Surface Science : Foundations of Catalysis and Nanoscience*, 3rd ed.; Wiley: West Sussex, United Kingdom, 2012.

(3) Givens, B. E.; Diklich, N. D.; Fiegel, J.; Grassian, V. H. Adsorption of Bovine Serum Albumin on Silicon Dioxide Nanoparticles: Impact of p H on Nanoparticle–protein Interactions . *Biointerphases* **2017**, *12*, 02D404.

(4) Lehman, S. E.; Mudunkotuwa, I. A.; Grassian, V. H.; Larsen, S. C. Nano-Bio Interactions of Porous and Nonporous Silica Nanoparticles of Varied Surface Chemistry: A Structural, Kinetic, and Thermodynamic Study of Protein Adsorption from RPMI Culture Medium. *Langmuir* **2016**, *32*, 731–742.

(5) Xu, Z.; Grassian, V. H. Bovine Serum Albumin Adsorption on TiO2 Nanoparticle Surfaces: Effects of Ph and Coadsorption of Phosphate on Protein-Surface Interactions and Protein Structure. *J. Phys. Chem. C* **2017**, *121*, 21763–21771.

(6) Schuttlefield, J. D.; Larsen, S. C.; Grassian, V. H. ATR-FTIR Spectroscopy in the Undergraduate Chemistry Laboratory. Part II: A Physical Chemistry Laboratory Experiment on Surface Adsorption. *J. Chem. Educ.* **2008**, *85*, 282–284.

(7) Mudunkotuwa, I. A.; Grassian, V. H. Citric Acid Adsorption on TiO2 Nanoparticles in Aqueous Suspensions at Acidic and Circumneutral PH: Surface Coverage, Surface Speciation, and Its Impact on Nanoparticle-Nanoparticle Interactions. *J. Am. Chem. Soc.* **2010**, *132*, 14986–14994.

(8) Pettibone, J. M.; Cwiertny, D. M.; Scherer, M.; Grassian, V. H. Adsorption of Organic Acids on TiO2 Nanoparticles: Effects of PH, Nanoparticle Size, and Nanoparticle Aggregation. *Langmuir* **2008**, *24*, 6659–6667.

(9) Kubicki, J. D.; Schroeter, L. M.; Itoh, M. J.; Nguyen, B. N.; Apitz, S. E. Attenuated Total Reflectance Fourier-Transform Infrared Spectroscopy of Carboxylic Acids Adsorbed onto Mineral Surfaces. *Geochim. Cosmochim. Acta* **1999**, *63*, 2709–2725.

(10) Mudunkotuwa, I. A.; Minshid, A. Al; Grassian, V. H. ATR-FTIR Spectroscopy as a Tool to Probe Surface Adsorption on Nanoparticles at the Liquid–solid Interface in Environmentally and Biologically Relevant Media. *Analyst* **2014**, *139*, 870–881.

(11) Schuttlefield, J. D.; Grassian, V. H. ATR–FTIR Spectroscopy in the Undergraduate Chemistry Laboratory. Part I: Fundamentals and Examples. *J. Chem. Educ.* **2008**, *85*, 279–281.

(12) Hase, M.; Scheffelmaier, R.; Hayden, S.; Rivera, D. Quantitative in Situ Attenuated Total Internal Reflection Fourier Transform Infrared Study of the Isotherms of Poly(Sodium 4-Styrene Sulfonate) Adsorption to a TiO2 Surface over a Range of Cetylpyridinium Bromide Monohydrate Concentration. *Langmuir* **2010**, *26*, 5534–

5543.

(13) Glassford, S. E.; Byrne, B.; Kazarian, S. G. Recent Applications of ATR FTIR Spectroscopy and Imaging to Proteins. *Biochimica et Biophysica Acta - Proteins and Proteomics*. Elsevier B.V. 2013, pp 2849–2858.

(14) Skoog, D. A.; Holler, F. J.; Crouch, S. R. *Principles of Instrumental Analysis*, 6th ed.; CEngage Learning: Delhi, India, 2007.

(15) Davis, A. R.; Chatterjee, R. M. A Vibrational-Spectroscopic Study of the SO2-H2O System. *J. Solution Chem.* **1975**, *4*, 399–412.

(16) Herlinger, A. W.; Long, T. V. An Investigation of the Structure of the Disulfite Ion in Aqueous Solution Using Raman and Infrared Spectroscopies. *Inorg. Chem.* **1969**, *8*, 2661–2665.

(17) Periasamy, A.; Muruganand, S.; Palaniswamy, M. Vibrational Studies of Na2SO4, K2SO4, NaHSO4 and KHSO4 Crystals. *Rasayan J. Chem.* **2009**, *2*, 981–989.

(18) Cochran, R. E.; Laskina, O.; Trueblood, J. V.; Estillore, A. D.; Morris, H. S.; Jayarathne, T.; Sultana, C. M.; Lee, C.; Lin, P.; Laskin, J.; Laskin, A.; Dowling, J. A.; Qin, Z.; Cappa, C. D.; Bertram, T. H.; Tivanski, A. V.; Stone, E. A.; Prather, K. A.; Grassian, V. H. Molecular Diversity of Sea Spray Aerosol Particles: Impact of Ocean Biology on Particle Composition and Hygroscopicity. *Chem* **2017**, *2*, 655–667.

(19) Laskina, O.; Morris, H. S.; Grandquist, J. R.; Estillore, A. D.; Stone, E. A.; Grassian, V. H.; Tivanski, A. V. Substrate-Deposited Sea Spray Aerosol Particles: Influence of Analytical Method, Substrate, and Storage Conditions on Particle Size, Phase, and Morphology. *Environ. Sci. Technol.* **2015**, *49*, 13447–13453.

(20) Ault, A. P.; Zhao, D.; Ebben, C. J.; Tauber, M. J.; Geiger, F. M.; Prather, K. A.; Grassian, V. H. Raman Microspectroscopy and Vibrational Sum Frequency Generation Spectroscopy as Probes of the Bulk and Surface Compositions of Size-Resolved Sea Spray Aerosol Particles. *Phys. Chem. Chem. Phys.* **2013**, *15*, 6206–6214.

(21) Dennis-Smither, B. J.; Hanford, K. L.; Kwamena, N.-O. A.; Miles, R. E. H.; Reid, J. P. Phase, Morphology, and Hygroscopicity of Mixed Oleic Acid/Sodium Chloride/Water Aerosol Particles before and after Ozonolysis. *J. Phys. Chem. A* **2012**, *116*, 6159–6168.

(22) Atkins, P.; de Paula, J. *Physical Chemistry*, 9th ed.; W. H. Freeman and Company: New York, 2010.

Chapter 3 Aerosol Optical Tweezer

3.1. Synopsis

This chapter provides an overview of the Aerosol Optical Tweezer (AOT) used for single particle studies. Details of the theoretical background of the Aerosol Optical Tweezer system are provided, including the physics of trapping a particle and an introduction to cavity enhanced Raman spectroscopy and whispering gallery modes that are used to calculate the radius and refractive index of a particle. The apparatus itself and general methods for trapping a particle are described. Various experiments were conducted to fully characterize the instrument, including the influence of exposure time and spectral intensity stability over the lifetime of a trap, the results of which are reported here. Additionally, the AOT was used to examine changes in aerosol pH as a function of relative humidity and the influence glyoxal has on S(IV) oxidation demonstrating how the AOT system can be used to study chemistry occurring in the aerosol phase.

3.2. Theoretical Background

3.2.1. Trapping a Particle

Optical tweezers utilize forces generated from the interaction of light with matter to trap a particle. In the AOT, forces from a high aperture laser beam trap a micron sized droplet. The two main forces that stably trap a particle in an optical trap are the gradient and scattering forces, as depicted in Figure 3.1.[1,2,11,3–10] These forces arise when light acts on an object with a refractive index that is different than the surrounding medium. In the scattering force, laser light reflects off the surface of the particle resulting in a force that

overcomes the gravitational force causing the particle to be pushed in the direction of beam propagation. The particle can also refract light resulting in a differential force pushing the particle downward. The reflecting and refracting forces act in opposition to stabilize the particle vertically and collectively makeup the scattering force. The scattering force can be described by equation 3.1.[12]

$$F_{scat} = \alpha^2 E^2 = \left(n_p - n_m\right)^2 r^6 I \qquad \text{(Eq. 3.1)}$$

where α is the polarizability, E is the electric field amplitude, r is the radius, I is the laser intensity, and n_p and n_m are the refractive indices of the particle and surrounding medium, respectively. In the gradient force, if the particle is not in the center of the laser beam it will experience an asymmetric distribution of light intensity caused by the optical gradient around the laser. The resulting gradient force pulls the particle towards the point of highest light intensity thereby stabilizing the particle laterally with respect to the direction of beam propagation. The gradient force can be described by equation 3.2.[1,12]

$$F_{grad} = \left(\frac{\alpha}{2}\right) \nabla E^2 \qquad \text{(Eq. 3.2)}$$

The gradient force must be greater than the scattering force, so the particle is always pulled back to the point of highest light intensity and therefore stably trapped. If the gradient force is greater than the scattering force, a restoring force acts to confine the particle to the point of highest light intensity and therefore stably trap the particle.[12] The high numerical aperture lens in the AOT setup provides a tightly focused laser beam allowing for a strong gradient force. The efficiency of the trap (i.e. the effectiveness of the

laser in exerting an optical force on the particle) is described by the dimensionless efficiency, *Q*,

$$F = \frac{n_m P Q}{c} \qquad \text{(Eq. 3.3)}$$

where *F* describes the optical forces acting on the particle, *P* is the power of the incident laser and *c* is the speed of light.[2,12]

3.2.2. Whispering Gallery Modes

Whispering gallery modes (WGMs), also known as morphology dependent resonances, are standing waves that form in a cavity with curved surfaces. WGMs were originally discovered as sound waves in St. Paul's Cathedral where Lord Rayleigh found that a sound wave, at a specific pitch or frequency, could resonate around the cathedral dome that acted as a cavity.[13,14] The wave totally internally reflects within the cavity leading to constructive interference and allowing someone on the opposite side of the cathedral to clearly hear a "whisper". While originally discovered as sound waves, WGMs can also exist for other types of waves including light waves. In the case of the AOT, a spherical droplet acts as a low-loss optical cavity where a light wave propagates around the droplet's circumference causing constructive interference resulting in the formation of a WGM resonating within the droplet. Specifically, the light propagating within the droplet, that has a refractive index greater than that of the surrounding medium, reaches the surface at an angle greater than the critical angle resulting in total internal reflection. As the name "morphology dependent resonances" would suggest, the formation of WGMs is dependent on the physical characteristics of the cavity itself including the size of the cavity and

refractive index of the cavity material. WGMs only form at specific wavelengths or frequencies within the cavity that are commensurate with Mie resonances.

WGMs can be characterized by the mode number, mode order, and specific polarization state. Mode number describes the number of angular maxima or the integer number of wavelengths forming the standing wave. Mode order describes the number of radial maxima. The penetration depth of the mode is dependent on the mode order and increases with increasing mode order.[15] The polarization state can be assigned as transverse electric (TE), no radial dependence in the electric field, or transverse magnetic (TM), no radial dependence in the magnetic field.

WGM wavelengths are dependent on the physical properties of the cavity and therefore can provide a fingerprint of the radius and refractive index of the particle. Specifically, WGMs are dependent on the size parameter. which is related to the radius, and refractive index of the particle. The size parameter, *x*, describes the ratio between the circumference of the particle and the WGM wavelength.[12,16]

$$x = \frac{2\pi r}{\lambda} \qquad \text{(Eq. 3.4)}$$

The penetration depth of a specific mode is approximately r/n_p. The lifetime of a WGM propagating within a cavity can be described by the quality factor, *Q*,

$$Q = \frac{2\pi \times Energy\ stored}{Energy\ lost\ per\ cycle} \qquad \text{(Eq. 3.5)}$$

and is dependent on the droplet size, refractive index and mode order.[12,17,18] For a micron sized droplet, quality factors of 10^5-10^8 are typical and increase with increasing

mode number but decrease with increasing mode order.[12,19] The pathlength, *P*, of the WGM, or the distance traversed by the light around the circumference of the particle is described by equation 3.6.[19]

$$P = \frac{\lambda Q}{2\pi n_p} \quad \text{(Eq. 3.6)}$$

For a cavity with a high quality factor, greater than 10^5, such as a droplet in an optical trap, the pathlength can be on the order of meters.[12,19]

3.2.3. Cavity Enhanced Raman Spectroscopy

Cavity enhanced Raman spectroscopy (CERS) is comprised of two components: spontaneous Raman scattering and stimulated Raman scattering. Figure 3.2 depicts both spontaneous and stimulated Raman scattering.[16] Spontaneous Raman scattering provides chemical information and the stimulated Raman scattering allows for determination of physical properties such as radius and refractive index. Collectively, the spontaneous and stimulated Raman scattering comprise cavity enhanced Raman scattering providing both chemical and physical information of the trapped particle.

3.2.3.1. Spontaneous Raman Scattering

Spontaneous Raman scattering is discussed in more detail in Chapter 2. Briefly, incident light interacts with a molecule causing a change in polarization of the electron cloud around the nuclei forming a short-lived virtual state. This virtual state is not stable, and the photon is quickly re-radiated, or scattered, elastically or inelastically. Raman scattering (i.e. inelastic scattering) occurs when the energy of the scattered photon is different than that of the incident radiation due to a transfer of energy to the molecule or to

the scattered photon. This change in energy is unique to the vibrational modes of the molecule and provides a chemical fingerprint of the molecule and sample composition.

3.2.3.2. Stimulated Raman Scattering

Stimulated Raman scattering (SRS) occurs when the trapped droplet acts as a low-loss optical cavity forming a standing wave at specific wavelengths commensurate with Mie resonances. As the resonating light totally internally reflects within the droplet, the intensity of the SRS reaches a threshold intensity above which scattering is amplified. The occurrence of WGMs in droplet provides a mechanism for optical feedback leading to enhanced Raman scattering and the occurrence of SRS.[20] The SRS intensity, I_{SRS}, at wavelength λ, is described by equation 3.7,

$$I_{SRS}(\lambda) = I_0(\lambda) exp[G(g(\lambda) - 1)] \quad \text{(Eq. 3.7)}$$

where I_0 is the intensity from the spontaneous Raman scatter at wavelength λ, G is the gain factor, and $g(\lambda)$ is the line shape function.[12,15,21] In CERS, the resonant structure appears superimposed on the spontaneous Raman spectrum and modes of the same order follow the contour of the spontaneous Raman scattering.[22] For example, in Figure 3.3 the SRS in the OH stretching region appears as sharp WGM peaks at wavelengths commensurate with Mie resonances following the contour of the OH stretching band arising from spontaneous Raman scattering.

3.2.3.3. Calculating Radius and Refractive Index

The wavelengths of the WGMs are dependent on the size of the droplet and therefore change depending on an increasing or decreasing droplet radius. Because of this, the spacing between the WGM wavelengths can be exploited to calculate the droplet radius.

The spacing between WGMs of the same mode order and polarization is given by equation 3.8.[15,16,19,20]

$$\Delta\lambda = \frac{\lambda^2 \tan^{-1}(n_m^2 - 1)^{1/2}}{2\pi r(n_m^2 - 1)^{1/2}} \quad \text{(Eq. 3.8)}$$

Therefore, if the wavelength spacing and refractive index are known then the particle radius can be calculated. In general, the spacing between WGM wavelengths increases as droplet radius decreases.[12,16,19,23] This trend can be seen in Figure 3.4 that shows the WGMs in the OH stretching region for three trapped sodium chloride droplets of varying sizes. As the radius of the sodium chloride droplets decreases from 4.5 to 3.7 μm, the spacing between the WGMs increases. Additionally, temporal variation in the droplet size can be examined by tracking the shifts in WGM wavelengths. Figure 3.5 shows the temporal evolution of the Raman spectra collected for a trapped sodium chloride droplet. For a given mode number, the WGM wavelengths blue shift as the droplet evaporates (decreases in radius) and red shift as the droplet grows (increase in radius).[16]

In the experiments described herein, the LARA software (proprietary Biral and University of Bristol software (LARA 2.0)) was used. In the software, an algorithm was developed to determine the radius and refractive index of the trapped droplet by comparing calculated theoretical Mie resonance wavelengths to the observed WGM wavelengths. The algorithm has been described in detail by Preston and Reid.[24] Briefly, a Mie resonance wavelength based on a first guess approximation of the droplet radius and refractive index is calculated. The error between the calculated wavelength and observed WGM wavelength is determined. The radius and refractive index are then varied iteratively, and an error is

recalculated until it is minimized. From this process a best fit is obtained. This calculation is first done without including dispersion then calculated again including dispersion using the results from the calculation without dispersion as a starting point. The error, $E(r, n_p)$, is determined by equation 3.9.[24]

$$E(r, n_p) = \frac{1}{J}\sum_{j=1}^{J}\left(\frac{s_j(r, n_p)}{2\pi r}\right)^2 \qquad \text{(Eq. 3.9)}$$

J is the number of experimental WGM peaks (where j=1,2,3…J) and s_j is the separation between observed and calculated Mie resonances. A similar/analogous equation can be written for determining error with the refractive index taking dispersion into account.

3.3. Experimental apparatus and method

A schematic of the AOT setup is shown in Figure 3.6.[21,23,25,26] In this setup, a continuous wave collimated Nd:YVO_4 (532 nm) laser passes through a spatial light modulator and a series of beam expansion optics before being reflected onto the back aperture of a microscope objective. The laser used for optical trapping of the droplet is the same laser used for Raman spectroscopy. The droplet is imaged by conventional brightfield microscopy using a blue LED. The Raman scattered light from the trapped particle and the blue light are collected by the objective and passed through a long pass filter. The short blue wavelengths are reflected to a CCD camera for imaging. The long wavelengths are directed to the Raman spectrometer with a diffraction grating of either 300 or 1200 g mm^{-1}.[21,26] The AOT is capable of trapping droplets within a 3 to10 μm radius range. The Raman

spectral resolution is 0.037 nm at 650 nm, a particle size is determined with a resolution of 1 nm, and a refractive index accuracy of 0.05%.

A detailed schematic of the trapping chamber is shown in Figure 3.7. The trapping chamber itself consists of a stainless-steel cell base and lid that houses a PTFE insert. A stainless-steel retainer with an O-ring seal holds a coverslip (~0.14 mm thick) in place on the bottom of the PTFE insert. The chamber lid has a window allowing for brightfield illumination with an LED for imaging of the trapped droplet. The relative humidity (RH) of the trapping environment is controlled by flowing humidified nitrogen, with a specified ratio of wet to dry nitrogen gas, into the chamber and is monitored by two relative humidity sensors, one before and one after the trapping chamber. The chamber is also equipped with a gas inlet through which a gas can be introduced into the trapping chamber to investigate gas-particle interactions and reactions. There are notches in the PTFE insert so that the trapped droplet is exposed to any gas introduced into the trapping environment evenly from all sides in order to minimize the possibility of knocking/blowing the droplet out of the laser focus. The ability to adjust relative humidity and introduce additional gases allows for complete control over the trapping environment throughout the duration of an experiment.

In a typical AOT experiment, a bulk solution is aerosolized using an ultrasonic nebulizer (MicroAIR U22, OMRON). The aerosolized solution is introduced to the trapping chamber where a single droplet is confined by the trapping laser. Once trapped, the droplet can be enlarged via coalescence with additional droplets from the nebulized solution.[25,27] After trapping, the chamber is sealed and allowed to equilibrate under a

humidified nitrogen flow set to a specific relative humidity. Raman spectra of the droplet are collected with a 300 or 1200 g mm^{-1} grating and a typical exposure time of 1 s. Spectra collected with the 1200 g mm^{-1} grating centered at 645 nm focuses on the O-H stretching region containing WGMs and is used for determination of the droplet radius and refractive index. Microscopy videos and images of the trapped droplet can be collected throughout the duration of the experiment; an example of an image collected for a trapped sodium chloride droplet is shown in Figure 3.8. The AOT-100 is controlled with the LARA 2.0 software; screenshots of the Imaging, Cell Conditions, Spectral Acquisition, WGM Analysis, and WGM Assignment tabs are show in Figures 3.9-3.13, respectively.

The ultrasonic nebulizer works well for aqueous solutions with low viscosities but is unable to nebulize more viscous or oily samples. In some cases, diluting the sample with a solvent like water or ethanol allows the sample to then be nebulized. However, for samples that cannot be nebulized with the ultrasonic nebulizer, despite dilution, a glass concentric nebulizer (Meinhard, TR-50-A1) can be used to aspirate the sample and produce micron-sized droplets. The concentric nebulizer is able to aspirate more viscous or oily samples and the size range of the droplets will depend on the flow rate of the carrier gas (nitrogen) and the flow rate of the sample solution (controlled using an automated syringe pump (World Precision Instruments, AL300-220).

3.4. Characterization of the AOT

3.4.1. Influence of Exposure Time

In confocal Raman, the acquisition time and number of accumulations can be varied to obtain optimum settings for spectra collection based on the sample. In the AOT, the

number of acquisitions cannot be changed but the exposure time (acquisition time) can be. In the initial characterization of the AOT setup, the influence of exposure time on Raman spectral intensity was explored and signal to noise ratios were calculated to gain an understanding of optimal settings. Ammonium sulfate and sodium nitrate droplets were trapped and once stable, cavity enhanced Raman spectra were collected with 0.5, 1, 2, 5 25, and 50 second exposure times. The Raman spectra for the varying exposure times for both ammonium sulfate and sodium nitrate are shown in Figure 3.14. As exposure time increases, the Raman spectral intensity also increases. The first standard deviation signal to noise ratio was calculated for each exposure time and is shown in the insets of Figure 3.14. A greater signal to noise ratio was calculated for higher exposure times. Increasing exposure time increases spectral intensity whereas decreasing exposure time reduces the spectral noise. Based on the needs of the experiment, exposure time should be increased to obtain greater spectral intensity but decreased if a low signal to noise is needed. For the AOT experiments described herein, an exposure time of 1 second is typical because it provides a decent signal to noise ratio and spectral intensity while also providing quick real time monitoring of droplet size in addition to changes in the chemistry of the droplet.

3.4.2. Influence of Lifetime on Raman Spectral Intensity

To examine the variation of the Raman spectral intensity collected during the lifetime of a given trap, spectral intensity was monitored as a function of time. If the trapping environment remains constant and the droplet therefor unchanged and stably trapped, the spectral intensity should not change over the lifetime of a trap. To test this, an ammonium sulfate or sodium nitrate droplet was trapped, allowed to equilibrate and the peak intensity was monitored for the sulfate stretching mode at 985 cm^{-1} or the nitrate

stretching mode at 1049 cm^{-1}, respectively. Figure 3.15 shows the peak intensities, average peak intensity and standard deviation in peak intensity for the trapped droplets. Additionally, Figure 3.15b and d show the Raman spectra of the trapped sulfate and nitrate droplets, offset with respect to the x-axis, depicting the temporal variation in the spectral intensity. While the droplets shown in Figure 3.15 had trapping lifetimes of only minutes, the same stability can be seen for droplets with much longer trapping lifetimes on the order of hours. For example, Figure 3.16 shows the peak intensities, average peak intensity and standard deviation for an ammonium sulfate droplet trapped for over 17 hours. As long as the environmental conditions in the trapping chamber (relative humidity, temperature, surrounding gaseous medium) remain constant, the Raman spectral intensity should also remain constant throughout the lifetime of the trap, no matter how long.

3.4.3. Concentration Dependence in CERS

The Raman spectral intensity was examined as a function of concentration for individually trapped droplets and compared to bulk aqueous phase measurements obtained with the confocal Raman spectrometer. The resulting cavity enhanced Raman spectra for a trapped ammonium sulfate or sodium nitrate droplet are shown in Figure 3.17a and3. d, respectively, where Raman spectral intensity increases linearly with increasing concentration. Similarly, the Raman spectra for bulk aqueous sulfate and nitrate solutions is shown in Figure 3.17b and e, respectively, again showing a linear increase in intensity with increasing concentration. Both methods result in good linear calibration curves (fits with R^2 values greater than 0.90). The main difference between the two methods being the relative intensities. Creating and using calibration curves such as these for concentration allows for semiquantitative analysis of trapped droplets, such as determining concentration

following a shift in chemical equilibrium of a trapped droplet, and comparison between bulk and aerosol.

Since peak intensities or integrated areas can be used in conjunction with calibration curves to determine amounts or concentrations it was imperative to ensure that the size of the droplet would not influence the peak intensity/integrated area. To test this, Raman spectra of sodium sulfate droplets of different concentrations were collected and compared to droplet radius. These measurements were carried out in triplicate for each concentration and the results are summarized in Figure 3.18. In Figure 3.18, the integrated peak area and droplet radius is denoted by circle and triangle markers, respectively. For a given concentration, each trial is shown in a different color (integrated peak area and radius for the same trial of a given concentration are the same color and only distinguished by the marker shape). If integrated peak area were dependent on droplet size, the largest droplet for each concentration would be expected to have the greatest integrated peak area. However, the data summarized in Figure 3.18 shows no correlation between droplet size and integrated peak area.

3.4.4. Droplet Size Dependence with Relative Humidity

In addition to monitoring the chemical properties of a trapped droplet from the Raman spectra, the physical properties, such as changes in droplet size, can be monitored with the AOT. To test this, changes in droplet radius were monitored while the relative humidity in the trapping chamber was altered. Figure 3.19 shows the changes in droplet radius as a function of RH for trapped ammonium sulfate droplet. As can be seen in Figure 3.19a, at each increase or decrease in RH within the trapping chamber, the droplet radius

changed accordingly. Figure 3.19b shows the droplet radius at specific RH values. When the droplet is first hydrated (increased RH) then dehydrated (decreased RH), the changes in radius follow the same curve demonstrating that the droplet returns to the same size at the same RH. For example, at 65% RH the droplet radius is 3.5 μm. RH is then increased to nearly 100% where the radius is measured at 4.7 μm. Lastly, as RH is decreased back to 65% and the droplet returns to a radius of 3.5 μm. It is expected that the changes in radius upon dehydration follow the same curve as the hydration based on reported literature for the uptake of water by ammonium sulfate.[28] It should be noted that a complete water uptake profile, over the full range of RH, is not possible with the AOT system because the trapped droplets lose stability and fall out of the trap at lower RH when the droplet loses water and becomes nonspherical. Therefore, no efflorescence or deliquescence points, such as those observed with salts like ammonium sulfate, can be observed because the droplet will fall out of the trap.

3.4.5. Relative Humidity Changes as a Method to Alter Droplet pH

As an aerosol's liquid water content, or amount of liquid in the particle, changes, the acidity of the aerosol will also change. Therefore, the changes in acidity were investigated as a particle takes up water or evaporates. This was done so by trapping a droplet of sulfuric acid with an adjusted bulk pH of 1.62. The droplet was trapped and allowed to equilibrate before the RH in the trapping chamber was first decreased from 94 % to 64 % then increased again to 89 %. At each RH the droplet was allowed to equilibrate, Raman spectra were collected, and radius information was collected. Changes in pH were estimated based on the SO_4^{2-}/HSO_4^- equilibrium using the Henderson-Hasselbalch equation and the ratio of the sulfate and bisulfate peak areas in the Raman spectra. Previous

work has shown that Raman spectra of conjugate acid base pairs can be used to determine droplet pH.[29–31] As the RH was initially decreased, the pH of the droplet increased by approximately 0.30 pH units and the radius decreased from 4.3 μm to 3.8 μm. An increase in pH is expected as decreasing RH shifts the SO_4^{2-}/HSO_4^- equilibrium in the direction of SO_4^{2-} thereby corresponding to an increase in pH. Increasing RH shifts the equilibrium toward HSO_4^- corresponding to a decrease in pH which was seen when the RH was increased to 89 %, the calculated pH decreased by approximately 0.03 pH units and radius increased from 3.8 μm to 4.4 μm. Using changes in relative humidity to induce changes in droplet acidity is limited to a small pH range near the initial pH of the trapped droplet. This small range in pH is due to the limited amount of water and acidity of the water itself that the droplet can take up or evaporate. Nonetheless, changing the relative humidity of the trapping environment can be used to induce small changes in droplet pH.

3.4.6. Droplet Coalescence as a Method to Induce Change in pH

Coalescence has been shown to be a useful method for inducing a reaction within optically trapped droplets.[27,32–38] Initial studies were conducted to determine if coalescence of a trapped droplet with either acidic or basic aerosol could induce changes in the droplets pH. To do this, a 0.5 M sodium sulfate droplet was trapped then first coalesced with acidic aerosol (HCl) then with basic aerosol (NaOH); the results are summarized in Figure 3.20. As the trapped droplet is coalesced with acidic aerosol, the bisulfate peak appears and then increases as coalescence continues. With each coalescence of acidic aerosols, the ratio of the ratio of SO_4^{2-}/HSO_4^- peak area decreases, indicating a shift in equilibrium towards bisulfate and therefore an overall decrease in droplet acidity. After one coalescence with

basic aerosol, the ratio of SO_4^{2-}/HSO_4^- begins to increase again indicating that the equilibrium shifts back toward SO_4^{2-} and therefore increases pH. Although the study described here does not directly determine the pH within the droplet, it does show that coalescence with acidic and basic aerosol can be used to induce changes in droplet pH. This method was further developed to include calculations of droplet pH and is discussed in detail in Chapter 4 of this dissertation.

3.4.7. Trapping Droplets Containing a Solid Inclusion

In the atmosphere, cloud or fog droplets can interact with solid particles, such as mineral dust or fly ash, and undergo heterogeneous or multiphase chemistry. This chemistry could be mimicked and studied in the laboratory by examining a droplet containing a solid inclusion. In order to stably trap a droplet in the AOT the droplet must be spherical; however, most natural and anthropogenic dust or ash particles are not spherical and, when included in a droplet, make trapping the droplet difficult. In previous studies using optical levitation, solid particles were trapped using a second laser for stability.[39,40] However, Laruain and Reid have shown that spherical polystyrene beads could be trapped and discuss how the WGMs are influenced based on the location of the bead within the trapped droplet.[35]

To test the ability of the AOT system described herein to trap solid inclusions, experiments were conducted to trap polystyrene beads. This was done by trapping a droplet from a bulk solution of dispersed 500 nm polystyrene beads (Polysciences) in a sodium chloride solution (approximately 1 M). Droplets containing a polystyrene bead were successfully trapped over multiple trials. Successful inclusion of a polystyrene bead in a

trapped droplet was determined by the video microscopy as well as the collected cavity enhanced Raman spectra. Figure 3.21 is a screenshot image from the video microscopy where the polystyrene bead is clearly visible within the droplet and Figure 3.21 is an example of Raman spectra collected from a trapped droplet containing a polystyrene bead. Figure 3.22a is a single Raman spectrum collected showing the spectral features of the polystyrene bead. Additionally, when a solid inclusion is contained within a droplet, the WGMs will be deformed or possibly quenched altogether based on the location of the inclusion within the droplet (edge vs center).[33,35,41] As seen in Figure 3.22a, the WGMs are quenched. Additionally, the spectral features characteristic of polystyrene are observed in the obtained spectra (more clearly seen in Figure 3.22b of the averaged Raman spectrum) and are in good agreement with the Raman bands of polystyrene reported in literature.[42,43] Both the quenching of WGMs and the spectral features characteristic of polystyrene present in the collected Raman spectra are evidence, in addition to the microscopy video, that a polystyrene bead was successfully confined within a trapped droplet. While further development of the AOT system is still needed to trap droplets containing authentic dust or metal oxide particles, trapping droplets containing metal coated polystyrene beads may act as a sufficient proxy in the meantime.

3.5. Figures

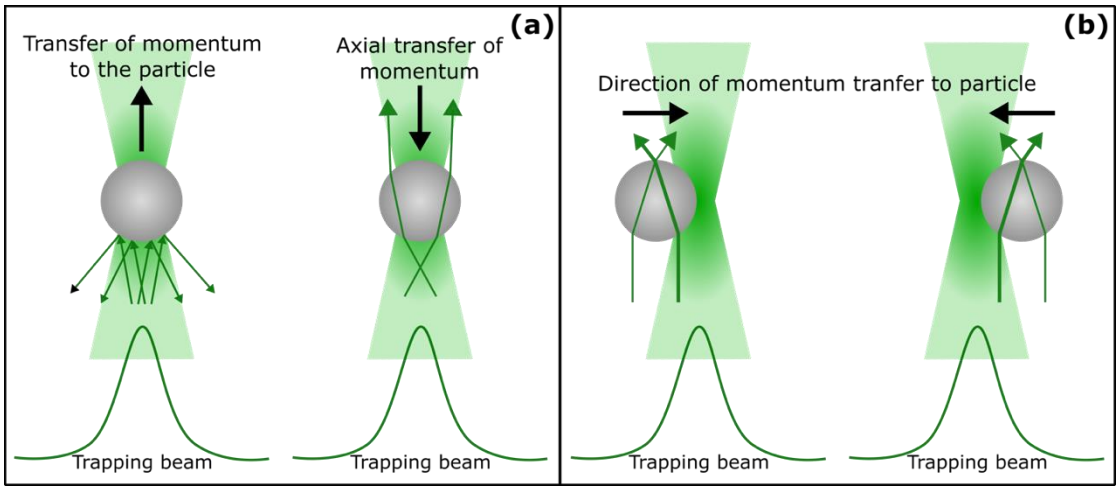

Figure 3.1: Depiction of the (a) scattering and (b) gradient forces involved in optical trapping. In the scattering force, the particle reflects laser light resulting in a force that overcomes the gravitational force causing the particle to be pushed in the direction of beam propagation. The particle also refracts light resulting in a differential force pushing the particle downward. The reflecting and refracting forces act in opposition to stabilize the particle vertically with respect to the direction of beam propagation. In the gradient force, the particle will experience an asymmetric distribution of light intensity caused by the optical gradient around the laser if it is not in the center of the laser beam resulting in a force that pulls the particle towards the point of highest light intensity and stabilizing the particle laterally with respect to the direction of beam propagation. A stable trap is obtained when the gradient force is greater than the scattering force resulting in an overall restoring force acting on the particle. Adapted from Ref. 3.

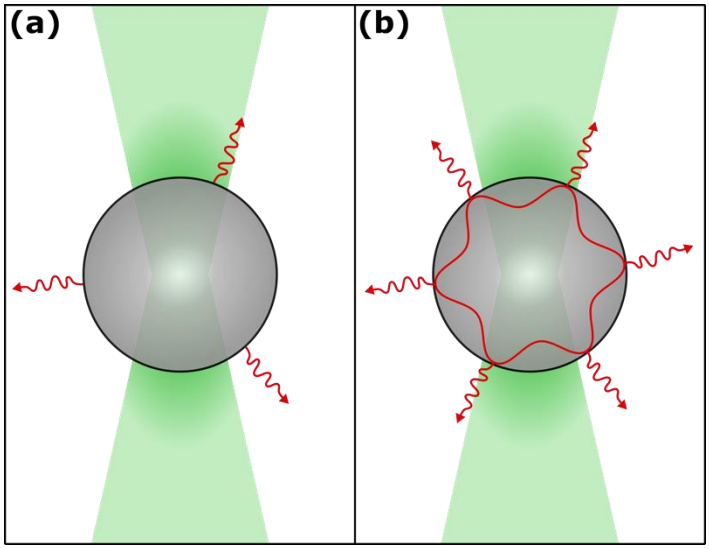

Figure 3.2: Depiction of (a) spontaneous and (b) stimulated Raman scattering processes. Spontaneous Raman scattering arises from the inelastic scatter of a photon that is characteristic to the specific vibrational mode of the molecule. Stimulated Raman scattering involves the formation of a standing wave, or whispering gallery mode, at wavelengths commensurate with Mie resonances, that propagates around the circumference of the trapped particle causing constructive interference resulting in the amplification of the Raman scatter. Together, spontaneous and stimulated Raman scattering makeup cavity enhanced Raman spectroscopy.

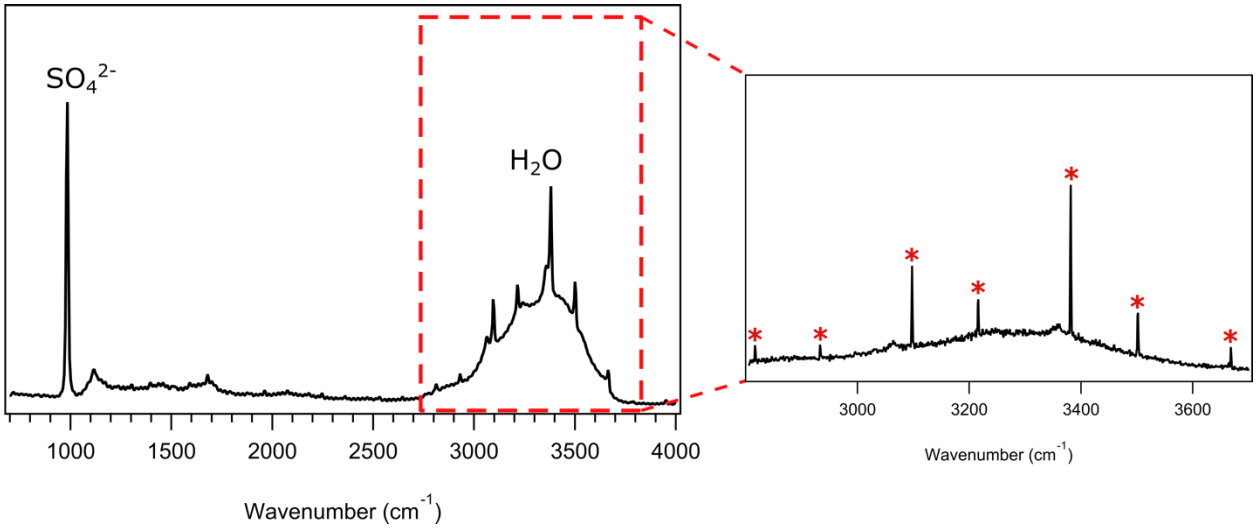

Figure 3.3: Cavity enhanced Raman spectra of ammonium sulfate showing both the spontaneous and stimulated Raman scattering. The spectrum on the left shows the stretching modes of OH from water and sulfate arising from spontaneous Raman scattering while the spectrum on the right, focused on the OH stretching region around 3200 cm^{-1}, shows the WGMs (identified by red asterisks) arising from the stimulated Raman scattering.

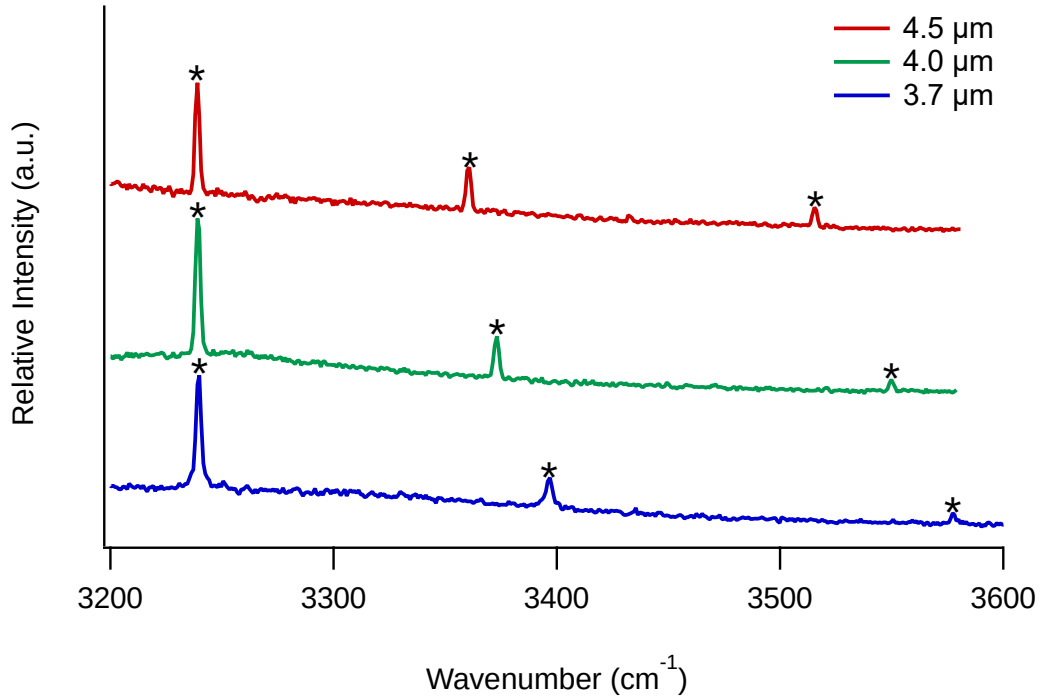

Figure 3.4: Raman spectra for trapped sodium chloride droplets showing the variation in WGM wavelength spacing as a function of droplet size. As droplet radius decreases from 4.5 µm to 3.7 µm the spacing between WGM wavelengths increases. WGMs in each spectrum are designated with asterisks.

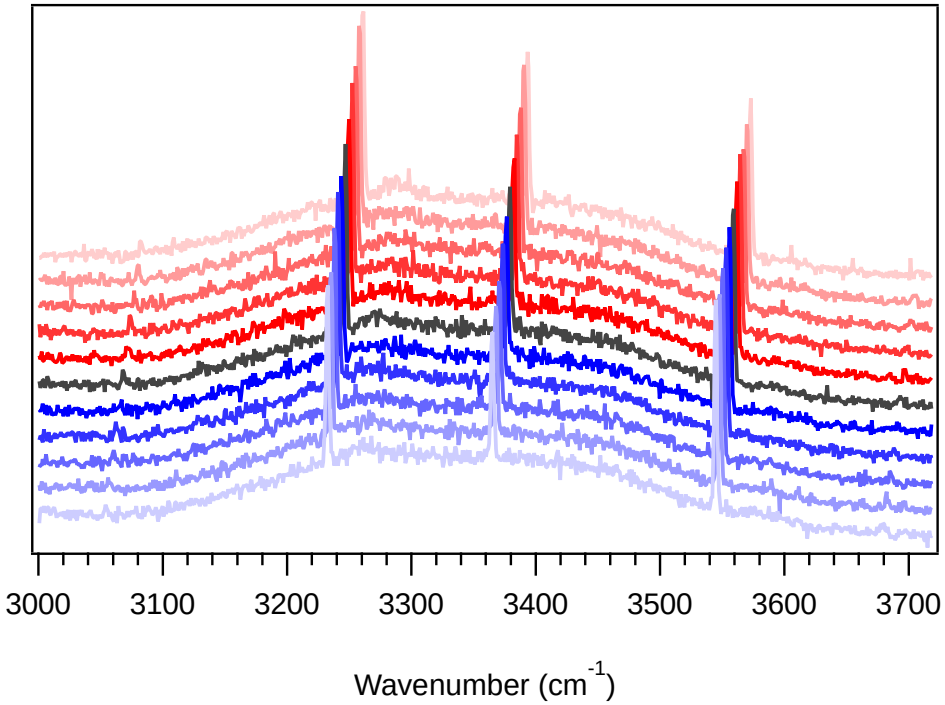

Figure 3.5: Temporal shift in WGM wavelengths for a trapped sodium chloride droplet as the droplet radius changes. With respect to the middle trace (gray), WGM wavelengths blue shift as the droplet radius decreases and red shift as the radius increases.

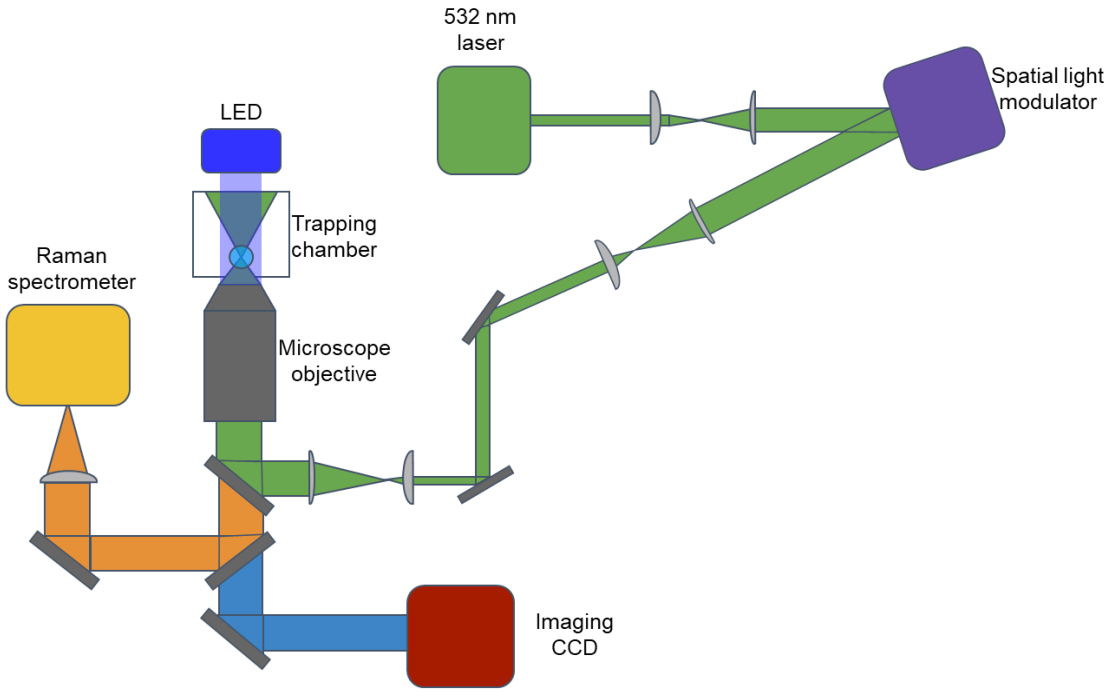

Figure 3.6: Schematic of the AOT-100 setup. A 532 nm laser is used as both the trapping laser and excitation laser for Raman spectroscopy. The laser light passes through a spatial light modulator and a series of beam expansion optics before being focused through the objective. Scattered laser light is directed to the Raman spectrometer. The trapped particle is illuminated with an LED and imaged via brightfield microscopy using a CCD camera. Adapted from Ref. 24.

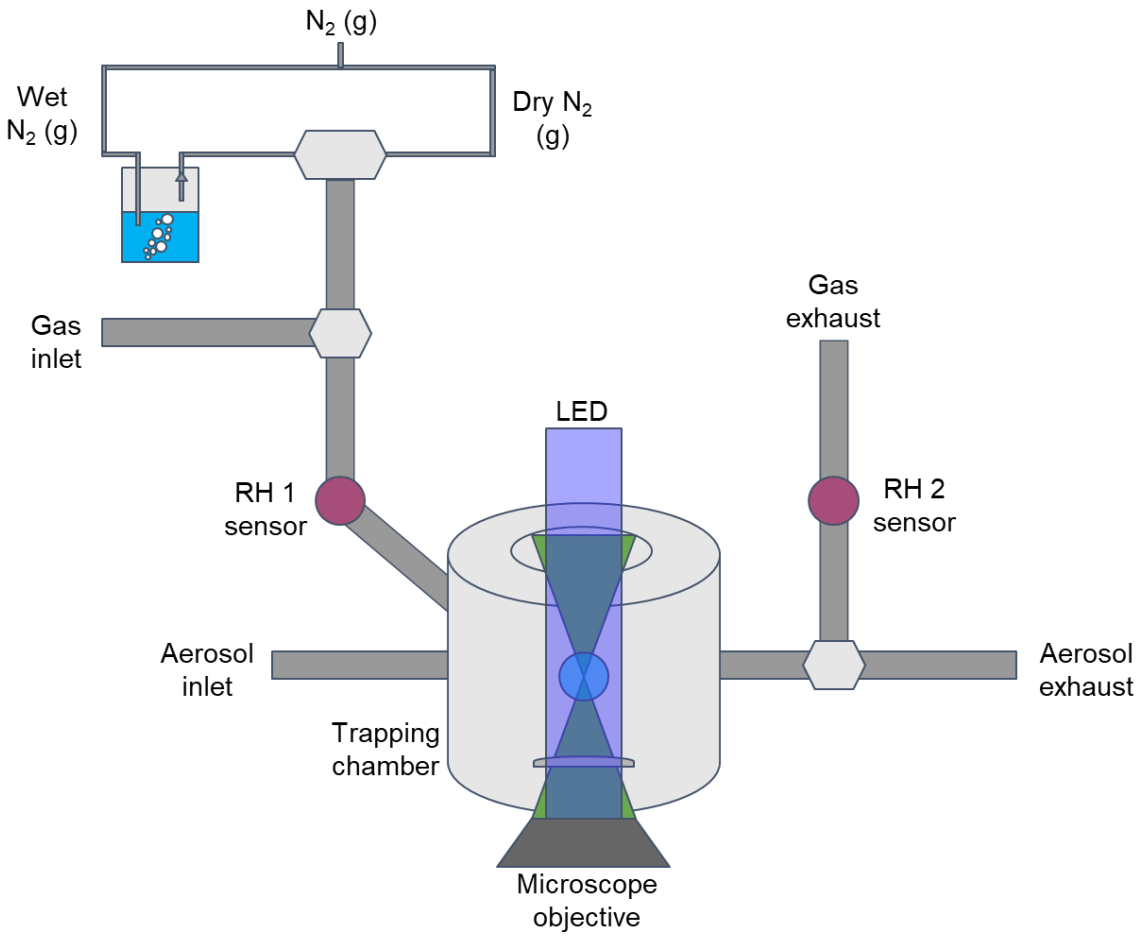

Figure 3.7: Schematic of the trapping chamber in the AOT. A particle is trapped in the focal point of the laser that sits above the microscope objective and a coverslip. The particle is illuminated with an LED for imaging with brightfield microscopy. Gases can be introduced into the trapping environment through the gas inlet allowing for studies of gas-particle interactions. Relative humidity is controlled by introducing a flow of humidified nitrogen and monitored by two relative humidity sensors, one before and one after the chamber.

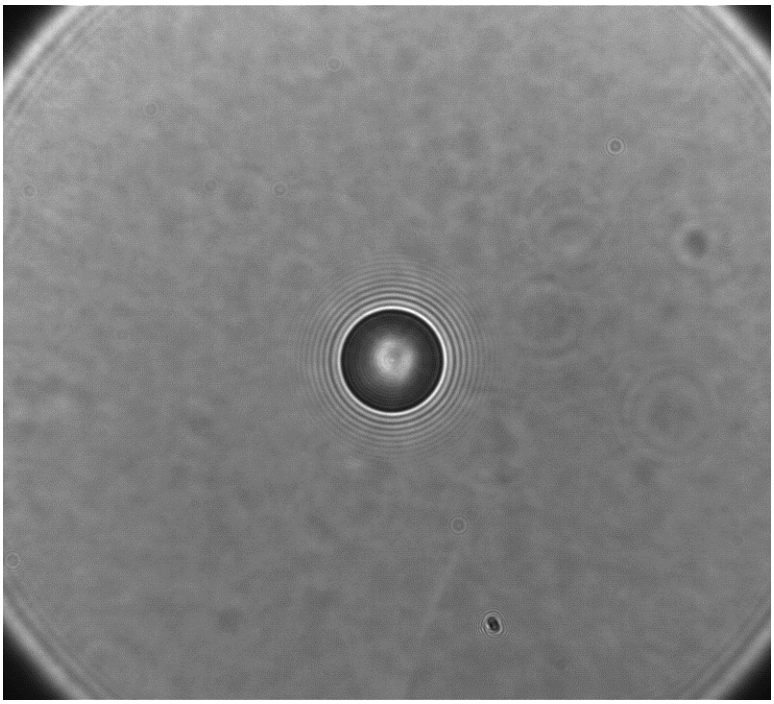

Figure 3.8: Brightfield microscopy image of a trapped sodium chloride droplet (5.02 μm).

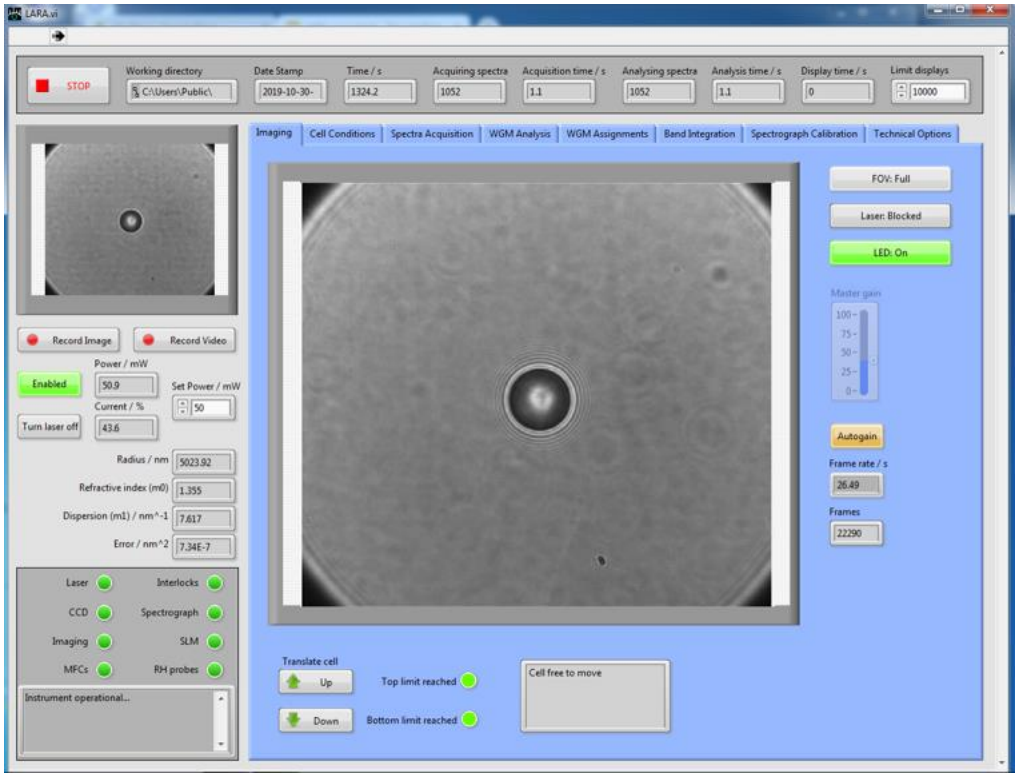

Figure 3.9: Screenshot of the LARA 2.0 software showing the Imaging tab during an experiment for a trapped sodium chloride (1 M) droplet. The Imaging tab shows the microscopy video of the trapped droplet. The trapping chamber is translated up or down, in order to locate the laser focal point, using the Imaging tab. An image or video of the trapped droplet can be captured from the left-hand panel.

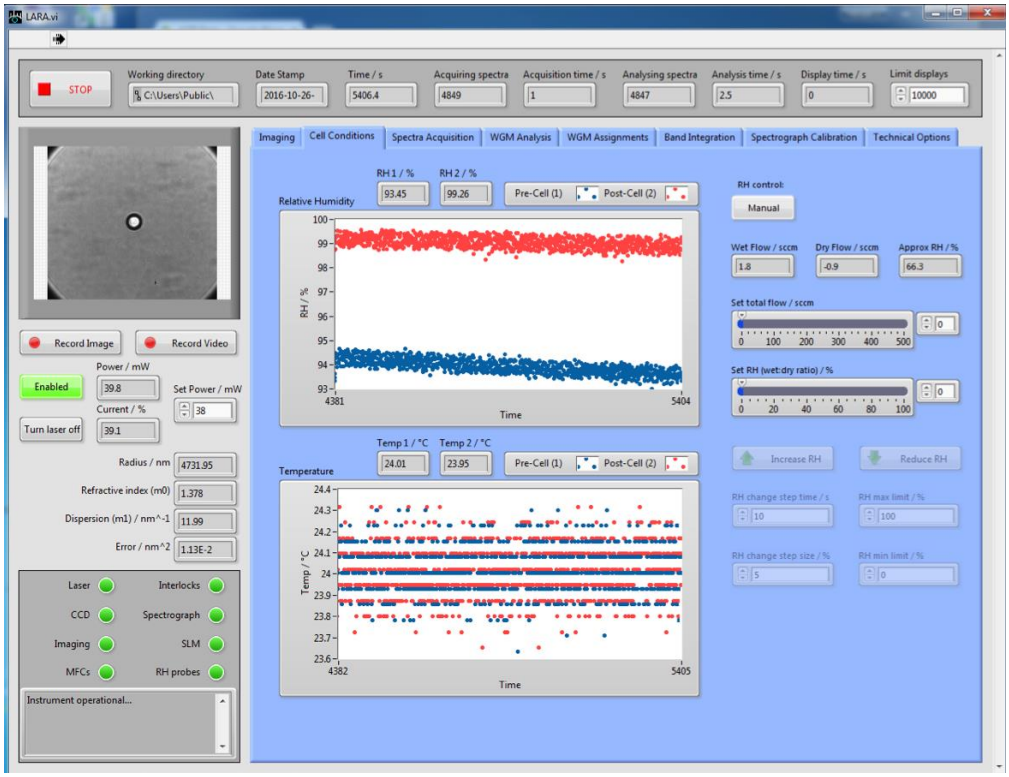

Figure 3.10: Screenshot of the LARA 2.0 software showing the Cell Conditions tab during an experiment for a trapped sodium chloride (1 M) droplet. The Cell Conditions tab shows the relative humidity (RH) and temperature measured by the two RH probes in the AOT system. RH is controlled automatically or manually by adjusting the ratio of wet to dry air and the total flow rate in the trapping chamber.

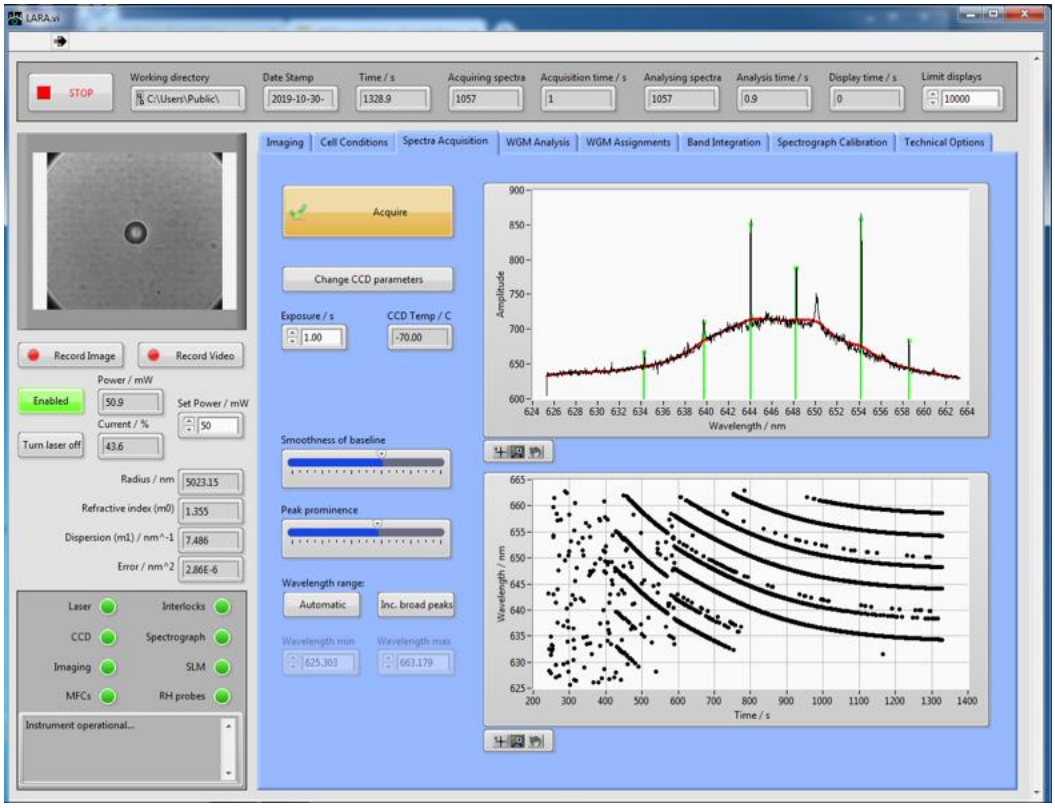

Figure 3.11: Screenshot of the LARA 2.0 software showing the Spectra Acquisition tab during an experiment for a trapped sodium chloride (1 M) droplet. The Spectra Acquisition tab shows the current Raman spectrum being collected and traces the wavelengths of the identified WGMs (denoted by the green lines in the Raman spectrum). The exposure time, smoothness of baseline, peak prominence and wavelength range are all parameters which are set in the Spectra Acquisition tab.

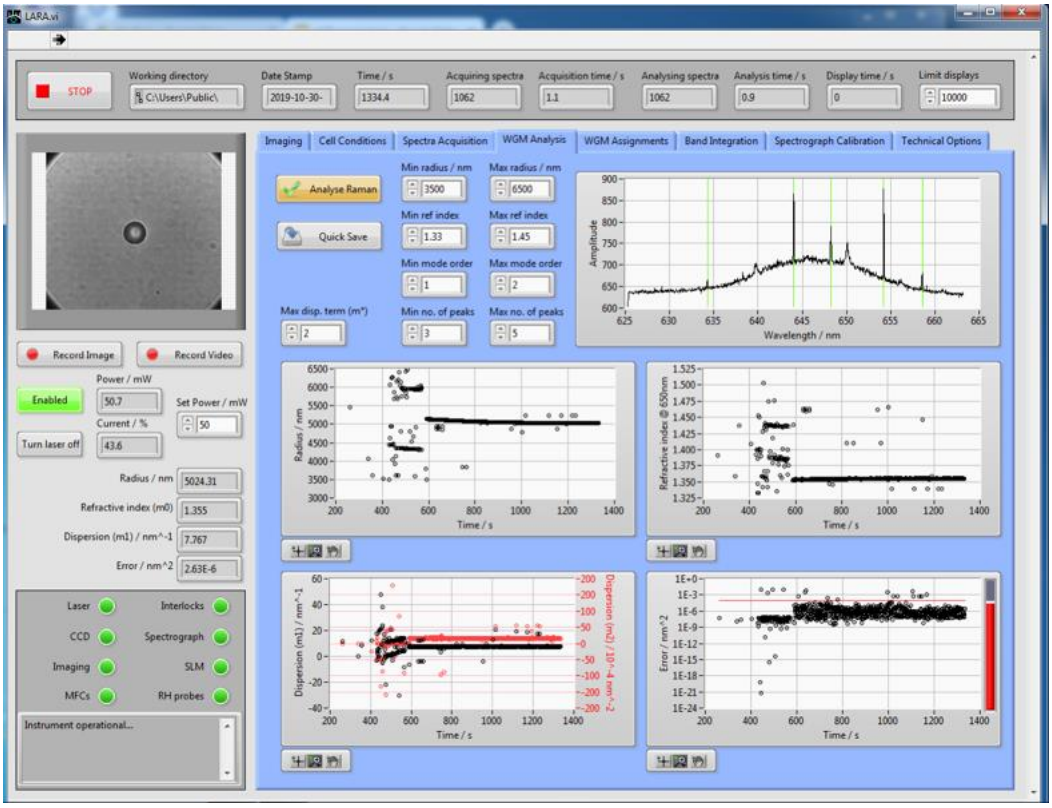

Figure 3.12: Screenshot of the LARA 2.0 software showing the WGM Analysis tab during an experiment for a trapped sodium chloride (1 M) droplet. The WGM Analysis tab shows the calculated radius, refractive index, dispersion, and error of the trapped droplet, as determined by the WGMs identified in the Raman spectra (denoted by the green lines), throughout the droplet's lifetime. The current radius, refractive index, dispersion and error are displayed in the left-hand panel at all times during the experiment.

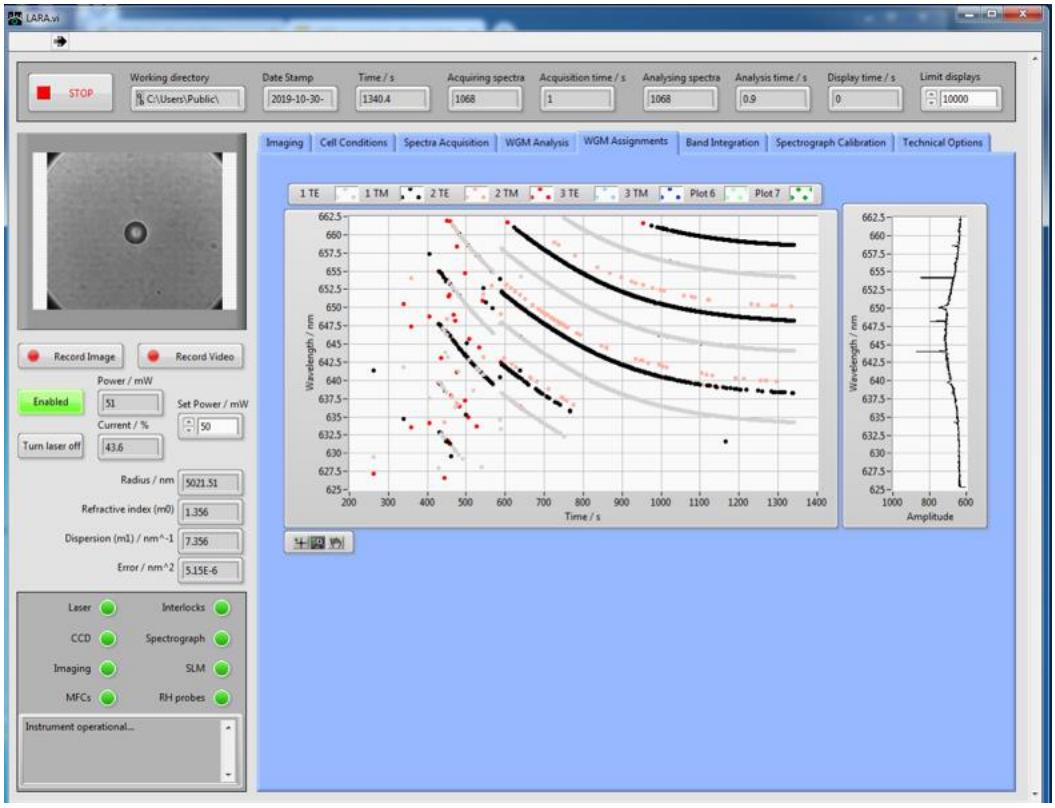

Figure 3.13: Screenshot of the LARA 2.0 software showing the WGM Assignment tab during an experiment for a trapped sodium chloride (1 M) droplet. In the WGM Assignment tab, WGMs identified in the Raman spectra are assigned polarization states (TE: transverse electric; TM: transverse magnetic).

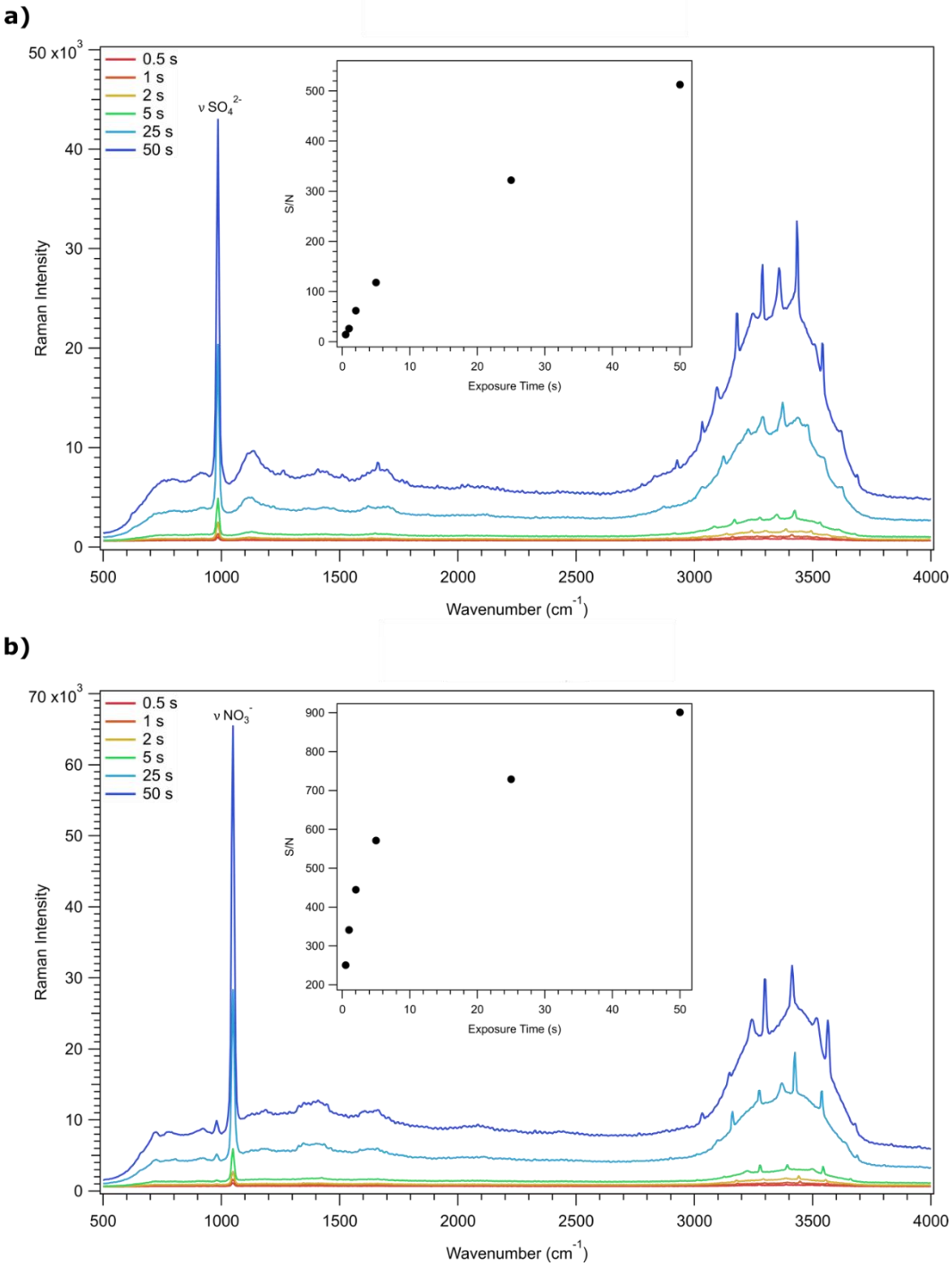

Figure 3.14: Cavity enhanced Raman spectra of (a) ammonium sulfate and (b) sodium nitrate as a function of exposure time. As exposure time is increased from 0.5 s to 50 s, the Raman intensity increases. The insets show the signal to noise ratio as a function of exposure time where the S/N ratio is calculated as a first standard deviation signal to noise ratio.

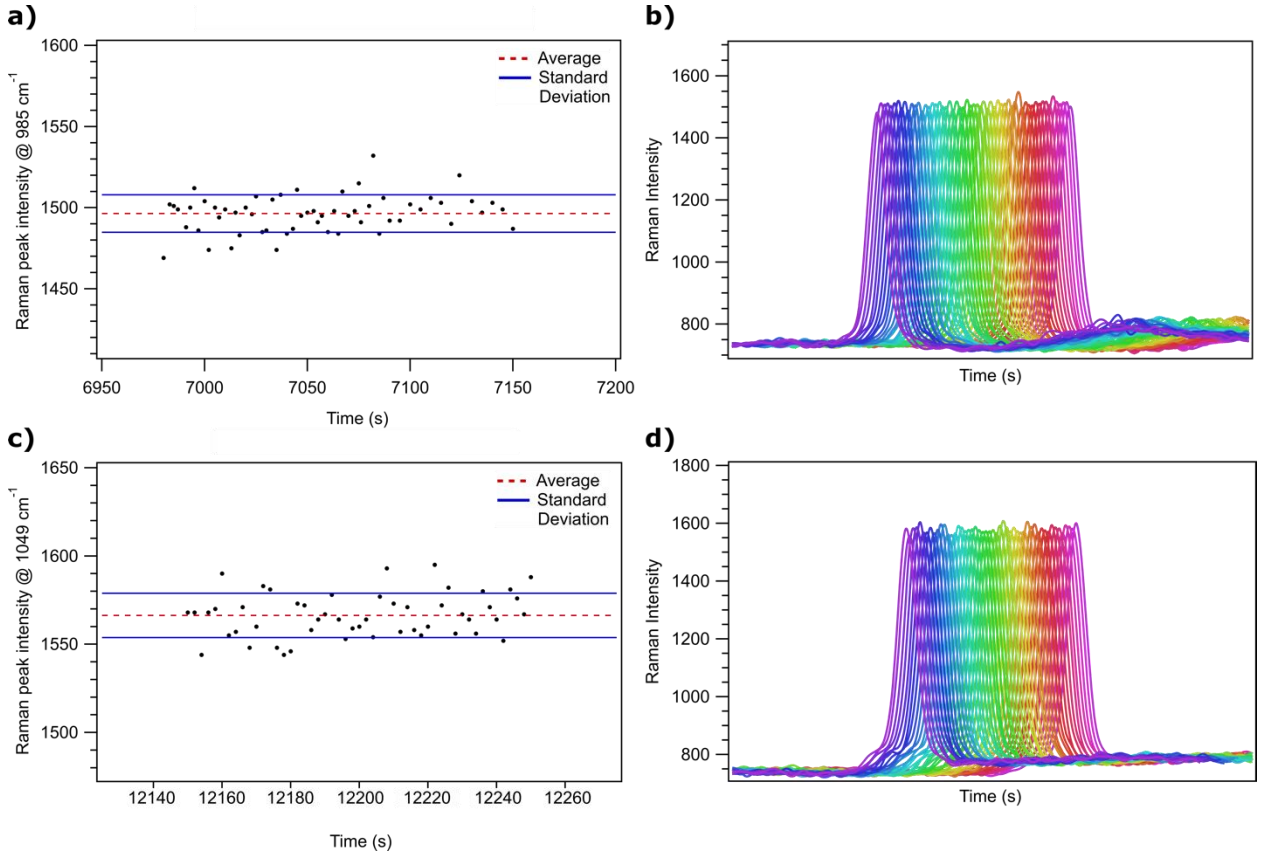

Figure 3.15: Peak stability as a function of time for trapped ammonium sulfate and sodium nitrate particles. Panels (a) and (c) show the peak intensities, average intensity and standard deviation for the sulfate stretching mode at 985 cm^{-1} and the nitrate stretching mode at 1049 cm^{-1}, respectively. Panels (b) and (d) show the Raman spectra of the sulfate stretching mode and nitrate stretching mode as a function of time.

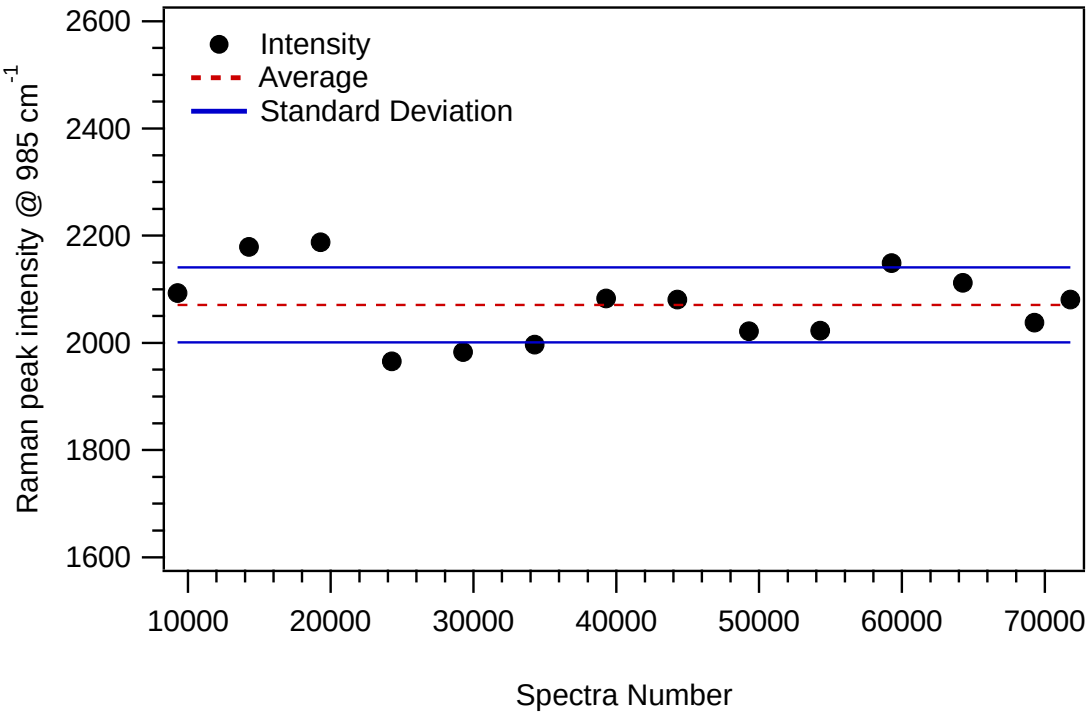

Figure 3.16: Stability of peak intensities over time for an ammonium sulfate droplet with a trapping lifetime greater than 17 hours. Raman peak intensities, average intensity and standard deviation for the sulfate stretching mode at 985 cm^{-1} are shown as a function of spectra number, which is directly related to time (in seconds) since a 1 s exposure was used in the collection of the spectra.

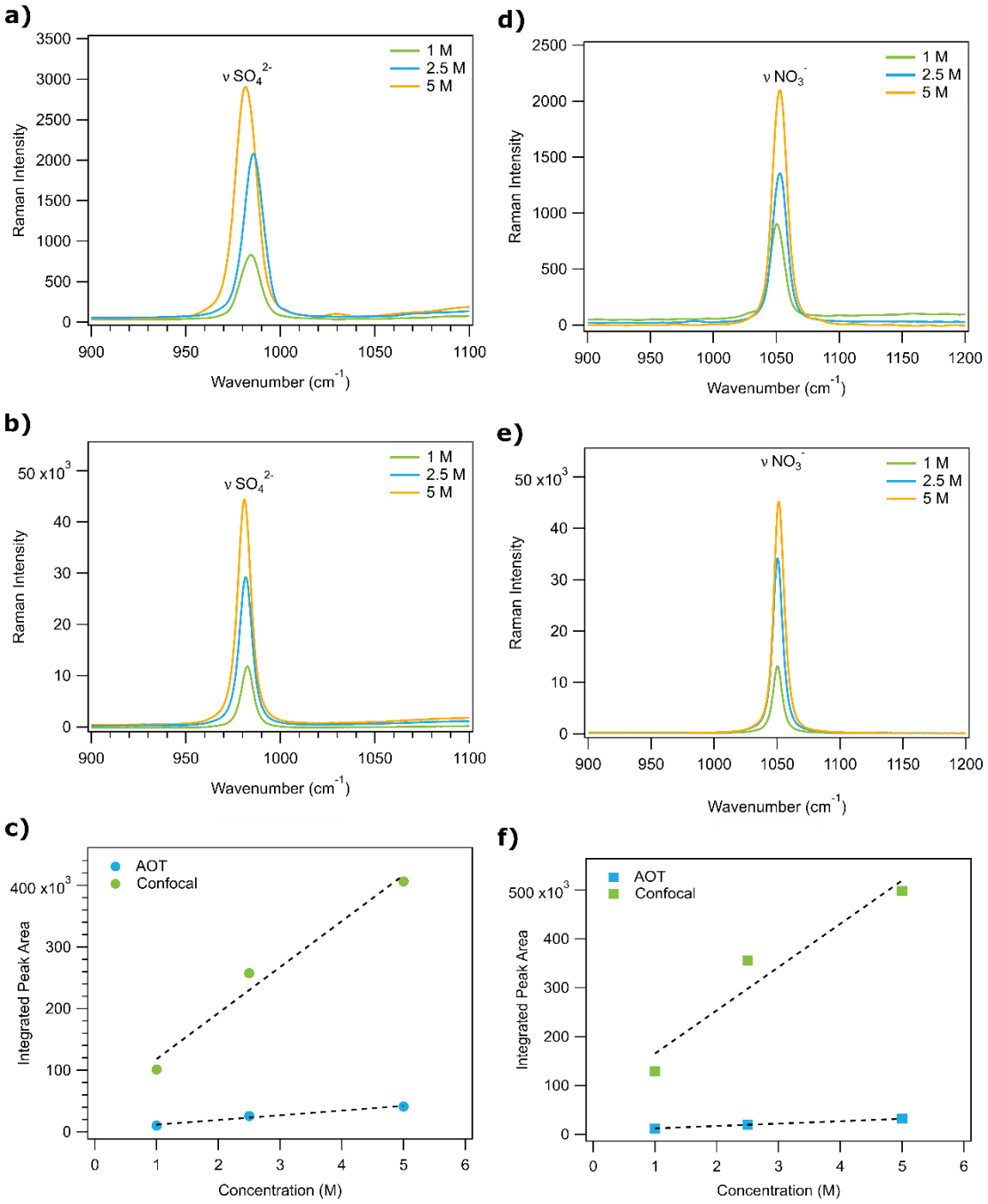

Figure 3.17: Comparison of single particle and bulk Raman spectra of ammonium sulfate and sodium nitrate as a function of concentration collected with the AOT and confocal Raman spectrometer, respectively. Cavity enhanced Raman spectra of trapped (a) ammonium sulfate droplets (1 M: 4.6μm, 2.5 M: 4.8 μm, 5 M: 4.2 μm) and (d) sodium nitrate droplets (1 M: 4.0 μm, 2.5 M: 4.8 μm, 5M: 5.5 μm). Confocal Raman spectra of bulk aqueous solutions of (b) ammonium sulfate and (e) sodium nitrate. Integrated peak area of the (c) sulfate stretching mode at 980 cm^{-1} and (f) nitrate stretching mode at 1049 cm^{-1} as a function of concentration from Raman spectra collected with the AOT (blue) or confocal Raman spectrometer (green).

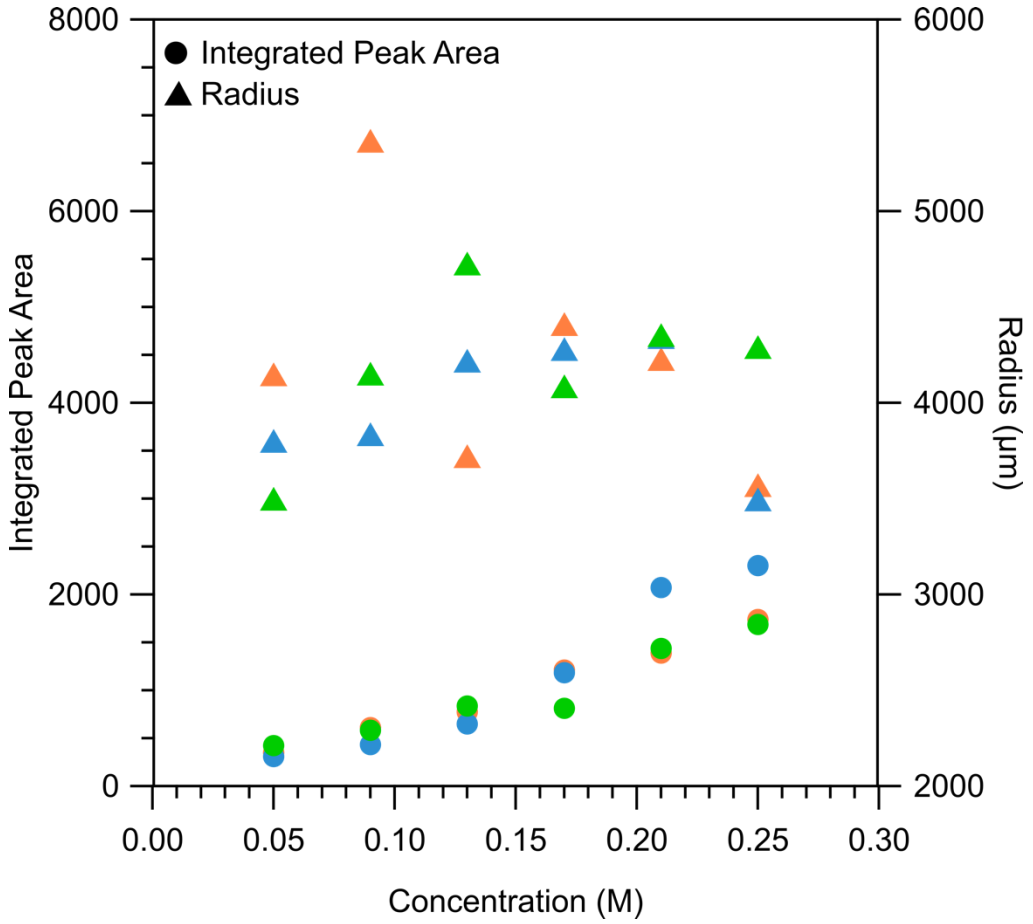

Figure 3.18: Integrated peak area (circles) and radius (triangles) for trapped sulfate droplets as a function of concentration. For a specific trial of a given concentration, the radius and integrated peak area are shown in the same color. Integrated peak area is determined for the sulfate stretching mode at 985 cm^{-1}. By comparing radius and integrated peak area for each concentration and trial the conclusion can be made that there is no correlation between droplet radius and integrated peak area.

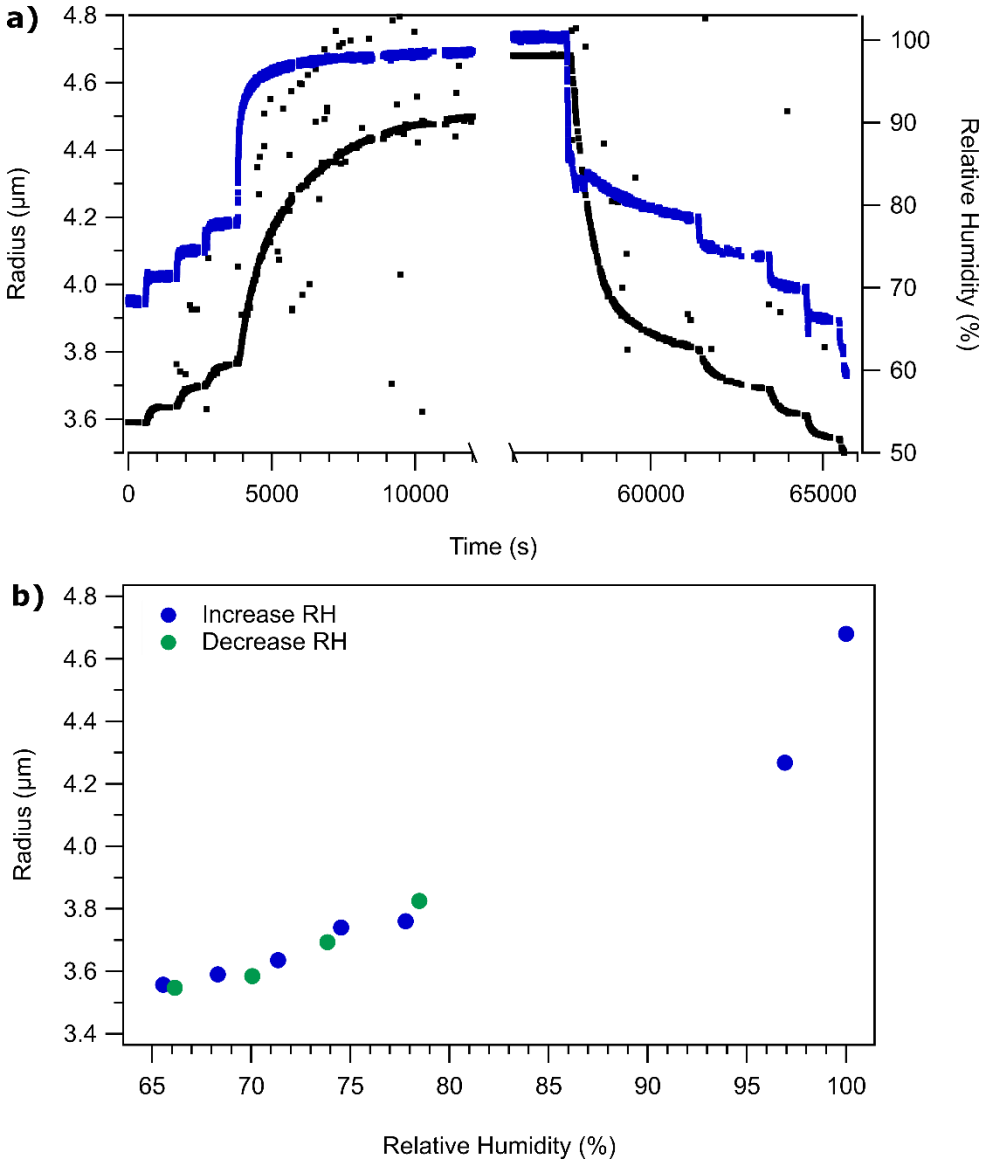

Figure 3.19: Changes in droplet size as a function of relative humidity for a trapped ammonium sulfate droplet. a) Throughout the lifetime of the trapped droplet, as RH (blue) increases or decreases, droplet radius (black) changes accordingly. b) Droplet radius increases as RH is first increased (blue), followed by decreased RH (green) with accompanying decreases in droplet radius. As RH is decreased, the changes in radius follow the same trace demonstrating that the droplet returns to the same size at a specified relative humidity.

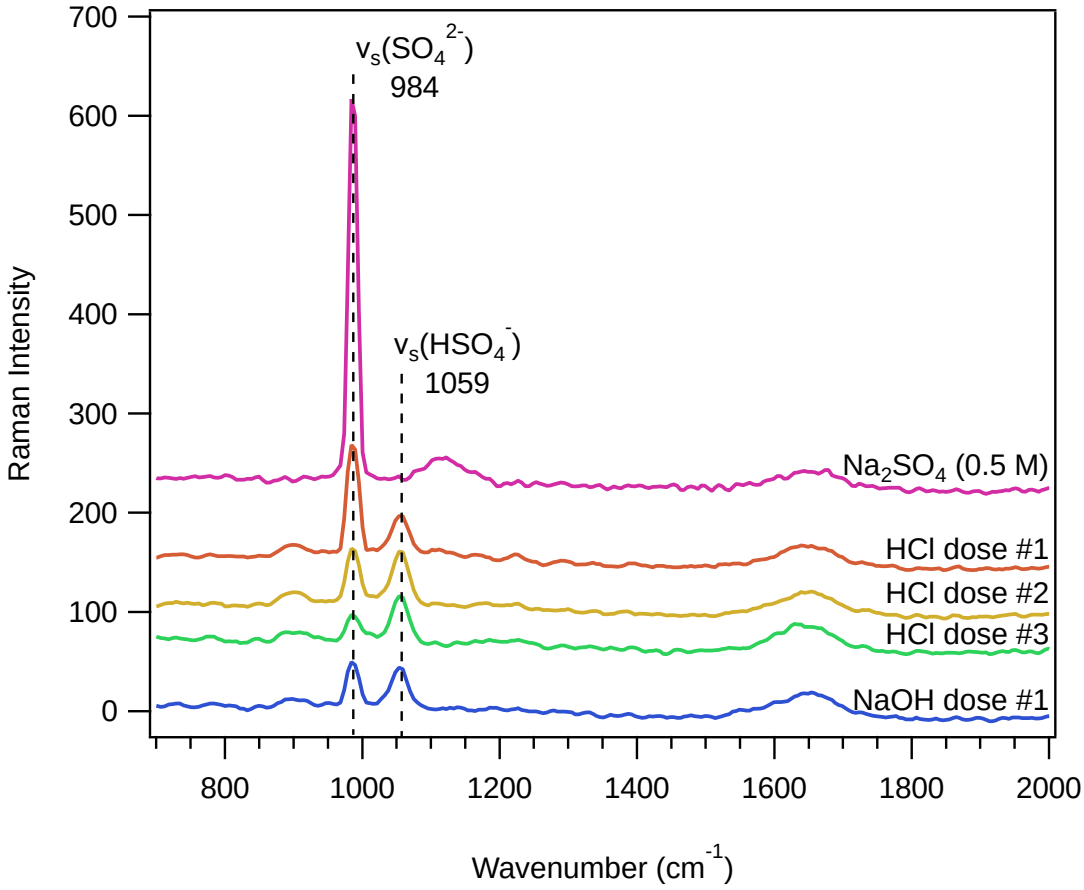

Figure 3.20: Cavity enhanced Raman spectra of a trapped 0.5 M sodium sulfate droplet. The initial trapped droplet (pink) is then coalesced or dosed with acidic aerosol (HCl, 1 M) three times (HCl dose #1-3). After the three coalescence events with acidic aerosol, the trapped droplet is then coalesced with basic aerosol (NaOH, 1 M). As the droplet is dosed with acidic or basic aerosol the equilibrium shifts between SO_4^{2-} and HSO_4^- as seen by the changes in the relative peak intensities of the SO_4^{2-} and HSO_4^- vibrational bands at 984 and 1059 cm^{-1}, respectively.

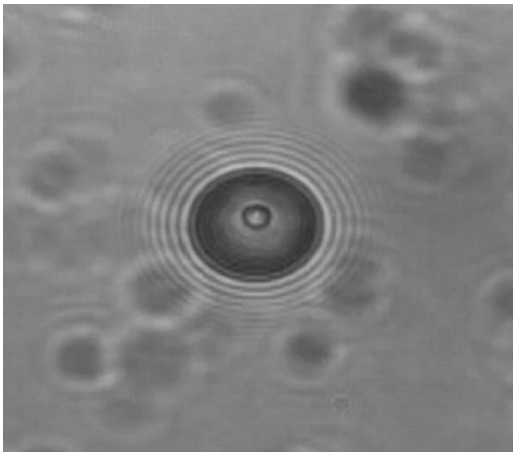

Figure 3.21: Screenshot from microscopy video of a trapped droplet containing a polystyrene bead inclusion.

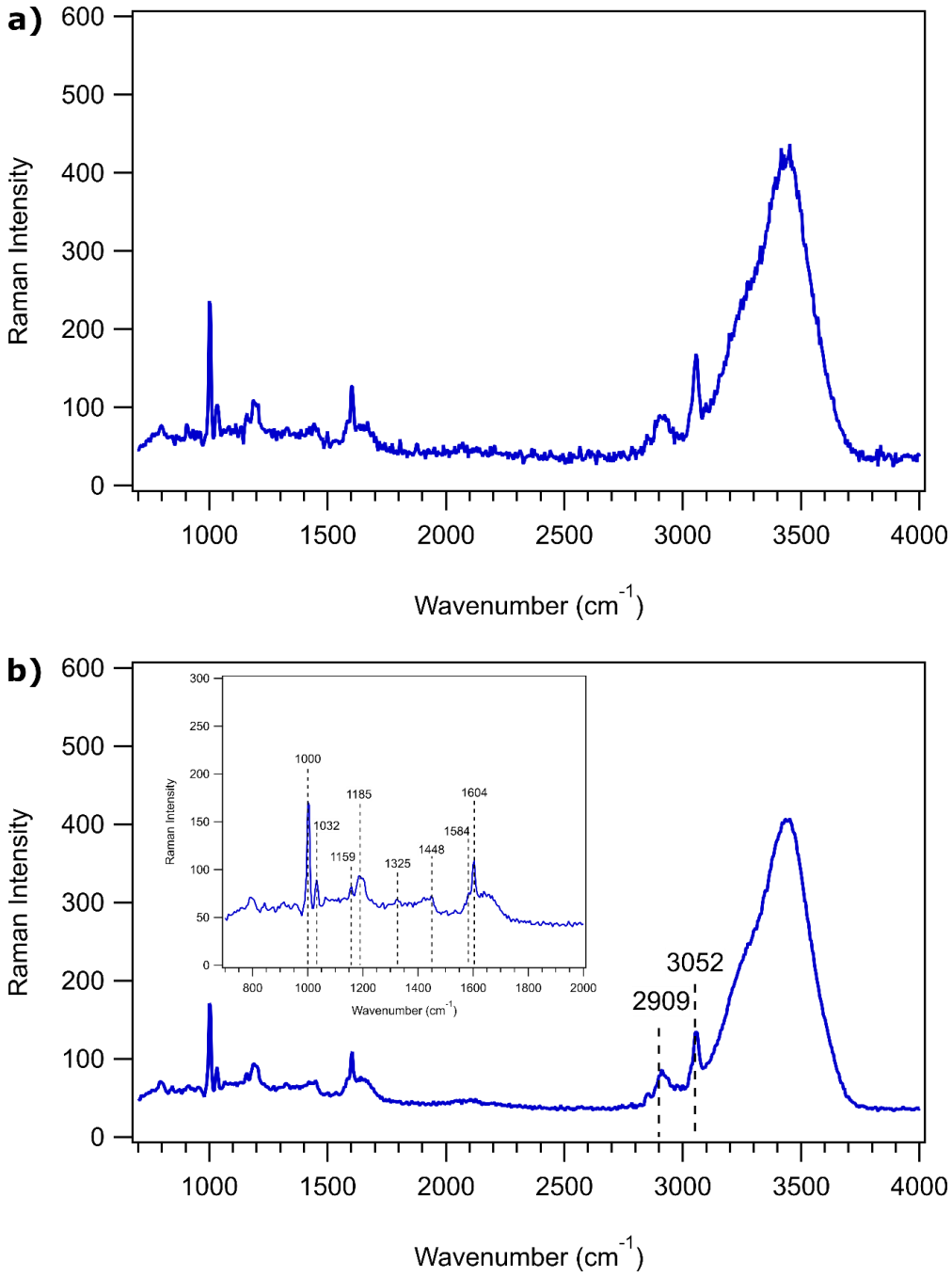

Figure 3.22: a) A single cavity enhanced Raman spectrum and b) averaged cavity enhanced Raman spectra collected from a trapped droplet containing a polystyrene inclusion. The inset in b) focuses on the 700-2000 cm^{-1} range.

3.6. References

(1) Ashkin, A.; Dziedzic, J. M.; Bjorkholm, J. E.; Chu, S. Observation of a Single-Beam Gradient Force Optical Trap for Dielectric Particles. *Opt. Lett.* **1986**, *11*, 288–290.

(2) Molloy, J. E.; Padgett, M. J. Lights, Action: Optical Tweezers. *Contemp. Phys.* **2002**, *43*, 241–258.

(3) Knox, K. J. Optical Manipulation in Aerosol Optical Tweezers. In *Light-Induced Processes in Optically-Tweezed Aerosol Droplets*; Springer Berlin Heidelberg: Berlin, Heidelberg, 2011; pp 81–109.

(4) Wills, J. B.; Knox, K. J.; Reid, J. P. Optical Control and Characterisation of Aerosol. *Chem. Phys. Lett.* **2009**, *481*, 153–165.

(5) Guo, H.; Li, Z. Optical Tweezers Technique and Its Applications. *Sci. China Physics, Mech. Astron.* **2013**, *56*, 2351–2360.

(6) Moffitt, J. R.; Chemla, Y. R.; Smith, S. B.; Bustamante, C. Recent Advances in Optical Tweezers. *Annu. Rev. Biochem.* **2008**, *77*, 205–228.

(7) Reid, J. P. Particle Levitation and Laboratory Scattering. *J. Quant. Spectrosc. Radiat. Transf.* **2009**, *110*, 1293–1306.

(8) Shaevitz, J. W. *A Practical Guide to Optical Trapping*; 2006.

(9) Block, S. M. Making Light Work with Optical Tweezers. *Nature* **1992**, *360*, 493–495.

(10) Grier, D. G. A Revolution in Optical Manipulation. *Nature* **2003**, *424*, 810–816.

(11) Clark, D. *Visibly Better Optical Trapping Airborne Particles*; Bristol, 2015.

(12) Mitchem, L.; Reid, J. P. Optical Manipulation and Characterisation of Aerosol Particles Using a Single-Beam Gradient Force Optical Trap. *Chem. Soc. Rev.* **2008**, *37*, 756.

(13) *Cavity-Enhanced Spectroscopy and Sensing*; Gagliardi, G., Loock, H.-P., Eds.; Springer: Berlin, Germany, 2014; Vol. 179.

(14) Foreman, M. R.; Swaim, J. D.; Vollmer, F. Whispering Gallery Mode Sensors. *Adv. Opt. Photonics* **2015**, *7*, 168–240.

(15) *Fundamentals and Applications in Aerosol Spectroscopy*, 1st ed.; Signorell, R., Reid, J., Eds.; CRC Press: Boca Raton, 2011.

(16) Reid, J. P.; Meresman, H.; Mitchem, L.; Symes, R. Spectroscopic Studies of the Size and Composition of Single Aerosol Droplets. *Int. Rev. Phys. Chem.* **2007**, No. 1, 139–192.

(17) Reid, J. P.; Mitchem, L. Laser Probing of Single-Aerosol Droplet Dynamics. *Annu. Rev. Phys. Chem.* **2006**, *57*, 245–271.

(18) Hill, S. C.; Benner, R. E. Morphology-Dependent Resonances. In *Optical Effects Associated with Small Particles*; Chang, R. K., Barber, P. W., Eds.; Advanced Series in Applied Physics; World Scientific: Singapore, 1988; Vol. 1, pp 1–61.

(19) Symes, R.; Sayer, R. M.; Reid, J. P. Cavity Enhanced Droplet Spectroscopy: Principles, Perspectives and Prospects. *Phys. Chem. Chem. Phys.* **2004**, *6*, 474–487.

(20) Sayer, R. M.; Gatherer, R. D. B.; Gilham, R. J. J.; Reid, J. P. Determination and Validation of Water Droplet Size Distributions Probed by Cavity Enhanced Raman Scattering. *Phys. Chem. Chem. Phys.* **2003**, *5*, 3732–3739.

(21) Laura Mitchem; Jariya Buajarern; Rebecca J. Hopkins; Andrew D. Ward; Richard J. J. Gilham; Roy L. Johnston; Jonathan P. Reid. Spectroscopy of Growing and Evaporating Water Droplets: Exploring the Variation in Equilibrium Droplet Size with Relative Humidity. *J. Phys. Chem. A* **2006**, *110*, 8116–8125.

(22) Krieger, U. K.; Marcolli, C.; Reid, J. P. Exploring the Complexity of Aerosol Particle Properties and Processes Using Single Particle Techniques. *Chem. Soc. Rev.* **2012**, *41*, 6631–6662.

(23) Butler, J. R.; Wills, J. B.; Mitchem, L.; Burnham, D. R.; Mcgloin, D.; Reid, J. P. Spectroscopic Characterisation and Manipulation of Arrays of Sub-Picolitre Aerosol Droplets. *Lab Chip* **2008**, *9*, 521–528.

(24) Preston, T. C.; Reid, J. P. Accurate and Efficient Determination of the Radius, Refractive Index, and Dispersion of Weakly Absorbing Spherical Particle Using Whispering Gallery Modes. *J. Opt. Soc. Am. B* **2013**, *30*, 2113–2122.

(25) Davies, J. F.; Wilson, K. R. Raman Spectroscopy of Isotopic Water Diffusion in Ultraviscous, Glassy, and Gel States in Aerosol by Use of Optical Tweezers. *Anal. Chem.* **2016**, *88*, 2361–2366.

(26) Miles, R. E. H.; Walker, J. S.; Burnham, D. R.; Reid, J. P. Retrieval of the Complex Refractive Index of Aerosol Droplets from Optical Tweezers Measurements. *Phys. Chem. Chem. Phys.* **2012**, *14*, 3037.

(27) Haddrell, A. E.; Miles, R. E. H.; Bzdek, B. R.; Reid, J. P.; Hopkins, R. J.; Walker, J. S. Coalescence Sampling and Analysis of Aerosols Using Aerosol Optical Tweezers. *Anal. Chem.* **2017**, *89*, 2345–2352.

(28) Estillore, A. D.; Hettiyadura, A. P. S.; Qin, Z.; Leckrone, E.; Wombacher, B.; Humphry, T.; Stone, E. A.; Grassian, V. H. Water Uptake and Hygroscopic Growth of Organosulfate Aerosol. *Environ. Sci. Technol.* **2016**, *50*, 4259–4268.

(29) Rindelaub, J. D.; Craig, R. L.; Nandy, L.; Bondy, A. L.; Dutcher, C. S.; Shepson, P. B.; Ault, A. P. Direct Measurement of PH in Individual Particles via Raman Microspectroscopy and Variation in Acidity with Relative Humidity. *J. Phys. Chem. A* **2016**, *120*, 911–917.

(30) Craig, R. L.; Ault, A. P. Aerosol Acidity: Direct Measurement from a Spectroscopic

Method. In *Multiphase Environmental Chemistry in the Atmosphere*; Hunt, S. W., Laskin, A., Nizkorodov, S. S., Eds.; American Chemical Society: Washington, D.C., 2018; pp 171–191.

(31) Craig, R. L.; Nandy, L.; Axson, J. L.; Dutcher, C. S.; Ault, A. P. Spectroscopic Determination of Aerosol PH from Acid−Base Equilibria in Inorganic, Organic, and Mixed Systems. *J. Phys. Chem. A* **2017**, *121*, 5690–5699.

(32) Davis, R. D.; Lance, S.; Gordon, J. A.; Ushijima, S. B.; Tolbert, M. A. Contact Efflorescence as a Pathway for Crystallization of Atmospherically Relevant Particles. *Proc. Natl. Acad. Sci. U. S. A.* **2015**, *112*, 15815–15820.

(33) Dennis-Smither, B. J.; Hanford, K. L.; Kwamena, N.-O. A.; Miles, R. E. H.; Reid, J. P. Phase, Morphology, and Hygroscopicity of Mixed Oleic Acid/Sodium Chloride/Water Aerosol Particles before and after Ozonolysis. *J. Phys. Chem. A* **2012**, *116*, 6159–6168.

(34) Buajarern, J. ariya; Mitchem, L.; Reid, J. P. Manipulation and Characterization of Aqueous Sodium Dodecyl Sulfate/Sodium Chloride Aerosol Particles. *J. Phys. Chem. A* **2007**, *111*, 13038–13045.

(35) Laurain, A. M. C.; Reid, J. P. Characterizing Internally Mixed Insoluble Organic Inclusions in Aqueous Aerosol Droplets and Their Influence on Light Absorption. *J. Phys. Chem. A* **2009**, *113*, 7039–7047.

(36) Mitchem, L.; Buajarern, J.; Ward, A. D.; Reid, J. P. A Strategy for Characterizing the Mixing State of Immiscible Aerosol Components and the Formation of Multiphase Aerosol Particles through Coagulation. *J. Phys. Chem. B* **2006**, *110*, 13700–13703.

(37) Davis, R. D.; Lance, S.; Gordon, J. A.; Tolbert, M. A. Long Working-Distance Optical Trap for in Situ Analysis of Contact-Induced Phase Transformations. *Anal. Chem.* **2015**, *87*, 6186–6194.

(38) Jacobs, M. I.; Davies, J. F.; Lee, L.; Davis, R. D.; Houle, F.; Wilson, K. R. Exploring Chemistry in Microcompartments Using Guided Droplet Collisions in a Branched Quadrupole Trap Coupled to a Single Droplet, Paper Spray Mass Spectrometer. *Anal. Chem.* **2017**, *89*, 12511–12519.

(39) Rkiouak, L.; Tang, M. J.; Camp, J. C. J.; McGregor, J.; Watson, I. M.; Cox, R. A.; Kalberer, M.; Ward, A. D.; Pope, F. D. Optical Trapping and Raman Spectroscopy of Solid Particles. *Phys. Chem. Chem. Phys.* **2014**, *16*, 11426–11434.

(40) Tang, M. J.; Camp, J. C. J.; Rkiouak, L.; McGregor, J.; Watson, I. M.; Cox, R. A.; Kalberer, M.; Ward, A. D.; Pope, F. D. Heterogeneous Interaction of SiO 2 with N 2 O 5 : Aerosol Flow Tube and Single Particle Optical Levitation-Raman Spectroscopy Studies. *J. Phys. Chem. A* **2014**, *118*, 8817–8827.

(41) Buajarern, J.; Mitchem, L.; Reid, J. P. Characterizing Multiphase Organic/Inorganic/Aqueous Aerosol Droplets. *J. Phys. Chem. A* **2007**, *111*, 9054–

9061.

(42) Boerkamp, M.; van Leest, T.; Heldens, J.; Leinse, A.; Hoekman, M.; Heideman, R.; Caro, J. On-Chip Optical Trapping and Raman Spectroscopy Using a TripleX Dual-Waveguide Trap. *Opt. Express* **2014**, *22*, 30528.

(43) Jasse, B.; Chao, R. S.; Koenig, J. L. Laser Raman Scattering in Uniaxially Oriented Atactic Polystyrene. *J Polym Sci Polym Phys Ed* **1978**, *16*, 2157–2169.

Chapter 4 Titration of Aerosol pH through Droplet Coalescence

4.1. Synopsis

The pH of aqueous aerosols, as well as cloud and fog droplets, has an important influence on the chemistry that takes place within these unique microenvironments. Utilizing conjugate acid/base pairs to infer pH changes, we investigate, for the first time, changes in aerosol pH upon droplet coalescence. In particular, we show that the pH within individual aqueous aerosol droplets that are ~8 μm in diameter can be titrated via droplet coalescence in an Aerosol Optical Tweezer (AOT). Using sulfate/bisulfate and carbonate/bicarbonate as model systems, the pH of trapped droplets is determined before and after introduction of smaller droplets containing a strong acid. The pH change upon coalescence of the acid within the trapped droplet is calculated using Specific Ion Interaction Theory (SIT). Furthermore, we show that the pH of an individual aerosol can be manipulated along a fairly wide range of pH values, paving the way for future studies requiring rigorous pH control of aqueous aerosol.

4.2. Introduction and Discussion

Acidity is a key factor in aerosol chemistry, as well as in the chemistry that occurs in cloud and fog droplets. The microenvironment within individual droplets can be very different from that of a bulk solution and therefore it is important that pH within individual suspended droplets be measured *and* controlled. Many atmospheric multiphase chemical processes are pH-dependent including transition metal catalyzed oxidation processes and secondary organic aerosol formation.[1–5] For inorganic and organic acids, molecular and

ionic speciation of acid/base conjugate pairs depend on pH and for metals, such as iron, solubility and speciation are highly pH dependent. Therefore, it is extremely important to take pH into account when studying aqueous aerosol chemistry.[6–15]

Although cloud water is generally acidic with a pH around 5, more alkaline cloud pH values around 7 have been reported and very low pH aqueous environments within aerosols (pH less than 3) have been proposed as well.[16–22] This indicates that droplets in the atmosphere, whether as aqueous aerosols or in cloud and fog waters, are highly variable in terms of pH. Furthermore, the chemistry *within* the microenvironment of a droplet and at the *surface* of the droplet can be different from that of a bulk solution.[23–26]

Given that pH is a key factor in aerosol, cloud and fog chemistry, there are very few direct measurements of aerosol pH. Most methods for determining aerosol pH in the past have used indirect proxy methods. The main proxy methods used to estimate aerosol acidity include the ion balance method, the molar ratio method, thermodynamic equilibrium models and phase partitioning of ammonia.[27] All of these methods provide valuable information yet each of these have limitations that prevent their widespread application. Therefore, there is a need for better methods for directly determining aerosol pH.[28] Recently, Ault and Dutcher, along with their co-workers, have made great strides in this regard. In several seminal papers, it was shown that the pH for substrate deposited aerosol particles can be directly determined using Raman microspectroscopy (*vide*

infra).[29–31] In more recent work, colorimetric image processing was used to determine the pH of aerosol particles that were directly deposited onto pH paper.[32]

Table 4.1 summarizes these different direct and indirect methods for determining aerosol pH. Table 4.1 includes the main advantages and disadvantages of each method, along with some key points.[29,30,39–41,31–38] The indirect methods were previously discussed in detail in a review by Hennigan et. al. [27]

In addition to various methods of measuring aerosol pH, there are also multiple approaches to calculating solution pH based on chemical equilibria. One widely used approach is the Henderson-Hasselbalch (H-H) equation (Eq. 4.1),

$$pH = pK_a + \log\frac{[A^-]}{[HA]} \qquad \text{(Eq. 4.1)}$$

where pH is calculated through knowledge of the pK_a and the ratio of the concentrations of acid, [HA], and its conjugate base, $[A^-]$.[42] The pH derived from the Henderson-Hasselbalch equation is simply from the definition of the equilibrium constant, K_a, in logarithmic form. However, equation 4.1 is applicable to a limited range of solution conditions and does not take into account non-ideal behavior and ion activity. This results in a breakdown of the H-H equation for relatively strong acids or bases as well as for systems where activity coefficients cannot be neglected.[43,44] The Debye-Hückel Theory (DHT) and Specific-Ion Interaction Theory (SIT) can be used to calculate ion activities. Both of these approaches more accurately determine pH by taking into account deviations from ideal solution behavior by calculating activity coefficients for strong electrolyte solutions.[42,45,46]

DHT was recently applied to substrate deposited aerosol particles. Aerosol pH was determined using experimental data from Raman spectroscopy of conjugate acid/base pairs along with extended DHT.[29–31] In this method, activity coefficients, γ_i, for species *i* are determined by the extended Debye-Hückel equation (Eq. 4.2),

$$-log\gamma_i = \frac{Az_i^2\sqrt{I}}{1 + aB\sqrt{I}} = D \qquad \text{(Eq. 4.2)},$$

where *A* and *B* are constants characteristic of the solvent (water) and *a* is the effective diameter of the ion in solution. *I* is the ionic strength of the solution,

$$I = \frac{1}{2}\sum c_i z_i^2 \qquad \text{(Eq. 4.3)}$$

which is calculated from the concentration, c_i, and charge, z_i, of each ion. The activity, a_i, can be related to the dissociation constant, K_a,

$$K_a = \frac{a_{H^+} \times a_{A^-}}{a_{HA}} = \frac{([H^+]\gamma_{H^+})([A^-]\gamma_{A^-})}{[HA]\gamma_{HA}} \qquad \text{(Eq. 4.4)}$$

for a system in equilibrium. The pH of the substrate-deposited droplet pH can be calculated

$$pH = -\log(a_{H^+}) = -log([H^+]\gamma_{H^+}) \qquad \text{(Eq. 4.5)}$$

after iteratively solving for γ_{H^+} and a_{H^+}.

The Debye-Hückel method works best for low electrolyte concentrations and is most accurate for aqueous solutions with ionic strengths ≤ 0.1 m.[45,47] Additionally, one of the major assumptions of the Debye-Hückel model is that the interactions between ions occurs only through long-range electrostatic interactions. However, in more concentrated electrolyte solutions, shorter-range specific ion-ion interactions need to be considered as

well.[46,48] Thus, in some cases DHT fails to account for interactions between ions based on their identity and therefore can poorly predict H^+ activity.

The SIT model provides an alternative method for predicting activity coefficients (Eq. 4.6)

$$\log \gamma_i = -z_i^2 D + \sum_k \varepsilon(i,k,I) m_k \qquad \text{(Eq. 4.6)}$$

by taking the interactions of specific ions in solution into account using ion interaction coefficients,

$$\varepsilon = \varepsilon_1 + \varepsilon_2 \times \log(I) \qquad \text{(Eq. 4.7)}$$

where ε is the interaction coefficient of species *i* with species *k* and the summation is extended over all species present at the molality m_k and is dependent on the ionic strength of the solution.[46,49,50] In equation 4.6, *D* is the Debye-Hückel term described by equation 4.2. The ion interaction coefficient, which depends on ionic strength, empirically describes the specific short-range interactions between species *i* and *k* in solution. The coefficients are determined from electrochemical measurements, and the coefficients of many common species are available in the literature.[46,51] A table of coefficients and constants used in DHT and SIT calculations can be found in the Supporting Information (Table 4.2).

Given the wide range of experimental and computational methods available for determining pH, it is essential that each method is validated to ensure the results accurately reflect the activity of H^+. In the current study, we first examine the validity of calculating the pH of individual droplets spectroscopically and using H-H, DHT, and SIT. The method

used in the present work does not require individual particles to be passed through a diffusion dryer or impacted onto a substrate, therefore removing the need to consider the impacts of these experimental apparatuses. With no additional aerosol processing, the method used here provides a direct depiction of the chemistry happening with aerosols under atmospherically relevant conditions. We also examine the extent to which this method can be used to calculate the changing pH of an aerosol upon titration as manipulation of aerosol pH would be essential to studying environmental reactions at atmospherically relevant pH values.

Here, pH is calculated for both bulk solutions and aerosol using DHT and SIT by first determining calibration curves of concentration versus integrated peak area from Raman spectra of one of the conjugate acid/base pairs (e.g. sulfate in the bisulfate/sulfate system and carbonate in the bicarbonate/carbonate system). For bulk solutions, a confocal Raman spectrometer is used to create the calibration curves for aqueous solutions. For an aerosol (~8 μm diameter), an aerosol optical tweezer combined with a cavity enhanced Raman spectrometer is used to determine the Raman intensity as a function of concentration. Calibration curves for sulfate and carbonate are given in Figures 4.7 and 4.8 in Supporting Information. The conjugate ion concentrations are calculated under the assumption that the total sulfur concentration is constant for sulfate/bisulfate, or in the case of carbonate/bicarbonate the total carbon is constant, and that the concentration in the trapped droplet is the same as in the bulk solution. Sulfate and bisulfate concentrations (or carbonate and bicarbonate concentrations) and ionic strength are then used to determine activity coefficients, and ultimately pH, by iteratively solving equations 4.2 through 4.7. For experiments in which aerosol pH is titrated via droplet coalescence with a more acidic

aerosol (*vide infra*), changes in ionic strength with acid dosing are taken into account. In comparison, when calculating pH using the H-H method, the ratio of sulfate to bisulfate is determined by comparing the integrated peak area of the sulfate and bisulfate vibrational bands from the Raman spectra.

Before applying these calculations to trapped aerosols, we first investigated bulk solutions near the same concentrations and pH that are used for aerosol experiments and calculate pH using the three methods discussed above, H-H, DHT, and SIT, to determine which one provides the most accurate calculation from known bulk solutions (see additional information in Supporting Information). The results are summarized in Figure 4.1 where the dashed line represents the case where bulk measured pH is equal to the calculated pH. By comparing all three methods, it can be seen that the SIT method is closest in agreement with the dashed line indicating that pH determined via the SIT method is in greatest agreement with the experimentally measured values compared to DHT or H-H method for these solutions. Therefore, SIT is used for determining aerosol pH.

Using bulk aqueous solutions of known pH, aerosols were generated using an ultrasonic nebulizer and the pH of the trapped droplet was calculated, as done above for bulk solutions, but with the calibration curve obtained for aerosol as shown in Figure 4.7b. Figure 4.2 compares the bulk measured pH to the calculated particle pH for trapped sulfate and carbonate droplets where the dashed line represents the case where the measured bulk pH is equal to that of the calculated particle pH. From this plot, it can be seen that the majority of the calculated pH values for the trapped aerosol lie below the 1:1 line indicating that there is acidification during the formation of the aerosol and trapping process. Ault

and Dutcher observed a similar trend in acidification during the aerosolization process, although, it should be noted that in these studies, the aerosol was sent through a diffusion drier leading to a decrease in pH.[29–31] Additionally, following the method described by Ault and co-workers,[32] pH was determined using colorimetric analysis by directly impacting aerosols generated by the nebulizer onto pH paper, the results of which are summarized in Figure 4.9 and confirm acidification upon nebulization (see Supporting Information for more detail). Overall, these results show that the bulk pH and aerosol pH are not the same and therefore should not be assumed in other aerosol experiments.

Once trapped, aerosol pH can be changed and further probed. This is done by introducing more acidic aerosol containing HCl into the trapping chamber while monitoring the Raman spectra before and after each coalescence event. A detailed description of the trapping and coalescence methods can be found in the Supporting Information. For each trapped droplet, the pH is calculated before and after each coalescence event. Calculated droplet pH as a function of coalescence event number for a sulfate aerosol repeatedly coalesced with acid is shown in Figure 4.3a. As radius increases, the calculated pH decreases with each consecutive coalescence event. Additionally, this change in pH can be seen spectroscopically by examining the ratio of conjugate acid/base pairs. For example, Figure 4.11 depicts the change in peak area ratios for sulfate/bisulfate as a trapped sulfate droplet is titrated with an acidic aerosol. With each coalescence event, the $\nu\ SO_4^{2-}$ band decreases while the $\nu\ HSO_4^-$ band increases corresponding to a shift in equilibrium and a decrease in pH. This decrease in pH upon coalescence demonstrates the ability to change or control the pH of a trapped droplet via coalescence with an acidic aerosol.

Control experiments were also done and are shown in Figure 4.3b. In this plot, the change in calculated pH and radii of a trapped sulfate droplet coalesced with a solution of the same pH, instead of a more acidic aerosol, are shown. Although the radius increases with each consecutive coalescence, there is little variation in calculated pH with each coalescence event indicating that, at a constant relative humidity, the aerosol grows due to coalescence but no significant change in aerosol pH is observed. This can also be seen by examining the sulfate vibrational mode ($\nu\ SO_4^{2-}$, 985 cm^{-1}) in the Raman spectra. The integrated peak area of the $\nu\ SO_4^{2-}$ clearly decreases with each coalescence event when coalesced with an acidic solution (Figure 4.12a) as compared to the minor changes in the vibrational band when coalesced with a solution of the same pH (Figure 4.12b). This conclusion is imperative for the coalescence methodology because it ensures that any changes in calculated pH are due to the addition of acid rather than dilution by water.

Similar experiments were performed to examine the influence concentration of the coalescing acid has on the change in pH of a trapped droplet. Figure 4.4 shows the calculated pH of sulfate droplets, trapped from the same initial bulk solution, titrated with 1 M or 3 M HCl. With both concentrations of acid, as coalescence progresses the calculated pH of the droplet decreases since the droplet is further acidified with each coalescence event. In Figure 4.4, the dashed line represents the pH value for which the calculated droplet pH begins to level off at after multiple coalescence events. As expected, this pH value is near the pH of the bulk acid sample (pH 0 and -0.48 for 1 M and 3 M HCl, respectively). This is because as the number of coalescences increases, the mole fraction of HCl increasingly dominates the droplet and therefore its pH approaches the pH of the

coalescing acid. This observation is important to note as it is validation that the SIT method is the best method to accurately determine droplet pH.

Additionally, the rate at which the droplet acidifies as it is titrated increases when coalescing with aerosol droplets prepared from 3 M HCl solutions compared to 1 M HCl solutions and fewer coalescence events are required to cause the same decrease in droplet pH when using the more concentrated acid. For example, as seen in Figure 4.4, only one coalescence event is required to reach a pH of approximately 0.5 with 3 M HCl whereas two coalescence events are needed to reach the same pH with 1 M HCl. However, it should be noted that the change in pH with each coalescence is not consistent which could be due to multiple reasons. First, the pH scale is logarithmic, as a result, if each coalescence added the same number of H^+ ions, the change in pH would be larger for cases where the starting pH is higher. Therefore, the *change* in pH is expected to diminish over time as the concentration of H^+ continues to increase. Second, the variation in amount of change in pH per coalescence event may be attributed to the inconsistency in the size of the coalescing droplet. With the current nebulization method, there is little control over the exact size of the coalescing droplet (i.e. the incoming aerosol to be coalesced with the already trapped droplet). The nebulizer used in these experiments produces a range of droplet sizes with a reported mass median aerodynamic diameter of 4.5 μm. Although there is currently little control of the size of the incoming droplet, the size can be estimated by calculating the change in radius of the trapped droplet after coalescence, for this experiment, the average coalescing droplet radius was 0.11 μm. To obtain better control of droplet size, additional nebulization methods should be considered. Nonetheless, the pH of a trapped droplet can be changed and titrated via coalescence with more acidic droplets.

To investigate if this method for determining and controlling droplet pH through coalescence is applicable for other chemical systems, the same method was applied to the carbonate/bicarbonate system. Using the concentration calibration curve determined via AOT cavity enhanced Raman spectroscopy (Figure 4.8), the pH of a trapped carbonate droplet titrated with acid was calculated and the results are summarized in Figure 4.5. Due to the difference in chemical properties of sulfate and carbonate, titration was limited to the pH region near the pK_a (specifically, $pK_{a2} = 10.33$ [52]) to avoid the formation and release of carbon dioxide which occurs at lower pH. As shown in Figure 4.5, there is a decrease in pH with each coalescence event and a leveling off of pH after multiple coalescences, similar to the case with sulfate. A larger error is associated with the carbonate system, as compared to sulfate, due to the changes in intensity in the Raman spectra. In the case for sulfate, as the droplet was coalesced with acid, the $\nu\ SO_4^{2-}$ vibrational mode remained prominent whereas for carbonate the $\nu\ CO_3^{2-}$ vibrational mode began to diminish with each coalescence therefore resulting in greater uncertainty associated with the peak fitting process. This error can be minimized by using a higher concentration of carbonate therefore making the carbonate vibrational mode more pronounced. Additionally, it should be noted that the calculated initial particle pH is lower than that of the bulk solution again demonstrating the acidification effect on aerosolization of a bulk solution.

4.3. Conclusions

From this work we have shown that control of droplet pH is attainable through coalescence with acid and can be applied to multiple chemical systems. Figure 4.6 summarizes the experimental technique used here to calculate and control droplet pH. Additionally, future experiments include coalescing a trapped droplet with a basic solution

to show that droplet pH can also be increased by coalescing with a basic solution. With both acid and base coalescence, droplet titration and pH control are possible over a range of pH values. In addition to control over droplet pH, this technique also allows for control over the gaseous medium and relative humidity surrounding the trapped droplet. This control over droplet pH and its environment would allow studies of individual droplets in dynamic environments, similar to those in the atmosphere, to be mimicked and probed in the laboratory. These laboratory-based single particle studies would provide valuable information, such as chemical kinetics of individual aerosols or elucidating surface effects by comparing bulk phase chemical reactions and kinetics to those in the aerosol phase, that can be used to update atmospheric models to more accurately predict and simulate aerosol chemistry. It is also worth noting that the method described in the current studies is capable of measuring pH of the aerosol as a whole but cannot differentiate between the surface or bulk of the aerosol. Therefore, future experiments designed to probe acidity or pKa at the aerosol surface would require additional development of the current method or a different technique all together.[53–55]

These results also underscore the necessity of applying appropriate theories to pH calculations. While DHT is appropriate for low ionic strength studies, SIT should be used where possible when working with high ionic strength aerosols, such as those from polluted environments. Here, two chemical validations of SIT calculations of pH have been provided: i) SIT calculations for bulk solutions are in good agreement with the measured bulk pH from the pH probe, an instrument which has been extensively characterized as an accurate measure of pH, and ii) SIT shows that a particle repeatedly coalesced with acidic aerosol approaches the pH of the bulk acid solution, which agrees with chemical intuition.

It is essential that similar validation experiments be performed for the other direct pH measurement techniques, listed in Table 4.1, in order to verify that each can be reliably used in appropriate contexts to measure environmental samples. Thus, the results presented here provide evidence for a reliable method of controlling and confidently calculating aerosol pH via droplet coalescence that will allow examination of pH dependent speciation and reactions within a single aerosol droplet**.**

4.4. Acknowledgements

This material is based upon work supported by the National Science Foundation under grant AGS1702488. Any opinions, findings, and conclusions or recommendations expressed in this material are those of the authors and do not necessarily reflect the views of the National Science Foundation.

Chapter 4 is reproduced with permission from: Coddens, E.M.; Angle, K.J.; Grassian, V. H. Titration of Aerosol pH through Droplet Coalescence. *J. Phys. Chem. Lett., 10 (15)*, 4476-4483, 2019. The dissertation author was the primary investigator and author of this paper.

4.5. Figures

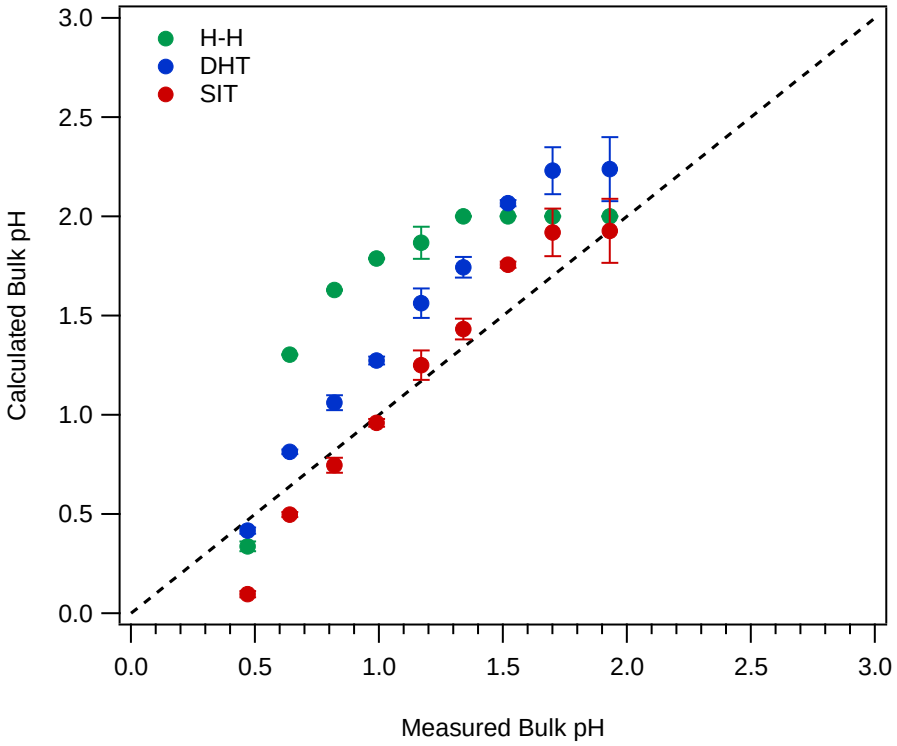

Figure 4.1: Comparison of experimentally measured bulk solution pH to calculated bulk solution pH using H-H equation (green), DHT (blue) or SIT (red) methods. Calculated pH values are determined using the equations provided in the main text and sulfate concentrations obtained from the calibration curve shown Figure 4.7a. The dashed line represents the 1:1 line where bulk measured pH is equal to that of calculated pH.

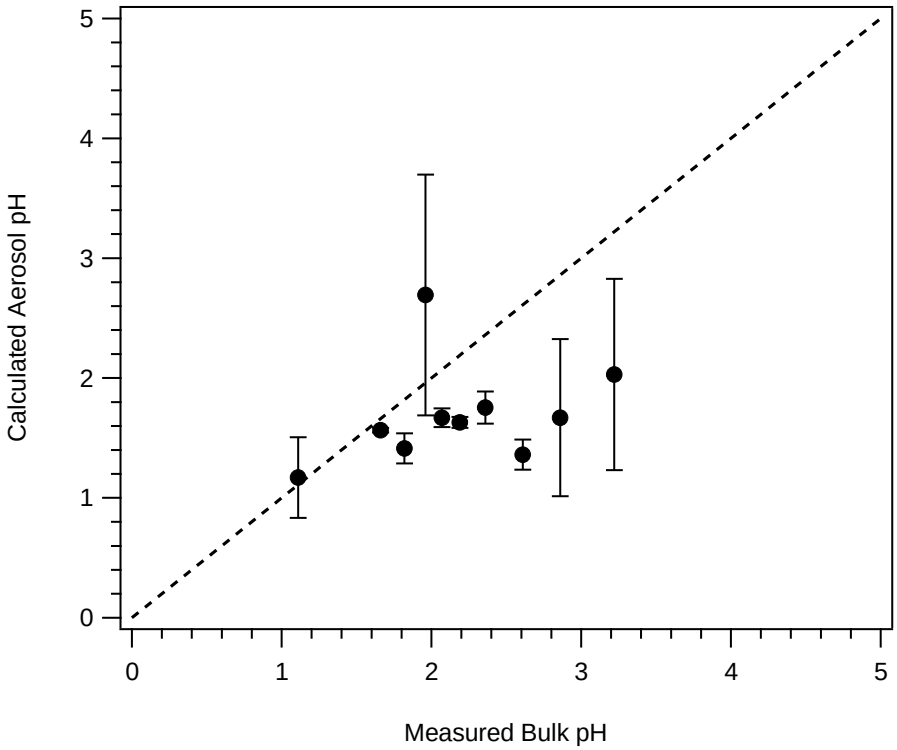

Figure 4.2: Comparison of measured bulk pH to calculated aerosol pH using the SIT method for trapped sulfate droplets. Calculated pH values are determined by equations 4.2-4.7 where sulfate concentration is obtained using the calibration curve from Figure 4.7b. The dashed line represents the 1:1 line where measured bulk pH is equal to the calculated aerosol pH. It can be seen that in most cases, the aerosol pH is more acidic than the bulk pH.

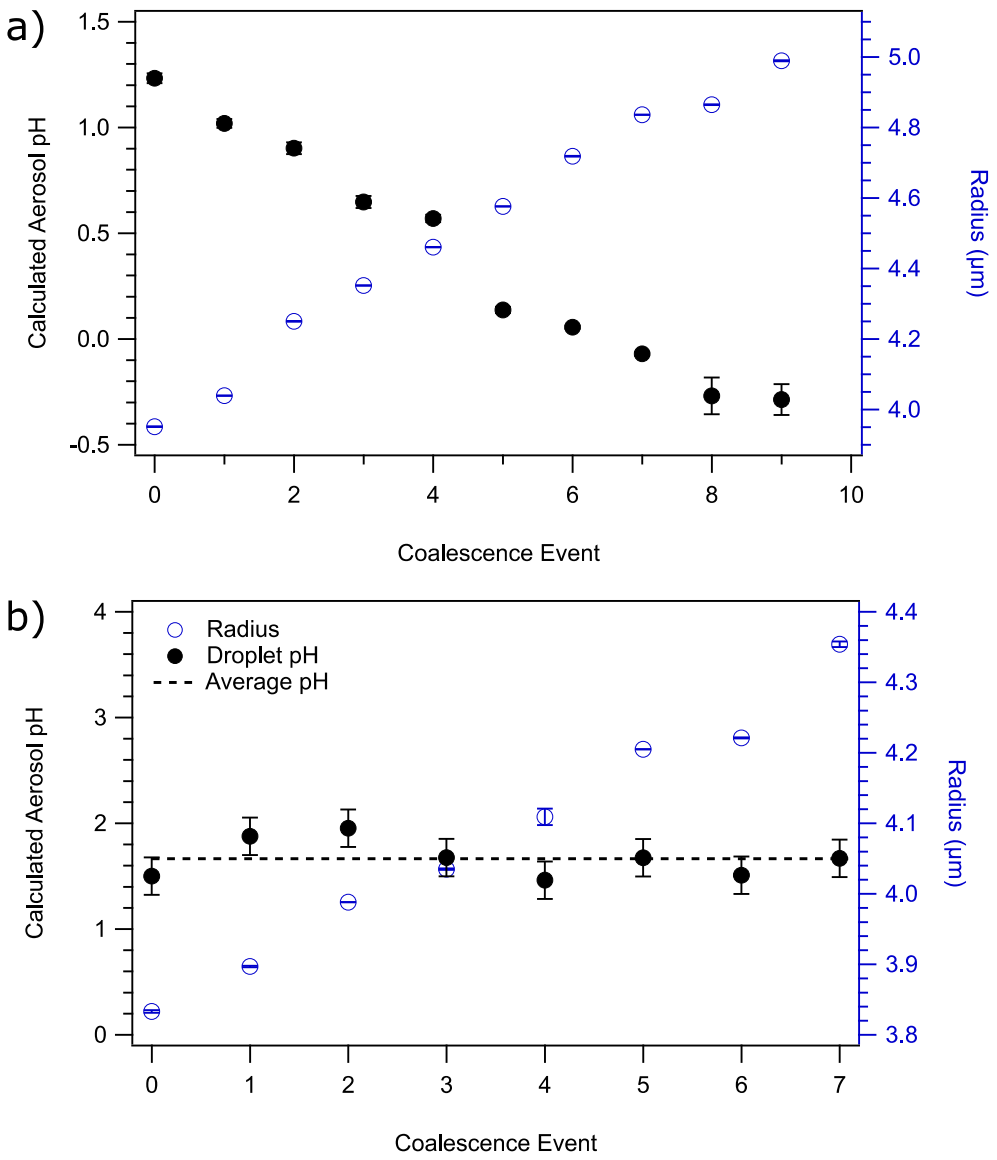

Figure 4.3: a) Calculated aerosol pH (closed, black circles) and radii (open, blue circles) of a trapped sulfate droplet coalesced with 1 M HCl showing the decrease in droplet pH and corresponding increase in radius as coalescence proceeds from coalescence event 0 to 9, where 0 is the initial droplet before any coalescence. b) Calculated droplet pH and radii of a trapped sulfate droplet coalesced with water of the same pH (2.09), indicating that taking up water from dosing, at a constant relative humidity, does not appear to significantly change droplet pH. The dashed line is the average calculated droplet pH.

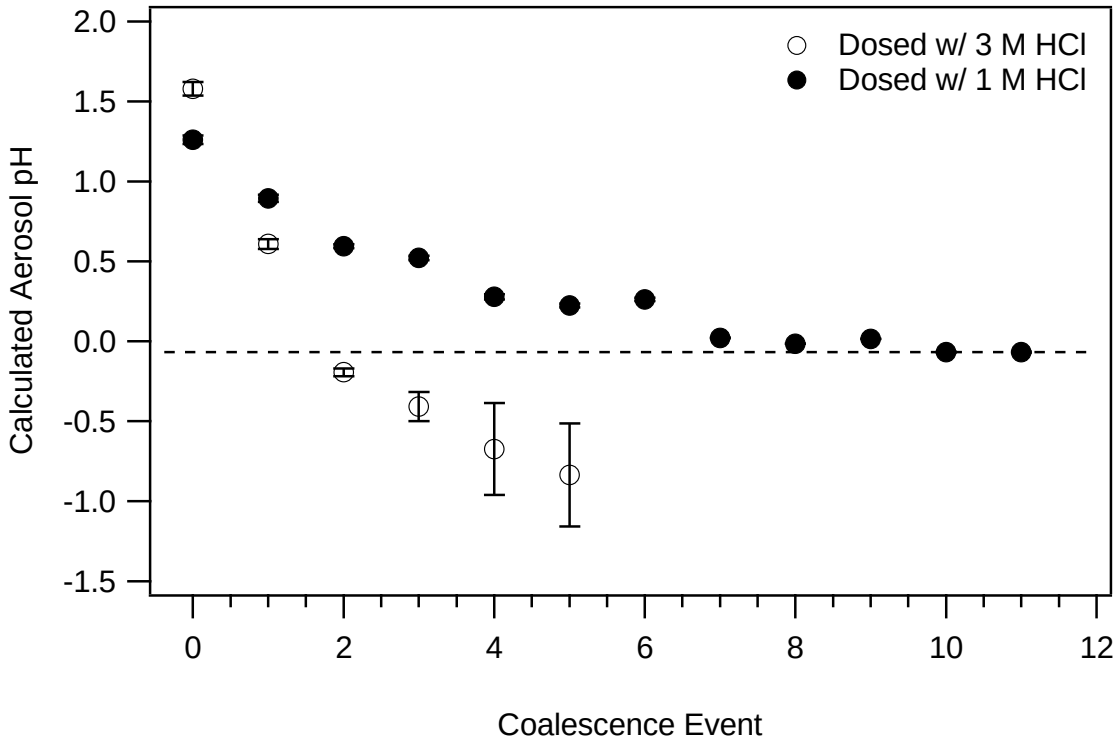

Figure 4.4: Calculated pH of trapped sulfate droplets coalesced with 1 M (closed circles) or 3 M (open circles) hydrochloric acid. Calculated pH is shown as a function of the number of coalescence events where 0 is the calculated pH of the trapped droplet prior to acid coalescence. The dashed line represents the value at which pH levels off for coalescence experiments with 1 M HCl.

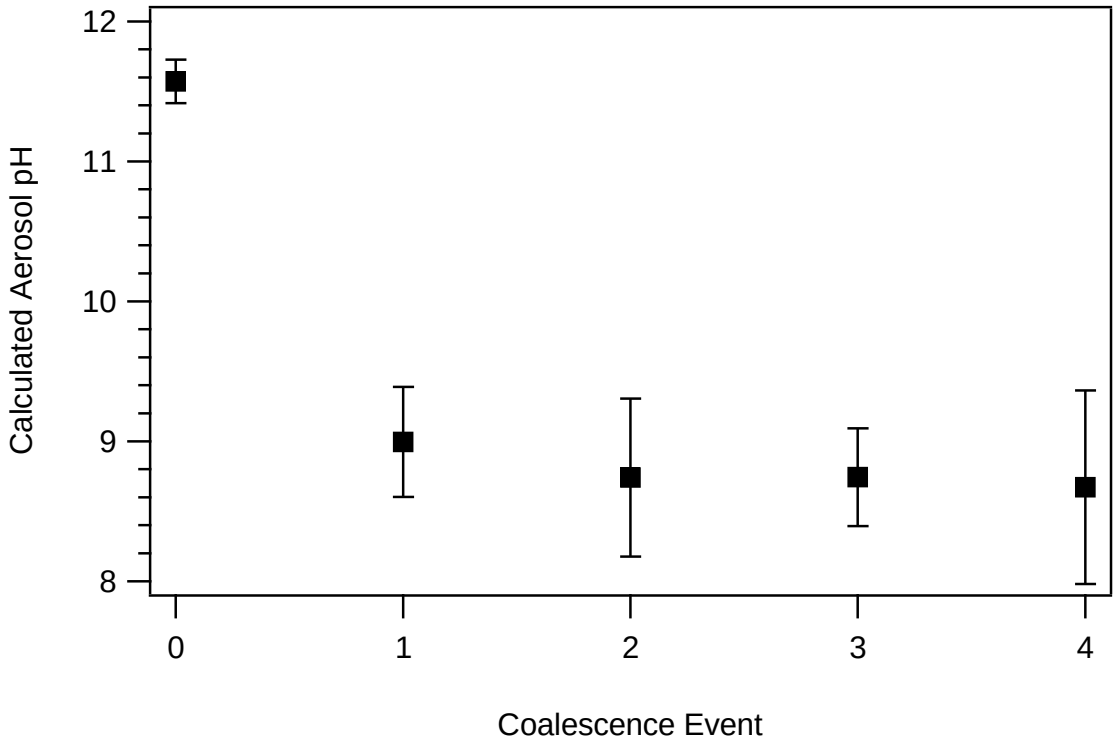

Figure 4.5: Calculated pH of a trapped carbonate droplet, from a bulk solution with a measured pH of 12.4, coalesced with 1 M HCl. Calculated pH is shown as a function of the number of coalescence events where 0 is the calculated pH of the trapped droplet prior to acid coalescence.

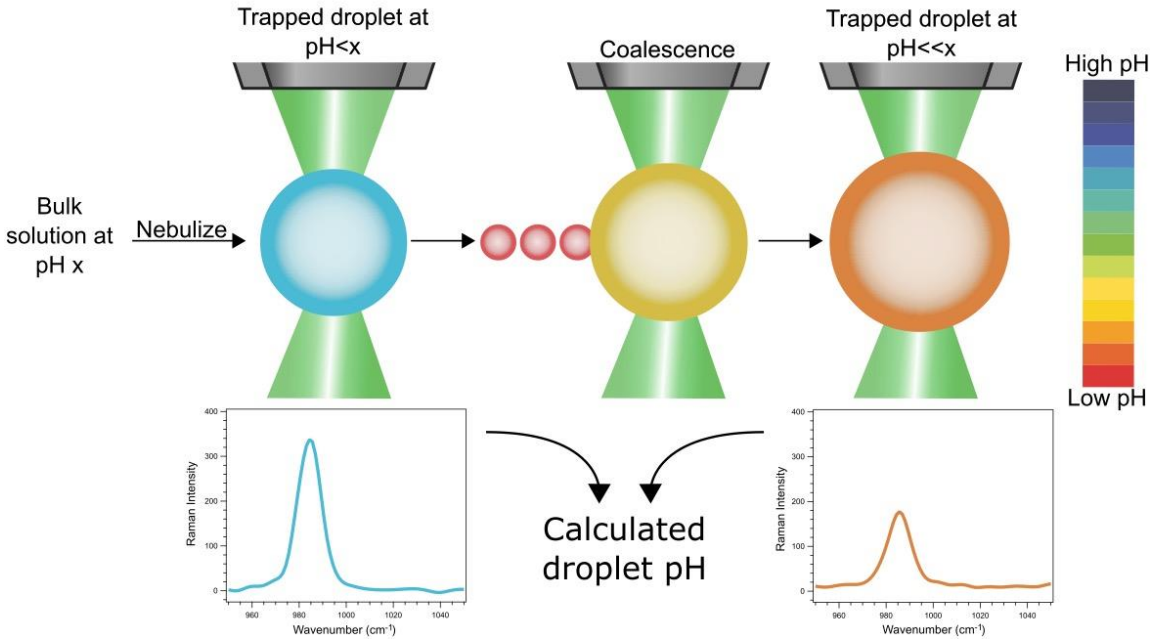

Figure 4.6: Schematic of the aerosol trapping process from bulk solutions of pH x. Initial pH of the aerosol is less than the bulk solution. The aerosol pH can be changed through coalescence with another aerosol at a different pH. Raman spectra from the trapped particle are used in conjunction with calibration curves to determine concentration and ultimately calculate aerosol pH following.

4.6. Tables

Table 4.1: Summary of direct and indirect methods for determining aerosol pH.

Method	Advantages	Disadvantages	Refs
Direct methods			
Inorganic or electrochemical measurement of filter extracts	Few empirical constants needed; some methods portable; useful to observe trends of changes in bulk properties	Requires time-intensive sample filtering; poor resolution; prone to sampling artifacts such as failure to denuder and remove alkaline particles or interaction of particles with denuder coating	27,35–37
Individual particle measurement via spectroscopy	Nondestructive; few assumptions required; precise information on size and refractive index simultaneously obtained	Useful ion pair (e.g. SO_4^{2-}/HSO_4^-) must be present at detectable concentrations; works for limited size range; works best when ion pair peaks are of similar intensity	29–31
Aerosol deposition onto pH paper	Particles need not be pre-dried or filtered; ambient results can be obtained in ~2 hours	Some indicators require correction for systematic bias; each indicator most useful in the middle of its range; need to account for species absorbing in the visible	32
Fluorescent probe microscopy	Highly sensitive; can monitor liquid-liquid phase separation	pH range limited to ~2 units	38
Surface-enhanced Raman spectroscopy	Information on pH distribution within a droplet can be obtained	There is discussion that this method may measure the concentration of H^+ rather than activity	34,41
Indirect methods			
Ion balance	Simple and useful for inorganic systems	Organic compounds complicate results; model failed to correlate with known results of some field campaigns	27
Molar ratio	Adaptable to various ion composition profiles and absolute concentrations	High uncertainty; disagrees with established models	27
Thermodynamic equilibrium models (e.g. E-AIM, ISORROPIA, AIOM-FAC)	Widely applicable; can use either total aerosol + gas content ("forward") or individual component ("reverse") concentrations as input	Various models substantially disagree; models diverge when ammonia is dilute; "reverse" mode highly sensitive to minor ionic measurement errors; low liquid water content of aerosols can result in low precision; many ignore organics; requires equilibrium	27,39,40
Phase partitioning	Recommended for high accuracy	Requires system to have reached equilibrium, which is often untrue, especially for large aerosols; sensitive to uncertainty in ammonia concentration and variations in ionic strength	33

4.7. Supporting Information

Details of the experimental methods, constants and table of ion interaction coefficients used in DHT and SIT calculations, Raman spectra and calibration curves for sulfate and carbonate, comparison of bulk and aerosol pH determined by deposition onto pH paper, images of a trapped droplet undergoing coalescence, spectra of trapped droplets coalesced with acidic aerosol and aerosol of the same pH, comparison of measured pH to calculated pH for carbonate.

4.7.1. Calculation of solution and aerosol pH

The extended Debye-Hückel Theory (DHT) (Eq. 4.2 in main text) and Specific Ion Interaction Theory (SIT) (Eq. 4.6 in main text) were employed to calculate activity coefficients. In the Debye-Hückel equation, *A* and *B* are constants characteristic of the solvent (water) the values of which are 0.5085 and 3.281×10^{-9}, respectively and effective diameter of the ion in solution, given by *a*, can be found in Table 4.2.[56,57] In Specific Ion Interaction Theory, ε (and ε_2 where applicable) is the ion interaction coefficient, values of which are listed in Table 4.2.[46,51] Additionally, the value for water activity in 2 M NaCl is 0.9284.[46] For the sulfate and carbonate equilibrium systems, K_a values of 1.0×10^{-2} and 4.7×10^{-11} were used, respectively.[52]

4.7.2. Sample preparation

All aqueous sodium sulfate (Fisher) and sodium carbonate (Fisher) solutions, of varying concentrations, were prepared using ultra-pure water (Thermo, Barnsted EasyPure- II; ≥18.2 MΩ cm resistivity) and the ionic strength of each sample was controlled to 2 M using sodium chloride (Fisher). Coalescence experiments were

preformed using 1 M HCl (Fisher) or 3 M HCl prepared from a 6 M HCl (Fisher) stock solution. All chemicals were used as is without any further purification.

4.7.3. Confocal Raman spectroscopy and bulk solution measurements

Bulk aqueous phase Raman spectroscopy measurements are preformed using a LabRam HR Evolution spectrometer (Horiba) equipped with an Olympus BX41 optical microscope with a 100X magnification lens. Raman spectra were collected with a 532 nm laser in the range of 100-4000 cm^{-1} with 10-second acquisitions and 5 accumulations. Bulk phase experiments are carried out with confocal Raman analysis by first collecting spectra of a bulk aqueous sulfate sample (1 M). Acid is then added drop wise to the solution, pH is measured with a standard bench top pH meter (OAKTON Instruments), and a new set of spectra are collected again. These bulk phase pH data are shown in Figure 4.1. Calibration curves for bulk sulfate solutions are shown in Figure 4.7a.

4.7.4. Aerosol Optical Tweezers (AOT)

The instrument used in these studies is a commercially available aerosol optical tweezer (AOT-100, Biral). In a typical experiment, a bulk aqueous solution is aerosolized using an ultrasonic nebulizer (MicroAIR U22, OMRON). The aerosolized solution is then introduced to the trapping chamber where a single droplet is confined by the trapping laser (532 nm) and can be enlarged via coalescence with additional droplets from the nebulized solution.[58,59] Once a droplet is trapped, the trapping chamber is sealed and allowed to equilibrate under a humidified nitrogen flow at a specific relative humidity, for these studies relative humidity was set to 100%. Raman spectra of the trapped droplet were collected with a 1 second exposure time and either a 300 or 1200 grove per mm grating.

Raman spectra provide information on the chemical composition of the droplet from the spontaneous Raman scattering while cavity enhanced Raman scattering (CERS) provides a fingerprint to determine droplet size and refractive index.[60,61] The proprietary Biral and University of Bristol software (LARA 2.0) determines the size and refractive index of the individual droplet from the wavelength position of whispering gallery modes (WGMs) within the droplet as detected by Raman spectroscopy.[58,62] Additionally, the droplet is imaged under brightfield illumination using a CCD camera that allows images and videos to be taken at any point in the experiment. To ensure accurate wavelength position, the spectrometer is calibrated using a Hg and Ne/Ar dual switchable USB light source (Princeton Instruments). Calibration curves using the AOT for sulfate and carbonate aerosol at different concentrations are shown in Figures 4.7b and Figure 4.8, respectively.

4.7.5. Description of pH measurements of aerosols deposited on pH paper

Colorimetric analysis was performed using ImageJ processing program with the RGB_Measure plugin.[63,64] The pH papers used in this study were for the ranges of 0-2.5 and 2-4.5 (MColorpHast, EMD Millipore) and 3.0-5.5 (Hydrion, Micro Essential Laboratory). For each aerosol trial, pH paper was placed in the center of AOT trapping chamber on the coverslip and dosed with a nebulized sulfate solution of known pH for one minute. Bulk solution pH was obtained by pipetting the solution directly onto the pH paper. Each analyzed image, collected with a cellular phone camera, contained three pH papers from the aerosol trials, one bulk solution pH paper, a blank pH paper and the pH color scale. The blank pH paper was included as a control and the pH color scale was included so a calibration curve could be created for each image therefore eliminating the need to

take slight differences due to factors such as lighting and camera angle into account. Each of these images were analyzed for R, G, and B values and a calibration curve was created relating pH to the R values or the difference between the G and B values, similar to the analysis performed by Craig et al.[32] From these calibration curves, aerosol pH was determined and the comparison of bulk and aerosol pH are shown in Figure 4.9.

4.7.6. Description of coalescence experiments with the AOT

The use of coalescence in an optical trap has been shown to be a useful technique by others in the field.[59,65–71] In a typical AOT coalescence experiment, a sulfate droplet is first trapped and fully characterized by Raman spectroscopy (chemical composition, size, refractive index). After obtaining the initial characterization of the droplet, the trapping chamber is opened and a nebulized solution, in this case hydrochloric acid at 1 or 3 M, is introduced to the chamber until coalescence occurs. After coalescence the chamber is sealed, allowed to equilibrate, and the droplet is characterized again for composition and size. It should be noted that for coalescence, a cap is added to the nebulizer to help filter out larger aerosol that are more likely to knock the trapped particle out of the laser. Coalescence events are determined by visual observation in the real-time video of the trapped droplet and then further verified by comparing the droplet radius before and after dosing. This process can be repeated many times as the aerosol is titrated. This coalescence process can be seen in the screenshots from the video, shown in Figure 4.10. In these images, a sulfate droplet is trapped (trapped droplet) while acidic aerosol are introduced to the trapping chamber (incoming droplet) until a coalescence occurs. Changes in the

spectra following coalescence to different pH values are shown in Figure 4.10 at high concentration and in Figure 4.11 at lower concentration.

4.7.7. Supporting Information Figures

Figure 4.7: Raman spectra and sulfate concentration calibration curves relating integrated

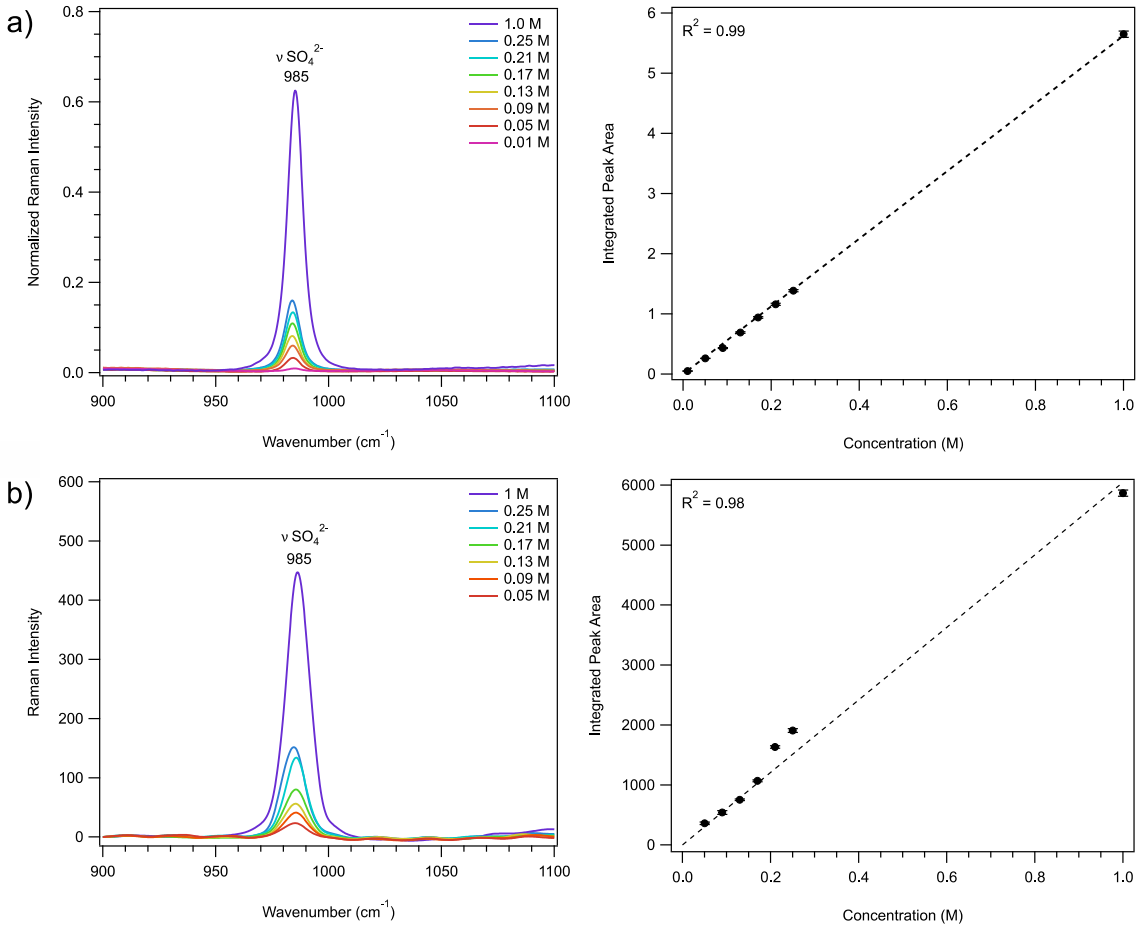

peak area of $\nu_s SO_4^{2-}$ (985 cm^{-1}) to sulfate concentration generated from the a) confocal Raman spectrometer and b) AOT cavity enhanced Raman spectrometer.

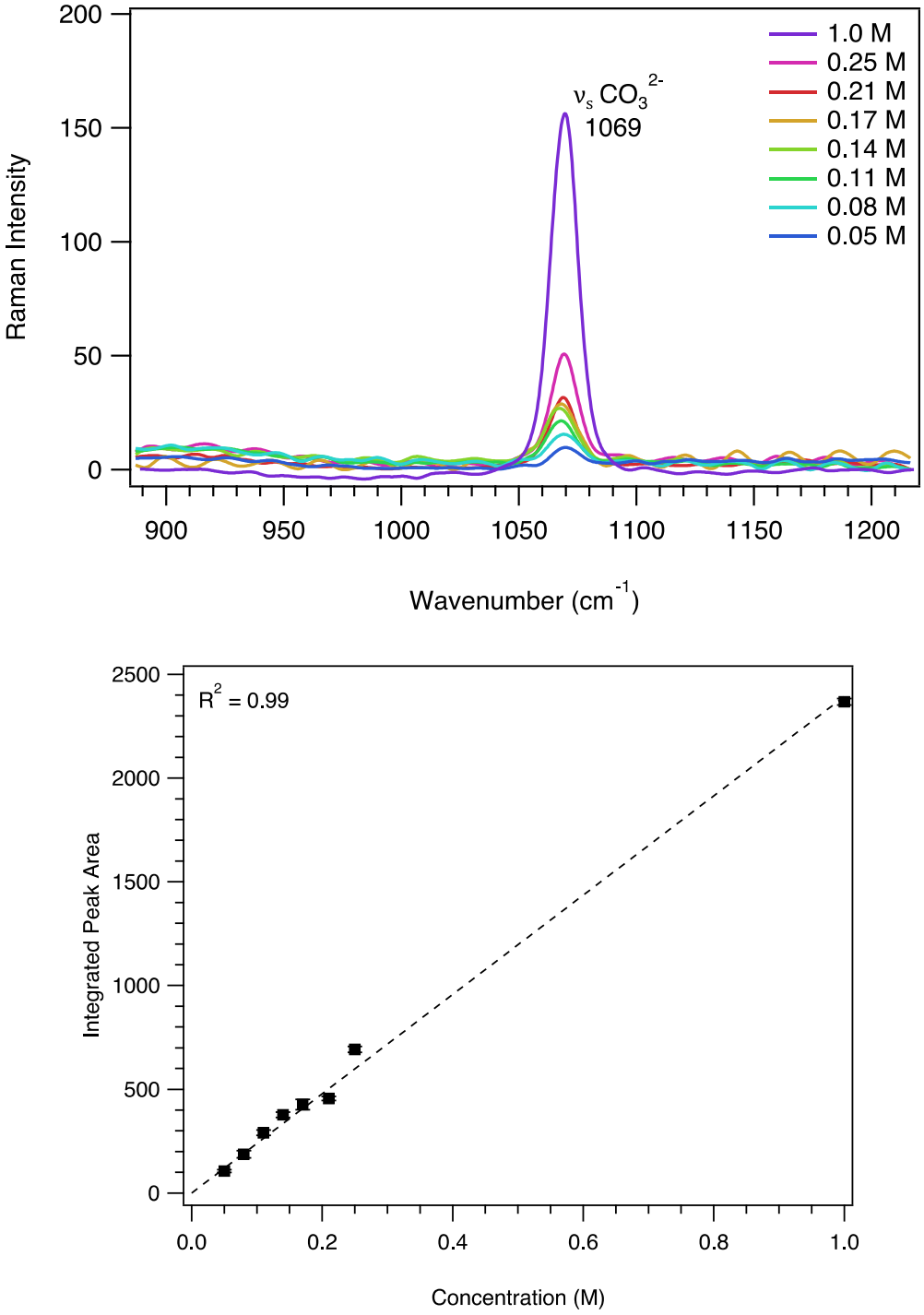

Figure 4.8: AOT Raman spectra and carbonate concentration calibration curve relating integrated peak area of $\nu_s CO_3^{2-}$ (1069 cm^{-1}) to carbonate concentration.

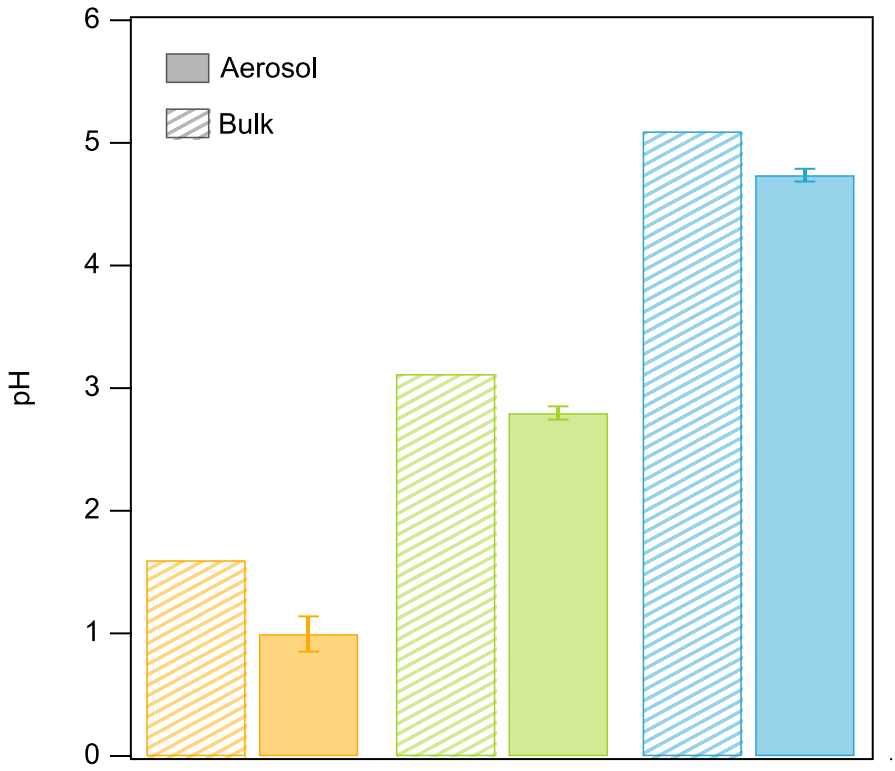

Figure 4.9: Bulk (striped) and aerosol (solid) pH determined by colorimetric analysis of pH paper for three sulfate solutions of different pH vales.

.

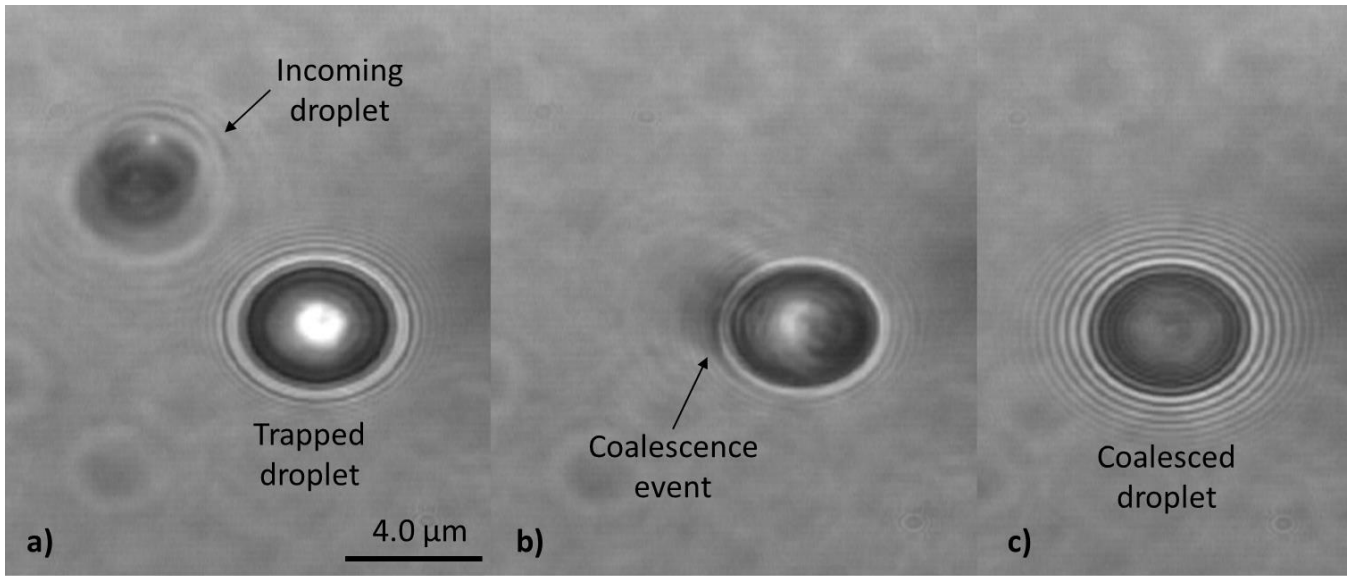

Figure 4.10: Images depicting the coalescence process where a) acidic aerosol is introduced to the trapping chamber where a sulfate droplet is stably trapped, b) the acidic aerosol coalesces with the trapped droplet, and c) the newly coalesced droplet stabilizes

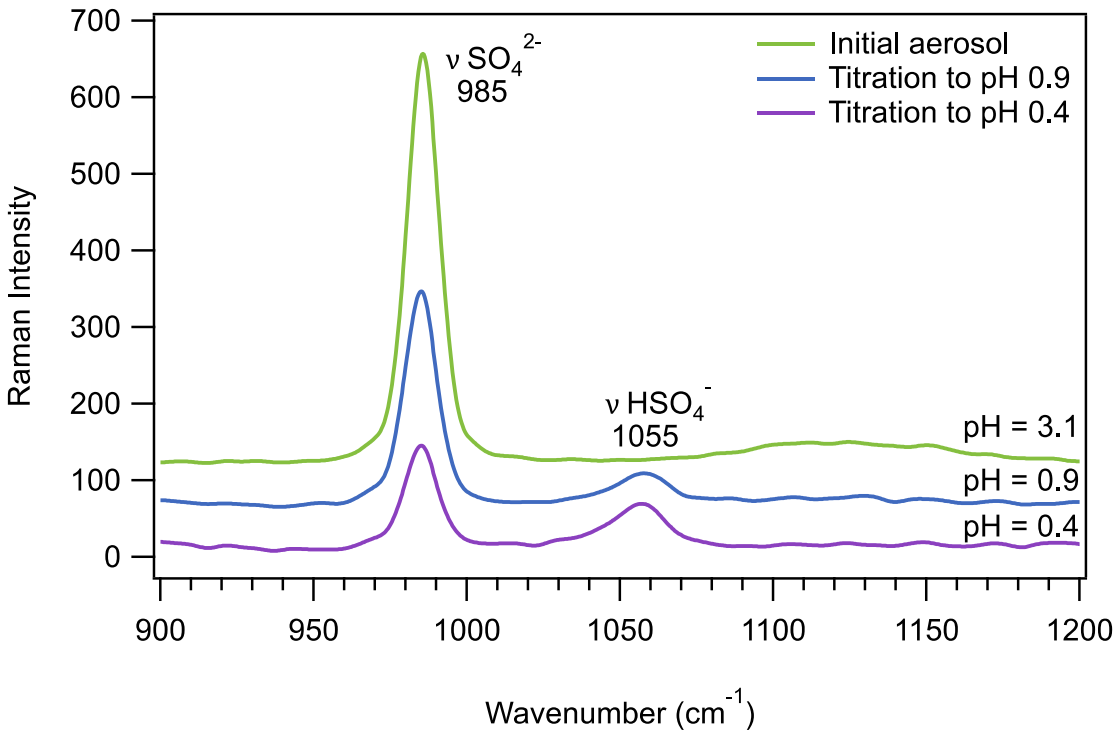

Figure 4.11: AOT cavity enhanced Raman spectra of a trapped sulfate droplet and the corresponding calculated particle pH shown at three representative pH values. As the droplet is titrated with acidic aerosol, calculated particle pH decreases and the ν SO_4^{2-} band at 985 cm^{-1} decreases while the ν HSO_4^- band at 1055 cm^{-1} increases.

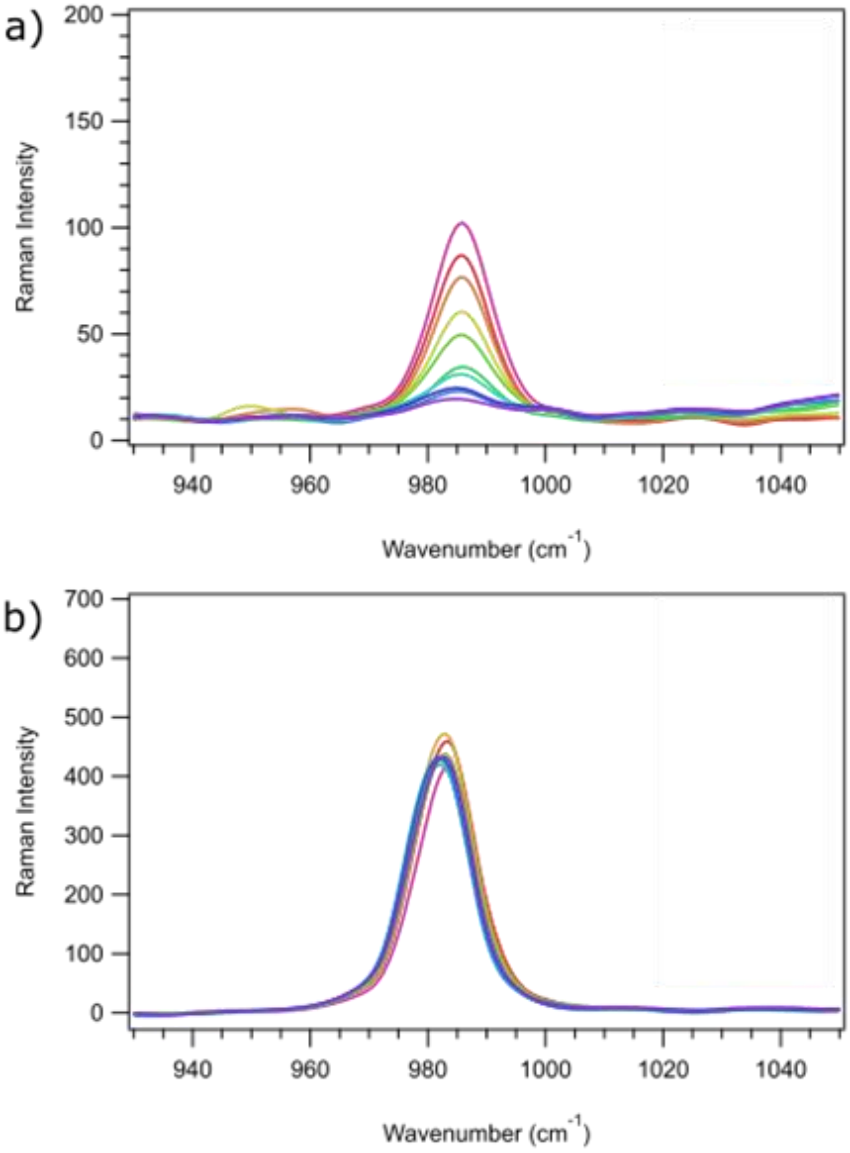

Figure 4.12: AOT Raman spectra showing changes in the ν SO_4^{2-} band at 985 cm^{-1} as the trapped sulfate droplet is coalesced with a) acidic aerosol (9 coalescence events) and b) aerosol of the same pH as the initial bulk solution (7 coalescence events). These spectra correspond to the coalescence experiments and calculated pH values shown in Figure 4.3.

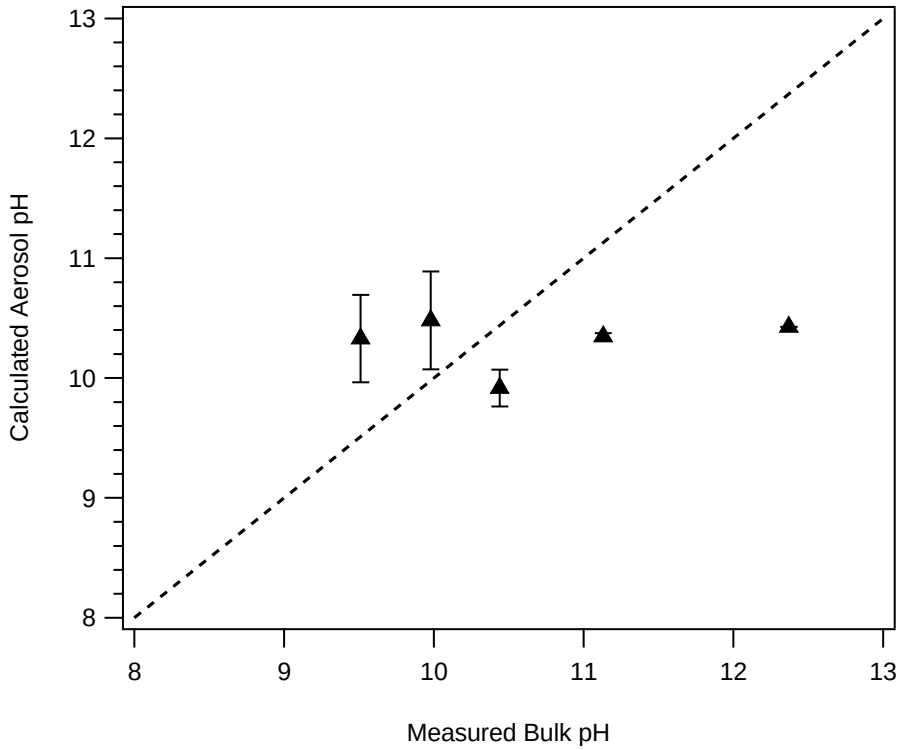

Figure 4.13: Comparison of measured bulk pH to calculated aerosol pH using the SIT method for a trapped carbonate droplet. Calculated pH values are determined by equations 4.2-4.7 where carbonate concentration is obtained using the calibration curve from Figure 4.8. The dashed line represents the 1:1 line where measured bulk pH is equal to the calculated aerosol pH. It can be seen that in most cases, the aerosol pH is more acidic than the bulk pH.

4.7.8. Supporting Information Tables

Table 4.2: Ion interaction coefficients, ε, and effective diameter, a, values.

	ε (kg mol^{-1})	ε_2 (kg mol^{-1})		a x 10^{8}
HSO_4^-/Na^+	-0.01		SO_4^{2-}	4
SO_4^{2-}/Na^+	-0.184	0.139	CO_3^{2-}	4.5
H^+/Cl^-	0.086	-0.017	HCO_3^-	4
HCO_3^-/Na^+	0		H^+	9
CO_3^{2-}/Na^+	-0.08			
Na^+/OH^-	0.028	0.079		

4.8. References

(1) Huang, L.; Cochran, R. E.; Coddens, E. M.; Grassian, V. H. Formation of Organosulfur Compounds through Transition Metal Ion-Catalyzed Aqueous Phase Reactions. *Environ. Sci. Technol. Lett.* **2018**, *5*, 315–321.

(2) Surratt, J. D.; Gómez-González, Y.; Chan, A. W. H.; Vermeylen, R.; Shahgholi, M.; Kleindienst, T. E.; Edney, E. O.; Offenberg, J. H.; Lewandowski, M.; Jaoui, M.; Maenhaut, W.; Claeys, M.; Flagan, R. C.; Seinfeld, J. H. Organosulfate Formation in Biogenic Secondary Organic Aerosol. *J. Phys. Chem. A* **2008**, *112*, 8345–8378.

(3) Limbeck, A.; Kulmala, M.; Puxbaum, H. Secondary Organic Aerosol Formation in the Atmosphere via Heterogeneous Reaction of Gaseous Isoprene on Acidic Particles. *Geophys. Res. Lett.* **2003**, *30*, 6-1-6–4.

(4) Jang, M.; Czoschke, N. M.; Lee, S.; Kamens, R. M. Heterogeneous Atmospheric Aerosol Production by Acid-Catalyzed Particle-Phase Reactions. *Science* **2002**, *298*, 814–817.

(5) Wong, J. P. S.; Lee, A. K. Y.; Abbatt, J. P. D. Impacts of Sulfate Seed Acidity and Water Content on Isoprene Secondary Organic Aerosol Formation. *Environ. Sci. Technol.* **2015**, *49*, 13215–13221.

(6) Cwiertny, D. M.; Baltrusaitis, J.; Hunter, G. J.; Laskin, A.; Scherer, M. M.; Grassian, V. H. Characterization and Acid-Mobilization Study of Iron-Containing Mineral Dust Source Materials. *J. Geophys. Res. Atmos.* **2008**, *113*, D05202.

(7) Fu, H.; Cwiertny, D. M.; Carmichael, G. R.; Scherer, M. M.; Grassian, V. H. Photoreductive Dissolution of Fe-Containing Mineral Dust Particles in Acidic Media. *J. Geophys. Res.* **2010**, *115*, D11304.

(8) Gankanda, A.; Coddens, E. M.; Zhang, Y.; Cwiertny, D. M.; Grassian, V. H. Sulfate Formation Catalyzed by Coal Fly Ash, Mineral Dust and Iron(Iii) Oxide: Variable Influence of Temperature and Light. *Environ. Sci. Process. Impacts* **2016**, *18*, 1484–1491.

(9) Mackie, D. S.; Boyd, P. W.; Hunter, K. A.; McTainsh, G. H. Simulating the Cloud Processing of Iron in Australian Dust: PH and Dust Concentration. *Geophys. Res. Lett.* **2005**, *32*, L06809.

(10) Pruppacher, H. R.; Jaenicke, R. The Processing of Water Vapor and Aerosols by Atmospheric Clouds, a Global Estimate. *Atmos. Res.* **1995**, *38*, 283–295.

(11) Shi, Z.; Bonneville, S.; Krom, M. D.; Carslaw, K. S.; Jickells, T. D.; Baker, A. R.; Benning, L. G. Iron Dissolution Kinetics of Mineral Dust at Low PH during Simulated Atmospheric Processing. *Atmos. Chem. Phys.* **2011**, *11*, 995–1007.

(12) Solmon, F.; Chuang, P. Y.; Meskhidze, N.; Chen, Y. Acidic Processing of Mineral Dust Iron by Anthropogenic Compounds over the North Pacific Ocean. *J. Geophys. Res.* **2009**, *114*, D02305.

(13) Spokes, L. J.; Jickells, T. D.; Lim, B. Solubilisation of Aerosol Trace Metals by Cloud Processing: A Laboratory Study. *Geochim. Cosmochim. Acta* **1994**, *58*, 3281–3287.

(14) Spokes, L. J.; Jickells, T. D. Factors Controlling the Solubility of Aerosol Trace Metals in the Atmosphere and on Mixing into Seawater. *Aquat. Geochemistry* **1996**, *1*, 355–374.

(15) Zhuang, G.; Yi, Z.; Duce, R. A.; Brown, P. R. Link between Iron and Sulphur Cycles Suggested by Detection of Fe(n) in Remote Marine Aerosols. *Nature* **1992**, *355*, 537–539.

(16) Khemani, L. T.; Momin, G. A.; Naik, M. S.; Prakasa Rao, P. S.; Safai, P. D.; Murty, A. S. R. Influence of Alkaline Particulates on PH of Cloud and Rain Water in India. *Atmos. Environ.* **1987**, *21*, 1137–1145.

(17) Weathers, K. C.; Likens, G. E.; Bormann, F. H.; Eaton, J. S.; Bowden, W. B.; Andersen, J. L.; Cass, D. A.; Galloway, J. N.; Keene, W. C.; Kimball, K. D.; Huth, P.; Smiley, D. A Regional Acidic Cloud/Fog Water Event in the Eastern United States. *Nature* **1986**, *319*, 657–658.

(18) Pöschl, U. Atmospheric Aerosols: Composition, Transformation, Climate and Health Effects. *Angew. Chemie Int. Ed.* **2005**, *44*, 7520–7540.

(19) Zhang, X. Y.; Wang, Y. Q.; Niu, T.; Zhang, X. C.; Gong, S. L.; Zhang, Y. M.; Sun, J. Y. Atmospheric Aerosol Compositions in China: Spatial/Temporal Variability, Chemical Signature, Regional Haze Distribution and Comparisons with Global Aerosols. *Atmos. Chem. Phys.* **2012**, *12*, 779–799.

(20) Xue, J.; Yuan, Z.; Griffith, S. M.; Yu, X.; Lau, A. K. H.; Yu, J. Z. Sulfate Formation Enhanced by a Cocktail of High NOx, SO2, Particulate Matter, and Droplet PH during Haze-Fog Events in Megacities in China: An Observation-Based Modeling Investigation. *Environ. Sci. Technol.* **2016**, *50*, 7325–7334.

(21) Seinfeld, J. H.; Pandis, S. N. *Atmospheric Chemistry and Physics : From Air Pollution to Climate Change*, 2nd ed.; John Wiley & Sons, Inc.: Hoboken, 2006.

(22) Ding, J.; Zhao, P.; Su, J.; Dong, Q.; Du, X. Aerosol PH and Its Influencing Factors in Beijing. *Atmos. Chem. Phys. Discuss.* **2018**.

(23) Wellen, B. A.; Lach, E. A.; Heather C Allen. Surface PK a of Octanoic, Nonanoic, and Decanoic Fatty Acids at the Air-Water Interface: Applications to Atmospheric Aerosol Chemistry. *Phys. Chem. Chem. Phys* **2017**, *19*, 26551–26558.

(24) Zhang, T.; Brantley, S. L.; Verreault, D.; Dhankani, R.; Corcelli, S. A.; Allen, H. C. Effect of PH and Salt on Surface PK a of Phosphatidic Acid Monolayers. *Langmuir* **2018**, *34*, 530–539.

(25) Eugene, A. J.; Pillar, E. A.; Colussi, A. J.; Guzman, M. I. Enhanced Acidity of Acetic and Pyruvic Acids on the Surface of Water. *Langmuir* **2018**, *34*, 9307–9313.

(26) Lin, P.-C.; Wu, Z.-H.; Chen, M.-S.; Li, Y.-L.; Chen, W.-R.; Huang, T.-P.; Lee, Y.-Y.; Wang, C. C. Interfacial Solvation and Surface PH of Phenol and Dihydroxybenzene Aqueous Nanoaerosols Unveiled by Aerosol VUV Photoelectron Spectroscopy. *J. Phys. Chem. B* **2017**, *121*, 1054–1067.

(27) Hennigan, C. J.; Izumi, J.; Sullivan, A. P.; Weber, R. J.; Nenes, A. A Critical Evaluation of Proxy Methods Used to Estimate the Acidity of Atmospheric Particles. *Atmos. Chem. Phys.* **2015**, *15*, 2775–2790.

(28) Keene, W. C.; Sander, R.; Pszenny, A. A. .; Vogt, R.; Crutzen, P. J.; Galloway, J. N. Aerosol PH in the Marine Boundary Layer: A Review and Model Evaluation. *J. Aerosol Sci.* **1998**, *29*, 339–356.

(29) Rindelaub, J. D.; Craig, R. L.; Nandy, L.; Bondy, A. L.; Dutcher, C. S.; Shepson, P. B.; Ault, A. P. Direct Measurement of PH in Individual Particles via Raman Microspectroscopy and Variation in Acidity with Relative Humidity. *J. Phys. Chem. A* **2016**, *120*, 911–917.

(30) Craig, R. L.; Nandy, L.; Axson, J. L.; Dutcher, C. S.; Ault, A. P. Spectroscopic Determination of Aerosol PH from Acid−Base Equilibria in Inorganic, Organic, and Mixed Systems. *J. Phys. Chem. A* **2017**, *121*, 5690–5699.

(31) Craig, R. L.; Ault, A. P. Aerosol Acidity: Direct Measurement from a Spectroscopic Method. In *Multiphase Environmental Chemistry in the Atmosphere*; Hunt, S. W., Laskin, A., Nizkorodov, S. S., Eds.; American Chemical Society: Washington, D.C., 2018; pp 171–191.

(32) Craig, R. L.; Peterson, P. K.; Nandy, L.; Lei, Z.; Hossain, M. A.; Camarena, S.; Dodson, R. A.; Cook, R. D.; Dutcher, C. S.; Ault, A. P. Direct Determination of Aerosol PH: Size-Resolved Measurements of Submicrometer and Supermicrometer Aqueous Particles. *Anal. Chem* **2018**, *90*, 11232–11239.

(33) Pilinis, C.; Capaldo, K. P.; Nenes, A.; Pandis, S. N. MADM-A New Multicomponent Aerosol Dynamics Model. *Aerosol Sci. Technol.* **2000**, *32*, 482–502.

(34) Wei, H.; Vejerano, E. P.; Leng, W.; Huang, Q.; Willner, M. R.; Marr, L. C.; Vikesland, P. J. Aerosol Microdroplets Exhibit a Stable PH Gradient. *Proc. Natl. Acad. Sci. U. S. A.* **2018**, *115*, 7272–7277.

(35) National Research Council. *Human Exposure Assessment for Airborne Pollutants*; National Academies Press: Washington, D.C., 1991.

(36) Freedman, M. A.; Ott, E.-J. E.; Marak, K. E. Role of PH in Aerosol Processes and Measurement Challenges. *J. Phys. Chem. A* **2019**, *123*, 1275–1284.

(37) Koutrakis, P.; Thompson, K. M.; Wolfson, J. M.; Spengler, J. D.; Keeler, G. J.; Slater, J. L. Determination of Aerosol Strong Acidity Losses Due to Interactions of Collected Particles: Results from Laboratory and Field Studies. *Atmos. Environ. Part A. Gen. Top.* **1992**, *26*, 987–995.

(38) Dallemagne, M. A.; Huang, X. Y.; Eddingsaas, N. C. Variation in PH of Model Secondary Organic Aerosol during Liquid− Liquid Phase Separation. *J. Phys. Chem. A* **2016**, *120*, 2868–2876.

(39) Keene, W. C.; Pszenny, A. A. P.; Maben, J. R.; Sander, R. Variation of Marine Aerosol Acidity with Particle Size. *Geophys. Res. Lett.* **2002**, *29*, 5-1-5–4.

(40) Song, S.; Gao, M.; Xu, W.; Shao, J.; Shi, G.; Wang, S.; Wang, Y.; Sun, Y.; McElroy, M. B. Fine-Particle PH for Beijing Winter Haze as Inferred from Different Thermodynamic Equilibrium Models. *Atmos. Chem. Phys.* **2018**, *18*, 7423–7438.

(41) Colussi, A. J. Can the PH at the Air/Water Interface Be Different from the PH of Bulk Water? *Proc. Natl. Acad. Sci. U. S. A.* **2018**, *115*, E7887.

(42) Harris, D. C. *Quantitative Chemical Analysis*, 7th ed.; W.H. Freeman and Co: New York, 2010.

(43) Po, H. N.; Senozan, N. M. The Henderson-Hasselbalch Equation: Its History and Limitations. *J. Chem. Educ.* **2001**, *78*, 1499–1503.

(44) Radić, N.; Prkić, A. Historical Remarks on the Henderson-Hasselbalch Equation: Its Advantages and Limitations and a Novel Approach for Exact PH Calculation in Buffer Region. *Rev. Anal. Chem.* **2012**, *31*, 93–98.

(45) Levine, I. N. *Physical Chemistry*, 5th ed.; McGraw-Hill: Boston, 2002.

(46) Grenthe, I.; Mompean, F.; Spahiu, K.; Wanner, H. *TDB-2 Guidelines for the Extrapolation to Zero Ionic Strength*; OECD Nuclear Energy Agency: Issy-les-Moulineaux (France), 2013.

(47) Skoog, D. A.; West, D. M.; Holler, F. J. *Analytical Chemistry: An Introduction*, 6th ed.; Saunders College Publishing: Philadelphia, 1994.

(48) Sipos, P. Application of the Specific Ion Interaction Theory (SIT) for the Ionic Products of Aqueous Electrolyte Solutions of Very High Concentrations. *J. Mol. Liq.* **2008**, *143*, 13–16.

(49) Ciavatta, L. The Specific Interaction Theory in Evaluating Ionic Equilibria. *Ann. Chim.* **1980**, 551–562.

(50) Guggenheim, E. A.; Turgeon, J. C. Specific Inteaction of Ions. *Trans. Faraday Soc.* **1955**, *51*, 747–761.

(51) Ekberg, C.; Brown, P. L. *Hydrolysis of Metal Ions*; Wiley-VCH: Germany, 2016.

(52) *CRC Handbook of Chemistry and Physics*, 84th ed.; David R. Lide, Ed.; CRC Press LLC: Boca Raton, 2003.

(53) Mishra, H.; Enami, S.; Nielsen, R. J.; Stewart, L. A.; Hoffmann, M. R.; Goddard, W. A.; Colussi, A. J. Brønsted Basicity of the Air-Water Interface. *Proc. Natl. Acad. Sci. U. S. A.* **2012**, *109*, 18679–18683.

(54) Enami, S.; Hoffmann, M. R.; Colussi, A. J. Proton Availability at the Air/Water Interface. *J. Phys. Chem. Lett.* **2010**, *1*, 1599–1604.

(55) Zhao, X.; Subrahmanyan, S.; Eisenthal, K. B. Determination of PKa at the Air/Water Interface by Second Harmonic Generation. *Chem. Phys. Lett.* **1990**, *171*, 558–562.

(56) Garrels, R. M.; Christ, C. L. *Solutions, Minerals, and Equilibria*; Harper & Row Publishers: New York, 1965.

(57) Kielland, J. Individual Activity Coefficients of Ions in Aqueous Solutions. *J. Am. Chem. Soc.* **1937**, *59*, 1675–1678.

(58) Davies, J. F.; Wilson, K. R. Raman Spectroscopy of Isotopic Water Diffusion in Ultraviscous, Glassy, and Gel States in Aerosol by Use of Optical Tweezers. *Anal. Chem.* **2016**, *88*, 2361–2366.

(59) Haddrell, A. E.; Miles, R. E. H.; Bzdek, B. R.; Reid, J. P.; Hopkins, R. J.; Walker, J. S. Coalescence Sampling and Analysis of Aerosols Using Aerosol Optical Tweezers. *Anal. Chem.* **2017**, *89*, 2345–2352.

(60) *Fundamentals and Applications in Aerosol Spectroscopy*, 1st ed.; Signorell, R., Reid, J., Eds.; CRC Press: Boca Raton, 2011.

(61) Butler, J. R.; Wills, J. B.; Mitchem, L.; Burnham, D. R.; Mcgloin, D.; Reid, J. P. Spectroscopic Characterisation and Manipulation of Arrays of Sub-Picolitre Aerosol Droplets. *Lab Chip* **2008**, *9*, 521–528.

(62) Preston, T. C.; Reid, J. P. Accurate and Efficient Determination of the Radius, Refractive Index, and Dispersion of Weakly Absorbing Spherical Particle Using Whispering Gallery Modes. *J. Opt. Soc. Am. B* **2013**, *30*, 2113–2122.

(63) Schneider, C. A.; Rasband, W. S.; Eliceiri, K. W. NIH Image to ImageJ: 25 Years of Image Analysis. *Nat. Methods* **2012**, *9*, 671–675.

(64) Rueden, C. T.; Schindelin, J.; Hiner, M. C.; DeZonia, B. E.; Walter, A. E.; Arena, E. T.; Eliceiri, K. W. ImageJ2: ImageJ for the next Generation of Scientific Image Data. *BMC Bioinformatics* **2017**, *18*, 529.

(65) Davis, R. D.; Lance, S.; Gordon, J. A.; Ushijima, S. B.; Tolbert, M. A. Contact Efflorescence as a Pathway for Crystallization of Atmospherically Relevant Particles. *Proc. Natl. Acad. Sci. U. S. A.* **2015**, *112*, 15815–15820.

(66) Dennis-Smither, B. J.; Hanford, K. L.; Kwamena, N.-O. A.; Miles, R. E. H.; Reid, J. P. Phase, Morphology, and Hygroscopicity of Mixed Oleic Acid/Sodium Chloride/Water Aerosol Particles before and after Ozonolysis. *J. Phys. Chem. A* **2012**, *116*, 6159–6168.

(67) Buajarern, J. ariya; Mitchem, L.; Reid, J. P. Manipulation and Characterization of Aqueous Sodium Dodecyl Sulfate/Sodium Chloride Aerosol Particles. *J. Phys. Chem. A* **2007**, *111*, 13038–13045.

(68) Laurain, A. M. C.; Reid, J. P. Characterizing Internally Mixed Insoluble Organic Inclusions in Aqueous Aerosol Droplets and Their Influence on Light Absorption. *J. Phys. Chem. A* **2009**, *113*, 7039–7047.

(69) Mitchem, L.; Buajarern, J.; Ward, A. D.; Reid, J. P. A Strategy for Characterizing the Mixing State of Immiscible Aerosol Components and the Formation of Multiphase Aerosol Particles through Coagulation. *J. Phys. Chem. B* **2006**, *110*, 13700–13703.

(70) Davis, R. D.; Lance, S.; Gordon, J. A.; Tolbert, M. A. Long Working-Distance Optical Trap for in Situ Analysis of Contact-Induced Phase Transformations. *Anal. Chem.* **2015**, *87*, 6186–6194.

(71) Jacobs, M. I.; Davies, J. F.; Lee, L.; Davis, R. D.; Houle, F.; Wilson, K. R. Exploring Chemistry in Microcompartments Using Guided Droplet Collisions in a Branched Quadrupole Trap Coupled to a Single Droplet, Paper Spray Mass Spectrometer. *Anal. Chem.* **2017**, *89*, 12511–12519.

Chapter 5 Influence of Glyoxal on the Catalytic Oxidation of S(IV) in Acidic Aqueous Media

5.1. Synopsis

The role of glyoxal in S(IV) oxidation in acidic aqueous solutions catalyzed by iron in the form of aqueous Fe^{3+} ions and solid iron oxide was investigated under different experimental conditions. It is found that the rate of Fe^{3+}(aq) ion catalyzed-S(IV) oxidation decreases in the presence of glyoxal. The results of mass spectral analysis and infrared spectra suggest that the trapping of SO_4^- radicals, as well as the formation of glyoxal-S(IV) adducts, are responsible for this inhibition effect. Interestingly, although sulfur oxidation is kinetically inhibited in the presence of glyoxal, S(IV) in the form of sulfite, is over time completely converted to sulfate. Additionally, the inhibition effects of glyoxal can also be observed in the reaction of S(IV) catalyzed by iron oxide particles, albeit less than that catalyzed by dissolved Fe^{3+}(aq). The observed inhibition effect for the iron oxide particles is proposed to be attributed to competitive surface adsorption on the iron oxide particle surface. Overall, these findings suggest that the effects of glyoxal on the catalytic oxidation of S(IV) are highly dependent on the mechanism, form of iron (dissolved versus solid), and the ambient conditions, including pH and concentration.

5.2. Introduction

The aqueous phase oxidation of sulfur dioxide (SO_2) in cloud or fog droplets, is considered the most important pathway for the formation of atmospheric sulfate.[1] In fact, it is estimated that 9–17% of the global sulfate production is formed specifically via the

oxidation of aqueous SO_2 in the presence of transition metal ions (TMI), e.g., iron and manganese.[2]

Earlier studies have shown that the catalytic oxidation of S(IV) by TMI is a complex process for which its mechanisms and kinetics are dependent on reaction conditions including pH, temperature and light.[3] Furthermore, recent studies have shown that this reaction can also be influenced by other reactions, in particular in the presence of organic compounds. For example, it has been established that some organic acids, such as oxalic acid and formic acid, have a strong inhibition effect on iron-catalyzed S(IV) oxidation due to the complexation of organic ligands with iron.[4–6] The catalytic oxidation of S(IV) is a free radical chain reaction,[3,7,8] where sulfoxy radicals i.e., SO_3^-, SO_4^- and SO_5^- radicals, are the major intermediates. Therefore, besides complexation with TMI, organic compounds can also react with sulfoxy radicals, resulting in the decrease of sulfoxy radical concentration and subsequently altering the rate of catalytic S(IV) oxidation as well as the conversion of S(IV).[9–16] The three main pathways for these reactions in aqueous phase are summarized in reactions R5.1–R5.3 (using SO_4^- radical as an example):[17,18]

$$\cdot SO_4^- + HR \rightarrow HSO_4^- + \cdot R \quad \text{(R5.1)}$$

$$\cdot SO_4^- + C_6H_6 \rightarrow C_6H_6^+ + SO_4^{2-} \quad \text{(R5.2)}$$

$$\cdot SO_4^- + H_2C = CHR \rightarrow -S(O)_2OCH_2-CHR \quad \text{(R5.3)}$$

Specifically, the $\cdot SO_4^-$ radical can react with saturated organic compounds through hydrogen abstraction (R5.1); transfer of an electron from an aromatic compound (R5.2); and undergo addition reactions with organic compounds containing carbon-carbon double

bonds (R5.3). Despite the fact that it is known that organic compounds can impact the catalytic oxidation of S(IV),[4–6,11–16] the understanding how this occurs for carbonyl compounds, which are important species involved in atmospheric chemistry with some having large apparent Henry's law constants (e.g. carbonyl compounds including formaldehyde, glyoxal and acetone),[19] is still limited. Furthermore, in addition to aqueous metal ions, previous studies have shown that S(IV) can also be oxidized by transition metal-containing particles in the aqueous phase through homogeneous as well as heterogeneous reactions,[20–26] indicating that the mechanism by which S(IV) reacts with these particle inclusions is different than that with TMI. However, very little is known about the process of S(IV) oxidation by mineral dust particles in the presence of organic compounds in the aqueous phase.

Glyoxal, the simplest α-dicarbonyl compound, is produced from the oxidation of biogenic and anthropogenic VOCs, including isoprene, terpenes and aromatic hydrocarbons.[27–30] Due to its high solubility (Henry's law constant of 3.0–4.2×10^5 M atm^{-1} at 25 °C),[31] glyoxal easily partitions into the aqueous phase and is found widely in atmospheric aerosols, clouds and fog droplets,[32] making it an important contributor to the formation of aqueous secondary organic aerosols (SOA) and a source of other water-soluble products.[33–38] Given its prevalence and importance in the atmosphere, glyoxal was selected to investigate the impact it has on the catalytic oxidation of S(IV). In particular, we have investigated the aqueous phase reaction of S(IV) and molecular oxygen catalyzed by iron (Fe^{3+}(aq) and Fe_2O_3) in the presence and absence of glyoxal. The purpose of this study is to determine the effect of glyoxal on the kinetics of this process under various atmospherically relevant conditions and relevant possible mechanisms.

5.3. Materials and Methods

5.3.1. Reagents and materials

Na_2SO_3 (LabChem) and $Na_2S_2O_5$ (>97%, Alfa Aesar) were used as the source of aqueous S(IV). Aqueous Fe(III) and solid Fe(III) were prepared from $FeCl_3$ (98%, Alfa Aesar)/$Fe_2(SO4)_3$ (Sigma-Aldrich) and iron oxide (γ-Fe_2O_3, 99%, Alfa Aesar), respectively. The characterization of iron oxide is described in detail in our previous study.[26] Briefly, the BET surface areas of γ-Fe_2O_3 was measured as 56±1 $m^2\ g^{-1}$. Solutions were prepared with Na_2SO_3/$Na_2S_2O_5$, glyoxal (Acros, 40 wt%), and Fe(III) diluted in ultrapure water (Milli-pore). Oxygen was dissolved in water by equilibration with atmospheric air. The initial pH of the solution was adjusted to 5.0 or 3.0 by HCl (1 M, Fisher)/H_2SO_4 (1 M, Fluka).

5.3.2. Aqueous phase reactor

In order to investigate the role of glyoxal in the reaction of S(IV) in the form of sulfite/bisulfite solutions catalyzed by iron, kinetic studies of aqueous phase reactions were conducted in a 0.1 L water jacketed quartz vessel. A solution of 0.1 mM $Na_2S_2O_5$ mixed with different glyoxal concentrations (0–0.5 mM) and $FeCl_3$ (~8 μM) or γ-Fe_2O_3 (0.1 g L^{-1}) was introduced into the reactor for a total volume of 75 mL. The remaining space was maintained over the liquid level for mixing. The details of the experimental conditions are listed in Table 5.2. For all experiments, reactors were continuously stirred, and the temperature was controlled to 25 °C in the dark. Aliquots of the reaction mixture were extracted every 3 or 5 minutes for the duration of 18 or 30 minutes. After reaction, 75 μL formaldehyde (CH_2O, 0.1 M) were added to each sample to prevent further oxidation. In the experiments with iron oxide, samples were filtered with a 0.2 μm

polytetrafluoroethylene (PTFE) filter to remove solid particles before adding HCHO. After reaction, samples were analyzed with ion chromatography to obtain accurate sulfite concentrations. Selected samples were analyzed to monitor S(IV) oxidation using attenuated total reflectance-Fourier transform infrared (ATR-FTIR) spectroscopy, However, for these studies initial concentration of reagents (S(IV) (50 mM), glyoxal (50 mM) and γ-Fe_2O_3 (1 g L^{-1})) were used.

In addition to investigating the kinetics of these reactions, we also carried out experiments to explore the mechanism of the reactions. The products from Na_2SO_3 reacted with $Fe_2(SO_4)_3$ in the presence and absence of glyoxal were investigated using a 20 mL glass reactor. The sample preparation for these experiments is described in detail elsewhere.[39] The initial concentrations of Na_2SO_3, glyoxal and Fe^{3+}(aq) were 2 mM, 2 mM and 0.25 mM, respectively. The highly concentrated solution was used to facilitate the characterization of reaction products. All experiments were performed at 277 K under dark conditions for ~12 h of reaction time and products were analyzed with a high-resolution hybrid linear ion trap mass spectrometer equipped with a heated electrospray ionization (HESI) source (HESI-HRMS, Thermo Orbitrap Elite).

5.3.3. Detection of reactants and products

5.3.3.1. The measurement of S(IV) and S(VI) concentration

The concentration of S(IV) and S(VI) were determined by ion chromatography (IC, Dionex ICS2000), equipped with a Dionex AS25 analytical column, which allowed peaks for sulfite and sulfate to be completely separated under the following gradient program: the concentration of eluent (KOH, Thermo Scientific) increased from 15 mM to 36 mM at 0–

20 min, held at 36 mM for 10 min, and then decreased to 10 mM from 30 min to 35 min. During each run, the eluent flow rate was maintained at 0.25 mL min^{-1} with a column temperature of 30 °C. For each analysis 25 μL of sample was injected.

As noted above, CH_2O was added to each sample immediately after solution extraction, thus, the unreacted S(IV) can be combined with CH_2O to form hydroxymethanesulfonate (HMS). Control experiments revealed that the addition of CH_2O does not interfere with the determination of S(IV) concentration in this study. Additionally, given that some residual S(IV) may be in the form of glyoxal-S(IV) adducts, we also evaluated the influence of different aldehyde-S(IV) adducts for the measurement of sulfite concentration by comparing the retention time and intensity of the S(IV) peak in the form of glyoxal-S(IV) adducts with that in the form of formaldehyde-S(IV) adduct. The results showed that the different form of aldehyde-S(IV) adduct does not induce a discrepancy of S(IV) measurement. Furthermore, we also determined the stability of the sample, finding that the intensity of the sample did not change within 48 hours. In order to avoid interferences, we measured the samples immediately after reaction.

5.3.3.2. Product analysis

Samples obtained from the experiments for mechanism studies were analyzed by HESI-HRMS under negative ionization mode. Samples were diluted by a factor of 20 with acetonitrile (ACN, Fluka) before analysis. The details of this method can be found in our previous work.[39]

ATR-FTIR spectroscopy measurements of sulfur oxidation were taken using a Thermo-Nicolet spectrometer equipped with an MCT/A detector. A background spectrum

was collected of water (Milli-Q) on the blank Ge crystal in a horizontal ATR cell (Pike Technologies, Inc.). Solution phase spectra were recorded for each aliquot extracted during dissolution experiments by depositing approximately 1 mL of each filtered aqueous sample onto the ATR crystal. A total of 200 scans were acquired at 4 cm^{-1} resolution for each spectrum.

5.3.3.3. Measured dissolved iron concentrations

Selected samples were analyzed with inductively coupled plasma-mass spectrometry (ICP-MS) (iCAP RQ ICPMS, Thermo Fisher Scientific) to determine total iron concentration. A 100 ppm Fe standard for ICP-MS (Inorganic Ventures) was diluted to concentrations of 1, 0.1, 0.01, 0.001, 0.0001, and 0.00001 ppm to generate a calibration curve. Samples were acidified using nitric acid and ICP-MS internal standard (Inorganic Ventures) was added to each sample. The average and standard deviation are reported for all dissolution measurements.

5.3.4. Aerosol Optical Tweezer Experiments

The oxidation of S(IV) in the presence of glyoxal was also examined in the aerosol phase using an Aerosol Optical Tweezer (AOT-100, Biral). The AOT setup and coalescence method used in these studies is described elsewhere (Chapter 3). Briefly, aerosols were generated from a 1 M glyoxal solution using an ultrasonic nebulizer (MicroAIR U22, OMRON) and introduced to the trapping chamber where a single micron-sized droplet is trapped by the trapping laser. The glyoxal droplet was allowed to equilibrate and cavity enhanced Raman spectra were collected. The stable glyoxal droplet was then coalesced with an aerosolized solution of 1 M sodium metabisulfite and the

occurrence of a successful coalescence was monitored visually with the real time video of the droplet and via the Raman spectra and calculated droplet radius. After coalescence, the droplet was again allowed to stabilize, and Raman spectra were collected. Metabisulfite was used as the source of S(IV) rather than sulfite because initial trapping tests with sulfite showed that oxidation occurred too fast during the nebulization and trapping process that by the time the droplet was stably trapped there were no vibrational bands corresponding to S(IV) species observed in the Raman spectra; the only band observed was that of the stretching mode for sulfate. Metabisulfite on the other hand, was able to be stably trapped and the Raman spectra showed characteristic S(IV) vibrational bands. However, it should be noted that metabisulfite did still oxidize to form S(VI) as detected by the appearance of the vibrational band for sulfate at 985 cm^{-1} but the oxidation occurred slower than sulfite allowing for S(IV) species to last long enough to get into the trapping chamber and react.

5.4. Results and Discussion

5.4.1. S(IV) oxidation with Fe(III) in the aqueous phase

Kinetic studies of S(IV) oxidized by Fe^{3+}(aq) in the absence and presence of glyoxal at pH 5 were investigated. Figure 5.1 shows the time dependence of $[S(IV)]_t/[S(IV)]_0$ ratio, where $[S(IV)]_t$ is the concentration of S(IV) at time *t* and $[S(IV)]_0$ is the initial concentration of S(IV). In this study, the loss of S(IV) with time is treated as a pseudo-first-order reaction in all cases in order to compare the results measured under different experimental conditions. Therefore, the reaction rate is described by:

$$-\frac{\mathrm{d[S(IV)]}}{\mathrm{dt}} = k[S(IV)]_0 \qquad \text{(E5.1)}$$

where *k* is the observed rate constant calculated from at least two repeated experiments. As shown in Table 5.1, in the presence of Fe^{3+}(aq) only, the value of k is measured as (9.1 ± 0.5) × 10^{-5} mM s^{-1}. Even though considering the contribution of S(IV) oxidized by O_2 (Figure 5.8), this value is still calculated to be (7.7 ± 0.5) × 10^{-5} mM s^{-1}, indicating that Fe3+ plays an important role in the S(IV) oxidation. However, in the presence of 0.1 mM glyoxal, the value of k decreases to (6.3 ± 0.3) × 10−5 mM s^{-1}, suggesting that glyoxal inhibits the reaction. It is expected that this inhibition effect is closely related to the glyoxal concentration. Increasing the glyoxal concentration from 0.1 mM to 0.5 mM resulted in a decrease of the rate by ~54%.

Solution pH is a major factor in the catalytic oxidation of S(IV), which can affect the mechanism and rate of reaction by controlling the distribution of both S(IV) and metal ion species and altering the stability of the produced metal-sulfur complexes.[3] Thus, the effect of glyoxal on this catalytic reaction at different pH was investigated. Analogously, the change of $[S(IV)]_t/[S(IV)]_0$ ratio as the function of time is depicted in Figure 5.2. It can be seen that the rate of S(IV) loss at pH 3 is much faster than that at pH 5, and the reaction order with respect to S(IV) changes to approximate first order (Figure 5.9). The change in reaction order at different pH values has been previously reported.[3] In the presence of Fe^{3+}(aq) only, the rate constant, *k*, was calculated to be 6.0±0.3×10^{-3} s^{-1} (Table 5.1). Similar to pH 5, we also find the rate constant to have a negative dependence on glyoxal concentration at pH 3. To estimate the magnitude of the inhibition effect of glyoxal on this reaction the ratio of *k/k'*, where *k'* is the observed rate constant in the presence of glyoxal, was determined. At pH 3, the value of the ratio of *k/k'* is 2.5, which is higher than that at pH 5 (*k/k'*=1.4), suggesting that the inhibition effect of glyoxal is more pronounced at pH

3; the possible explanations are discussed below. Interestingly, as shown in Figure 5.2, the remaining S(IV) is barely detected after 30 minutes of reaction, even in the presence of glyoxal. We calculated the sulfur balance, i.e., the measured concentration of S(IV) added with SO_4^{2-}, during the reaction. Figure 5.3 shows a decrease in S(IV) concentration with a concomitant increase of SO_4^{2-} concentration. The value of the sulfur balance after reaction is nearly identical to that in the beginning, suggesting that almost all of the S(IV) is converted to sulfate. This observation is in agreement with mass spectral data that shows that other organosulfur compounds are not observed, except adducts, during this process (Figure 5.4). This result indicates that although the presence of glyoxal can slow the oxidation of S(IV) by Fe^{3+}, S(IV) is ultimately oxidized to S(VI) over time.

Based on the experimental and literature results, the possible mechanisms for explaining the inhibition effect of glyoxal on the Fe^{3+}-catalyzed S(IV) oxidation were elucidated. Schaefer et al.[40] measured the rate constant for the reaction of the SO_4^- radical with glyoxal as 2.4×10^7 L mol^{-1} s^{-1}, indicating that SO_4^- radicals can also abstract a H atom of glyoxal like OH radicals. They suggested that this value is comparable with those of other mono and polyfunctional alcohols.[41] However, previous study reported that the hydrogen abstraction by the SO_3^- radical can be negligible for alcohol.[42] Therefore, although the SO_3^- radical is the primary radical formed in the catalytic reaction, the reaction of glyoxal with SO_3^- radicals is not considered to be important here. If alcohol inhibits the reaction via trapping SO_4^- radicals,[14] glyoxal may undergo a similar mechanism. The main products generated through this pathway are glyoxylic acid and oxalic acid assuming that the mechanism of H atom abstraction by SO_4^- radicals is analogous to OH radicals in aqueous phase reaction.[40] Figure 5.4 shows the negative-ion mass spectra of glyoxal

reacted with S(IV) in the absence and presence of Fe^{3+}(aq) at pH 5. The peak at *m/z* 154.97 corresponding to the structure of $C_2H_3SO_6$ was observed, which is produced from the reversible reaction of HSO_3^- with glyoxylic acid that has been previously proposed.[43] The observation of the formation of glyoxylic acid demonstrates that the inhibition effect of glyoxal can contribute to some of the consumption of the SO_4^- radicals. The more convincing evidence is that this peak does not exist in the absence of Fe^{3+}(aq). However, the peak of another major product, oxalic acid, is not observed in the mass spectra. This may be attributed to oxalate formation and oxalate complexation with iron during the reaction. It is worth noting that the formation of oxalate will reduce the concentration of Fe^{3+}(aq), thereby affecting the catalytic oxidation as well.

Because of its high solubility, glyoxal can react with S(IV) to form aldehyde-bisulfite adducts in the aqueous phase. In this study, the formation of glyoxal-S(IV) adducts was verified using ATR-FTIR. Figure 5.10 shows the IR spectra of the sulfite solution and the sulfite solution mixed with glyoxal. In the spectra of sulfite mixed with glyoxal the band at 1023 cm^{-1}, which is assigned to the stretching mode of bisulfite, disappears while a new band appears at 1032 cm^{-1}.[44,45] Kaun et al.[46] reported that one of the characteristic IR peaks of the HCHO-S(IV) adduct is at 1037 cm^{-1}. Thus, the band at 1032 cm^{-1} observed in this study is assigned to hydroxyalkylsulfonate. The mechanism for glyoxal-S(IV) adduct formation under acidic conditions has been proposed previously. Here, the simplified mechanism is shown in reactions R5.4–R5.7:[47]

$$CHOCHO + H_2O \rightleftharpoons CH(OH)_2CHO \qquad \text{(R5.4)}$$

$$CH(OH)_2CHO + H_2O \rightleftharpoons (CH(OH)_2)_2 \quad \text{(R5.5)}$$

$$CHOCHO + HSO_3^- \rightleftharpoons CHOCH(OH)SO_3^- \quad \text{(R5.6)}$$

$$CHOCHO + 2HSO_3^- \rightleftharpoons (CH(OH)SO_3^-)_2 \quad \text{(R5.7)}$$

Since the formation of the dihydrate (R5.5) is an extremely favorable process for the hydration of glyoxal in aqueous phase, [48,49] the glyoxal-monobisulfite adduct, as well as the glyoxal-dibisulfite adduct, can be formed during the process of adduct formation. As shown in Figure 5.4, the observed peaks at *m/z* 138.97 ($C_2H_3O_5S$) and 156.98 ($C_2H_5O_6S$) verify the existence of these two species. Interestingly, in addition to the monomer adducts, the peaks at *m/z* 196.97 and 214.99 correspond to the structures of $C_4H_5O_7S$ and $C_4H_7O_8S$, respectively, indicating the formation of oligomeric adducts that have not been reported previously. Given that glyoxal can undergo oligomerization in the aqueous phase, particularly under acidic conditions,[50,51] it is expected that the mechanism for the formation of oligomeric adducts may be similar to monomer adducts. Previous studies reveal that the formation of adducts are not directly oxidizable by oxidants, such as O_2, H_2O_2 and O_3.[52] Thus, in addition to trapping SO_4^- radicals, this nonradical reaction may be responsible for the inhibition of S(IV) catalytic oxidation as well.

To investigate the contribution of these two mechanisms, we carried out control experiments under the same experimental conditions with the exception of the initial S(IV) concentration at pH 3. The concentration of S(IV) was adjusted to 2 mM, which is 10 times larger than that used before. If the inhibition effect is mainly induced by reacting with SO_4^- radicals, a significant inhibition effect should still be observed since the protected S(IV) only accounts for less than 10% of the total S(IV). However, the rate of S(IV) loss in the

absence of glyoxal is only 1.1 times larger than that in the presence of glyoxal, indicating that the inhibition effect is dominated by the formation of glyoxal-S(IV) adducts. Furthermore, these results also reveal that this inhibition effect is closely related to the ratio of S(IV) to glyoxal in the solution. If the concentration of glyoxal is comparable to S(IV), the presence of glyoxal can significantly affect the oxidation of S(IV), however, if the concentration of S(IV) is excessive, the presence of glyoxal will have a weaker impact on this catalytic reaction.

It is worth noting that the trapping of SO_4^- radicals and the formation of adducts explains the significant decrease in the loss of S(IV) with increasing glyoxal concentration. The higher concentration of glyoxal can accelerate the hydrogen abstraction as well as the formation of glyoxal-S(IV) adducts resulting in the enhancement of the inhibition effect. However, the inhibition effect is significantly enhanced with decreasing pH, which cannot be explained by the mechanism mentioned hereinbefore. Schaefer et al.[40] found that the rate SO_4^- radicals reacted with glyoxal is pH independent. Thus, the discrepancy of the inhibition effect between pH 3 and pH 5 may not be related to the mechanism of trapping SO_4^- radicals. Additionally, Olson and Hoffmann[47] investigated the kinetics of glyoxal-S(IV) adduct formation as a function of pH and found that the rate of adduct formation increases with increasing pH, but the dissociation of these adducts is also positively pH dependent. Although they have not investigated the adduct stability constants of glyoxal-adducts as a function of pH, they suggested that this constant should be independent over the range of pH 3–5 since the form of adducts, S(IV) and glyoxal species remain the same in this pH range. However, the major assumption of their inference is that the glyoxal-adduct contains two monomer structures, i.e., glyoxal-monobisulfite and glyoxal-

dibisulfite. In this study, we point out the existence of oligomeric adducts and find that the intensity of $C_4H_5O_7S$ peak at pH 3 is twice as large compared to that at pH 5 suggesting that oligomeric adducts may be easily formed at lower pH. The oligomeric adducts formed may be more stable than monoadducts, thus, we speculate that the more pronounced inhibition effect at more acidic conditions results from the higher amount of oligomeric adducts formed. Further studies should be carried out to verify this speculation.

5.4.2. S(IV) oxidation in solid phase Fe(III)

In addition to aqueous Fe(III), previous studies have also shown that the oxidation of S(IV) can be driven by aqueous suspensions of solid catalysts, such as iron oxide.[3,21,28] Therefore, in this study, we also investigated the influence of glyoxal on S(IV) oxidation by solid Fe(III), i.e., γ-Fe_2O_3. Figure 5.5 shows the change of $[S(IV)]_t/[S(IV)]_0$ ratio over time for the reaction of S(IV) with γ-Fe_2O_3 particles in the presence and absence of glyoxal at different pH values. The rates of reaction are summarized in Table 5.1. At pH 5, the rate constant in the absence of glyoxal was measured as 4.7×10^{-5} s^{-1}, which is 1.4 times large than in the presence of 0.1 mM glyoxal. Interestingly, at pH 3, in contrast to Fe^{3+}(aq), the extent of the inhibition effect significantly decreased, where the reaction is only slightly influenced by the presence of glyoxal (Figure 5.5), suggesting that the mechanism of S(IV) oxidation may be quite different. Note that, under acidic conditions, iron can be leached from particles and then participate in homogeneous catalytic reactions.[20,53,54] Thus, the contribution of heterogeneous reaction to the overall S(IV) oxidation is evaluated. We employed ICP-MS to measure the concentration of total dissolved iron (Fe^{3+} + Fe^{2+}), which showed that at pH 5 the concentration of dissolved Fe is estimated to be less than 0.01 uM, meaning that there is little dissolved Fe^{3+} to participate in the oxidation of S(IV). However,

the rate constant of S(IV) reacted with γ-Fe_2O_3 particles is 3.5 times higher than with oxygen only (Figure 5.8); hence, we infer that the oxidation of S(IV) is dominated by heterogeneous surface reaction. At pH 3, the concentration of dissolved iron is 2 orders of magnitude larger than at pH 5, which is attributed to increased proton promoted dissolution, but the measured concentration of dissolved iron is still less than 1 uM, and the loss of S(IV) is also much higher than that with oxygen only (Figure 5.8). Furthermore, the observed weak inhibition effect in the presence of glyoxal is not in agreement with the homogenous catalytic reaction discussed above. Therefore, the heterogeneous catalysis may also contribute to the loss of S(IV) at pH 3.

Since the oxidation of S(IV) is dominated by the heterogeneous reaction, the mechanism for observed inhibition effect here seems to be different to that observed for aqueous Fe(III). The possible explanation for this is as follows. It is well known that surface hydroxyl groups are the principal reactive sites on metal oxides surfaces and participate in the conversion of S(IV) to S(VI) on the surface of Fe_2O_3 particles. As noted previously, glyoxal and S(IV) can form glyoxal-S(IV) adducts to resist the oxidization by some oxidants (e.g., H_2O_2 and O_3), but it can be fairly rapidly oxidized by aqueous OH radicals producing glyoxal and SO_3^- radicals.[55] According to the results of formaldehyde-S(IV) adducts investigated by previous studies,[56,57] the rate of glyoxal-S(IV) adducts reacted with OH radicals may be lower than that of HSO_3^- reacted with OH radicals.[58] Thus, the different reactivity of HSO_3^- and glyoxal-S(IV) adducts can potentially induce the different rates of S(IV) loss. Another possible explanation is competition between S(IV) and glyoxal for adsorption and reaction with hydroxyl groups. Faust et al.[21] suggested that the number density of surface hydroxyl groups on α-Fe_2O_3 particles is 9 nm^{-2}. Assuming that the

density of surface hydroxyl groups on these Fe_2O_3 particles is on the same order, the amount of surface hydroxyl groups is estimated to be ~4×10^{18} and the amount of S(IV) and glyoxal in solution is ~7×10^{18} and 4.5×10^{18}, respectively. Although the heterogenous reaction of glyoxal on Fe_2O_3 particles has not been explored, previous studies reported that glyoxal can react with Al_2O_3 particles to produce organic acid.[59] Given that γ-Fe_2O_3 are also active particles, it is reasonable to infer that glyoxal can be adsorbed on the surface of γ-Fe_2O_3 particles and undergo further conversion. Since the amounts of S(IV) and glyoxal are comparable to surface hydroxyl groups, the observed inhibition effect of glyoxal may be partially explained by competition of surface OH groups with S(IV). Importantly, a glyoxal molecule is released from the reaction of glyoxal-S(IV) adducts with the surface hydroxyl group, suggesting that the formation of glyoxal-S(IV) adducts in the initial step do not retard the competition between glyoxal and S(IV) due to the regeneration of glyoxal. Furthermore, we performed the reaction at a much higher ratio of glyoxal/S(IV) to surface OH groups (~50) using ATR-FTIR spectroscopy. Figure 5.6 shows the spectra of the filtered solution obtained from the reaction of S(IV) with γ-Fe_2O_3 particles in the presence and absence of glyoxal. Previous studies revealed that S(IV) is capable of displacing sulfate ions from surface coordination sites after their production,[20,26] thus the formed sulfate remaining on the surface of particles during solution extraction can be excluded. In the absence of glyoxal, the distinct formation of sulfate is observed with the high intensity of the band at 1102 cm^{-1}, assigned to the asymmetric stretching of sulfate,[26,60,61] whereas the

1102 cm^{-1} peak is barely visible in the presence of high concentrations of glyoxal. This result indicates that the reaction is significantly inhibited under the conditions used.

5.4.3. Reactions of Organic Aqueous Aerosols with S(IV)

The results of the oxidation of S(IV) in the presence of glyoxal in the aerosol phase are summarized in Figure 5.7. Figure 5.7 shows the Raman spectra of the initial trapped glyoxal droplet and the resulting spectra after coalescing, or dosing, with metabisulfite as well as the Raman spectrum for a trapped metabisulfite droplet. Additionally, for reference, the Raman spectra of glyoxal and metabisulfite, for both bulk and aerosol phase, are shown in the Supporting Information (Figures 4.11-4.15). In the metabisulfite spectrum of Figure 5.7, the vibrational bands and 1060 cm^{-1} and 1098 cm^{-1} are assigned to $S_2O_5^{2-}$ while the band at 986 cm^{-1} is characteristic SO_4^{2-}.[62–68] As previously mentioned, although metabisulfite is able to be trapped with S(IV) species present, the droplet will oxidize resulting in the appearance of this sulfate band regardless. After the glyoxal droplet is coalesced with the S(IV) solution, the vibrational band near 1050 cm^{-1}, with a shoulder at approximately 1040 cm^{-1}, appears. This band can be assigned to an RSO_3 group and appears likely due to the formation of glyoxal-S(IV) adducts.[69] As mentioned above, the bulk phase reaction between glyoxal and S(IV) results in the formation of glyoxal-S(IV) adducts and the presence of glyoxal inhibits the oxidation of S(IV) to S(VI); the formation mechanism and extent of inhibition are dependent on concentration, pH and presence of transition metal ions.[70] The sulfate stretching band is present in the Raman spectra of metabisulfite in the presence and absence of glyoxal indicating S(IV) to S(VI) oxidation occurs but the relative peak intensity in the presence of glyoxal is much less when compared to the absence of glyoxal which may be indicative of the inhibitory effect of

glyoxal on the oxidation of S(IV). However, additional studies should be conducted to quantitatively compare the relative amounts of S(VI) formed in the presence and absence of glyoxal. Additional studies in the aerosol phase examining the reaction kinetics as well as the influence of transition metal ions should also be conducted to gain a better understanding of any differences in the glyoxal-S(IV) reaction as compared to bulk phase studies.

5.5. Conclusions

The present study shows that the catalytic oxidation of S(IV) can be inhibited by the presence of glyoxal. The extent of the inhibition effect depends on the concentration of glyoxal as well as solution pH. For TMI catalyzed sulfur oxidation, this inhibition effect is proposed to arise from the trapping of SO_4^- radicals as well as the formation of glyoxal-S(IV) adducts and the contribution of these processes depends on the ratio of S(IV) to glyoxal. Although the presence of glyoxal can slow the rate of S(IV) catalytic oxidation, the conversion of S(IV) to S(VI) does eventually occur, suggesting that the S(IV) lifetime is longer in aqueous aerosols as well as cloud and fog droplets. Additionally, with the exception of glyoxal-S(IV) adducts, there is no observation of organosulfur compounds formed. This observation is quite different from our previous study,[39] which investigated the mechanism of TMI-catalyzed S(IV) oxidation influenced by two other carbonyl compounds, methacrolein (MACR) and methyl vinyl ketone (MVK), finding that various organosulfur compounds can be formed during this process. This discrepancy can be

ascribed to the much faster rate of the sulfoxy radical addition reactions across the carbon-carbon double bond within MACR and MVK than the hydrogen abstraction reactions.

Additionally, we also investigated the role glyoxal plays in the reaction of S(IV) with solid iron oxide particles when the oxidation of S(IV) is dominated by heterogeneous reaction. For these particles, inhibition effects of glyoxal on sulfur oxidation is ascribed to competitive adsorption of glyoxal and sulfite with surface hydroxyl groups. Overall, our findings shows that glyoxal can inhibit the oxidation of S(IV) catalyzed by aqueous Fe(III) as well as solid Fe(III), which is the most abundant transition metal in the atmospheric aqueous phase and mineral dust.[71,72] Given that the catalytic oxidation of S(IV) is an important in-cloud sulfate formation pathway, consideration of the effects of water soluble organics such as glyoxal, as well as other carbonyl compounds, on this catalytic reaction is needed in order to accurately predict the formation of sulfate in the atmosphere.

5.6. Acknowledgements

This material is based upon work supported by the National Science Foundation under grant AGS1702488. The authors also acknowledge the use of instruments within the Environmental Complex Analysis Laboratory located in the Department of Chemistry and Biochemistry on the University of California, San Diego campus.

A portion of Chapter 5 is reproduced with permission from the American Chemical Society: Coddens, E. M.; Huang, L.; Wong, C.; Grassian, V. H. (2018). Influence of Glyoxal on the Catalytic Oxidation of S(IV) in Acidic Aqueous Media. *ACS Earth and*

Space Chemistry, 3 (1), 142-149, 2018. The dissertation author was the primary investigator and co-first author of this paper.

5.7.Figures

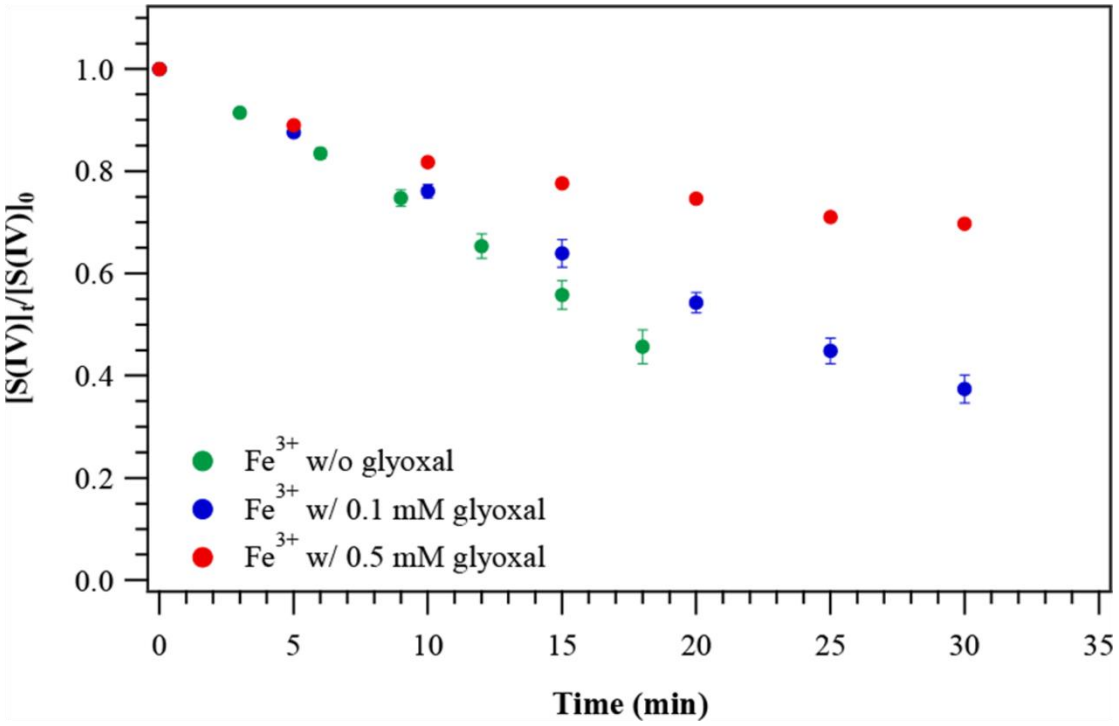

Figure 5.1: Effect of glyoxal on Fe^{3+}-catalyzed S(IV) oxidation at pH 5. Experimental conditions: $[S(IV)]_0$ = 0.18 mM; [glyoxal] = 0.1–0.5 mM; $[Fe^{3+}]$ = 8 μM; T = 25 °C.

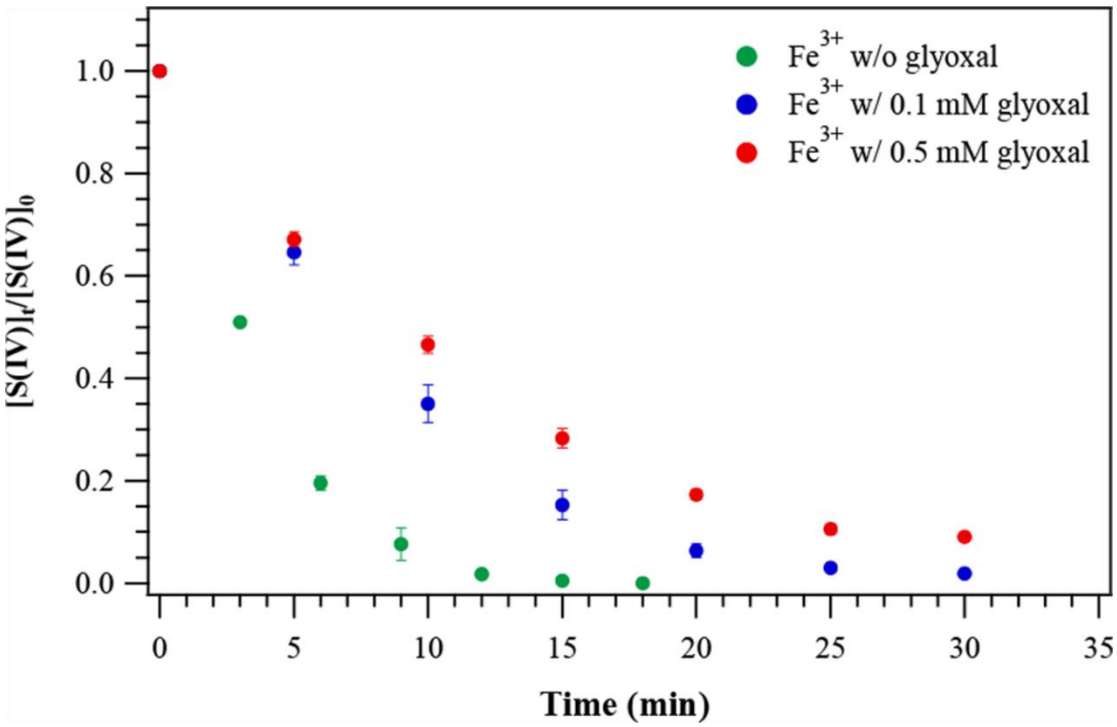

Figure 5.2: Effect of glyoxal on Fe^{3+}-catalyzed S(IV) oxidation at pH 3. Experimental conditions: $[S(IV)]_0$ = 0.16 mM; [glyoxal] = 0.1–0.5 mM; $[Fe^{3+}]$ = 8 μM; T = 25 °C.

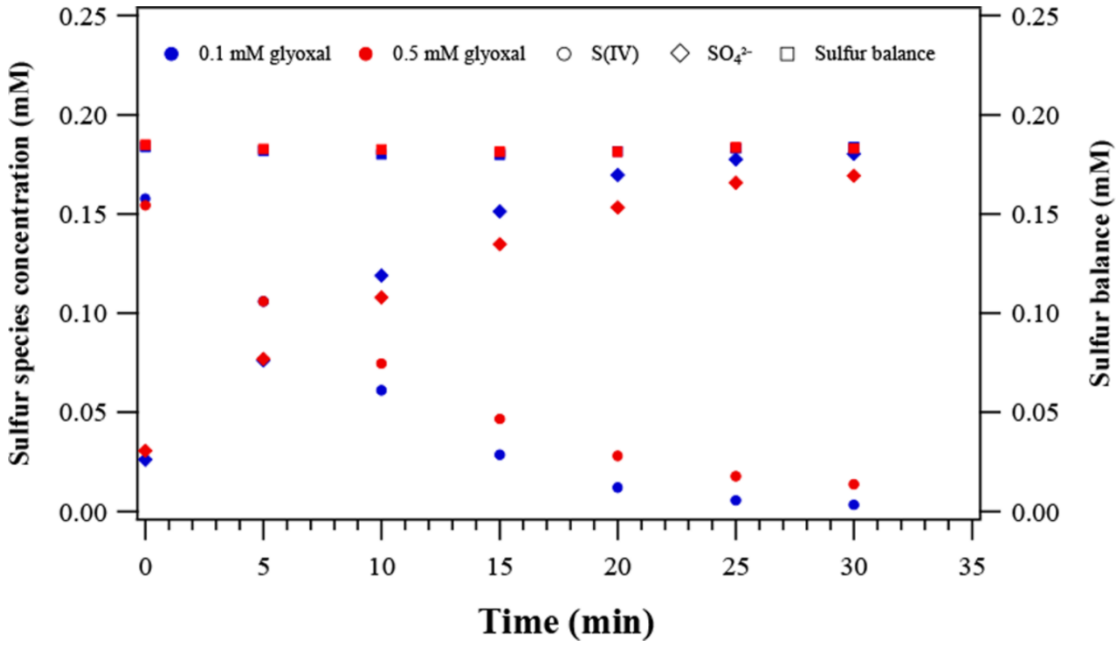

Figure 5.3: The sulfur balance during the oxidation of S(IV) to S(VI) (SO_4^{2-}) by Fe^{3+}(aq) in the presence of 0.1 and 0.5 mM glyoxal at pH3.

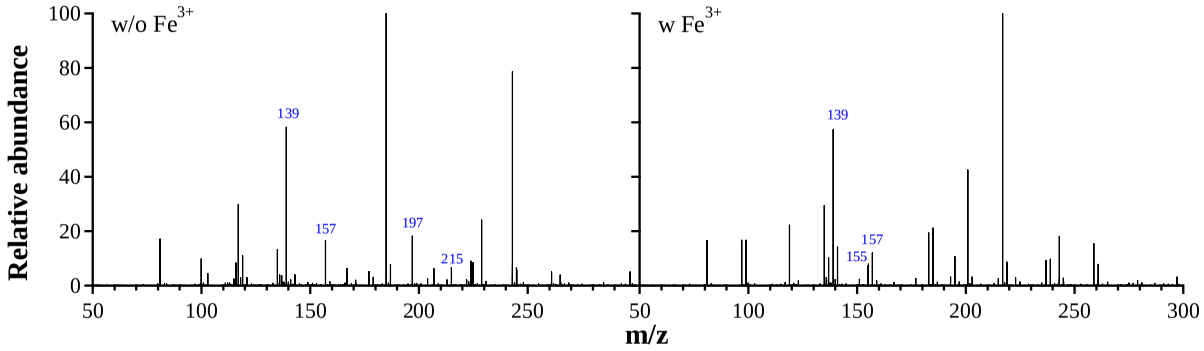

Figure 5.4: Mass spectra of glyoxal reacted with Na_2SO_3 in the absence and presence of Fe^{3+}(aq) at pH 5. Several peaks are highlighted in blue due to the presence of adducts (see text for further details).

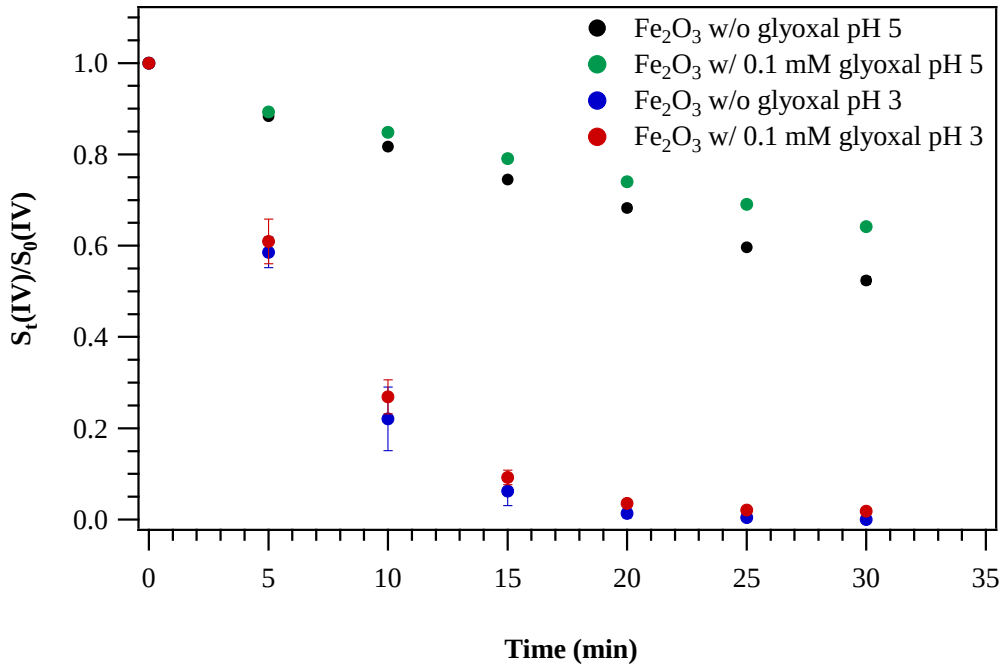

Figure 5.5: Effect of glyoxal on the reaction of S(IV) with Fe_2O_3 particles. Experimental conditions: $[S(IV)]_0$ = ~0.16 mM; [glyoxal] = 0.1 mM; Fe_2O_3 = 0.1 g L^{-1}; T = 25 °C.

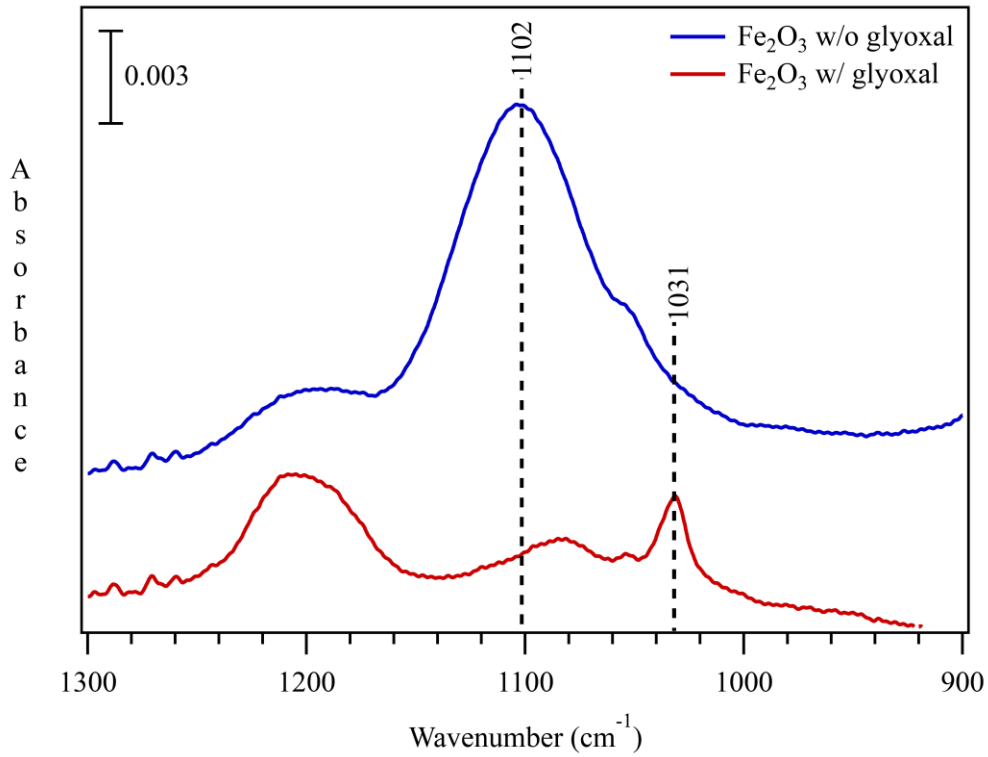

Figure 5.6: ATR-FTIR spectra of oxidation products from S(IV) oxidation by Fe_2O_3 particles in the presence and absence of glyoxal at pH 5. Experimental conditions: $[S(IV)]_0$ = 50 mM; [glyoxal] = 50 mM; Fe_2O_3 = 1 g L^{-1}; T = 25 °C. The spectra were collected after 1 hour of reaction. The band at 1102 cm^{-1} is characteristic of aqueous phase sulfate. Under these conditions of pH, temperature and glyoxal concentrations the S(IV) oxidation is inhibited during the 1-hour reaction time.

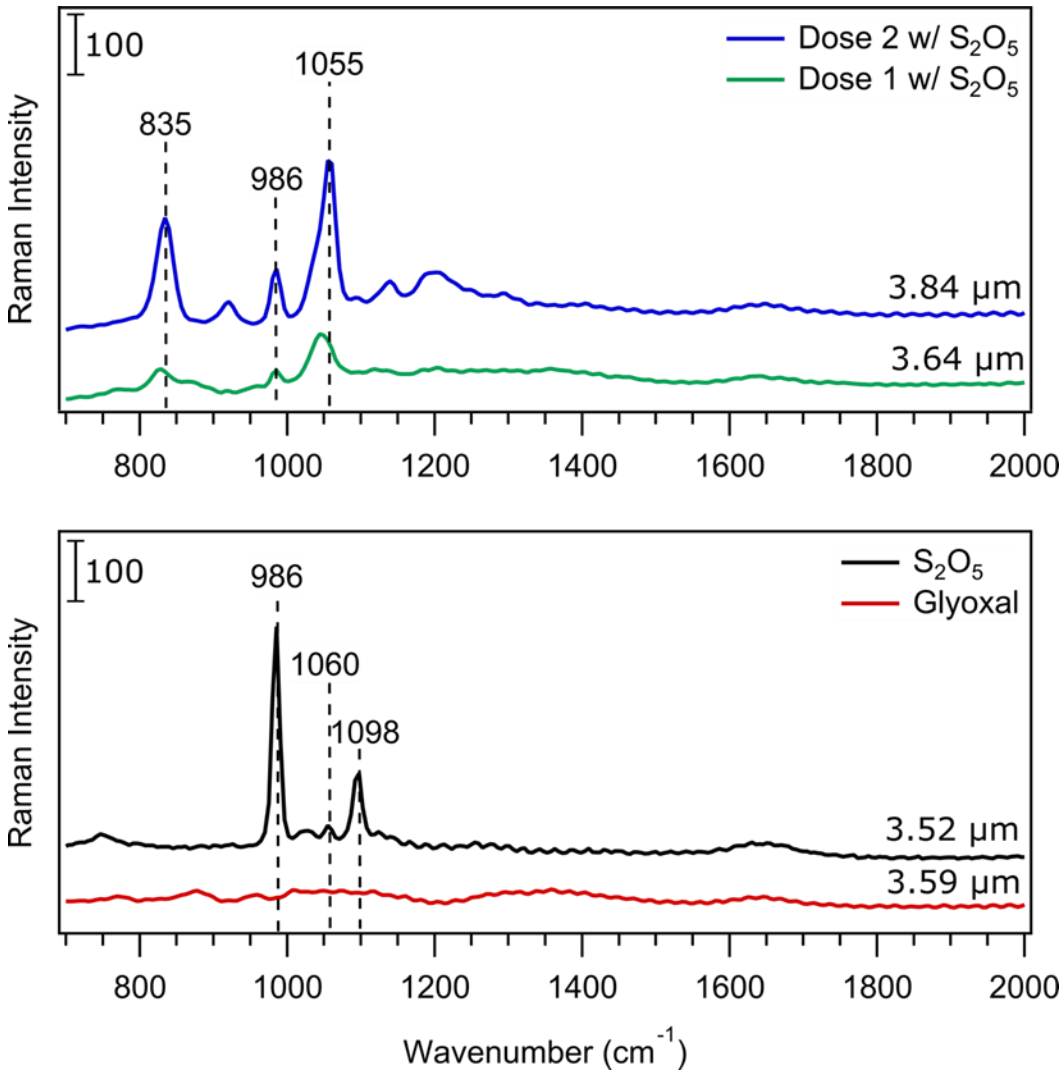

Figure 5.7: Cavity enhanced Raman spectra from trapped droplets of glyoxal (red), metabisulfite (black), and the reaction of glyoxal with metabisulfite via coalescence (green and blue). A glyoxal droplet is first trapped then coalesced with metabisulfite and coalescence is confirmed by comparing the droplet radius which increases from 3.59 µm to 3.64 µm with the first coalescence and then increases again to 3.84 µm after a second coalescence. The sulfate stretching mode at 986 cm^{-1} is inhibited in the presence of glyoxal and the spectral band at 1055 cm^{-1} is attributed to RSO_3 likely due to the formation of glyoxal-S(IV) adducts.

5.8. Tables

Table 5.1: Observed rate constants, *k*, for the catalytic oxidation of S(IV) in the presence and absence of glyoxal.

	[Glyoxal] (mM)	k (mM s^{-1})	k (s^{-1})
		pH 5	pH 3
Fe^{3+}	0	$9.1\pm0.5\times10^{-5}$	$6.0\pm0.3\times10^{-3}$
	0.1	$6.3\pm0.3\times10^{-5}$	$2.4\pm0.1\times10^{-3}$
	0.5	$2.9\pm0.1\times10^{-5}$	$1.4\pm0.1\times10^{-3}$
γ-Fe_2O_3	0	$4.6\pm0.1\times10^{-5}$	$3.7\pm0.2\times10^{-3}$
	0.1	$3.5\pm0.1\times10^{-5}$	$2.8\pm0.1\times10^{-3}$

5.9. Supporting Information

5.9.1. Supporting Information Figures

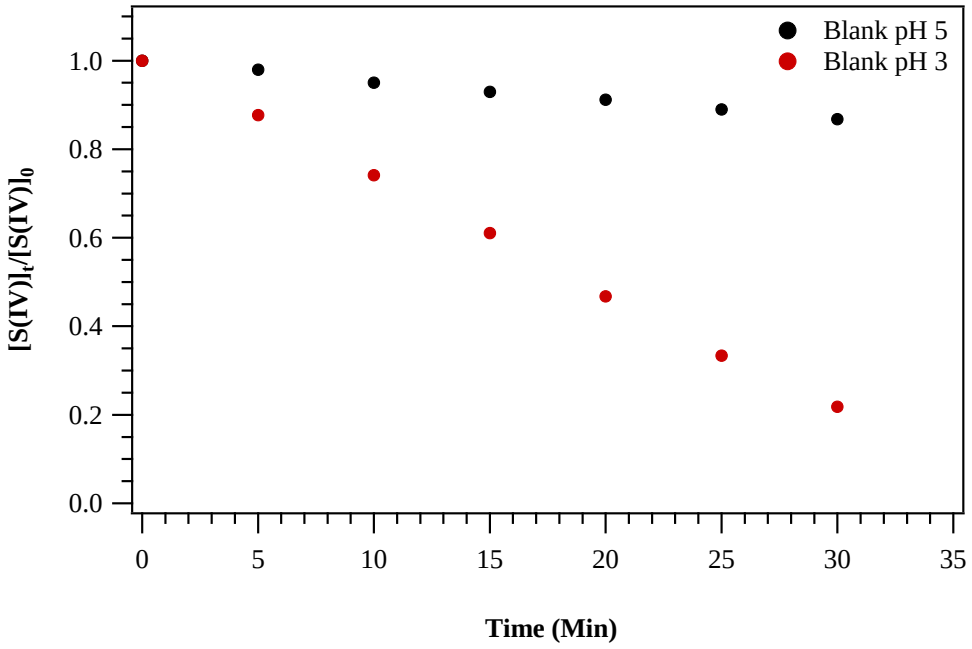

Figure 5.8: Time dependence of S(IV) oxidized by O_2 at different pHs. Experimental conditions: $[S(IV)]_0$ = 0.18 mM (pH 5), 0.16 mM (pH 3); T = 25 °C.

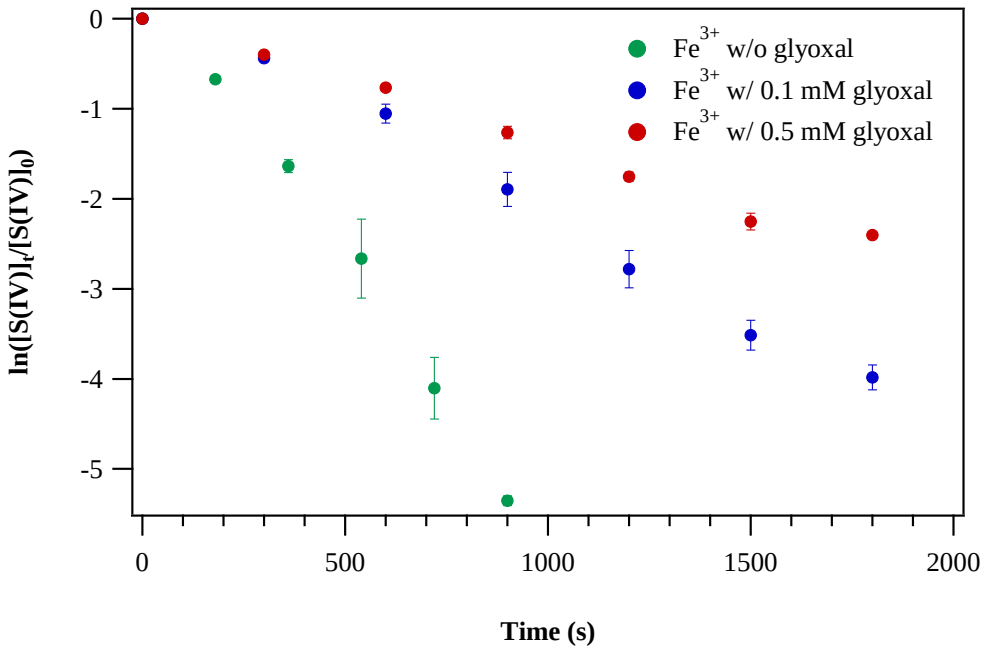

Figure 5.9: $\ln([S(IV)]_t/[S(IV)]_0)$–time plots for Fe^{3+}-catalyzed S(IV) oxidation in the presence of different glyoxal concentration at pH 3. Experimental conditions: $[S(IV)]_0$ = 0.16 mM; [glyoxal] = 0–0.5 mM; $[Fe^{3+}]$ = 8 μM; T = 25 °C.

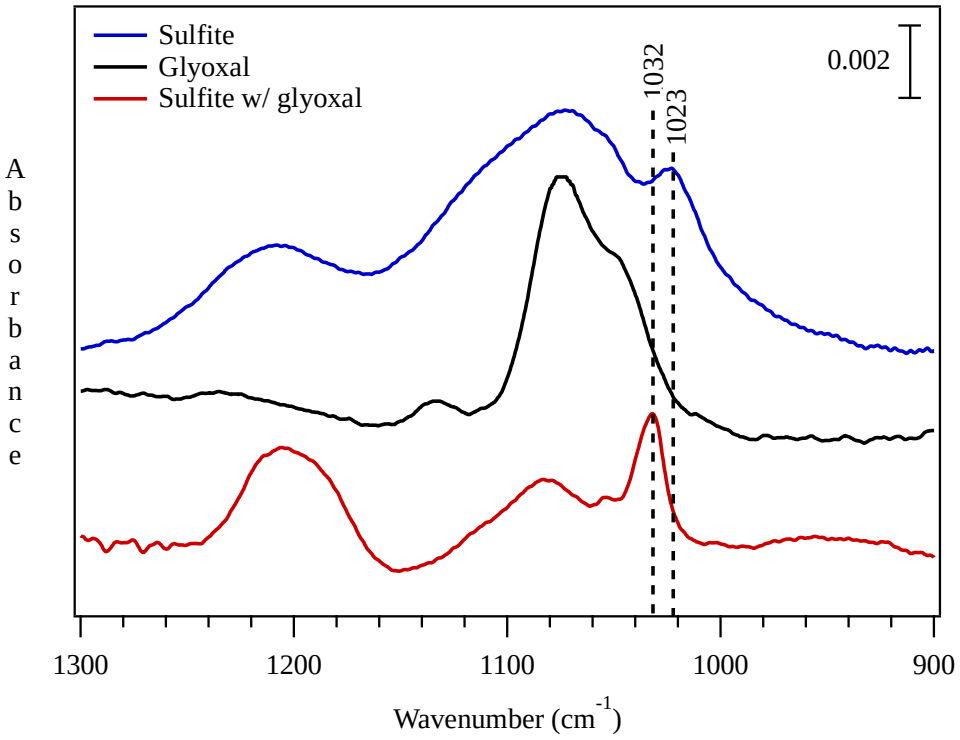

Figure 5.10: ATR-FTIR spectra of Na_2SO_3 (50 mM), glyoxal (50 mM) and Na_2SO_3 (50 mM) mixed with glyoxal (50 mM) at pH5. Several vibrational bands between 1000 and 1100 cm^{-1} correspond to the different forms of S(IV) in the aqueous phase.

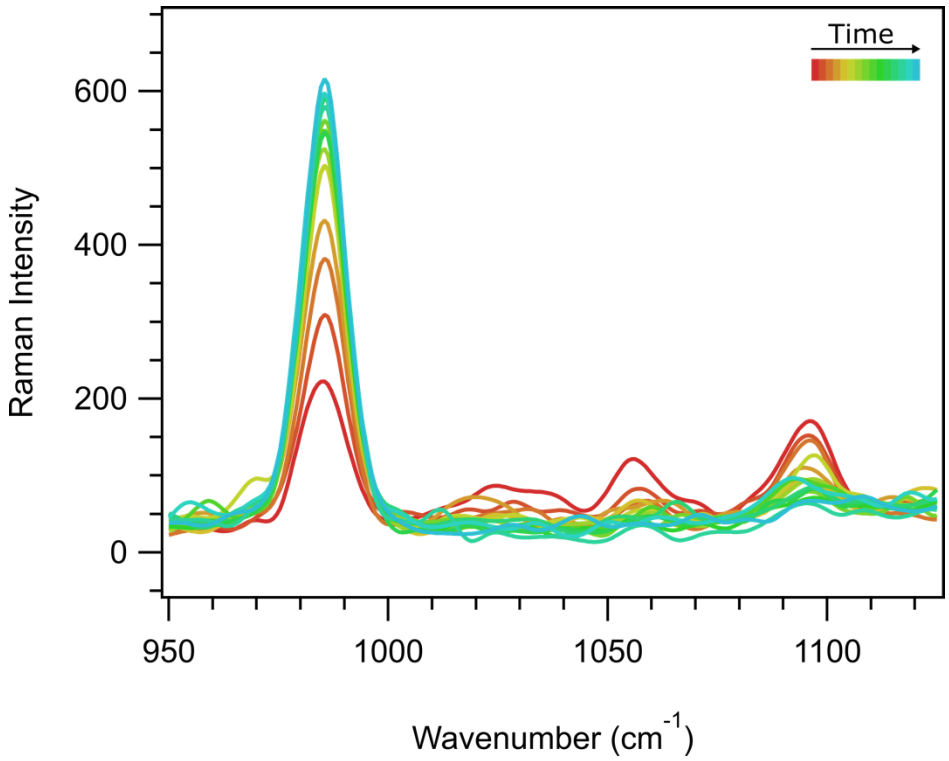

Figure 5.11: Cavity enhanced Raman spectra for a trapped 1 M sodium metabisulfite droplet showing the oxidation of metabisulfite to sulfate over time (approximately 6 minutes). As time progresses the vibrational bands corresponding to $S_2O_5^{2-}$ at 1060 cm^{-1} and 1098 cm^{-1} disappear while the SO_4^{2-} band at 986 cm^{-1} grows in.

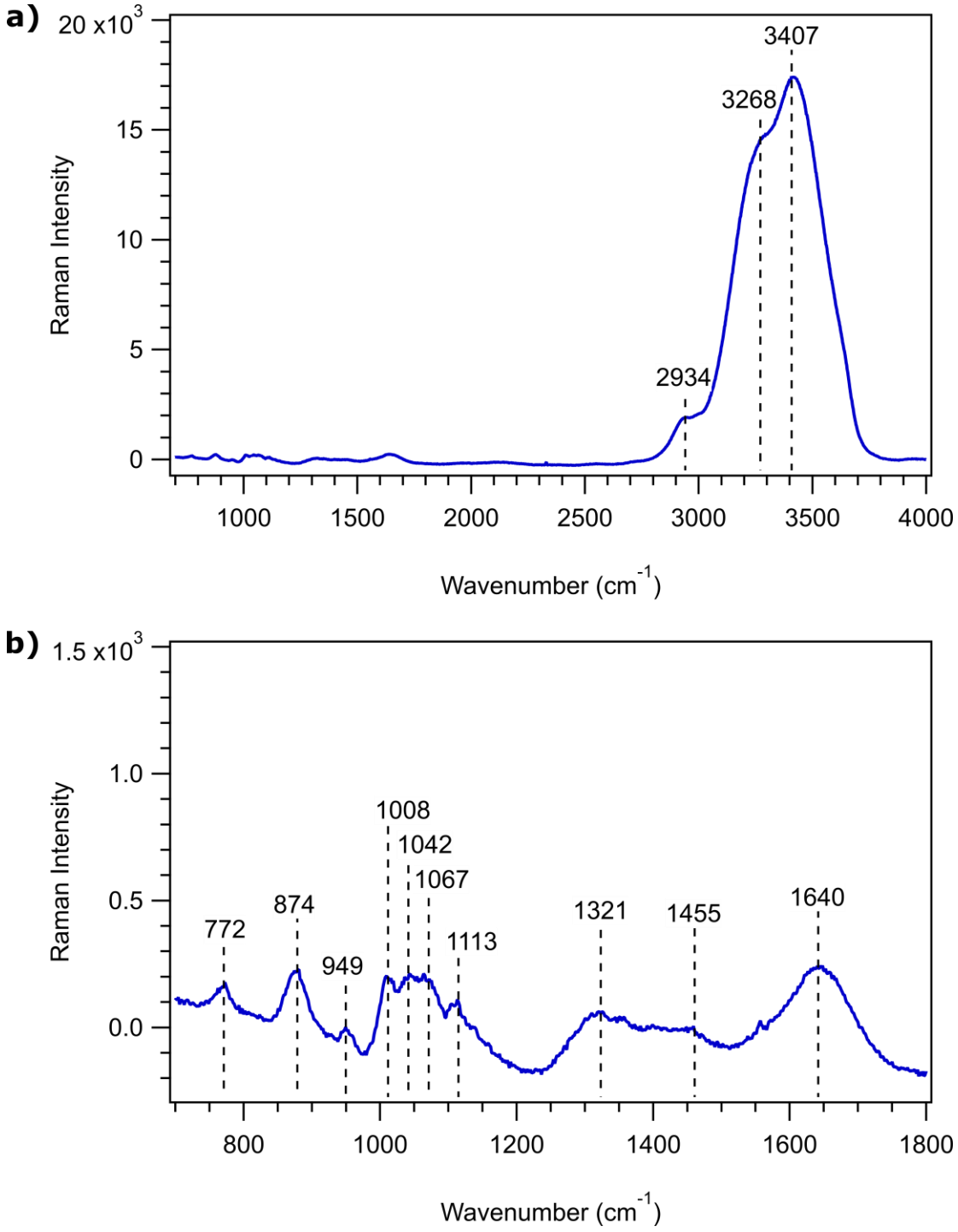

Figure 5.12: Confocal Raman spectrum of bulk 1 M glyoxal over the a) full range and b) focusing in on the 700-1800 cm^{-1} range. A full table of peak assignments for glyoxal can be found in Table 5.3.

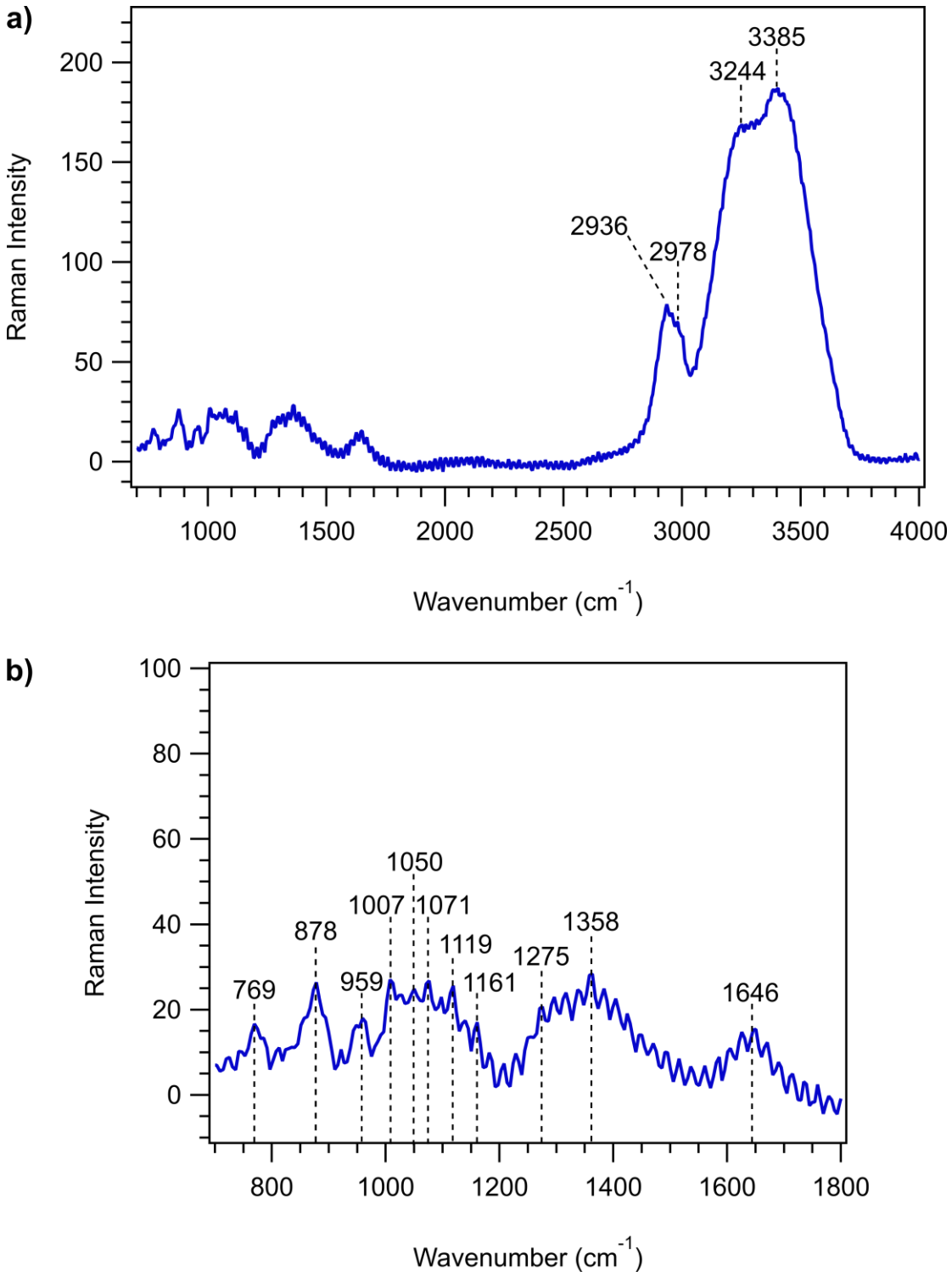

Figure 5.13: Cavity enhanced Raman spectrum of a trapped 1 M glyoxal droplet over the a) full range and b) focusing in on the 700-1800 cm^{-1} range. A full table of peak assignments for glyoxal can be found in Table 5.3.

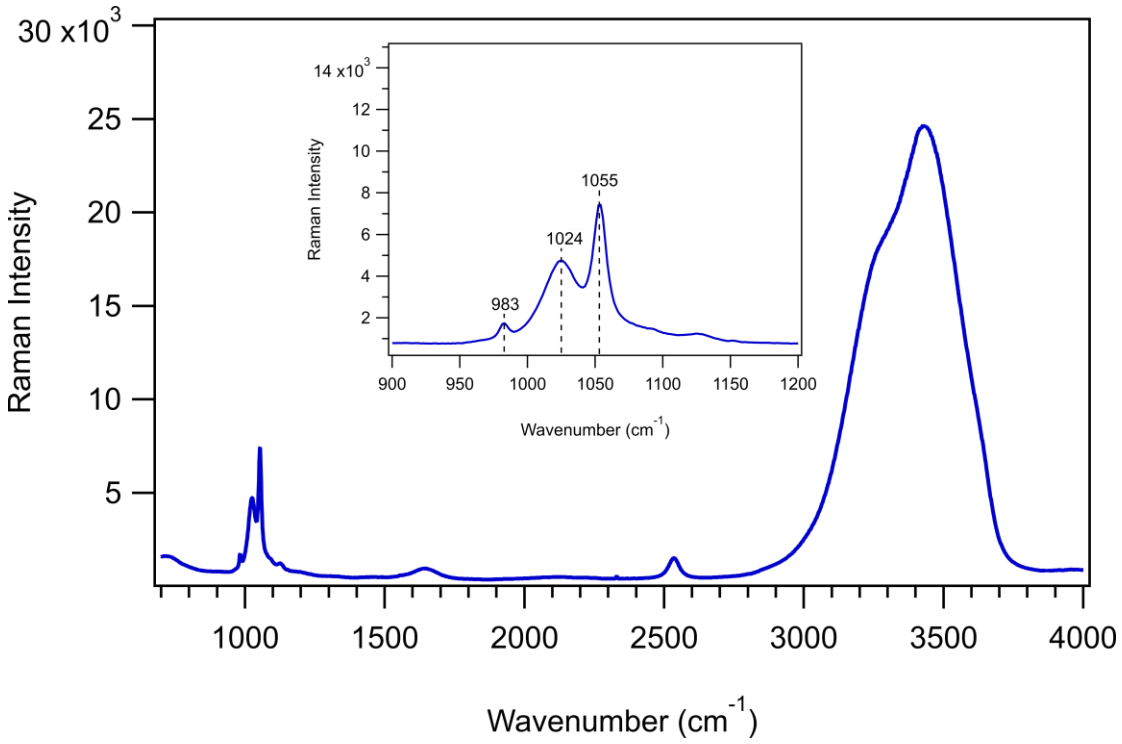

Figure 5.14: Confocal Raman spectrum of bulk 1 M sodium metabisulfite at pH 5 The inset focuses on the 900-1200 cm^{-1} range showing the S(IV) vibrational bands at 1055 cm^{-1} and 1024 cm^{-1} corresponding to $S_2O_5^{2-}$ and HSO_3^-, respectively, in addition to a small band at 983 cm^{-1} corresponding to SO_4^{2-}.

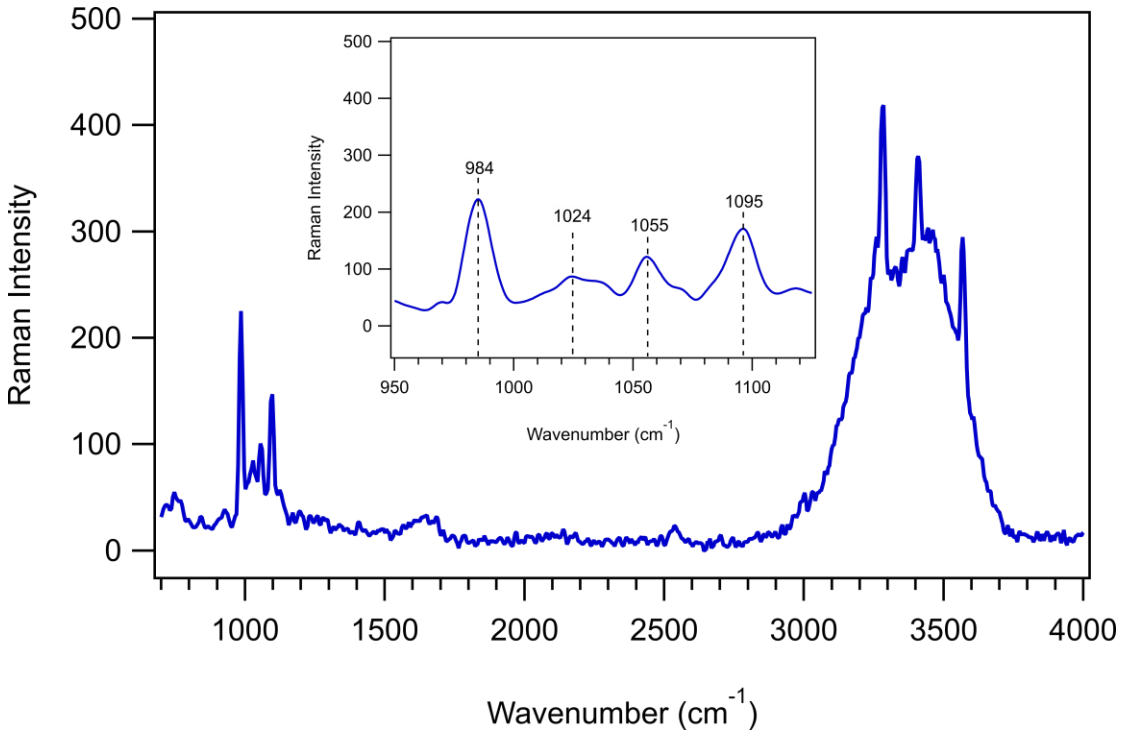

Figure 5.15: Cavity enhanced Raman spectrum of a trapped 1 M sodium metabisulfite at pH 3.8. The inset focuses on the 900-1200 cm^{-1} range showing the $S_2O_5^{2-}$ vibrational bands at 1055 cm^{-1} and 1095 cm^{-1} in addition to a small band at 983 cm^{-1} corresponding to SO_4^{2-} .

5.9.2. Supporting Information Tables

Table 5.2: Experimental conditions of the aqueous reactions of $Na_2S_2O_5$ mixed with glyoxal and iron.

$Na_2S_2O_5$ (mM)	Glyoxal (mM)	$FeCl_3$ (μM)	γ- Fe_2O_3 (g L^{-1})	pH
0.1	–	–	–	5/3
0.1	0/0.1/0.5	8	–	5/3
0.1	0/0.1	–	0.1	5/3
1	0.1	8	–	3

Table 5.3: Peak assignments for the Raman spectrum of glyoxal collected in the bulk phase with confocal Raman spectroscopy and the aerosols phase with AOT cavity enhanced Raman spectroscopy.

Confocal	AOT	Literature	Assignment
772	769	762[a]	δ O-C-O
874	878	872[a]	ν C-C + δ O-H
949	959	952[a]	ring stretching
1008	1007	1008[a]	ν C-O + δ C-OH
1042	1050	1042[a]	
1067	1071	1065[a]	ν C-OH
1113	1119	1110[a]	ν C-OH
----	1161	1155[a]	ν C-C + ring stretch
-----	1275	1278[a]	δ C-H + δ O-H
1321	1358	1353[a]	δ C-H
1455	----	1466[b]	
1640	1646	1640[a]	δ O-H
2934	2936	2800-3100[c]	ν C-H
----	2978		
3268	3244	3200-3600[c]	ν O-H
3407	3385		

[a] Avzianova, 2013;[51] [b] Brand, 1954;[73] [c] Socrates, 2001.[74]

5.10. References

(1) Seinfeld, J. H.; Pandis, S. N. *Atmospheric Chemistry and Physics : From Air Pollution to Climate Change*, 2nd ed.; John Wiley & Sons, Inc.: Hoboken, 2006.

(2) Alexander, B.; Park, R. J.; Jacob, D. J.; Gong, S. Transition Metal-Catalyzed Oxidation of Atmospheric Sulfur: Global Implications for the Sulfur Budget. *J. Geophys. Res.* **2009**, *114*, D02309.

(3) Brandt, C.; van Eldik, R. Transition Metal-Catalyzed Oxidation of Sulfur(IV) Oxides. Atmospheric-Relevant Processes and Mechanisms. *Chem. Rev.* **1995**, *95*, 119–190.

(4) Wolf, A.; Deutsch, F.; Hoffmann, P.; Ortner, H. M. The Influence of Oxalate on Fe-Catalyzed S(IV) Oxidation by Oxygen in Aqueous Solution. *J. Atmos. Chem.* **2000**, *37*, 125–135.

(5) Podkrajšek, B.; Grgić, I.; Turšič, J.; Berčič, G. Influence of Atmospheric Carboxylic Acids on Catalytic Oxidation of Sulfur(IV). *J. Atmos. Chem.* **2006**, *54*, 103–120.

(6) Grgić, I.; Podkrajšek, B.; Barzaghi, P.; Herrmann, H. Scavenging of SO4− Radical Anions by Mono- and Dicarboxylic Acids in the Mn(II)-Catalyzed S(IV) Oxidation in Aqueous Solution. *Atmos. Environ.* **2007**, *41*, 9187–9194.

(7) Herrmann, H. Kinetics of Aqueous Phase Reactions Relevant for Atmospheric Chemistry. *Chem. Rev.* **2003**, *103*, 4691–4716.

(8) Opletal, M.; Novotný, P.; Rejl, F. J.; Moucha, T.; Kordač, M. Kinetics of Catalytic Oxidation of Sulfite in Diluted Aqueous Solutions. *Chem. Eng. Technol.* **2015**, *38*, 1919–1924.

(9) Clifton, C. L.; Huie, R. E. Rate Constants for Hydrogen Abstraction Reactions of the Sulfate Radical, SO4-. Alcohols. *Int. J. Chem. Kinet.* **1989**, *21*, 677–687.

(10) Huie, R. E.; Clifton, C. L. Rate Constants for Hydrogen Abstraction Reactions of the Sulfate Radical, SO4-. Alkanes and Ethers. *Int. J. Chem. Kinet.* **1989**, *21*, 611–619.

(11) Pasiuk-Bronikowska, W.; Bronikowski, T.; Ulejczyk, M. Inhibition of the S(IV) Autoxidation in the Atmosphere by Secondary Terpenic Compounds. *J. Atmos. Chem.* **2003**, *44*, 97–111.

(12) Pasiuk-Bronikowska, W.; Bronikowski, T.; Ulejczyk, M. Synergy in the Autoxidation of S(IV) Inhibited by Phenolic Compounds. *J. Phys. Chem. A* **2003**, *107*, 1742–1748.

(13) Ziajka, J.; Pasiuk-Bronikowska, W. Rate Constants for Atmospheric Trace Organics Scavenging SO4− in the Fe-Catalysed Autoxidation of S(IV). *Atmos. Environ.* **2005**, *39*, 1431–1438.

(14) Ziajka, J.; Rudzinski, K. J. Autoxidation of SIV Inhibited by Chlorophenols Reacting with Sulfate Radicals. *Environ. Chem.* **2007**, *4*, 355–363.

(15) Rudziński, K. J.; Gmachowski, L.; Kuznietsova, I. Reactions of Isoprene and Sulphoxy Radical-Anions – a Possible Source of Atmospheric Organosulphites and Organosulphates. *Atmos. Chem. Phys.* **2009**, *9*, 2129–2140.

(16) Meena, V. K.; Dhayal, Y.; Rathore, D. S.; Chandel, C. P. S.; Gupta, K. S. Inhibition of Atmospheric Aqueous Phase Autoxidation of Sulphur Dioxide by Volatile Organic Compounds: Mono-, Di- and Tri-Substituted Benzenes and Benzoic Acids. *Prog. React. Kinet. Mech.* **2017**, *42*, 111–125.

(17) Neta, P.; Madhavan, V.; Zemel, H.; Fessenden, R. W. Rate Constants and Mechanism of Reaction of Sulfate Radical Anion with Aromatic Compounds. *J. Am. Chem. Soc.* **1977**, *99*, 163–164.

(18) Raber, W. H.; Moortgat, G. K. *Progress and Problems in Atmospheric Chemistry*; Barker, J., Ed.; Advanced Series in Physical Chemistry; World Scientific Publishing: Singapore, 1996; Vol. 3.

(19) Carlier, P.; Hannachi, H.; Mouvier, G. The Chemistry of Carbonyl Compounds in the Atmosphere—A Review. *Atmos. Environ.* **1986**, *20*, 2079–2099.

(20) Faust, B. C.; Hoffmann, M. R. Photoinduced Reductive Dissolution of Alpha-Iron Oxide (Alpha-Fe2O3) by Bisulfite. *Environ. Sci. Technol.* **1986**, *20*, 943–948.

(21) Faust, B. C.; Hoffmann, M. R.; Bahnemann, D. W. Photocatalytic Oxidation of Sulfur Dioxide in Aqueous Suspensions of Alpha-Iron Oxide (Fe2O3). *J. Phys. Chem.* **1989**, *93*, 6371–6381.

(22) Prasad, D. S. N.; Rani, A.; Gupta, K. S. Surface-Catalyzed Autoxidation of Sulfur(IV) in Aqueous Silica and Copper(II) Oxide Suspensions. *Environ. Sci. Technol.* **1992**, *26*, 1361–1368.

(23) Ansari, A.; Peral, J.; Domènech, X.; Rodríguez-Clemente, R.; Roig, A.; Molins, E. Photo-Oxidation of Sulfite Ions in the Presence of Some Iron Oxides. *J. Photochem. Photobiol. A Chem.* **1995**, *87*, 121–125.

(24) Ansari, A.; Peral, J.; Domènech, X.; Rodriquez-Clemente, R. Oxidation of HSO_3^- in Aqueous Suspensions of α-Fe2O3, α-FeOOh, β-FeOOH and γ-FeOOH in the Dark and under Illumination. *Environ. Pollut.* **1997**, *95*, 283–288.

(25) Gupta, K. S.; Mehta, R. K.; Sharma, A. K.; Mudgal, P. K.; Bansal, S. P. Kinetics of the Uninhibited and Ethanol-Inhibited CoO, Co2O3 and Ni2O3 Catalyzed Autoxidation of Sulfur(IV) in Alkaline Medium. *Transit. Met. Chem.* **2008**, *33*, 809–817.

(26) Gankanda, A.; Coddens, E. M.; Zhang, Y.; Cwiertny, D. M.; Grassian, V. H. Sulfate Formation Catalyzed by Coal Fly Ash, Mineral Dust and Iron(III) Oxide: Variable

Influence of Temperature and Light. *Environ. Sci. Process. Impacts* **2016**, *18*, 1484–1491.

(27) Atkinson, R. Atmospheric Chemistry of VOCs and NOx. *Atmos. Environ.* **2000**, *34*, 2063–2101.

(28) Volkamer, R.; Platt, U.; Wirtz, K. Primary and Secondary Glyoxal Formation from Aromatics: Experimental Evidence for the Bicycloalkyl−Radical Pathway from Benzene, Toluene, and p-Xylene. *J. Phys. Chem. A* **2001**, *105*, 7865–7874.

(29) Volkamer, R.; Molina, L. T.; Molina, M. J.; Shirley, T.; Brune, W. H. DOAS Measurement of Glyoxal as an Indicator for Fast VOC Chemistry in Urban Air. *Geophys. Res. Lett.* **2005**, *32*, L08806.

(30) Galloway, M. M.; Huisman, A. J.; Yee, L. D.; Chan, A. W. H.; Loza, C. L.; Seinfeld, J. H.; Keutsch, F. N. Yields of Oxidized Volatile Organic Compounds during the OH Radical Initiated Oxidation of Isoprene, Methyl Vinyl Ketone, and Methacrolein under High-NOx Conditions. *Atmos. Chem. Phys.* **2011**, *11*, 10779–10790.

(31) Sander, R. Compilation of Henry's Law Constants (Version 4.0) for Water as Solvent. *Atmos. Chem. Phys.* **2015**, *15*, 4399–4981.

(32) Matsumoto, K.; Kawai, S.; Igawa, M. Dominant Factors Controlling Concentrations of Aldehydes in Rain, Fog, Dew Water, and in the Gas Phase. *Atmos. Environ.* **2005**, *39*, 7321–7329.

(33) Carlton, A. G.; Turpin, B. J.; Altieri, K. E.; Seitzinger, S.; Reff, A.; Lim, H.-J.; Ervens, B. Atmospheric Oxalic Acid and SOA Production from Glyoxal: Results of Aqueous Photooxidation Experiments. *Atmos. Environ.* **2007**, *41*, 7588–7602.

(34) Volkamer, R.; San Martini, F.; Molina, L. T.; Salcedo, D.; Jimenez, J. L.; Molina, M. J. A Missing Sink for Gas-Phase Glyoxal in Mexico City: Formation of Secondary Organic Aerosol. *Geophys. Res. Lett.* **2007**, *34*, L19807.

(35) De Haan, D. O.; Corrigan, A. L.; Smith, K. W.; Stroik, D. R.; Turley, J. J.; Lee, F. E.; Tolbert, M. A.; Jimenez, J. L.; Cordova, K. E.; Ferrell, G. R. Secondary Organic Aerosol-Forming Reactions of Glyoxal with Amino Acids. *Environ. Sci. Technol.* **2009**, *43*, 2818–2824.

(36) Lim, Y. B.; Tan, Y.; Perri, M. J.; Seitzinger, S. P.; Turpin, B. J. Aqueous Chemistry and Its Role in Secondary Organic Aerosol (SOA) Formation. *Atmos. Chem. Phys.* **2010**, *10*, 10521–10539.

(37) Herrmann, H.; Schaefer, T.; Tilgner, A.; Styler, S. A.; Weller, C.; Teich, M.; Otto, T. Tropospheric Aqueous-Phase Chemistry: Kinetics, Mechanisms, and Its Coupling to a Changing Gas Phase. *Chem. Rev.* **2015**, *115*, 4259–4334.

(38) Woo, J. L.; Mcneill, V. F. SimpleGAMMA v1.0-a Reduced Model of Secondary Organic Aerosol Formation in the Aqueous Aerosol Phase (AaSOA). *Geosci. Model Dev* **2015**, *8*, 1821–1829.

(39) Huang, L.; Cochran, R. E.; Coddens, E. M.; Grassian, V. H. Formation of Organosulfur Compounds through Transition Metal Ion-Catalyzed Aqueous Phase Reactions. *Environ. Sci. Technol. Lett.* **2018**, *5*, 315–321.

(40) Schaefer, T.; van Pinxteren, D.; Herrmann, H. Multiphase Chemistry of Glyoxal: Revised Kinetics of the Alkyl Radical Reaction with Molecular Oxygen and the Reaction of Glyoxal with OH, NO_3, and SO_4^- in Aqueous Solution. *Environ. Sci. Technol.* **2015**, *49*, 343–350.

(41) Hoffmann, D.; Weigert, B.; Barzaghi, P.; Herrmann, H. Reactivity of Poly-Alcohols towards OH, NO3 and SO4− in Aqueous Solution. *Phys. Chem. Chem. Phys.* **2009**, *11*, 9351–9363.

(42) Hayon, E.; Treinin, A.; Wilf, J. Electronic Spectra, Photochemistry, and Autoxidation Mechanism of the Sulfite-Bisulfite-Pyrosulfite Systems. SO2-, SO3-, SO4-, and SO5- Radicals. *J. Am. Chem. Soc.* **1972**, *94*, 47–57.

(43) Olson, E. M.; Hoffmann, M. R. Formation Kinetics, Mechanism, and Thermodynamics of Glyoxylic Acid-S(IV) Adducts. *J. Phys. Chem.* **1988**, *92*, 4246–4253.

(44) Townsend, T. M.; Allanic, A.; Noonan, C.; Sodeau, J. R. Characterization of Sulfurous Acid, Sulfite, and Bisulfite Aerosol Systems. *J. Phys. Chem. A* **2012**, *116*, 4035–4046.

(45) Zhang, Z.; Ewing, G. E. Infrared Spectroscopy of SO2 Aqueous Solutions. *Spectrochim. Acta Part A Mol. Biomol. Spectrosc.* **2002**, *58*, 2105–2113.

(46) Kaun, N.; Vellekoop, M. J.; Lendl, B. Time-Resolved Fourier Transform Infrared Spectroscopy of Chemical Reactions in Solution Using a Focal Plane Array Detector. *Appl. Spectrosc.* **2006**, *60*, 1273–1278.

(47) Olson, T. M.; Hoffmann, M. R. *Kinetics, Mechanism, and Thermodynamics of Glyoxal-S(IV) Adduct Formation*; 1988; Vol. 92.

(48) Yu, G.; Bayer, A. R.; Galloway, M. M.; Korshavn, K. J.; Fry, C. G.; Keutsch, F. N. Glyoxal in Aqueous Ammonium Sulfate Solutions: Products, Kinetics and Hydration Effects. *Environ. Sci. Technol.* **2011**, *45*, 6336–6342.

(49) Ervens, B.; Volkamer, R. Glyoxal Processing by Aerosol Multiphase Chemistry: Towards a Kinetic Modeling Framework of Secondary Organic Aerosol Formation in Aqueous Particles. *Atmos. Chem. Phys.* **2010**, *10*, 8219–8244.

(50) Kirsten W. Loeffler; Charles A. Koehler; Paul, N. M.; De Haan, D. O. Oligomer Formation in Evaporating Aqueous Glyoxal and Methyl Glyoxal Solutions. *Environ. Sci. Technol.* **2006**, *40*, 6318–6323.

(51) Avzianova, E.; Brooks, S. D. Raman Spectroscopy of Glyoxal Oligomers in Aqueous Solutions. *Spectrochim. Acta Part A* **2013**, *101*, 40–48.

(52) Olson, T. M.; Hoffmann, M. R. Hydroxyalkylsulfonate Formation: Its Role as a S(IV) Reservoir in Atmospheric Water Droplets. *Atmos. Environ.* **1989**, *23*, 985–997.

(53) Rubasinghege, G.; Lentz, R. W.; Scherer, M. M.; Grassian, V. H. Simulated Atmospheric Processing of Iron Oxyhydroxide Minerals at Low PH: Roles of Particle Size and Acid Anion in Iron Dissolution. *Proc. Natl. Acad. Sci. U. S. A.* **2010**, *107*, 6628–6633.

(54) Chen, H.; Laskin, A.; Baltrusaitis, J.; Gorski, C. A.; Scherer, M. M.; Grassian, V. H. Coal Fly Ash as a Source of Iron in Atmospheric Dust. *Environ. Sci. Technol.* **2012**, *46*, 2112–2120.

(55) Jacob, D. J.; Gottlieb, E. W.; Prather, M. J. Chemistry of a Polluted Cloudy Boundary Layer. *J. Geophys. Res.* **1989**, *94*, 12975–13002.

(56) Martin, L. R.; Easton, M. P.; Foster, J. W.; Hill, M. W. Oxidation of Hydroxymethanesulfonic Acid by Fenton's Reagent. *Atmos. Environ.* **1989**, *23*, 563–568.

(57) Olson, T. M.; Fessenden, R. W. *Pulse Radlolysls Study of the Reaction of OH' Radicals with Methanesulfonate and Hydroxymethanesulfonate*; 1992; Vol. 96.

(58) Huie, R. E.; Neta, P. Rate Constants for Some Oxidations of S(IV) by Radicals in Aqueous Solutions. *Atmos. Environ.* **1987**, *21*, 1743–1747.

(59) Shen, X.; Wu, H.; Zhao, Y.; Huang, D.; Huang, L.; Chen, Z. Heterogeneous Reactions of Glyoxal on Mineral Particles: A New Avenue for Oligomers and Organosulfate Formation. *Atmos. Environ.* **2016**, *131*, 133–140.

(60) Hug, S. J. In SituFourier Transform Infrared Measurements of Sulfate Adsorption on Hematite in Aqueous Solutions. *J. Colloid Interface Sci.* **1997**, *188*, 415–422.

(61) Liu, C.; Ma, Q.; Liu, Y.; Ma, J.; He, H. Synergistic Reaction between SO2 and NO2 on Mineraloxides: A Potential Formation Pathway of Sulfate Aerosol. *Phys. Chem. Chem. Phys.* **2012**, *14*, 1668–1676.

(62) Herlinger, A. W.; Long, T. V. An Investigation of the Structure of the Disulfite Ion in Aqueous Solution Using Raman and Infrared Spectroscopies. *Inorg. Chem.* **1969**, *8*, 2661–2665.

(63) Davis, A. R.; Chatterjee, R. M. A Vibrational-Spectroscopic Study of the SO2-H2O System. *J. Solution Chem.* **1975**, *4*, 399–412.

(64) Meyer, B.; Peter, L.; Shaskey-Rosenlund, C. Raman Spectra of Isotopic Bisulfite and Disulfite Ions in Alkali Salts and Aqueous Solution. *Spectrochim. Acta Part A* **1979**, *35*, 345–354.

(65) Daly, F. P.; Brown, C. W.; Kester, D. R.; Daly, F. P.; Brown, C. W.; Kester, D. R. Sodium and Magnesium Sulfate Ion Pairing: Evidence from Raman Spectroscopy. *J. Phys. Chem.* **1972**, *76*, 3664–3668.

(66) Fung, K. .; Tang, I. . Composition Analysis of Suspended Aerosol Particles by Raman Spectroscopy: Sulfates and Nitrates. *J. Colloid Interface Sci.* **1989**, *130*, 219–224.

(67) Mabrouk, K. Ben; Kauffmann, T. H.; Aroui, H.; Fontana, M. D. Raman Study of Cation Effect on Sulfate Vibration Modes in Solid State and in Aqueous Solutions. *J. Raman Spectrosc.* **2013**, *44*, 1603–1608.

(68) Peter, L.; Meyer, B. Preparation and Raman Spectra of Thallium(I) Disulfite and Thallium(I) Sulfite. *Inorg. Chem.* **1985**, *24*, 3071–3073.

(69) Houlton, H. G.; Tartar, V. Raman Spectra of Sodium Alkyl Sulfonates and Sulfinates. *J. Am. Chem. Soc.* **1938**, *60*, 544–548.

(70) Coddens, E. M.; Huang, L.; Wong, C.; Grassian, V. H. Influence of Glyoxal on the Catalytic Oxidation of S(IV) in Acidic Aqueous Media. *ACS Earth Sp. Chem.* **2019**, *3*, 142–149.

(71) Deguillaume, L.; Leriche, M.; Desboeufs, K.; Mailhot, G.; George, C.; Chaumerliac, N. Transition Metals in Atmospheric Liquid Phases: Sources, Reactivity, and Sensitive Parameters. *Chem. Rev.* **2005**, *105*, 3388–3431.

(72) Zhang, Y.; Mahowald, N.; Scanza, R. A.; Journet, E.; Desboeufs, K.; Albani, S.; Kok, J. F.; Zhuang, G.; Chen, Y.; Cohen, D. D.; Patey, M. D.; Achterberg, E. P.; Engelbrecht, J. P.; Fomba, K. W. Modeling the Global Emission, Transport and Deposition of Trace Elements Associated with Mineral Dust. *Biogeosciences* **2015**, *12*, 5771–5792.

(73) Brand, J. C. D. Vibrational Analysis of the Low-Frequency Absorption System of Glyoxal as a $^{1}A_{g} - {}^{1}A_{u}$ Transition. *Trans. Faraday Soc.* **1954**, *50*, 431–444.

(74) Socrates, G. *Infrared and Raman Characteristic Group Frequencies. Tables and ChartsGeorge Socrates John Wiley and Sons, Ltd, Chichester, Third Edition, 2001. Price £135*, 3rd ed.; John Wiley & Sons, Ltd: Chichester, England, 2001.

Chapter 6 Aqueous Phase Catalytic Oxidation of S(IV): Influence of pH, Ionic Strength, and the Presence of Organic Compounds

6.1. Synopsis

The aqueous phase oxidation of S(IV) is an important oxidation pathway of SO_2 in the atmosphere leading to the formation of particulate sulfate. Although the catalytic oxidation of S(IV) has been well studied, the effects of a number of atmospherically relevant variables on the reaction mechanism and kinetics are not well understood. Therefore, herein we have investigated the influence of a range of variables including pH, ionic strength, and presence of organic compounds on the aqueous phase oxidation of S(IV) in the presence and absence of transition metals to gain a better understanding of how this reaction may be altered under various atmospheric conditions found for aqueous aerosols as well as cloud and fog droplets. As discussed in more detail below, these results show that at relatively low ionic strength, the effect of ionic strength on sulfur oxidation varies depending on the pH and type of transition metal ion present. However, at high ionic strength, S(IV) oxidation to S(VI) is greatly inhibited. The presence of atmospherically relevant organic compounds, glyoxal and methacrolein, also inhibit the transition metal catalyzed oxidation of inorganic S(IV) to inorganic S(VI) with concomitant increase in organosulfur compound formation. These results considerably expand upon the conditions that have been previously studied on this important sulfur oxidation chemistry and clearly demonstrates that the variety of conditions found in aqueous droplets (high ionic strength,

presence of organics, etc.) influences atmospheric sulfur processes that need to be understood in order to be included in atmospheric chemistry models.

6.2. Introduction

It has been well known for some time that sulfur oxidation chemistry plays an important role in atmospheric chemistry as SO_2 is a primary pollutant from many anthropogenic sources and contributes to the formation of acid rain and sulfate aerosol.[1–3] Reaction mechanisms and kinetics for the oxidation of S(IV) and catalysis by transition metals has been studied for many years. Although many atmospheric sulfur oxidation pathways and sulfate formations mechanisms have been elucidated, current atmospheric models underestimate sulfate concentrations partly due to a lack of understanding as to how the reaction kinetics are influenced under various atmospheric conditions (pH and ionic strength) or by the presence of atmospherically relevant organics.[4–7] With some of the highest levels of particulate sulfate measured in China and an estimated increase in fine particulate matter (PM2.5) of 0.55 $\mu g/m^3/yr$, the increased complexity of the atmosphere and atmospheric conditions need to be accounted for in atmospheric chemical models.[7–10]

Previous studies have shown that sulfate production can be enhanced by the catalytic oxidation of aqueous inorganic S(IV) (sulfite and bisulfite) in the presence of transition metal ions.[4,11,12] Transition metal ion catalyzed oxidation of S(IV) is considered as a major in-cloud oxidation pathway of SO_2 and contributes 9 to 17% to the global sulfate budget with greater percentages reported in polluted industrial regions.[5,13–15] The transition metal catalyzed oxidation of S(IV) can proceed through a homogeneous pathway in the solution phase or a heterogeneous pathway at the particle-water interface.[12,16] The main

mechanism for the transition metal ion catalyzed oxidation of S(IV) by dissolved oxygen is summarized in reactions R1-R6.[12,17,18]

$$\mathbf{SO_3^{2-} + M^{n+} \rightleftharpoons SO_3^{\bullet -} + M^{(n-1)+}} \quad \text{(R1)}$$

$$\mathbf{SO_3^{\bullet -} + O_2 \rightleftharpoons SO_5^{\bullet -}} \quad \text{(R2)}$$

$$\mathbf{SO_5^{\bullet -} + SO_3^{2-} \rightleftharpoons SO_5^{2-} + SO_3^{\bullet -}} \quad \text{(R3)}$$

$$\mathbf{SO_5^{\bullet -} + SO_3^{2-} \rightleftharpoons SO_4^{2-} + SO_4^{\bullet -}} \quad \text{(R4)}$$

$$\mathbf{SO_3^{2-} + SO_5^{2-} \rightleftharpoons 2\,SO_4^{2-}} \quad \text{(R5)}$$

$$\mathbf{SO_4^{\bullet -} + SO_3^{2-} \rightleftharpoons SO_4^{2-} + SO_3^{\bullet -}} \quad \text{(R6)}$$

A similar mechanism can be written for the oxidation of S(IV) in the form of bisulfite, HSO_3^-. In this mechanism, transition metals with multiple stable oxidation states, such as iron, manganese, copper, cobalt and vanadium, can catalyze the oxidation of S(IV) with iron and manganese being the most efficient catalysts under atmospheric conditions.[19]

Besides the presence of transition metals ions, there are a variety of other factors that can potentially influence sulfur oxidation reaction pathways and kinetics. Atmospheric conditions readily change with factors such as pollution or regional emissions, acidity, relative humidity, temperature, and solar radiation, all of which can influence reaction pathways and kinetics. For example, cloud water is generally acidic, with a pH around 5, but more alkaline cloud pH values around 7 have been reported and very low pH aqueous environments within aerosols (pH less than 3) have been proposed as well.[1,9,20–24] Additionally, pollution and other regional emissions sources will impact

the amount and type of organic compounds present. Previous studies have shown that the presence of organics can inhibit the oxidation of S(IV)[25,26] and, depending on the type of organic, can also lead to the formation of organosulfur compounds.[27–33] Interestingly, results from recent studies examining the formation of organosulfates and other organosulfur compounds suggest that the reaction rates and mechanisms can be affected by numerous factors including physical state of the reactants, nature of the double bonds (cis, trans, terminal), use of irradiation, the presence of an acid group, and the presence of transition metal ions.[28,32,33] These results highlight the variables that can influence atmospheric chemical processes leading to not only impacted reaction kinetics and pathways but also the formation of new products.

Due to the complexity of the atmosphere, such as the wide range of acidity and presence of salts, metals, and organics in atmospheric cloud or fog water, it is imperative to understand the influence these variables can have on atmospheric processes like sulfur oxidation. Therefore, in the current study, we aim to gain a better understanding of the influences of these different scenarios by investigating the influence of acidity, ionic strength, and the presence of organics on the oxidation of inorganic S(IV) as sulfite/bisulfite to S(VI) as sulfate/bisulfate in the presence and absence of transition

metals. Overall, understanding processes that influence sulfur chemistry is crucial to being able to accurately model atmospheric chemical processes.

6.3. Materials and Methods

6.3.1. Reagents and materials

Aqueous sulfur (IV) solutions were prepared using Na_2SO_3 (LabChem). The pH of each S(IV) solution was controlled using hydrochloric acid (HCl, Fisher). Solid iron oxide (γ-Fe_2O_3, Alfa Aesar) and manganese oxide (Mn_2O_3, 99.2%, US Research Nanomaterials Inc) were used as the sources of transition metal ions. The Brunauer-Emmett-Teller (BET) surface area of γ-Fe_2O_3 and Mn_2O_3 were measured as 56 ± 1 and 9.2 ± 0.6 m^2 g^{-1}, respectively. The ionic strength was controlled using NaCl (Fisher). Aqueous solutions containing organics were prepared from glyoxal (40 wt%, Acros) or methacrolein (MACR, 96%, Alfa Aesar). For ion chromatography analysis, VeriSpec Sulfite and VeriSpec Sulfate (Ricca Chemical) were used to prepare S(IV) and S(VI) standard solutions, respectively. All aqueous solutions were prepared with ultra-pure water (Thermo, Barnsted EasyPure-II; ≥18.2 MΩ cm resistivity).

6.3.2. Aqueous phase reactor

Bulk aqueous phase reactions were carried out using custom water-jacketed glass reactors described in detail in Chapter 2. Each reactor is filled with 0.2 mM S(IV) solution, controlled to pH 3, 5, or 7, for a total volume of 50 mL. Powdered forms of the metal oxides were added to the reactors using a 1 g/L solid loading of iron or manganese oxide. For experiments investigating ionic strength, the ionic strength of each S(IV) solution was controlled to 1 mM or 50 mM. For experiments investigating the influence of organics, 0.2

mM solutions of glyoxal or methacrolein were used and each reactor contained a 1:1 ratio of S(IV) solution to organic solution. Throughout the duration of the experiments, temperature was held constant at 25 °C and the reactors were continuously stirred and remained fully sealed to exclude any additional air from taking part in the reaction. The temperature in the reactor was controlled using a refrigerated water circulator (Julabo) to flow water, at a specified temperature, through each water-jacketed reactor. Aliquots were extracted every 5 minutes for a total of 30 minutes. After extraction, each 1.5 mL aliquot was filtered with a 0.2 μm polytetrafluoroethylene (PTFE) filter to remove any solid particles then added to a vial containing 45 μL of 0.1 M formaldehyde (HCHO, Fisher) to quench the reaction.

6.3.3. Detection of reactants and products

Inorganic S(IV) and S(VI) concentrations were determined by ion chromatography (IC, Dionex ICS2000). The IC was equipped with a Dionex AS25 analytical column, which allowed for sulfite and sulfate peaks to be completely separated using the following gradient program: the concentration of eluent (KOH, Thermo Scientific) increased from 15 mM to 36 mM at 0–20 min, held at 36 mM for 10 min, and then decreased to 10 mM from 30 min to 35 min. Throughout each run, the eluent flow rate was held at 0.25 mL min^{-1} with a column temperature of 30 °C. For each analysis, an injection volume of 25 μL was used for each sample. Additionally, for each experiment, 0.1, 1, 5 and 10 ppm standard

solutions were prepared for S(IV) and S(VI) from which calibration curves were created to determine S(IV) and S(VI) concentrations.

6.4. Results and Discussion

6.4.1. Influence of Different Oxide Particles as Transition Metal Ion Sources

The results of the oxidation of S(IV) in the absence and in the presence of iron or manganese are shown in Figure 6.1 with corresponding rate constants, *k*, summarized in Table 6.1. Figure 6.1 shows that, at a constant pH, iron and manganese oxides enhance the rate of S(IV) loss. This is also reflected in the rate constants where the rate of S(IV) loss in the presence of the metal oxides is at least an order of magnitude greater than in the absence. The extent of the catalytic effect varies with each metal oxide and with acidity. Additionally, the catalytic effect of the formation of sulfate in the presence of the transition metal oxides can be seen spectroscopically. For example, Figure 6.2 shows the ATR-FTIR spectra for the oxidation of S(IV) on thin films of iron or manganese oxides. When these metal oxide films are present, there is an enhancement in the growth of the sulfate stretching mode near 1100 cm^{-1} indicating a catalytic effect on the transformation of S(IV) to S(VI) (i.e. sulfite to sulfate) compared to when these oxide films are not present (control experiments).

The oxidation of S(IV) was also examined when both iron and manganese oxides are present in a 1:1 ratio. The concentration of S(IV) was below the limit of detection for the instrument for some trials and therefore the total amount of S(VI) (i.e. sulfate) after reaction was examined. When both metal oxides are present, the rate of sulfate formation increases as pH increases. Additionally, when both metals are present in a 1:1 mixture, the

total amounts of S(VI) formed after 30 minutes of reaction were ca. 9, 6, and 3 times greater than when no metals are present for pH 3, 5, and 7, respectively. The increased concentrations of S(VI) after 30 minutes confirms there is a catalytic effect of iron and manganese on the oxidation of S(IV) to inorganic S(VI). Furthermore, the total amount of S(VI) formed after 30 minutes of reaction was greater in the presence of the iron/manganese mixture as compared to when only iron or manganese is present which may suggest a synergistic catalytic effect which would be consistent with previous studies.[12,26,34–37]

6.4.2. Influence of pH

The results of the oxidation of S(IV) in the absence of any metal oxides and in the presence of iron or manganese oxide as a function of pH are shown in Figure 6.1. When no metal oxide is present the rate of S(IV) loss by oxidation with O_2 increases as pH increases. However, when iron is present, the reaction is catalyzed, and extent of the catalysis increases at lower pH showing a greater catalytic effect at pH 3 as compared to pH 7, consistent with earlier studies.[12,38] Additionally, the presence of manganese oxide catalyzed the oxidation of S(IV) and the rate of S(IV) loss decreases under strongly acidic conditions. The increased rate of S(IV) loss with increasing pH observed for the oxidation of S(IV) in the absence of any transition metals may be explained by a change in the predominate S(IV) species present at each pH (see Figure 1.3 in Chapter 1). At pH 3 and 5 bisulfite (HSO_3^-) is the main S(IV) species but at pH 7 sulfite (SO_3^{2-}) is the primary S(IV) species. Sulfite is easier oxidized by oxygen than bisulfite and bisulfite has been shown to be 20-40 times less reactive than sulfite.[12,39] For example, Ali et al. report the reactivity order $SO_3^{2-} > HSO_3^- > SO_2 \bullet H_2O$ for the oxidation of S(IV) by a cobalt(III) complex.[40]

Similarly, the rate of S(IV) loss in the presence of manganese increased from pH 3 to 5, but then decreased slightly from pH 5 to 7. Similar trends in acidity for the manganese catalyzed oxidation of S(IV) have been reported and is explained by differences in the ratios of S(IV) species present at each pH.[41,42] The increased catalytic activity for iron at lower pH values may be attributed to the contribution from the homogeneous reaction with iron. Under acidic conditions, iron can be leached from solid particles and participate in homogeneous catalysis with iron ions in addition to the heterogeneous catalysis with solid iron particles.[38,43–46]

6.4.3. Influence of Ionic Strength

The influence of ionic strength on the iron or manganese catalyzed oxidation of S(IV) is summarized in Figure 6.3. In Figure 6.3, the change in S(IV) concentration as a function of time, for both iron and manganese, at ionic strengths of 0, 1, and 50 mM are shown. At an ionic strength of 1 mM the iron-catalyzed oxidation of S(IV) is enhanced. Additionally, at 1 mM ionic strength, the rate of S(IV) loss increases as pH decreases similar to the case when there is no ionic strength control. However, when the ionic strength is increased to 50 mM, catalytic activity of iron is suppressed, as compared to the lower ionic strength, and at pH 3 and 7 iron catalysis is shutdown. Similar results of reaction rate acceleration or inhibition based on anion concentration have been previously reported.[12,47–49] For example, Dasgupta et al. report an increase in reaction rate with increasing chloride concentration up to a certain point before decreasing again.[47] Additionally, Brandt et al.

report a higher observed rate constant at higher ionic strength for the iron(III) catalyzed autoxidation of S(IV) similar to what is observed here.[50]

The manganese catalyzed oxidation of S(IV), shown in Figure 6.3b, is inhibited by an ionic strength of 1 mM. This inhibition effect is accentuated when the ionic strength is further increased to 50 mM, resulting in a shutdown of any catalytic behavior by manganese under all three pH conditions. This observed inhibition effect on the oxidation rate of S(IV) is consistent with previous studies.[41,51,52] For example, Martin and Hill[53] found that the reaction rate of the manganese catalyzed oxidation of S(IV) slowed as the ionic strength of the reaction medium increased.

The influence of ionic strength on the oxidation of S(IV) was also examined when both iron and manganese are present. However, because the concentration of S(IV) was below the limit of detection for these experiments, the formation of S(VI) was examined instead. Figure 6.4 shows the change in concentration of sulfate (plotted as $1-e^{-kt}$) as a function of time for 0, 1, and 50 mM ionic strength at pH 3, 5, and 7. At pH 5 and 7, the initial rate of S(VI) formation decreased with 1 mM ionic strength and this inhibition effect was enhanced as ionic strength increased. However, at pH 3 1 mM ionic strength showed very little influence on the rate of S(VI) formation but under high ionic strength conditions the rate of S(VI) formation increased.

The effect of ionic strength on the transition metal catalyzed oxidation of S(IV) reported in the literature varies across different studies.[12,47–49,51–53] While the influence of ionic strength on reaction rate is complex and the reasons for enhancement or inhibition are not well understood, one possible explanation is that ionic strength affects reaction rate

through effects on the activity coefficients of reactants and products.[49,52] Related through the extended Debye-Hückel equation, increasing ionic strength influences the activity coefficients thereby impacting the reaction rate constant.[48,49,52] Additionally, Tursic et al. report that the inhibition effect observed for the manganese catalyzed S(IV) oxidation in an NaCl medium is due to both the primary kinetic salt effect and the ability of Cl^- to act as a radical scavenger for the SO_4^- radical thereby reducing the concentration of the catalytically active species and inhibiting the reaction (reactions R4 and R6 mentioned above).[48] Furthermore, Dasgupta et al. explains the accelerated reaction rate at low chloride concentrations but inhibited rate at higher chloride concentrations by a shift in complexation with chloride at higher concentrations at the expense of complexation with sulfite.

6.4.4. Influence of Organics

The influence of organics on the oxidation of S(IV) was also examined. Specifically, the effects of glyoxal and methacrolein were examined on the oxidation of S(IV) in the presence and absence of iron or manganese under three pH conditions. The results are summarized in Figure 6.5. Firstly, in conjunction with our previous work, in the presence of glyoxal at pH 3 and 5, the iron catalyzed oxidation of inorganic S(IV) to inorganic S(VI) is inhibited.[25] However, at pH 7 this oxidation reaction is slightly enhanced. Similarly, the presence of MACR also enhances the rate of S(IV) loss at pH 7 as well as at pH 5. At pH 3 the presence of MACR has a similar inhibitory effect on the iron-catalyzed oxidation of S(IV) as glyoxal. Additionally, a trend in acidity is observed in the presence of MACR showing an increase is the rate of S(IV) loss as pH decreases. For glyoxal, the rate of S(IV) loss at pH 5 and 7 are similar and both slower than the rate at pH

3 exhibiting a similar inverse relationship between the rate of S(IV) loss and pH. The influence of organics on the manganese catalyzed oxidation of S(IV) is summarized in Figure 6.5b. In the presence of either glyoxal or MACR, the rate of S(IV) loss is inhibited under all three pH conditions. The inhibition effect is greatest at pH 3 where catalytic activity is essentially shutdown in the presence of both glyoxal and MACR. At pH 5 and 7 glyoxal appears to have a stronger inhibition effect than MACR. Both organics, at each pH, exhibit some sort of effect on the oxidation of S(IV), whether an inhibition or enhancement, which may be ascribed to the ability of the organic compounds to scavenge or react with radicals. Previous work by Brandt et al. has shown that radical scavengers can influence the iron catalyzed oxidation of S(IV).[50] Glyoxal and MACR have both been shown to react with sulfoxy radicals (SO_3^-, SO_4^-, SO_5^-) forming organosulfur compounds and their oligomers rather than following reactions R6.1-R6.6 to form sulfate.[25,28,54] Similarly, Meena et al. report the inhibition of sulfur(IV) oxidation via scavenging of sulfate radicals when volatile organic compounds are present.[55]

In addition to examining the rate of S(IV) loss for the influence organics have on the oxidation of S(IV), the relative amount of organosulfur compounds formed was calculated. Table 6.2 summarizes the percentage of organosulfur compounds formed, relative to the total amount of sulfur, at pH 3, 5, and 7 in the presence of manganese, iron, or a 1:1 mixture of manganese and iron. The amount of organosulfur compounds formed is determined by the difference between the concentration of inorganic sulfur (S(IV) + S(VI)) and total sulfur. More details on the organosulfur calculations can be found in our previous work.[54] Approximately 10-25% more S(IV) is converted to organosulfur compounds in the presence of iron as compared to manganese which may indicate that iron

is a more efficient catalyst for forming organosulfur compounds. Interestingly, when iron and manganese are both present, the percent of organosulfur compounds formed is less than that formed when only iron is present indicating there is no enhancement due to synergistic effects on the formation of organosulfur compounds. In fact, in most cases, the percentage of organosulfur compounds formed when both iron and manganese were present is less than when only manganese is present. Nonetheless, the relatively high yields indicate that these pathways with iron and manganese for the formation of organosulfur compounds may be important in the atmosphere. However, as discussed in our previous work, it should be noted that the retention time of unreacted sulfite, in the form of MACR-S(IV), is different than that of free S(IV) resulting in an underestimation of residual inorganic sulfite and therefore an overestimation of the amount of organosulfur compounds formed.[54] This is not an issue in the case of glyoxal because the retention time of glyoxal-S(IV) adducts is the same as free S(IV).

The influence of organics on S(IV) oxidation in the presence of both iron and manganese oxides were also examined. A direct comparison of the influence organics have on the oxidation of S(IV) cannot be made since the amount of S(IV) is below the limit of detection for the "blank" synergism (i.e. S(IV) oxidation with a 1:1 ratio of iron and manganese with no organics present). Therefore, the total amounts of S(VI) (i.e. inorganic sulfate) after 30 minutes of reaction were compared. Figure 6.6 shows the total amount of S(VI), after 30 minutes of reaction, in the absence and presence of glyoxal or MACR at pH 3, 5, and 7. The results shown in Figure 6.6 clearly depict the inhibitory effect the presence of glyoxal and MACR have on the oxidation of S(IV) to inorganic S(VI). When no organic compounds are present, the total amount of S(VI) is approximately 1.6-2.3 times greater

than when either glyoxal or MACR is present. More inorganic S(VI) was measured at pH 3 in the presence of glyoxal and MACR, as compared to pH 5 and 7, indicating that the catalytic effect of iron and manganese is strongest at lower pH despite the overall inhibition from the organic compounds. This observed trend in acidity, increase in rate of oxidation as pH decreases, is similar to that observed when only iron is present which may suggest that the oxidation is dominated by iron when both metals are present.

6.5. Conclusions

The data presented here show that acidity, ionic strength, and presence of organics can have an influence on the kinetics of inorganic S(IV) oxidation to inorganic S(VI). In particular, high ionic strength conditions and the presence of organics can significantly inhibit the oxidation of S(IV). The impact of solution pH is likely due to changes in S(IV) speciation and contributions to transition metal ion mechanisms due to solubility of these oxide minerals. Further studies should be conducted to examine influences over a full range of ionic strengths and other organic compounds in addition to exploring how the variables investigated here influence S(IV) oxidation catalyzed by other minerals. Gaining a more complete understanding of the variables that influence key atmospheric processes, such as sulfur oxidation, is key to reducing the uncertainties in atmospheric chemistry models.

6.6. Acknowledgements

This material is based upon work supported by the National Science Foundation under grant AGS1702488. The authors also acknowledge the use of instruments within the

Environmental Complex Analysis Laboratory located in the Department of Chemistry and Biochemistry on the University of California, San Diego campus.

Chapter 6 is in preparation: Coddens, E. M., Sony, R., Grassian, V. H. Aqueous Phase Catalytic Oxidation of S(IV): Influence of pH, Ionic Strength, and the Presence of Organic Compounds. The dissertation author was the primary investigator and author of this paper.

6.7. Figures

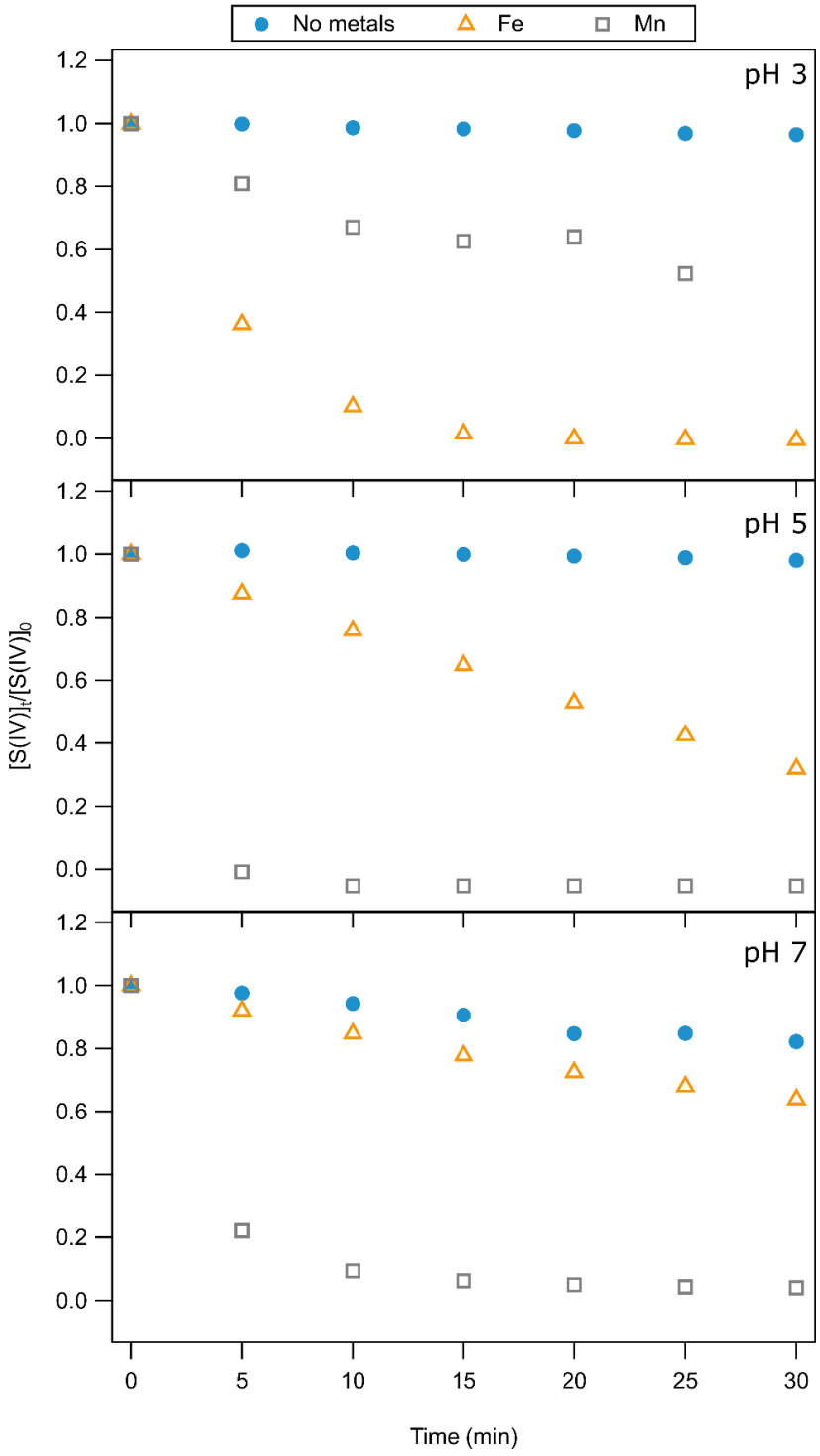

Figure 6.1: Time dependence of S(IV) oxidation in the presence of O_2 at pH 3, 5, and 7 in the absence of any metals (blue circles) and in the presence of iron (orange triangles) or manganese (grey squares).

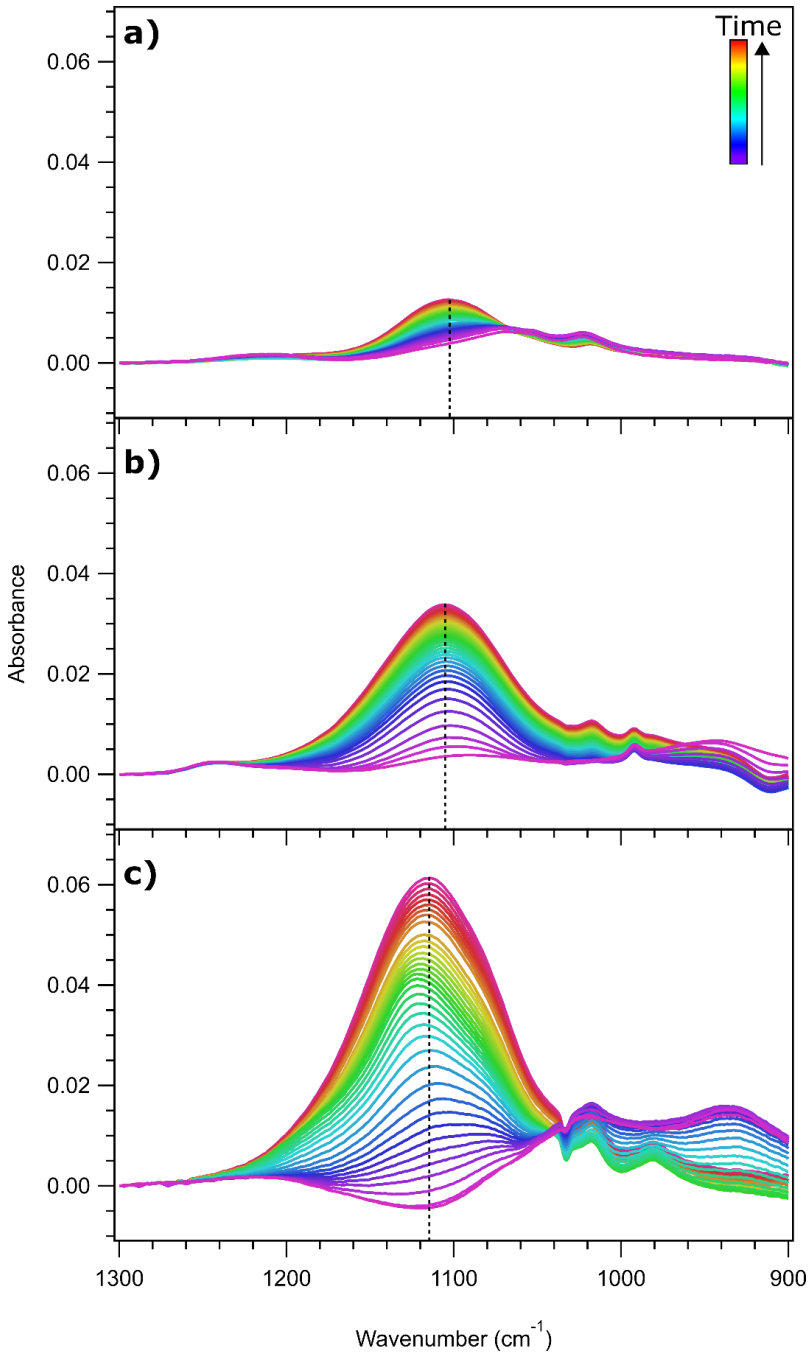

Figure 6.2: ATR-FTIR spectra for the oxidation of S(IV) a) in the absence of metals and in the presence of b) manganese or c) iron. The dashed line marks the sulfate stretching mode at ~1100 cm^{-1} for each reaction. It should be noted that ATR-FTIR experiments were carried out with a higher concentration of S(IV) (50 mM Na_2SO_3, pH 5). Details of the ATR-FTIR experiments can be found in Chapter 2.

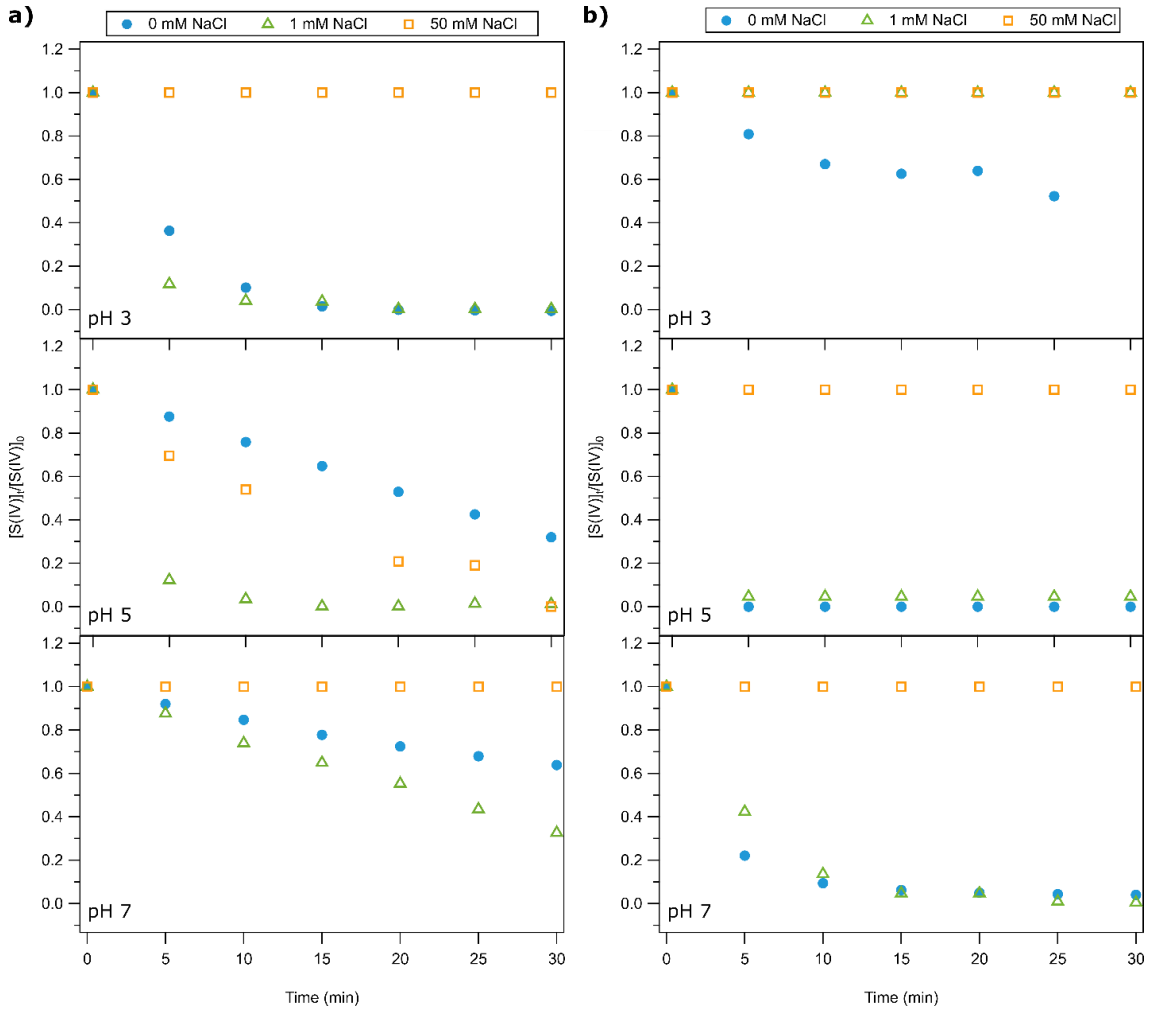

Figure 6.3: Influence of ionic strength on the transition metal catalyzed oxidation of S(IV) at pH 3, 5 and 7 in the presence of a) iron and b) manganese. Ionic strength is varied using 0 mM (blue circles), 1 mM (green triangles), or 50 mM (orange squares) sodium chloride.

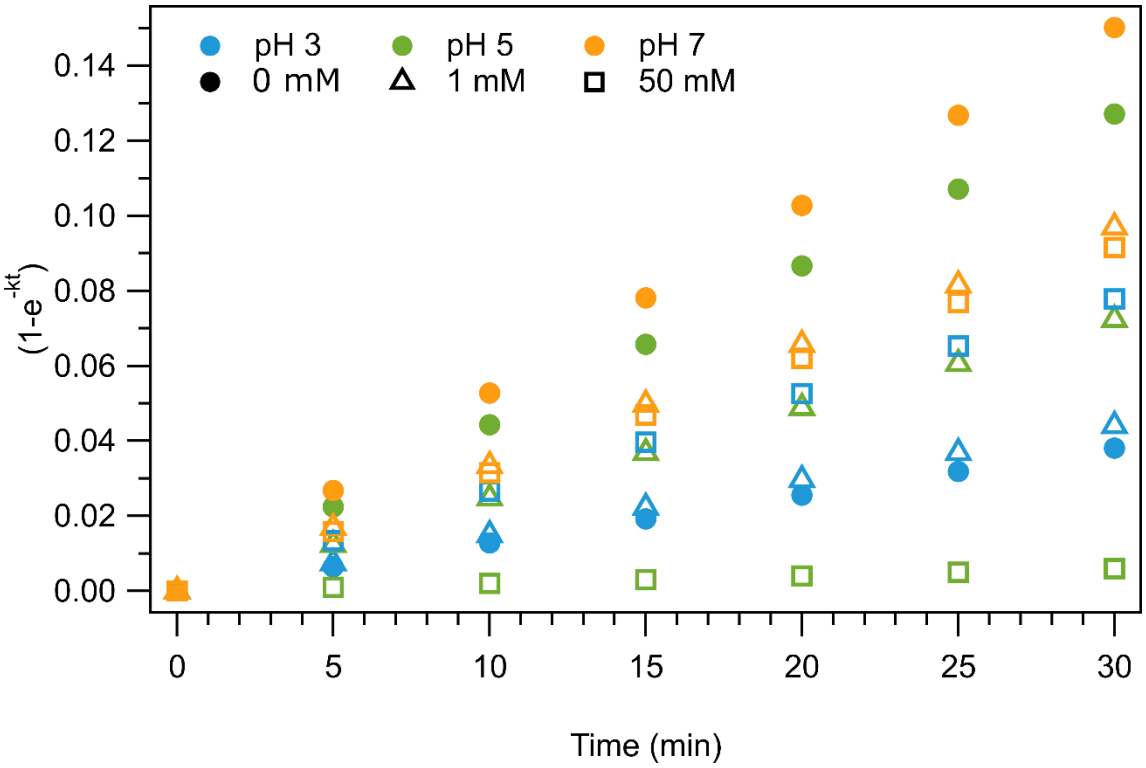

Figure 6.4: Plot of $1-e^{-kt}$ for sulfate formation in the presence of a 1:1 mixture of iron and manganese oxides at pH 3 (blue), pH 5 (green), and pH 7 (orange) with ionic strength of 0 mM (closed circles), 1 mM (open triangles) or 50 mM (open squares).

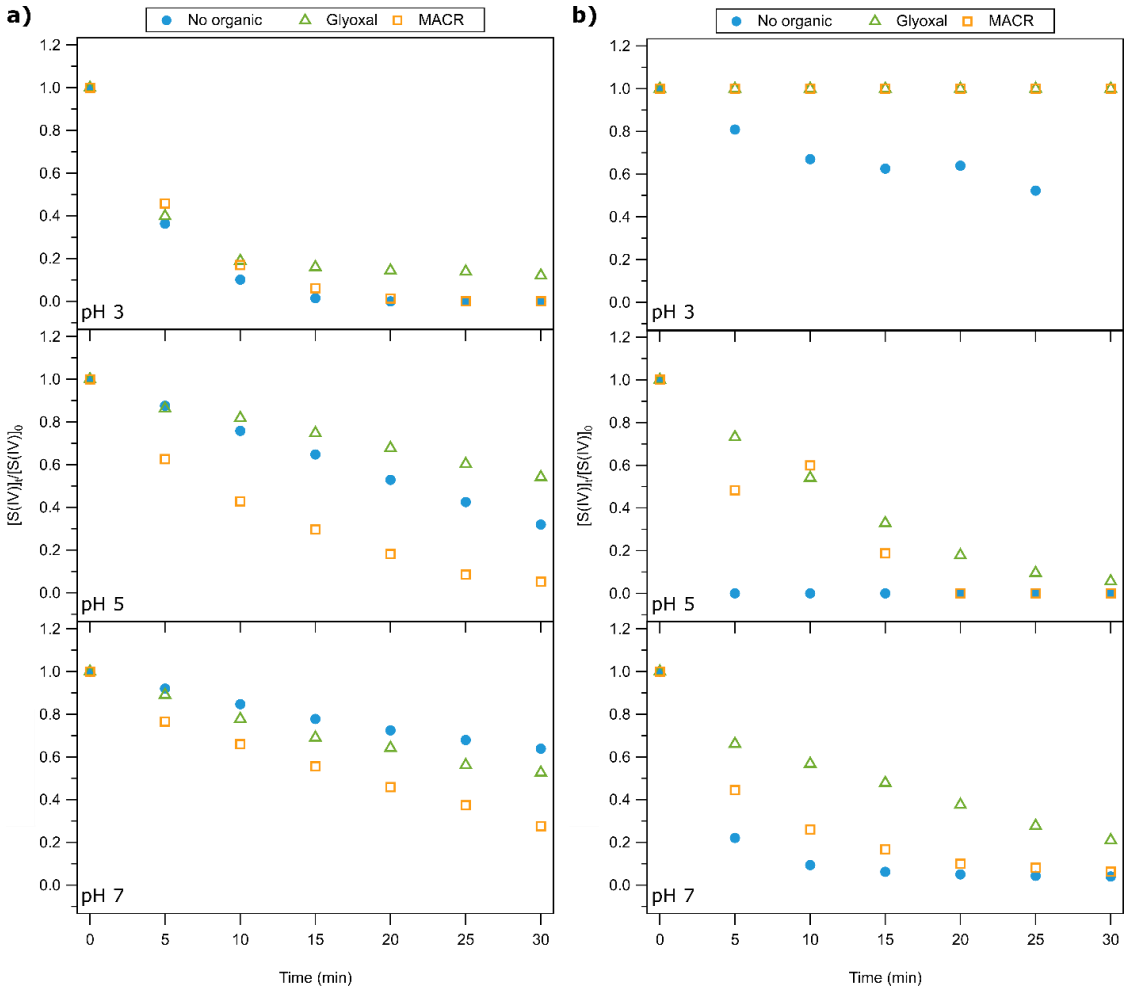

Figure 6.5: Influence of organics (glyoxal or methacrolein) on the transition metal catalyzed oxidation of S(IV) at pH 3, 5 and 7 in the presence of a) iron and b) manganese.

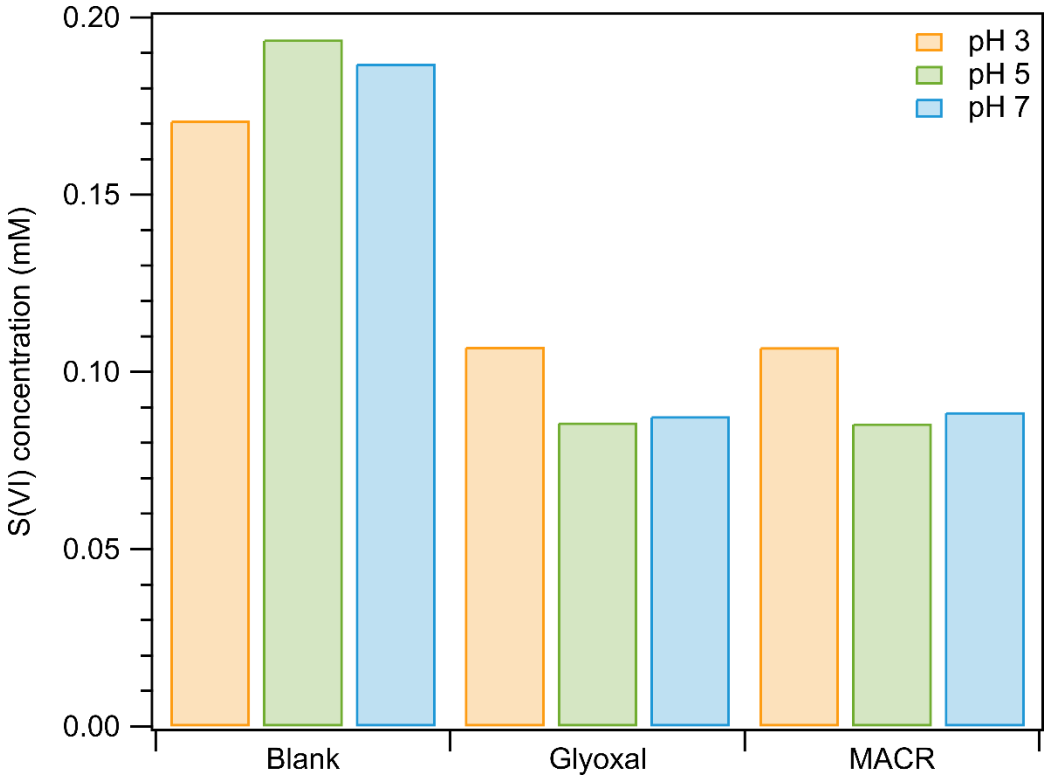

Figure 6.6: Total S(VI) concentration after 30 minutes of reaction formed from the oxidation of S(IV) in the presence of iron and manganese in a 1:1 ratio at pH 3 (orange), 5 (green), and 7 (blue) in the presence of glyoxal, MACR or no organics (blank).

6.8. Tables

Table 6.1: Observed rate constants, *k*, for the oxidation of S(IV) in the presence and absence of transition metals.

	k (s^{-1})	k ($mM\ s^{-1}$)	k ($mM^{-1}\ s^{-1}$)
	pH 3	pH 5	pH 7
No metals	$1.25 \pm 0.08 \times 10^{-3}$	$1.17 \pm 0.05 \times 10^{-3}$	$7.70 \pm 0.6 \times 10^{-3}$
Iron	$2.76 \pm 0.3 \times 10^{-1}$	$2.27 \pm 0.03 \times 10^{-2}$	$1.90 \pm 0.02 \times 10^{-2}$
Manganese	$2.29 \pm 0.4 \times 10^{-2}$	$2.15 \pm 0.8 \times 10^{-2}$	$8.30 \pm 0.6 \times 10^{-1}$

Table 6.2: Percentage of organosulfur compounds formed relative to the total amount of sulfur at pH 3, 5, and 7 in the presence of manganese, iron, or a 1:1 mixture of manganese and iron.

	Mn	**Mn/Fe**	**Fe**
		pH 3	
Glyoxal	63%	59%	88%
MACR	68%	59%	86%
		pH 5	
Glyoxal	63%	67%	85%
MACR	64%	67%	85%
		pH 7	
Glyoxal	66%	65%	84%
MACR	75%	66%	86%

6.9. References

(1) Seinfeld, J. H.; Pandis, S. N. *Atmospheric Chemistry and Physics : From Air Pollution to Climate Change*, 2nd ed.; John Wiley & Sons, Inc.: Hoboken, 2006.

(2) Manahan, S. E. *Environmental Chemistry*, 7th ed.; Lewis : Boca Raton, 1999.

(3) Baird, C.; Cann, M. *Environmental Chemistry*, 5th ed.; W. F. Freeman: New York, 2012.

(4) Huang, X.; Song, Y.; Zhao, C.; Li, M.; Zhu, T.; Zhang, Q.; Zhang, X. Pathways of Sulfate Enhancement by Natural and Anthropogenic Mineral Aerosols in China. *J. Geophys. Res. Atmos.* **2014**, *119*, 14165–14179.

(5) Ervens, B. Modeling the Processing of Aerosol and Trace Gases in Clouds and Fogs. *Chem. Rev.* **2015**, *115*, 4157–4198.

(6) Luo, C.; Wang, Y.; Mueller, S.; Knipping, E. Diagnosis of an Underestimation of Summertime Sulfate Using the Community Multiscale Air Quality Model. *Atmos. Environ.* **2011**, *45*, 5119–5130.

(7) He, H.; Wang, Y.; Ma, Q.; Ma, J.; Chu, B.; Ji, D.; Tang, G.; Liu, C.; Zhang, H.; Hao, J. Mineral Dust and NOx Promote the Conversion of SO2 to Sulfate in Heavy Pollution Days. *Sci. Rep.* **2014**, *4*.

(8) Wang, Y.; Zhang, Q.; Jiang, J.; Zhou, W.; Wang, B.; He, K.; Duan, F.; Zhang, Q.; Philip, S.; Xie, Y. Enhanced Sulfate Formation during China's Severe Winter Haze Episode in January 2013 Missing from Current Models. *J. Geophys. Res.* **2014**, *119*, 10,425-10,440.

(9) Xue, J.; Yuan, Z.; Griffith, S. M.; Yu, X.; Lau, A. K. H.; Yu, J. Z. Sulfate Formation Enhanced by a Cocktail of High NOx, SO2, Particulate Matter, and Droplet PH during Haze-Fog Events in Megacities in China: An Observation-Based Modeling Investigation. *Environ. Sci. Technol.* **2016**, *50*, 7325–7334.

(10) Van Donkelaar, A.; Martin, R. V.; Brauer, M.; Boys, B. L. Use of Satellite Observations for Long-Term Exposure Assessment of Global Concentrations of Fine Particulate Matter. *Environ. Health Perspect.* **2015**, *123*, 135–143.

(11) Sullivan, R. C.; Guazzotti, S. A.; Sodeman, D. A.; Prather, K. A. Direct Observations of the Atmospheric Processing of Asian Mineral Dust. *Atmos. Chem. Phys.* **2007**, *7*, 1213–1236.

(12) Brandt, C.; van Eldik, R. Transition Metal-Catalyzed Oxidation of Sulfur(IV) Oxides. Atmospheric-Relevant Processes and Mechanisms. *Chem. Rev.* **1995**, *95*, 119–190.

(13) Harris, E.; Sinha, B.; Van Pinxteren, D.; Tilgner, A.; Fomba, K. W.; Schneider, J.; Roth, A.; Gnauk, T.; Fahlbusch, B.; Mertes, S.; Taehyoung, L.; Collett, J.; Foley, S.; Borrmann, S.; Hoppe, P.; Herrmann, H. Enhanced Role of Transition Metal Ion

Catalysis During In-Cloud Oxidation of SO 2. *Science (80-.).* **2013**, *340*, 727–730.

(14) Alexander, B.; Park, R. J.; Jacob, D. J.; Gong, S. Transition Metal-Catalyzed Oxidation of Atmospheric Sulfur: Global Implications for the Sulfur Budget. *J. Geophys. Res.* **2009**, *114*, D02309.

(15) Li, J.; Wang, Z.; Zhuang, G.; Luo, G.; Sun, Y.; Wang, Q. Mixing of Asian Mineral Dust with Anthropogenic Pollutants over East Asia: A Model Case Study of a Super-Duststorm in March 2010. *Atmos. Chem. Phys.* **2012**, *12*, 7591–7607.

(16) Deguillaume, L.; Leriche, M.; Desboeufs, K.; Mailhot, G.; George, C.; Chaumerliac, N. Transition Metals in Atmospheric Liquid Phases: Sources, Reactivity, and Sensitive Parameters. *Chem. Rev.* **2005**, *105*, 3388–3431.

(17) Bäckström, H. L. J. Der Kettenmechanismus Bei Der Autoxydation von Natriumsulfitlösungen. *Zeitschrift für Phys. Chemie* **1934**, *25B*, 122–138.

(18) Opletal, M.; Novotný, P.; Rejl, F. J.; Moucha, T.; Kordač, M. Kinetics of Catalytic Oxidation of Sulfite in Diluted Aqueous Solutions. *Chem. Eng. Technol.* **2015**, *38*, 1919–1924.

(19) Berglund, J.; Elding, L. I. Manganese-Catalysed Autoxidation of Dissolved Sulfur Dioxide in the Atmospheric Aqueous Phase. *Atmos. Environ.* **1995**, *29*, 1379–1391.

(20) Khemani, L. T.; Momin, G. A.; Naik, M. S.; Prakasa Rao, P. S.; Safai, P. D.; Murty, A. S. R. Influence of Alkaline Particulates on PH of Cloud and Rain Water in India. *Atmos. Environ.* **1987**, *21*, 1137–1145.

(21) Weathers, K. C.; Likens, G. E.; Bormann, F. H.; Eaton, J. S.; Bowden, W. B.; Andersen, J. L.; Cass, D. A.; Galloway, J. N.; Keene, W. C.; Kimball, K. D.; Huth, P.; Smiley, D. A Regional Acidic Cloud/Fog Water Event in the Eastern United States. *Nature* **1986**, *319*, 657–658.

(22) Pöschl, U. Atmospheric Aerosols: Composition, Transformation, Climate and Health Effects. *Angew. Chemie Int. Ed.* **2005**, *44*, 7520–7540.

(23) Zhang, X. Y.; Wang, Y. Q.; Niu, T.; Zhang, X. C.; Gong, S. L.; Zhang, Y. M.; Sun, J. Y. Atmospheric Aerosol Compositions in China: Spatial/Temporal Variability, Chemical Signature, Regional Haze Distribution and Comparisons with Global Aerosols. *Atmos. Chem. Phys.* **2012**, *12*, 779–799.

(24) Ding, J.; Zhao, P.; Su, J.; Dong, Q.; Du, X. Aerosol PH and Its Influencing Factors in Beijing. *Atmos. Chem. Phys. Discuss.* **2018**.

(25) Coddens, E. M.; Huang, L.; Wong, C.; Grassian, V. H. Influence of Glyoxal on the Catalytic Oxidation of S(IV) in Acidic Aqueous Media. *ACS Earth Sp. Chem.* **2019**, *3*, 142–149.

(26) Ibusuki, T.; Takeuchi, K. Sulfur Dioxide Oxidation by Oxygen Catalyzed by Mixtures of Manganese(II) and Iron(III) in Aqueous Solutions at Environmental Reaction Conditions. *Atmos. Environ.* **1987**, *21*, 1555–1560.

(27) Surratt, J. D.; Gómez-González, Y.; Chan, A. W. H.; Vermeylen, R.; Shahgholi, M.; Kleindienst, T. E.; Edney, E. O.; Offenberg, J. H.; Lewandowski, M.; Jaoui, M.; Maenhaut, W.; Claeys, M.; Flagan, R. C.; Seinfeld, J. H. Organosulfate Formation in Biogenic Secondary Organic Aerosol. *J. Phys. Chem. A* **2008**, *112*, 8345–8378.

(28) Huang, L.; Cochran, R. E.; Coddens, E. M.; Grassian, V. H. Formation of Organosulfur Compounds through Transition Metal Ion-Catalyzed Aqueous Phase Reactions. *Environ. Sci. Technol. Lett.* **2018**, *5*, 315–321.

(29) Rudziński, K. J.; Gmachowski, L.; Kuznietsova, I. Reactions of Isoprene and Sulphoxy Radical-Anions – a Possible Source of Atmospheric Organosulphites and Organosulphates. *Atmos. Chem. Phys.* **2009**, *9*, 2129–2140.

(30) Shang, J.; Passananti, M.; Dupart, Y.; Ciuraru, R.; Tinel, L.; Rossignol, S.; Perrier, S.; Zhu, T.; George, C. SO2 Uptake on Oleic Acid: A New Formation Pathway of Organosulfur Compounds in the Atmosphere. *Environ. Sci. Technol. Lett.* **2016**, *3*, 67–72.

(31) Shen, X.; Wu, H.; Zhao, Y.; Huang, D.; Huang, L.; Chen, Z. Heterogeneous Reactions of Glyoxal on Mineral Particles: A New Avenue for Oligomers and Organosulfate Formation. *Atmos. Environ.* **2016**, *131*, 133–140.

(32) Schmidt, M.; Jansen van Beek, S. M.; Abou-Ghanem, M.; Oliynyk, A. O.; Locock, A. J.; Styler, S. A. Production of Atmospheric Organosulfates via Mineral-Mediated Photochemistry. *ACS Earth Sp. Chem.* **2019**, *3*, 424–431.

(33) Passananti, M.; Kong, L.; Shang, J.; Dupart, Y.; Perrier, S.; Chen, J.; Donaldson, D. J.; George, C. Organosulfate Formation through the Heterogeneous Reaction of Sulfur Dioxide with Unsaturated Fatty Acids and Long-Chain Alkenes. *Angew. Chemie Int. Ed.* **2016**, *55*, 10336–10339.

(34) Martin, L. R.; Good, T. W. Catalyzed Oxidation of Sulfur Dioxide in Solution: The Iron-Manganese Synergism. *Atmos. Environ. Part A, Gen. Top.* **1991**, *25*, 2395–2399.

(35) Reda, M. Homogeneous Catalytic Oxidation of Aqueous Sulfur(IV) by Transition Metal Ions, Part III: Effect of Iron(III), Copper(II) and Manganese (II) and Synergistic Catalysis. *Water Sci. Technol.* **1988**, *20*, 45–47.

(36) Peter, L.; Meyer, B. Preparation and Raman Spectra of Thallium(I) Disulfite and Thallium(I) Sulfite. *Inorg. Chem.* **1985**, *24*, 3071–3073.

(37) Coichev, N.; Bal Reddy, K.; van Eldik, R. The Synergistic Effect of Manganese (II) in the Sulfite-Induced Autoxidation of Metal Ions and Complexes in Aqueous Solution. *Atmos. Environ. Part A, Gen. Top.* **1992**, *26*, 2295–2300.

(38) Fuzzi, S. Study of Iron(III) Catalysed Sulphur Dioxide Oxidation in Aqueous Solution over a Wide Range of PH. *Atmos. Environ.* **1978**, *12*, 1439–1442.

(39) Anast, J. M.; Margerum, D. W. Trivalent Copper Catalysis of the Autoxidation of

Sulfite. Kinetics and Mechanism of the Copper(III/II) Tetraglycine Reactions with Sulfite. *Inorg. Chem.* **1981**, *20*, 2319–2326.

(40) Ali, M.; Saha, S. K.; Banerjee, P. Oxidation of Sulfite and Thiosulfate by the Cobalt(III) Complex of Dipicolinate in Aqueous Medium. *Bull. Chem. Soc. Jpn.* **1991**, *64*, 2497–2501.

(41) Huss, A.; Lim, P. K.; Eckert, C. A. Oxidation of Aqueous Sulfur Dioxide. 1. Homogeneous Manganese(II) and Iron(II) Catalysis at Low PH. *J. Phys. Chem.* **1982**, *86*, 4224–4228.

(42) Ibusuki, T.; Barnes, H. M. Manganese(II) Catalyzed Sulfur Dioxide Oxidation in Aqueous Solution at Environmental Concentrations. *Atmos. Environ.* **1984**, *18*, 145–151.

(43) Faust, B. C.; Hoffmann, M. R. Photoinduced Reductive Dissolution of α-Fe2O3 by Bisulfite. *Environ. Sci. Technol.* **1986**, *20*, 943–948.

(44) Rubasinghege, G.; Lentz, R. W.; Scherer, M. M.; Grassian, V. H. Simulated Atmospheric Processing of Iron Oxyhydroxide Minerals at Low PH: Roles of Particle Size and Acid Anion in Iron Dissolution. *Proc. Natl. Acad. Sci. U. S. A.* **2010**, *107*, 6628–6633.

(45) Chen, H.; Laskin, A.; Baltrusaitis, J.; Gorski, C. A.; Scherer, M. M.; Grassian, V. H. Coal Fly Ash as a Source of Iron in Atmospheric Dust. *Environ. Sci. Technol.* **2012**, *46*, 2112–2120.

(46) Gankanda, A.; Coddens, E. M.; Zhang, Y.; Cwiertny, D. M.; Grassian, V. H. Sulfate Formation Catalyzed by Coal Fly Ash, Mineral Dust and Iron(III) Oxide: Variable Influence of Temperature and Light. *Environ. Sci. Process. Impacts* **2016**, *18*, 1484–1491.

(47) Dasgupta, P. K.; Mitchell, P. A.; West, P. W. Study of Transition Metal Ion-S(IV) Systems. *Atmos. Environ.* **1979**, *13*, 775–782.

(48) Turšič, J.; Grgić, I.; Podkrajšek, B. Influence of Ionic Strength on Aqueous Oxidation of SO2 Catalyzed by Manganese. *Atmos. Environ.* **2003**, *37*, 2589–2595.

(49) Herrmann, H. Kinetics of Aqueous Phase Reactions Relevant for Atmospheric Chemistry. *Chem. Rev.* **2003**, *103*, 4691–4716.

(50) Brandt, C.; Fabian, I.; van Eldik, R. Kinetics and Mechanism of the Iron(III)-Catalyzed Autoxidation of Sulfur(IV) Oxides in Aqueous Solution. Evidence for the Redox Cycling of Iron in the Presence of Oxygen and Modeling of the Overall Reaction Mechanism. *Inorg. Chem.* **1994**, *33*, 687–701.

(51) Martin, L. R.; Hill, M. W. The Iron Catalyzed Oxidation of Sulfur: Reconciliation of the Literature Rates. *Atmos. Environ.* **1987**, *21*, 1487–1490.

(52) Cheng, Y.; Zheng, G.; Wei, C.; Mu, Q.; Zheng, B.; Wang, Z.; Gao, M.; Zhang, Q.; He, K.; Carmichael, G.; Poschl, U.; Su, H. Reactive Nitrogen Chemistry in Aerosol

Water as a Source of Sulfate during Haze Events in China. *Sci. Adv.* **2016**, *2*, e1601530.

(53) Robbin Martin, L.; Hill, M. W. The Effect of Ionic Strength on the Manganese Catalyzed Oxidation of Sulfur(IV). *Atmos. Environ.* **1987**, *21*, 2267–2270.

(54) Huang, L.; Coddens, E. M.; Grassian, V. H. Formation of Organosulfur Compounds from Aqueous Phase Reactions of S(IV) with Methacrolein and Methyl Vinyl Ketone in the Presence of Transition Metal Ions. *ACS Earth Sp. Chem.* **2019**.

(55) Meena, V. K.; Dhayal, Y.; Rathore, D. S.; Chandel, C. P. S.; Gupta, K. S. Inhibition of Atmospheric Aqueous Phase Autoxidation of Sulphur Dioxide by Volatile Organic Compounds: Mono-, Di- and Tri-Substituted Benzenes and Benzoic Acids. *Prog. React. Kinet. Mech.* **2017**, *42*, 111–125.

Chapter 7 Conclusions and Future Work

7.1.Synopsis

The overall goal of this dissertation was to perform laboratory studies designed to obtain a better understanding of the various factors influencing the oxidation of S(IV) to S(VI) in the atmosphere and to further develop the Aerosol Optical Tweezer system to study the chemistry within individual droplets. Aerosols are unique microenvironments, distinct from the bulk, and therefore result in differences between bulk and aerosol phase processes, such as reactivity and kinetics, acidity and interaction with light, due to the unique physiochemical properties of aerosols. By better understanding the chemical processes occurring within aerosols, as well as cloud or fog droplets, and the factors influencing them, we can help reduce some of the uncertainties in atmospheric models. This thesis aimed to do so with laboratory-based studies using spectroscopic and analytical techniques. First, the Aerosol Optical Tweezer coupled with cavity enhanced Raman spectroscopy was further developed as a method to study chemistry occurring within individual droplets. This technique was shown that this method can be used for studying changes within a droplet, such as monitoring pH changes induced by coalescence with acidic aerosol or changes in relative humidity, or reactions with the droplet, like monitoring the oxidation of S(IV) or reaction of glyoxal with sulfite. Then the influence of various atmospherically relevant conditions (presence of organic compounds, ionic strength, etc.) on the oxidation of S(IV) in the presence and absences of transition metals were examined. The findings from these studies can improve our understanding of the factors influencing sulfur oxidation chemistry and help to further develop a method to study the chemistry

occurring within individual aerosols in order to reduce some of the uncertainty associated with aerosols chemistry and improve atmospheric chemistry models. The following sections summarize the main conclusions from each study and introduce future studies.

7.2. Chapter 2 Summary

Chapter 2 provided details on the primary spectroscopic and analytical techniques used to qualitatively and quantitatively study sulfur oxidation chemistry in the experiments described herein. Attenuated total reflectance-Fourier transform infrared spectroscopy (ATR-FTIR) and confocal Raman spectroscopy were the primary spectroscopic techniques used. Additionally, bulk aqueous phase reactions were carried out using batch reactors in conjunction with analytical methods such as ion chromatography or inductively coupled plasma-mass spectrometry.

7.3. Chapter 3 Summary

Chapter 3 focused on the theoretical background and characterization of the Aerosol Optical Tweezer (AOT) system. Unlike the spectroscopic techniques described in Chapter 2, the AOT allowed for studies of individual optically levitated micron-sized droplets. This AOT system was developed to study the physiochemical properties and chemical reactions occurring within individual trapped droplets. Details of the forces involved in trapping a droplet, the components of cavity enhanced Raman spectroscopy, and calculations from whispering gallery modes were also presented. Various experiments to characterize the instrument were conducted. These include examining the influence of trapping lifetime on spectral intensity and the influence of exposure time on cavity enhanced Raman spectra. Other experiments included inducing changes in droplet pH

using coalescence, using relative humidity to alter size and acidity of droplets, and trapping droplets containing solid inclusions. These characterization experiments helped us to optimize and better understand the limitations of the instrument while also exploring methods that will be potentially useful in future studies.

7.4. Chapter 4 Summary

The acidity of aqueous aerosols, including cloud and fog droplets, is an important factor influencing the chemical processes that occur within these unique microenvironments. The microenvironment within individual droplets can be quite different from that of a bulk solution and therefore it was imperative to develop a method in which the pH of individual droplets could be measured and controlled. This was done by calculating and controlling changes in pH of a suspended micron sized droplet using an Aerosol Optical Tweezer coupled with cavity enhanced Raman spectroscopy. Specifically, we showed that the pH within individual aqueous aerosol droplets could be titrated via droplet coalescence with acidic aerosol. Using conjugate acid/base pairs to infer pH changes, the pH of trapped droplets was determined before and after coalescence with smaller droplets containing a strong acid. The pH within the trapped droplet was calculated using Specific Ion Interaction Theory (SIT). Results from this work showed that not only can the pH of individual droplets be calculated from the Raman spectra, but that control of droplet pH is attainable through coalescence with acid and can be applied to multiple chemical systems.

This study also highlighted the importance of applying appropriate theories to pH calculations. For example, Debye-Hückel theory is appropriate for low ionic strength

studies, whereas SIT is better suited for high ionic strength aerosols, such as those from polluted environments. The results presented here provided two validations of SIT calculations: i) SIT calculations for bulk solutions were in good agreement with the measured bulk pH from the pH probe and ii) SIT showed that a particle repeatedly coalesced with acidic aerosol approached the pH of the bulk acid solution.

Results from this study provided evidence for a reliable method of controlling and confidently calculating aerosol pH via droplet coalescence allowing for the examination of pH dependent speciation and reactions within a single aerosol droplet**.** Controlling the pH within individual suspended droplets takes us one step closer to being able to more accurately mimic and probe the dynamic environments within individual droplets, similar to those in the atmosphere. Laboratory-based single particle studies simulating the complexity of aerosol microenvironments could provide valuable information, like chemical kinetics of individual aerosols or elucidation of surface effects by comparison with bulk phase chemical reactions and kinetics to those in the aerosol phase, that can be used to update atmospheric models to more accurately predict and simulate aerosol chemistry.

7.5. Chapter 5 Summary

The aqueous phase oxidation of S(IV) catalyzed by transition metal ions is considered to be the most important pathway for the formation of atmospheric sulfate. However, this oxidation pathway can be influenced by organic compounds, like glyoxal, present in atmospheric aerosols, cloud and fog droplets. Therefore, in Chapter 5 the role of glyoxal on the oxidation of S(IV) in acidic aqueous solutions catalyzed by iron in the form

of aqueous Fe^{3+} ions and solid iron oxide was investigated under various experimental conditions. This was done using batch reactors in conjunction with ion chromatography and high-resolution hybrid linear ion trap mass spectrometry analysis. In addition to these analytical techniques, spectroscopic methods were also used to study these reactions. Attenuated total reflectance-Fourier transform infrared spectroscopy was used to monitor the bulk aqueous phase reaction while cavity enhanced Raman spectroscopy in the AOT system was used to study the reaction within a single droplet using droplet coalescence to induce the reaction.

Results from these studies showed that the presence of glyoxal can inhibit the catalytic oxidation of S(IV) and that the extent of the inhibition effect depends on the concentration of glyoxal as well as solution pH. The inhibition effect on the transition metal ion catalyzed oxidation of S(IV) was proposed to arise from the trapping of SO_4^- radicals and the formation of glyoxal-S(IV) adducts. However, the observed inhibition caused by glyoxal in the oxidation of S(IV) catalyzed by solid iron particles, where the oxidation is dominated by the heterogeneous reaction, was ascribed to competitive adsorption of glyoxal and sulfite with surface hydroxyl groups. Additionally, with the exception of glyoxal-S(IV) adducts, the formation of organosulfur compounds was not observed. The inhibition effect and the formation of glyoxal-S(IV) adducts was also observed spectroscopically in both the bulk phase and within a single particle.

The lack of organosulfur compounds formed from the reaction of glyoxal with S(IV) was quite different than our previous findings. In our previous study that investigated the mechanism of the transition metal ion catalyzed oxidation of S(IV) in the presence of

two other carbonyl compounds, methacrolein and methyl vinyl ketone, we showed that various organosulfur compounds were formed.[1] The discrepancy between these two studies was ascribed to the much faster rate of the sulfoxy radical addition reactions across the C=C double bond in methacrolein and methyl vinyl ketone as compared to the hydrogen abstraction reactions.

Overall, our findings showed that glyoxal can inhibit the oxidation of S(IV) catalyzed by aqueous or solid Fe(III) and that the effects of glyoxal are dependent on the mechanism, form of iron (dissolved versus solid), and the ambient conditions, including pH and concentration. Given that the catalytic oxidation of S(IV) is an important in-cloud sulfate formation pathway, the effects of water-soluble organics such as glyoxal, as well as other carbonyl compounds, on this catalytic reaction should be considered in order to accurately predict the formation of sulfate in the atmosphere.

7.6. Chapter 6 Summary

Although the catalytic oxidation of S(IV) has been well studied, the effects of a number of atmospherically relevant variables on the reaction mechanism and kinetics are not well understood. Therefore, in Chapter 6 we investigated the influence of a range of variables including pH, ionic strength, and presence of organic compounds on the aqueous phase oxidation of S(IV) in the presence and absence of transition metals to gain a better understanding of how this reaction may be altered under various atmospheric conditions found for aqueous aerosols as well as cloud and fog droplets. Experiments were conducted

in batch reactors followed by analysis of S(IV) and S(VI) concentration with ion chromatography.

Results from this study showed that acidity, ionic strength, and presence of organics influence the kinetics of the transition metal catalyzed oxidation of S(IV) to inorganic S(VI). Specifically, at relatively low ionic strength, the effect of ionic strength on sulfur oxidation varies depending on the pH and type of transition metal ion present, but at high ionic strength S(IV) oxidation to S(VI) is greatly inhibited. The transition metal catalyzed oxidation of S(IV) to inorganic S(VI) was also inhibited by the presence of atmospherically relevant organic compounds, glyoxal and methacrolein, with concomitant increase in organosulfur compound formation. The impact of solution pH was likely due to changes in S(IV) speciation (sulfite vs bisulfite) and contributions of transition metal ion mechanisms due to solubility of these oxide minerals. The observed inhibition effects may be explained by scavenging of sulfate radicals and the formation of organosulfur products for reactions with organic compounds. Overall, this study demonstrated that the variety of conditions found in aqueous droplets (high ionic strength, presence of organics, etc.) influence atmospheric sulfur processes that need to be understood in order to be included in and reduce uncertainties atmospheric chemistry models.

7.7. Future Studies

Although the studies presented in this thesis worked to better understand the factors influencing S(IV) oxidation and develop a method to study the chemistry of individual

droplets, many questions and unexplored areas still remain and require further investigation. Future work and directions include:

1. Expanding on our previous work investigating the formation of organosulfur compounds from reactions of S(IV) with glyoxal, MVK, or MACR with iron by exploring the effects other transition metals (e.g. copper) and atmospheric variables (temperature or light) on these reactions. After thorough examination of the influence transition metals, as ions and solid particles, have on the formation of organosulfur products, increase complexity by investigating the effects of authentic dust samples (e.g. mineral dust or fly ash), which contain multiple transition metals, on these reactions.

2. Identification of additional organosulfur compounds and elucidation of formation mechanisms and kinetics from reactions of S(IV) with additional atmospherically relevant organic compounds.

3. Comparing bulk phase (batch reactor studies) and aerosol phase (AOT) reactions and kinetics of atmospheric relevance, especially those related to sulfur oxidation chemistry, to elucidate any differences between the two phases.

4. Further development of the AOT to study the chemistry occurring within trapped droplets containing solid inclusions. Previous studies as well as some preliminary experiments of our own have shown that droplets containing solid inclusions can be stably trapped in the AOT.[2–4] Trapping a droplet containing a transition metal

oxide or mineral dust particle would allow us to more accurately mimic aerosol and cloud or fog droplets, similar to those found in the atmosphere, in the laboratory.

5. Exploring gas-particle reactions in the AOT by introducing gas phase reactants to the trapping chamber. This would allow us to not only explore multiphase chemical reactions and gas partitioning but would also expand the range of chemicals we are able to study with the AOT due to limitations of the current nebulization methods for aqueous or solution phase samples.

6. Expanding beyond sulfur chemistry in the AOT to study additional chemical systems or more complex chemical systems. One direction may be studying marine related aerosols and their reaction or aging with various atmospherically relevant compounds.

In summary, these studies have improved our understanding of the factors influencing sulfur oxidation chemistry and helped to develop a method to investigate the chemistry occurring within single droplets; the future directions of these studies will continue to expand our knowledge of atmospheric aerosol chemistry.

7.8. References

(1) Huang, L.; Cochran, R. E.; Coddens, E. M.; Grassian, V. H. Formation of Organosulfur Compounds through Transition Metal Ion-Catalyzed Aqueous Phase Reactions. *Environ. Sci. Technol. Lett.* **2018**, *5*, 315–321.

(2) Rkiouak, L.; Tang, M. J.; Camp, J. C. J.; McGregor, J.; Watson, I. M.; Cox, R. A.; Kalberer, M.; Ward, A. D.; Pope, F. D. Optical Trapping and Raman Spectroscopy of Solid Particles. *Phys. Chem. Chem. Phys.* **2014**, *16*, 11426–11434.

(3) Tang, M. J.; Camp, J. C. J.; Rkiouak, L.; McGregor, J.; Watson, I. M.; Cox, R. A.; Kalberer, M.; Ward, A. D.; Pope, F. D. Heterogeneous Interaction of SiO 2 with N 2 O 5 : Aerosol Flow Tube and Single Particle Optical Levitation-Raman Spectroscopy Studies. *J. Phys. Chem. A* **2014**, *118*, 8817–8827.

(4) Laurain, A. M. C.; Reid, J. P. Characterizing Internally Mixed Insoluble Organic Inclusions in Aqueous Aerosol Droplets and Their Influence on Light Absorption. *J. Phys. Chem. A* **2009**, *113*, 7039–7047.

A Spectral Library

Library of spectra collected with ATR-FTIR, confocal Raman spectroscopy, or AOT cavity enhanced Raman spectroscopy.

7.9. ATR-FTIR spectra

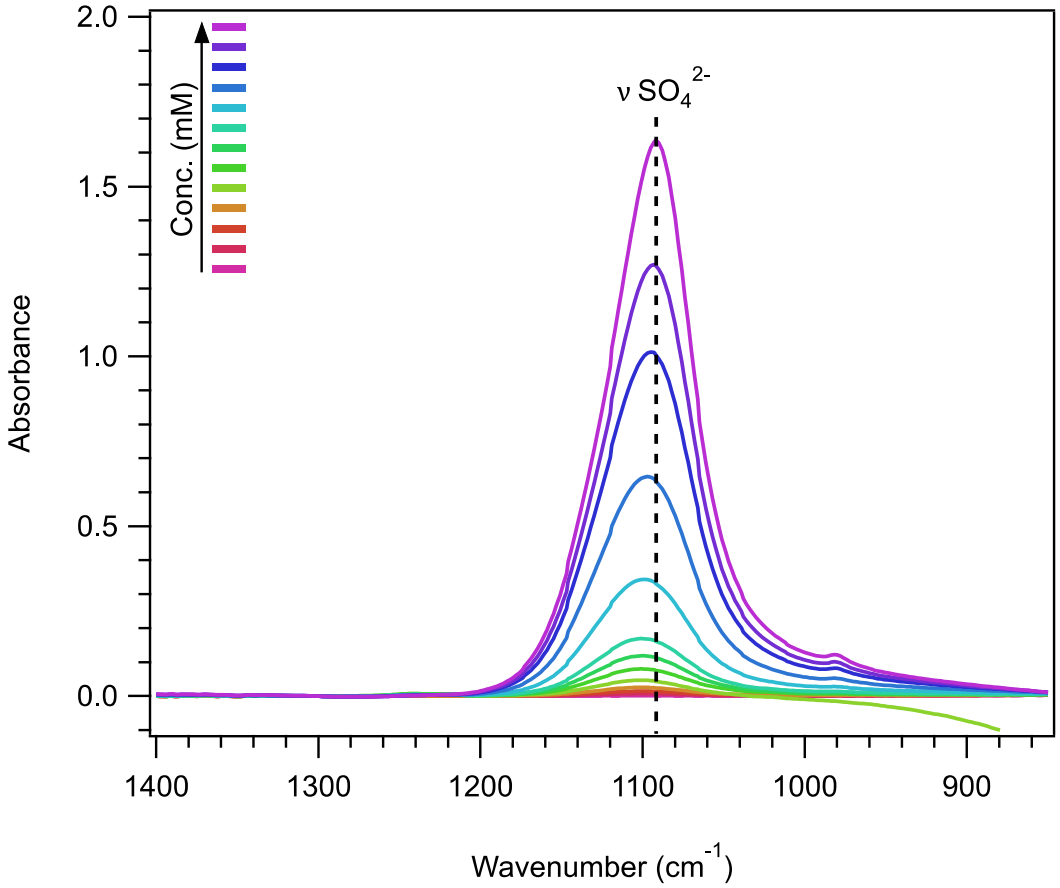

Figure A.1: ATR-FTIR spectra of sodium sulfate, Na_2SO_4, (pH unadjusted) as a function of concentration.

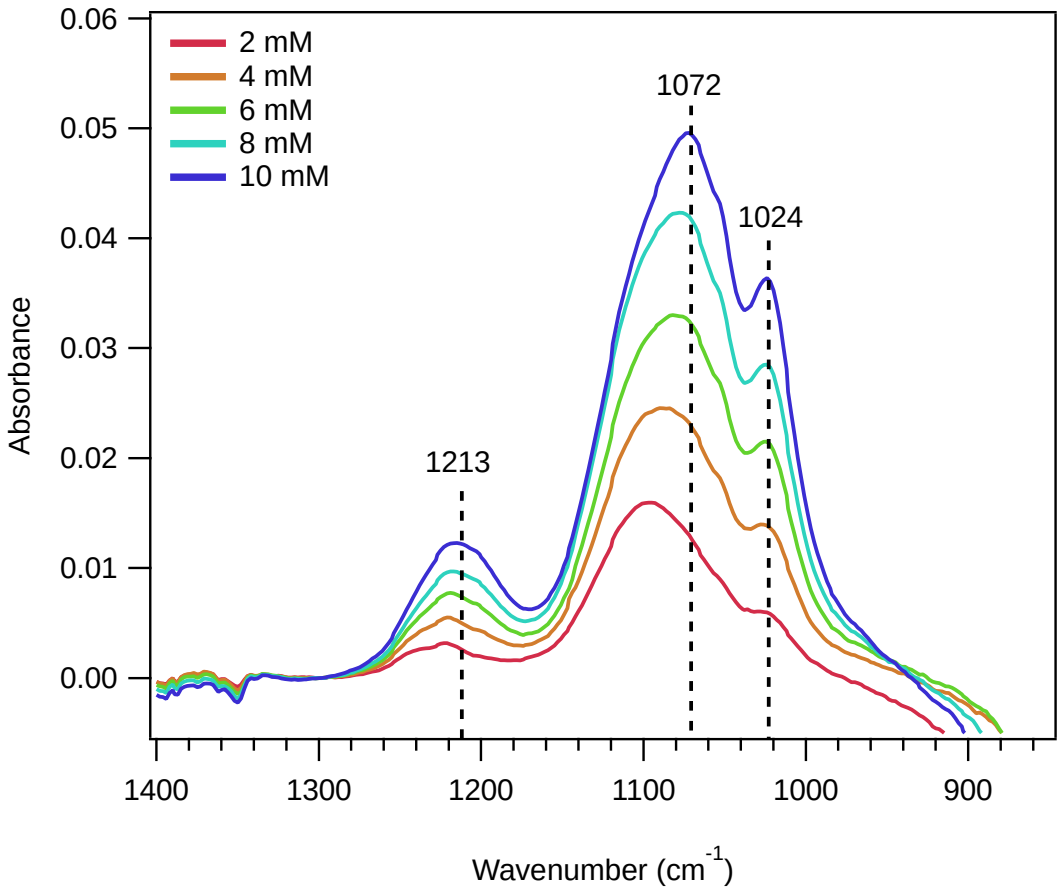

Figure A.2: ATR-FTIR spectra of sodium sulfite, Na_2SO_3, as a function of concentration at pH 5.

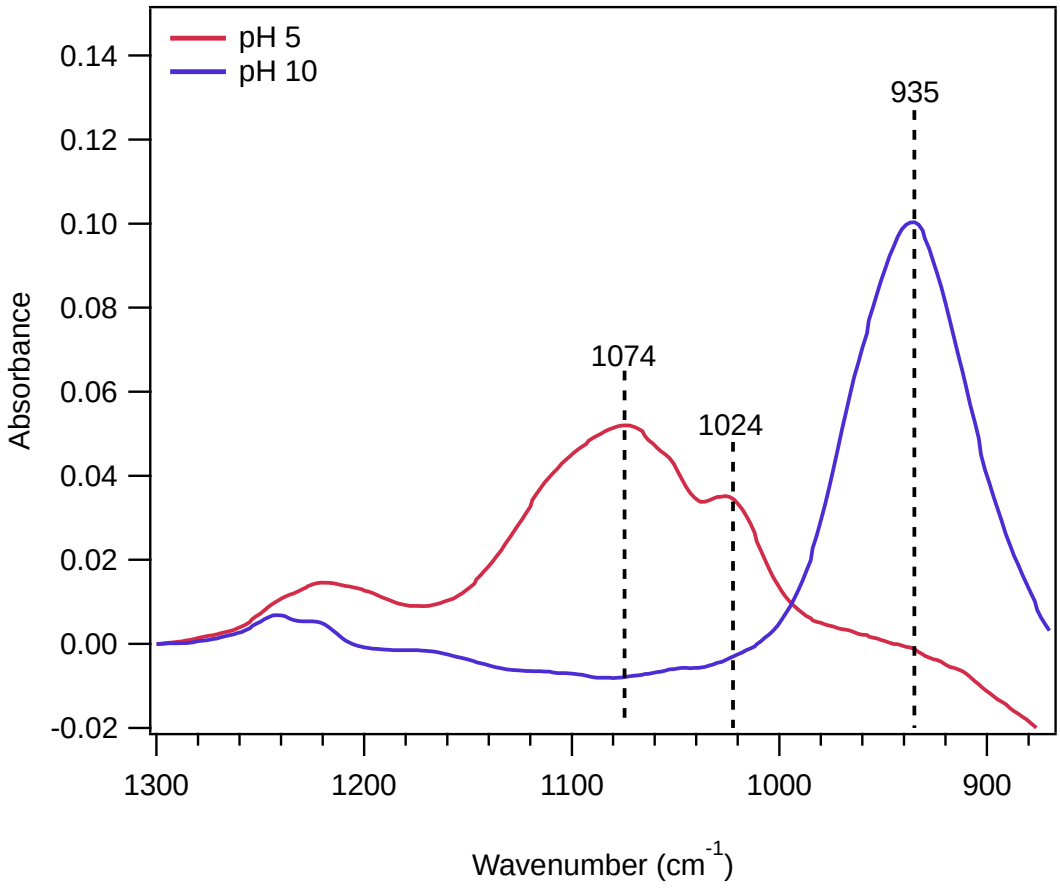

Figure A.3: ATR-FTIR spectra of sodium sulfite, Na_2SO_3, (50 mM) as a function of pH showing the change in speciation from HSO_3^- to SO_3^{2-} as pH increases from 5 to 10.

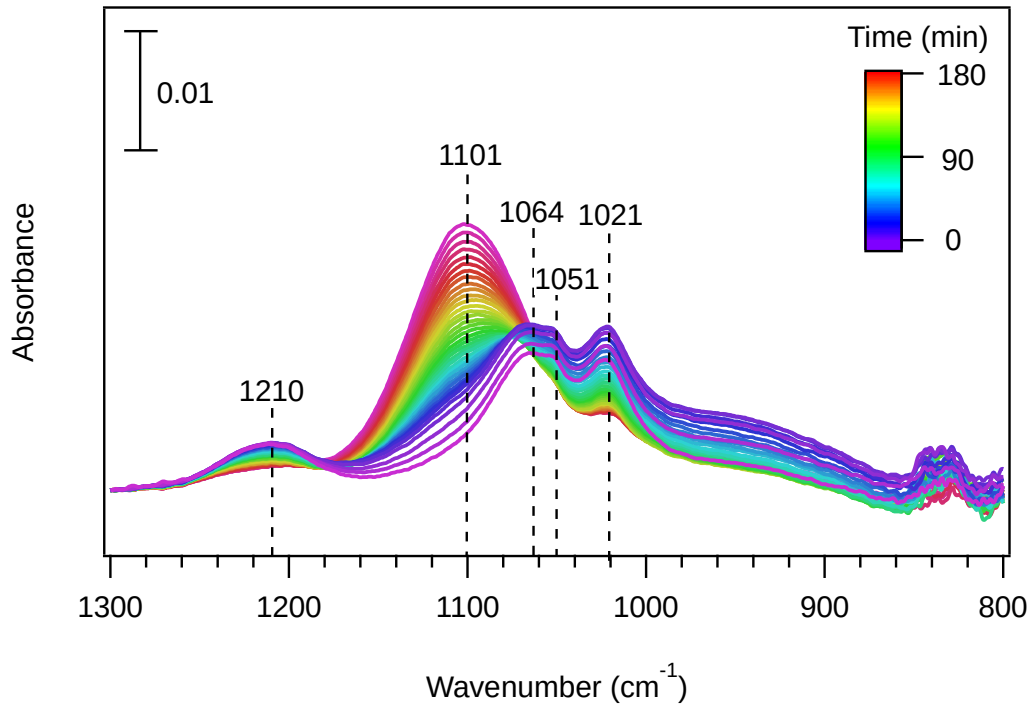

Figure A.4: ATR-FTIR spectrum of sodium metabisulfite, $Na_2S_2O_5$ (50 mM, pH 5). As time proceeds, the S(IV) bands near 1060-1020 cm^{-1} disappear while the S(VI) band at 1100 cm^{-1} grows in.

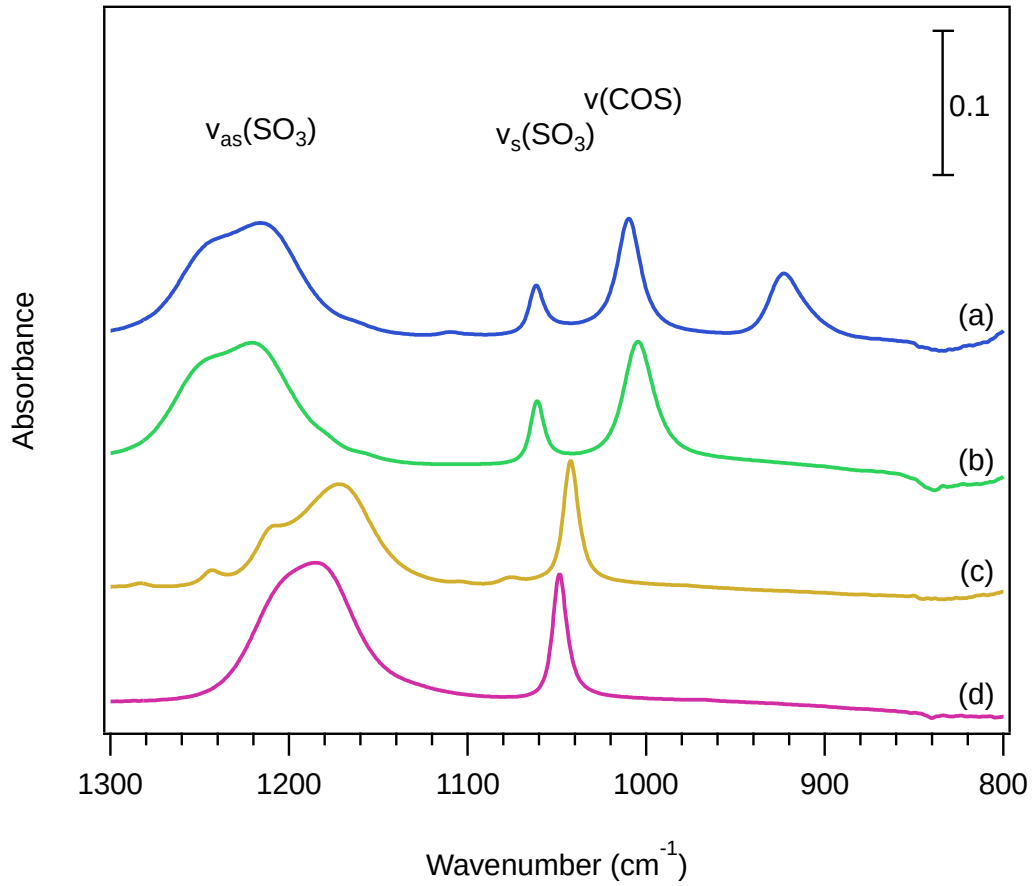

Figure A.5: ATR-FTIR spectra of standard organosulfur solutions; a) ethyl sulfate, b) methyl sulfate, c) butanesulfonic acid, and d) methanesulfonate.

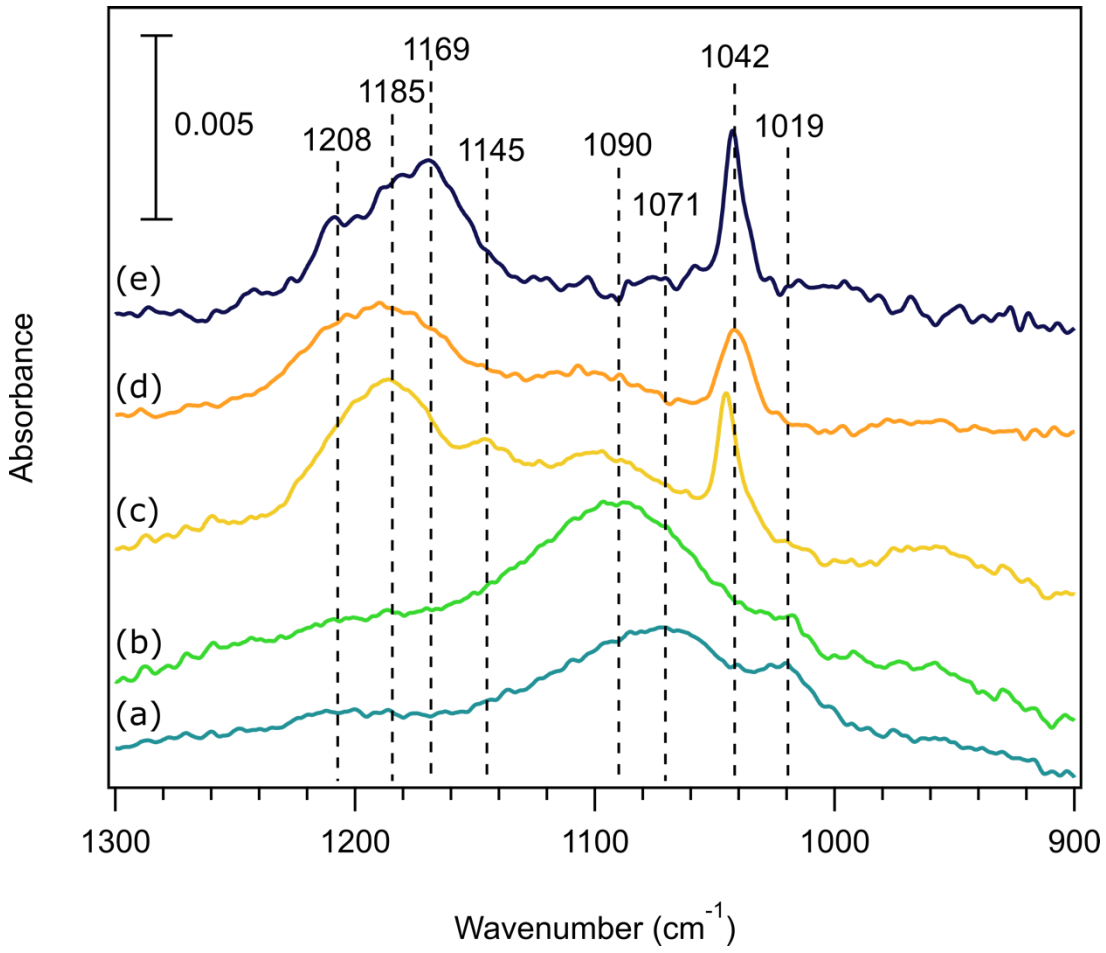

Figure A.6: ATR-FTIR spectra of a) sodium sulfite, b) sodium sulfite with iron chloride c) methyl vinyl ketone (MVK) with sodium sulfite and iron chloride, d) methacrolein (MACR) with sodium sulfite and iron chloride, and e) butanesulfonic acid for reference. Sodium sulfite: 20 mM and pH 5; MVK: 20 mM; MACR: 20 mM; iron chloride: 2.5 mM; butanesulfonic acid: 0.1 M.

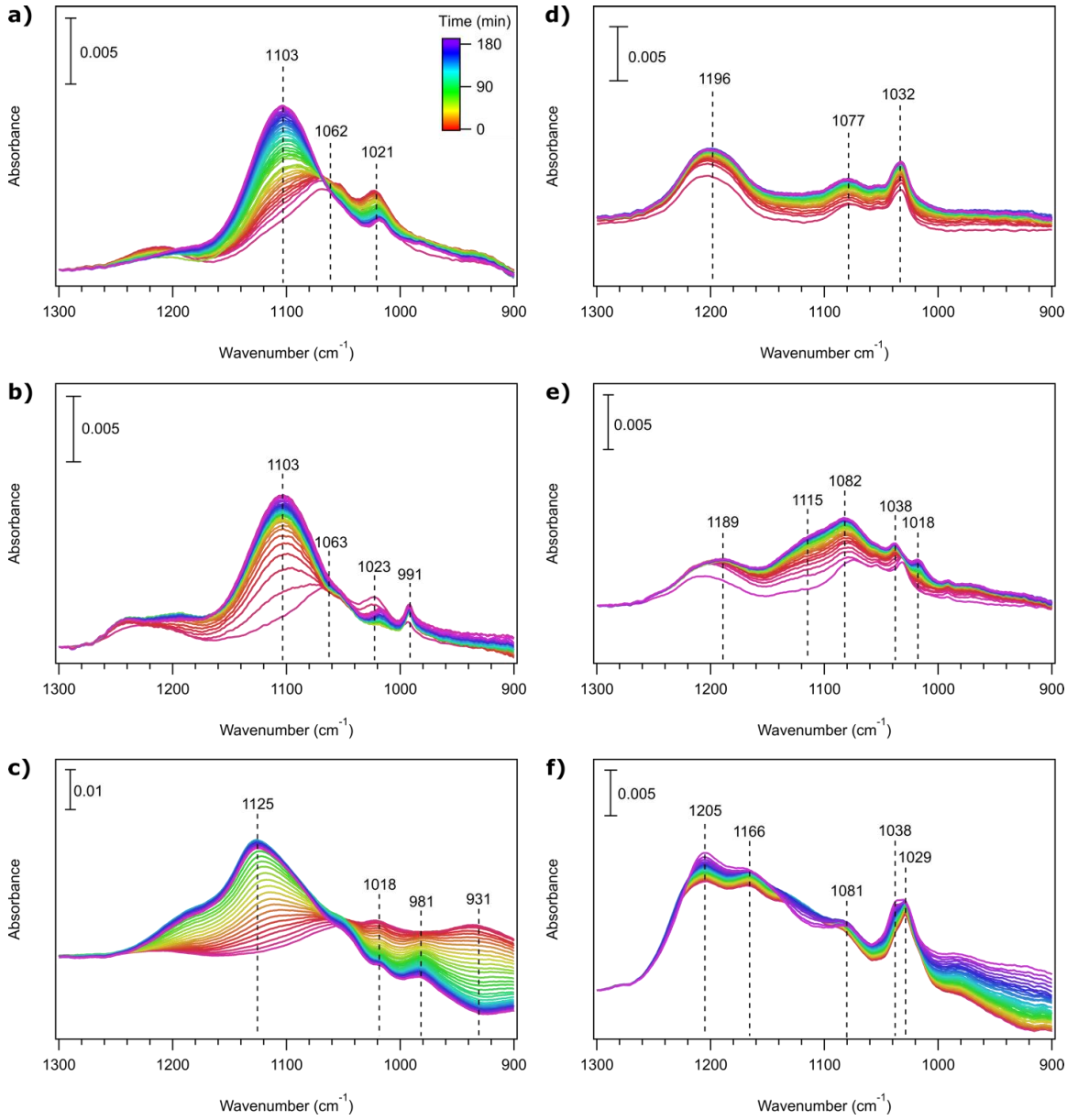

Figure A.7: ATR-FTIR spectra of the oxidation of sodium sulfite a) in the absence of metals b) in the presence of iron ions (iron chloride, $FeCl_3$), c) iron particles (iron oxide, γ-Fe_2O_3) and in the presence of glyoxal d) without metals, e) in the presence of iron ions, and f) in the presence of iron particles. Sodium sulfite: 50 mM; glyoxal: 50 mM; iron chloride: 2.5 mM; iron oxide: 0.1 g L^{-1} solid loading.

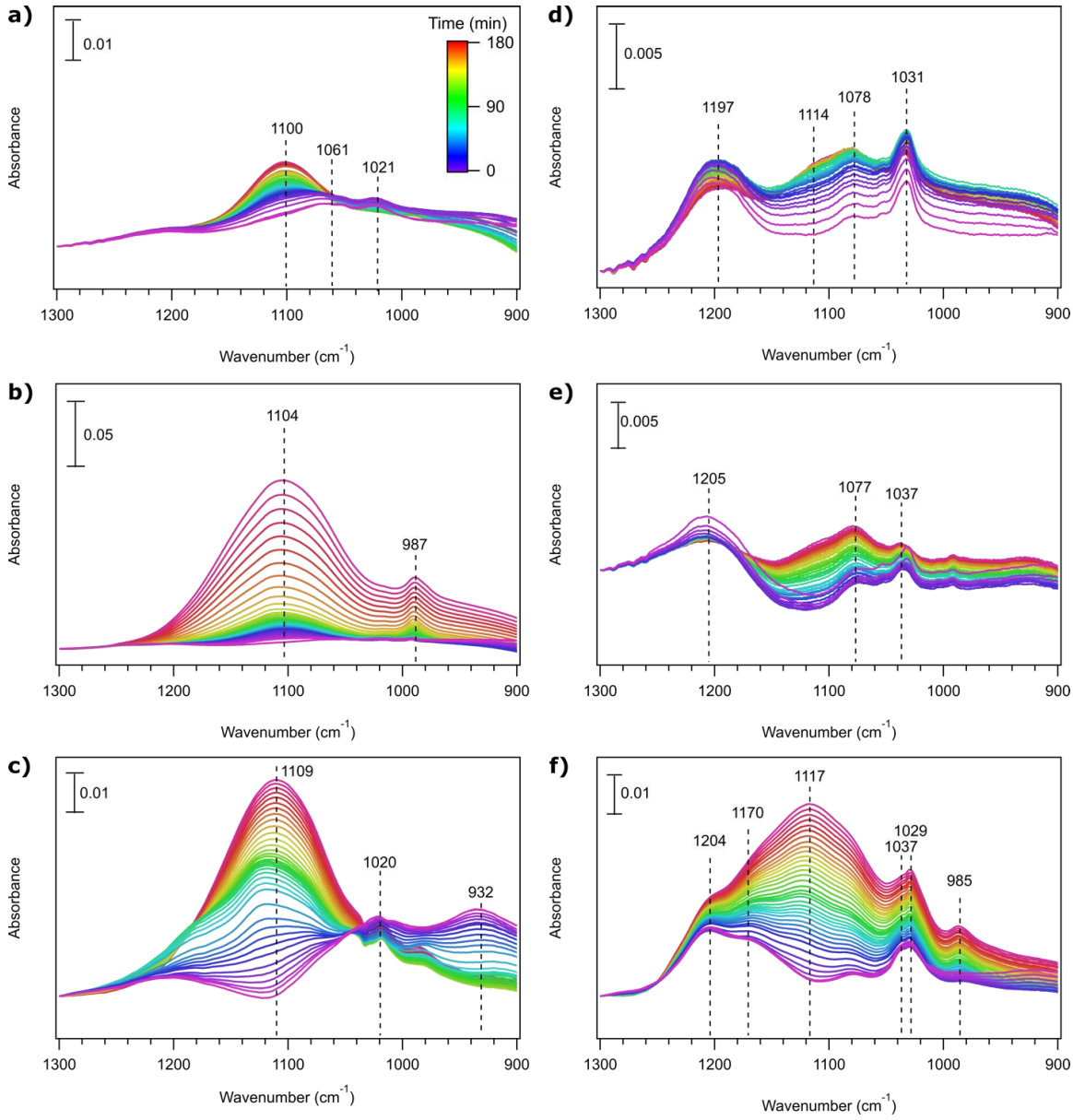

Figure A.8: ATR-FTIR spectra of the photochemical oxidation of a) sodium sulfite with no metals, b) in the presence of iron ions (iron chloride. $FeCl_3$), c) iron particles (iron oxide, γ-Fe_2O_3) and in the presence of glyoxal d) without metals, e) in the presence of iron ions, and f) in the presence of iron particles. Sodium sulfite: 50 mM; glyoxal: 50 mM; iron chloride: 2.5 mM; iron oxide: 0.1 g L^{-1} solid loading.

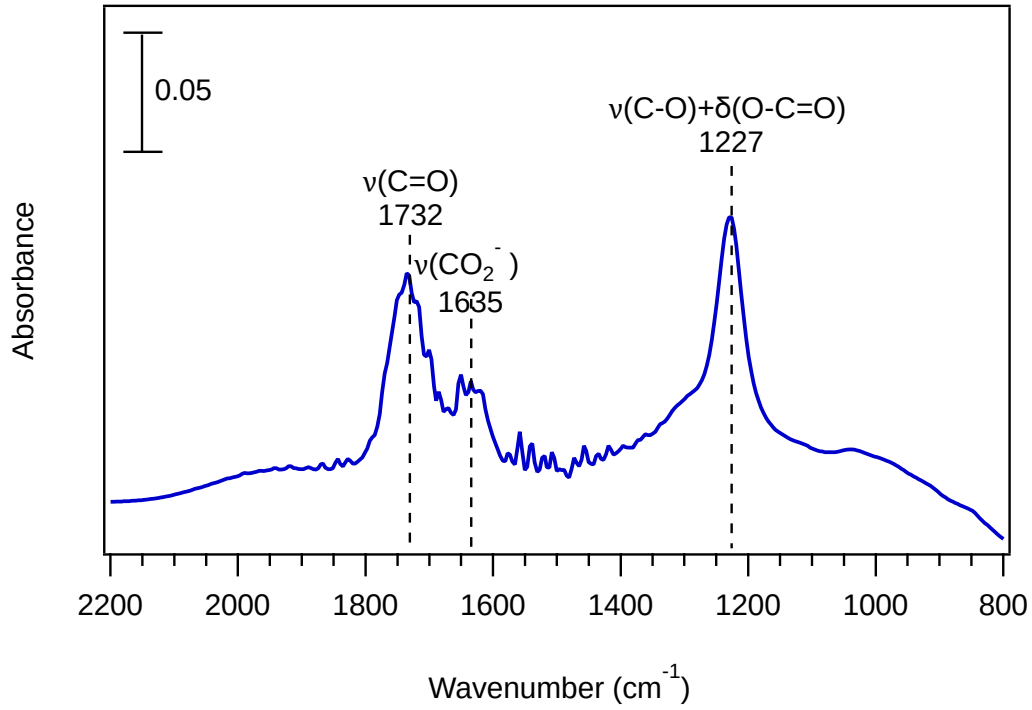

Figure A.9: ATR-FTIR Spectra of oxalic acid, $C_2H_2O_4$, (1 M, pH unadjusted).

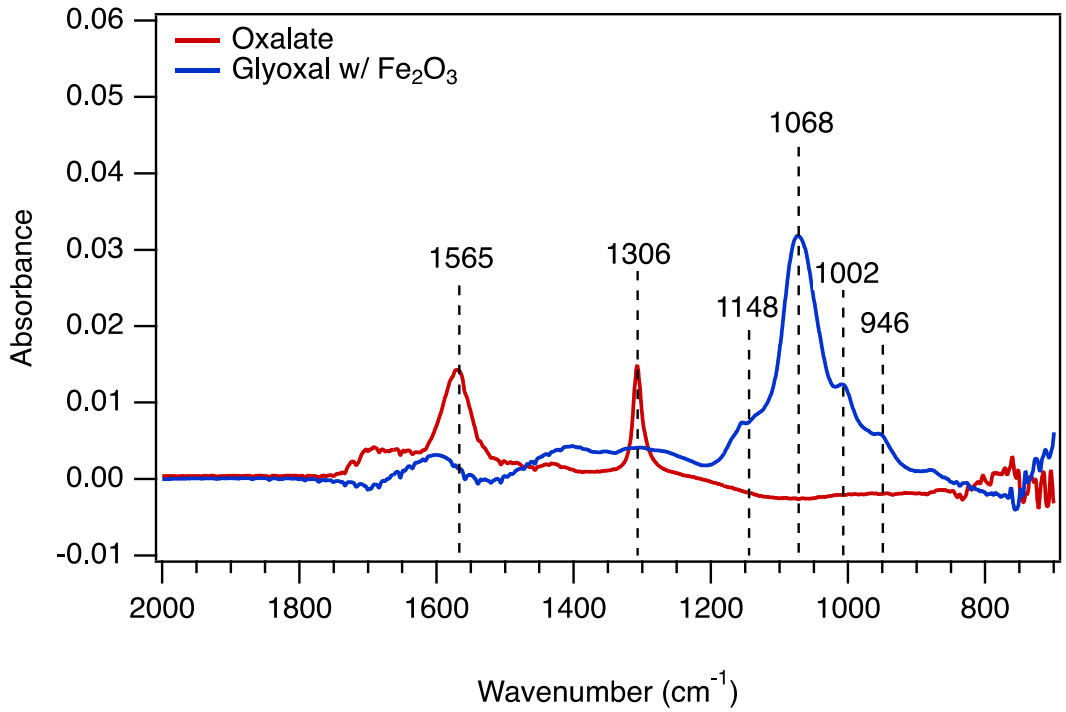

Figure A.10: ATR-FTIR spectra sodium oxalate, $Na_2C_2O_4$, (0.5 M, pH unadjusted) and the reaction of aqueous glyoxal (0.5 M) with solid iron oxide particles (γ-Fe_2O_3).

7.10. Confocal Raman spectra

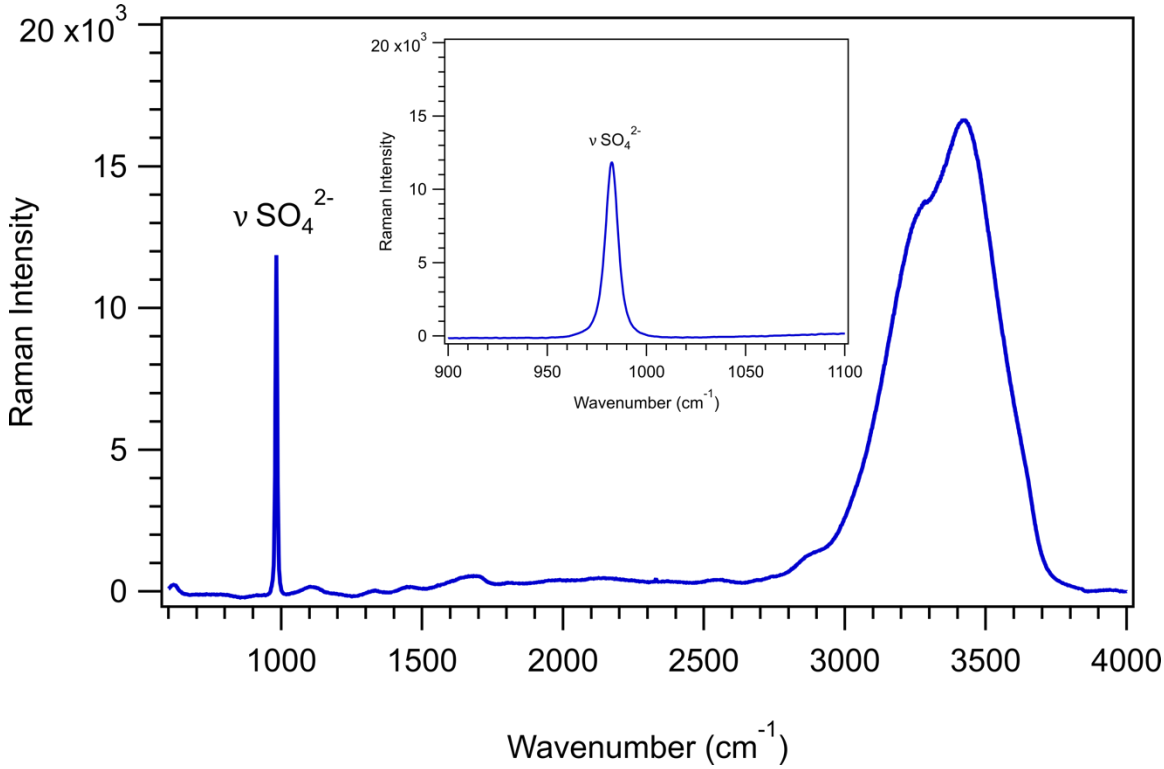

Figure A.11: Confocal Raman spectrum of ammonium sulfate, $(NH_4)_2SO_4$, (1 M, pH unadjusted). Inset shows the spectrum in the 900-1100 cm^{-1} range.

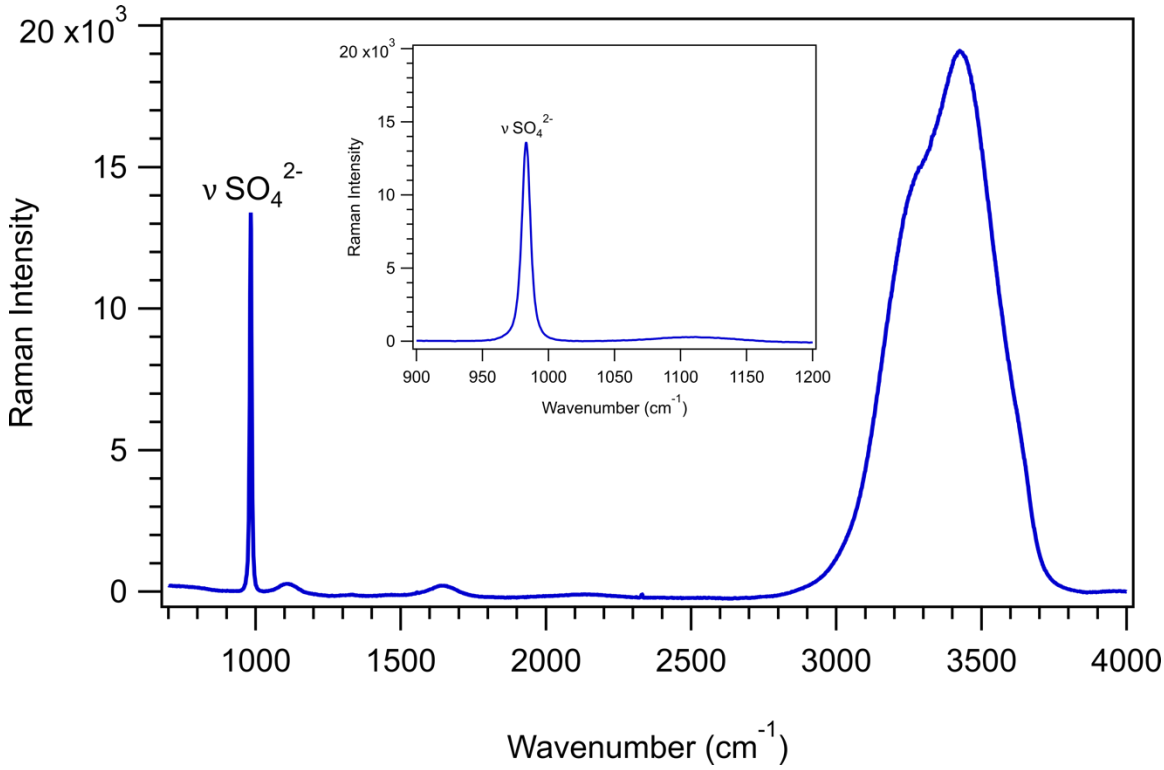

Figure A.12: Confocal Raman spectrum of sodium sulfate, Na_2SO_4, (1 M, pH unadjusted). Inset shows the spectrum in the 900-1200 cm^{-1} range.

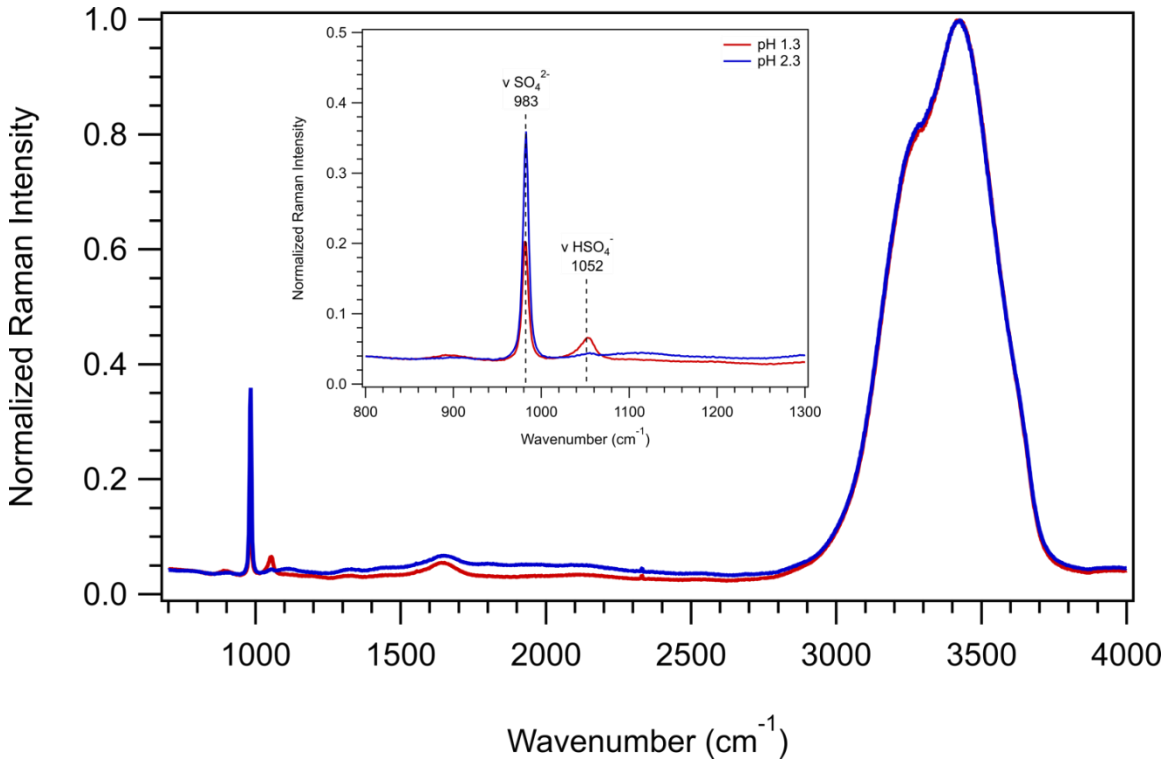

Figure A.13: Confocal Raman spectra of sodium sulfate, Na_2SO_4, (0.5 M) as a function of pH. Inset shows the spectra over the 800-1300 cm^{-1} range.

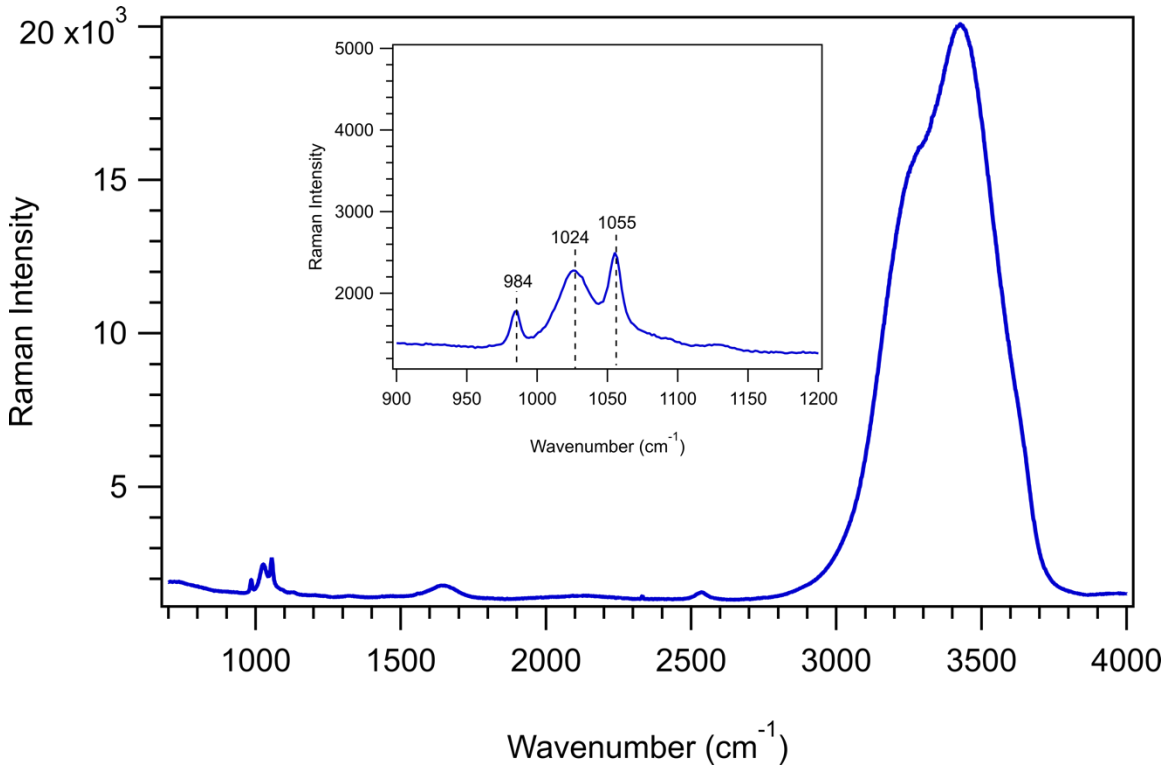

Figure A.14: Confocal Raman spectrum of sodium sulfite, Na_2SO_3, (1 M) at pH 5. Inset shows the spectrum in the 900-1200 cm^{-1} range.

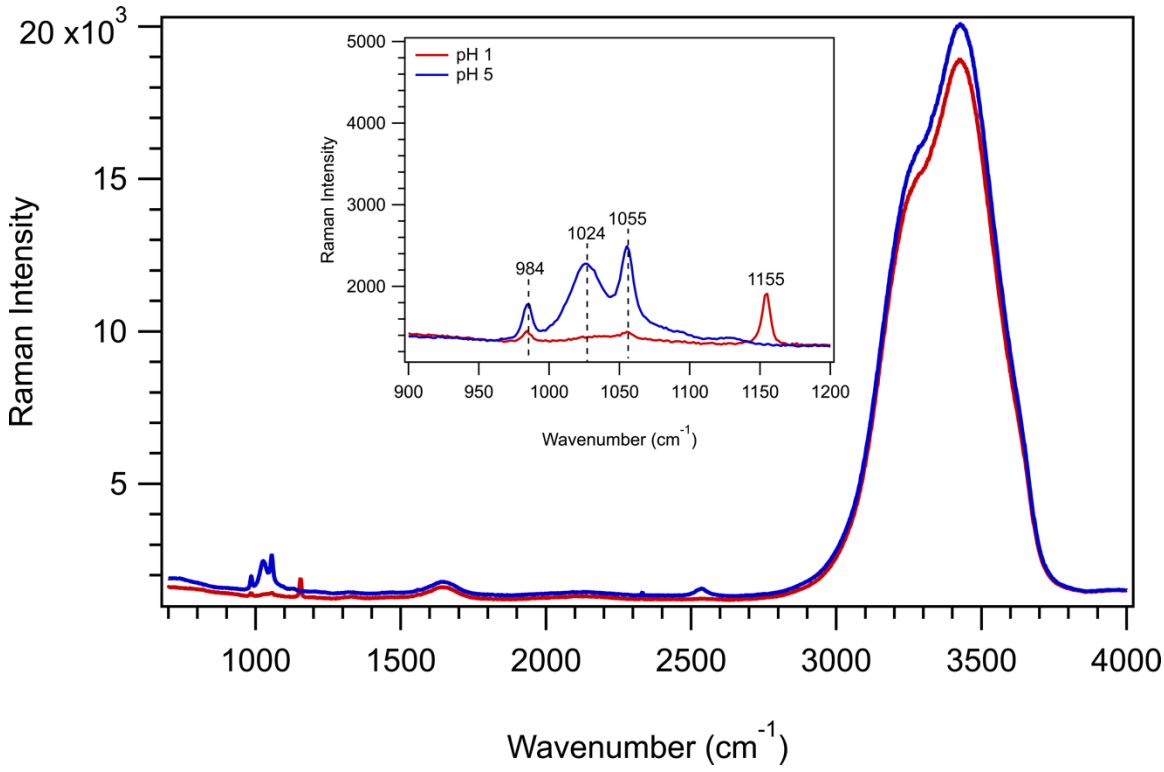

Figure A.15: Confocal Raman spectrum of sodium sulfite, Na_2SO_3, (1 M) as a function of pH. Inset shows the spectrum in the 900-1200 cm^{-1} range.

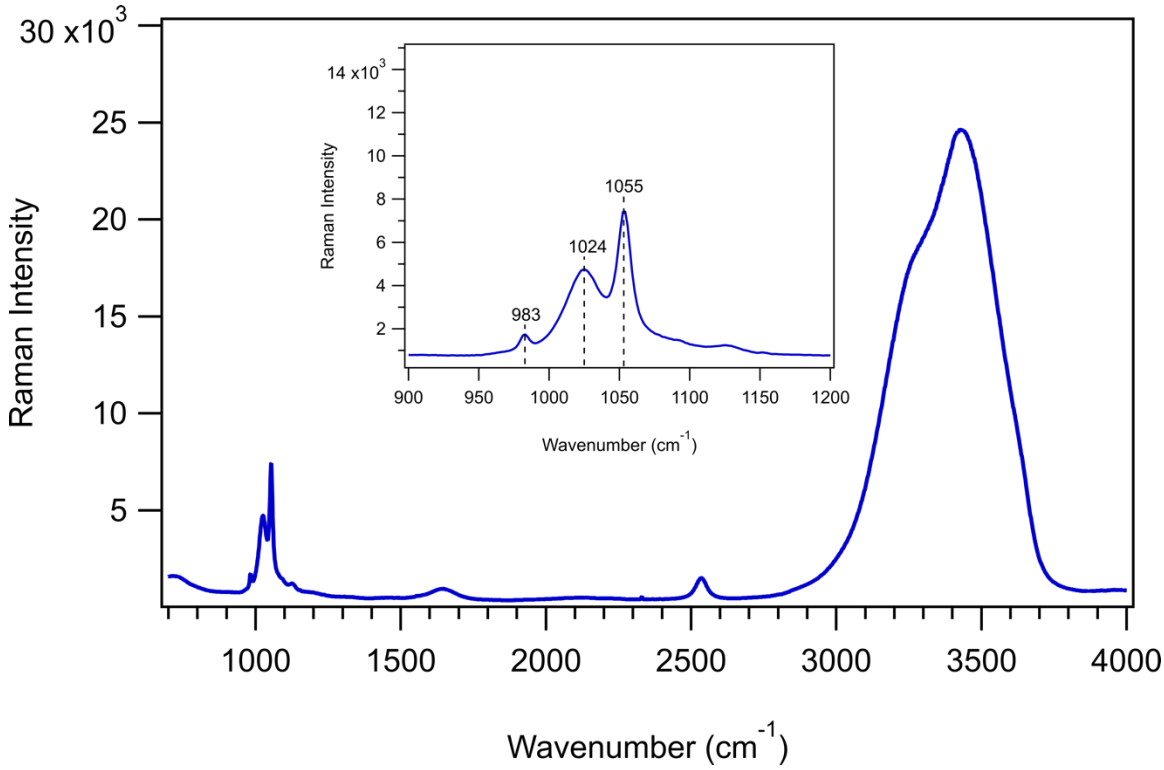

Figure A.16: Confocal Raman spectrum of sodium metabisulfite, $Na_2S_2O_5$, (1 M) at pH 5. Inset shows the spectrum in the 900-1200 cm^{-1} range.

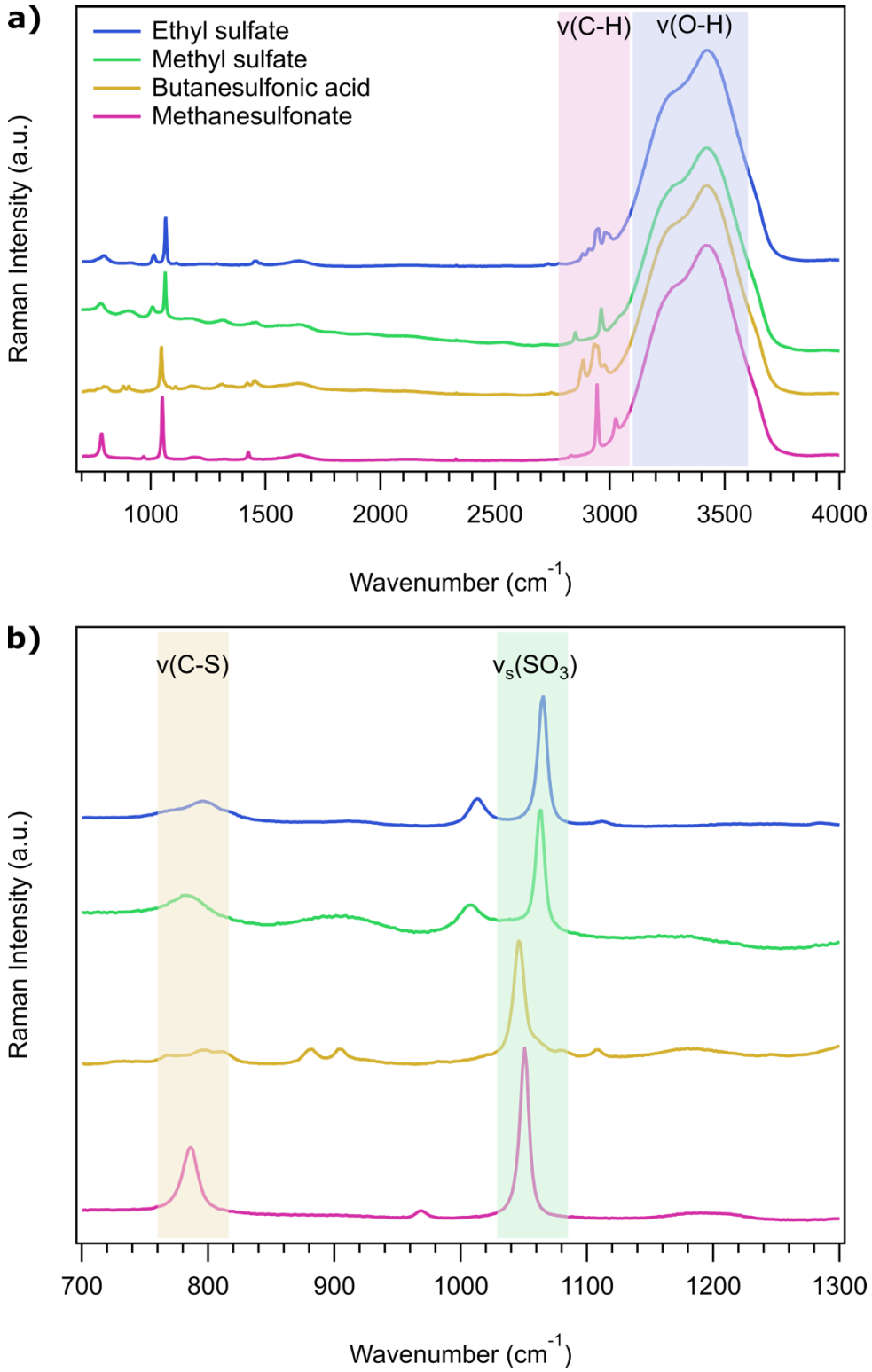

Figure A.17: Confocal Raman spectra of organosulfur solutions (0.5 M); ethyl sulfate, methyl sulfate, butanesulfonic acid, and methanesulfonate over a) the full spectral range 700-4000 cm^{-1} and b) the 700-1300 cm^{-1} range.

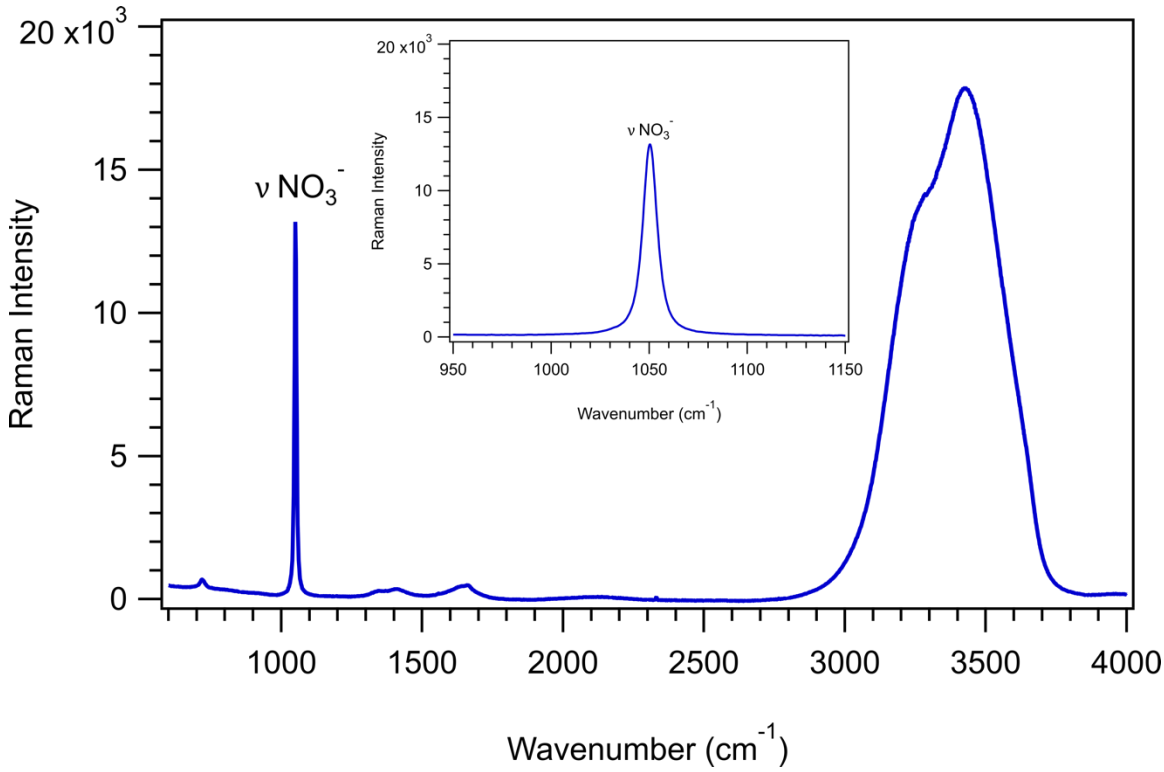

Figure A.18: Confocal Raman spectrum of sodium nitrate, $NaNO_3$. (1 M, pH unadjusted). Inset shows the spectrum in the 900-1150 cm^{-1} range.

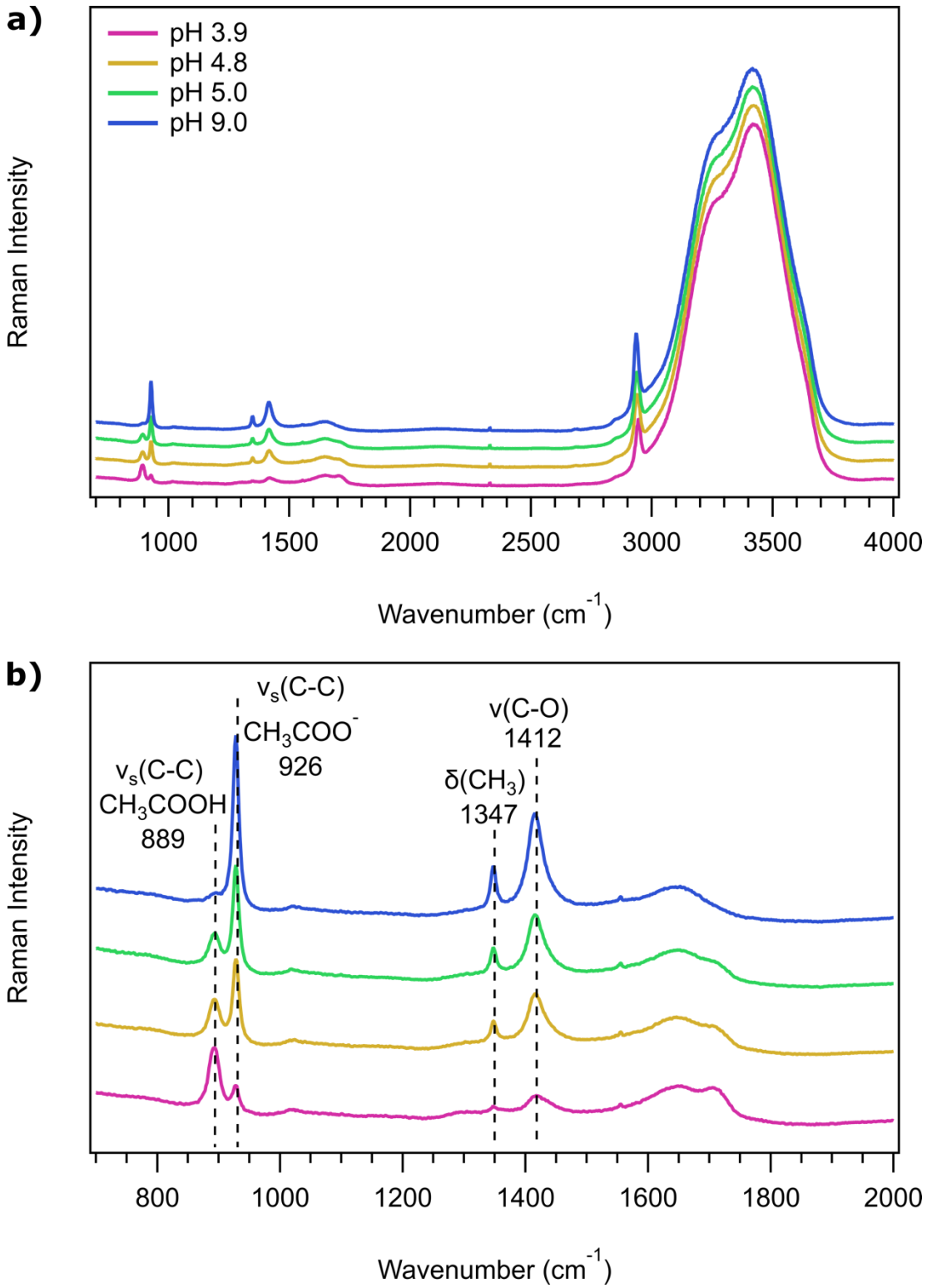

Figure A.19: Confocal Raman spectra of sodium acetate, CH_3COONa, (1 M) as a function of pH over a) full spectral range and b) in the 700-1700 cm^{-1} range.

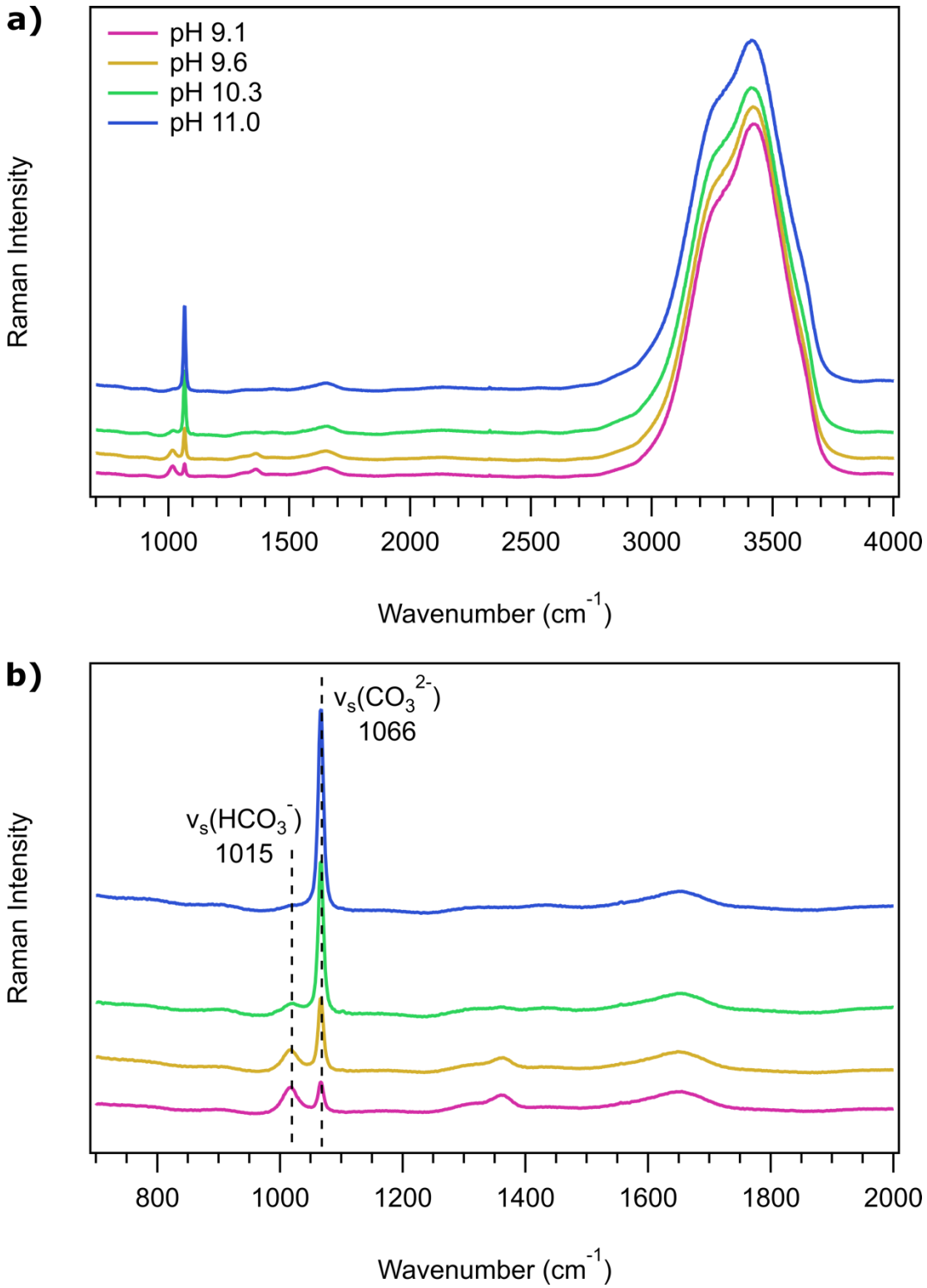

Figure A.20: Confocal Raman spectra of sodium carbonate, Na_2CO_3, (1 M) as a function of pH over a) full spectral range and b) in the 700-1700 cm^{-1} range.

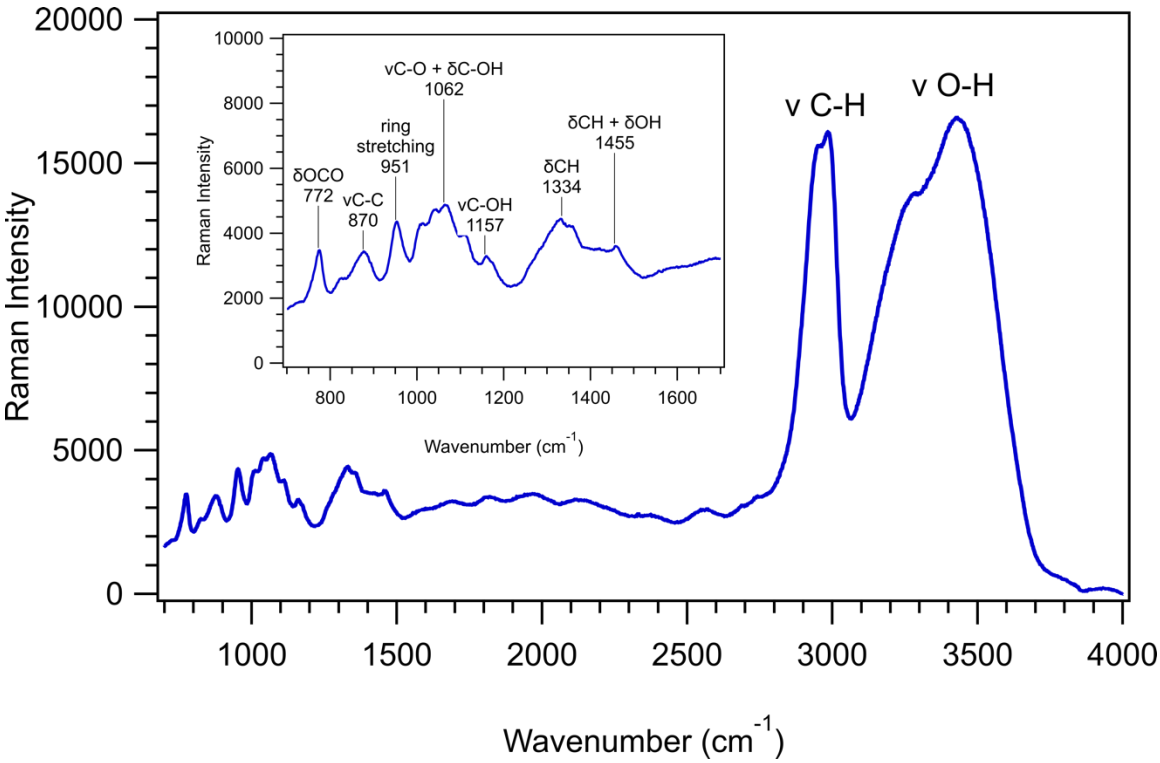

Figure A.21: Confocal Raman spectrum of glyoxal, $C_2H_2O_2$, (40% wt, stock solution, pH unadjusted). Inset shows the spectrum over the 700-1700 cm^{-1} range.

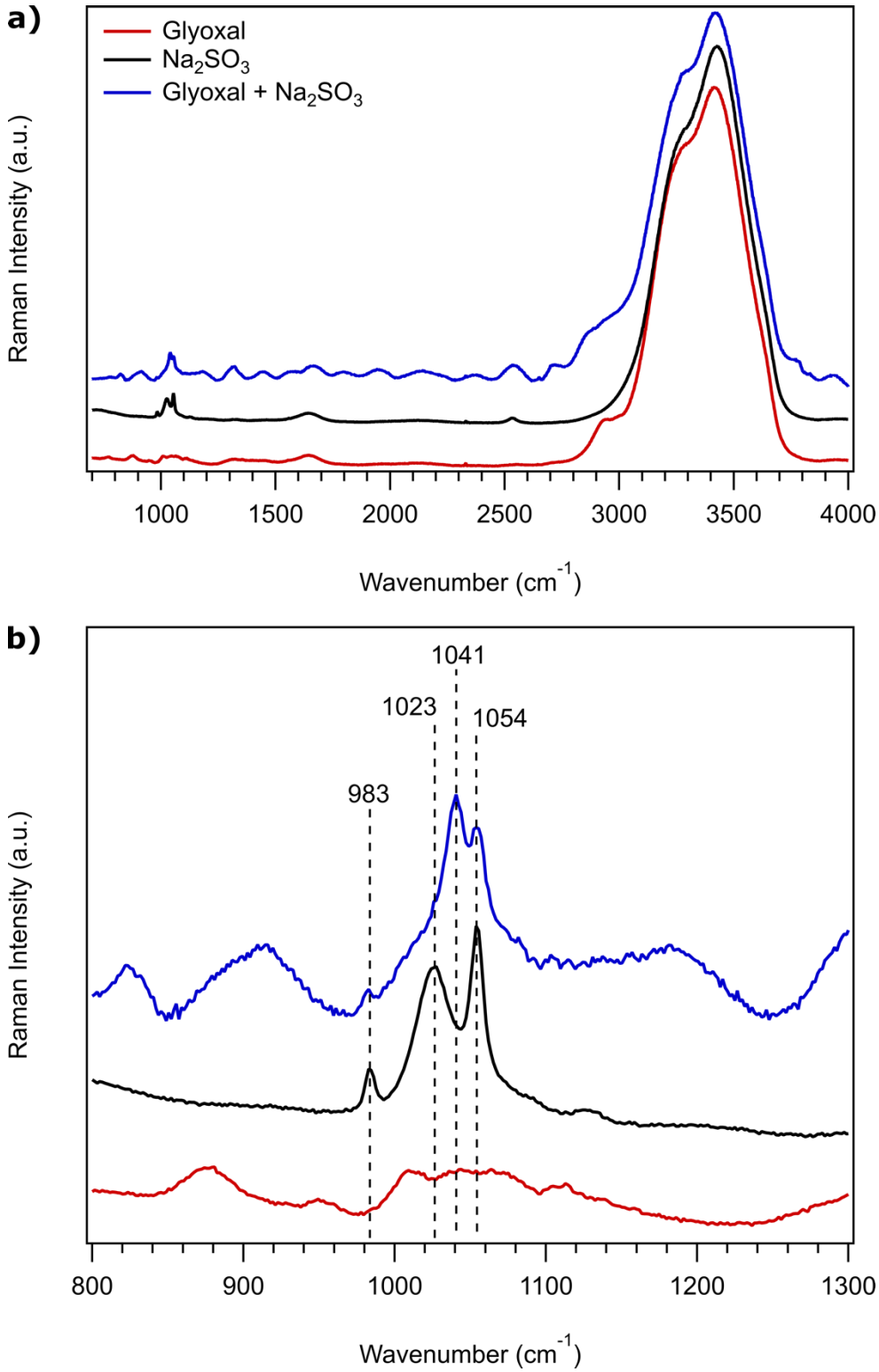

Figure A.22: Confocal Raman spectra of glyoxal (1 M) (red), sodium sulfite, Na_2SO_3, (1 M, pH 5) (black), and the reaction between a 1:1 ratio of glyoxal and sodium sulfite (blue) over a) full spectral range and b) in the 800-1300 cm^{-1} range.

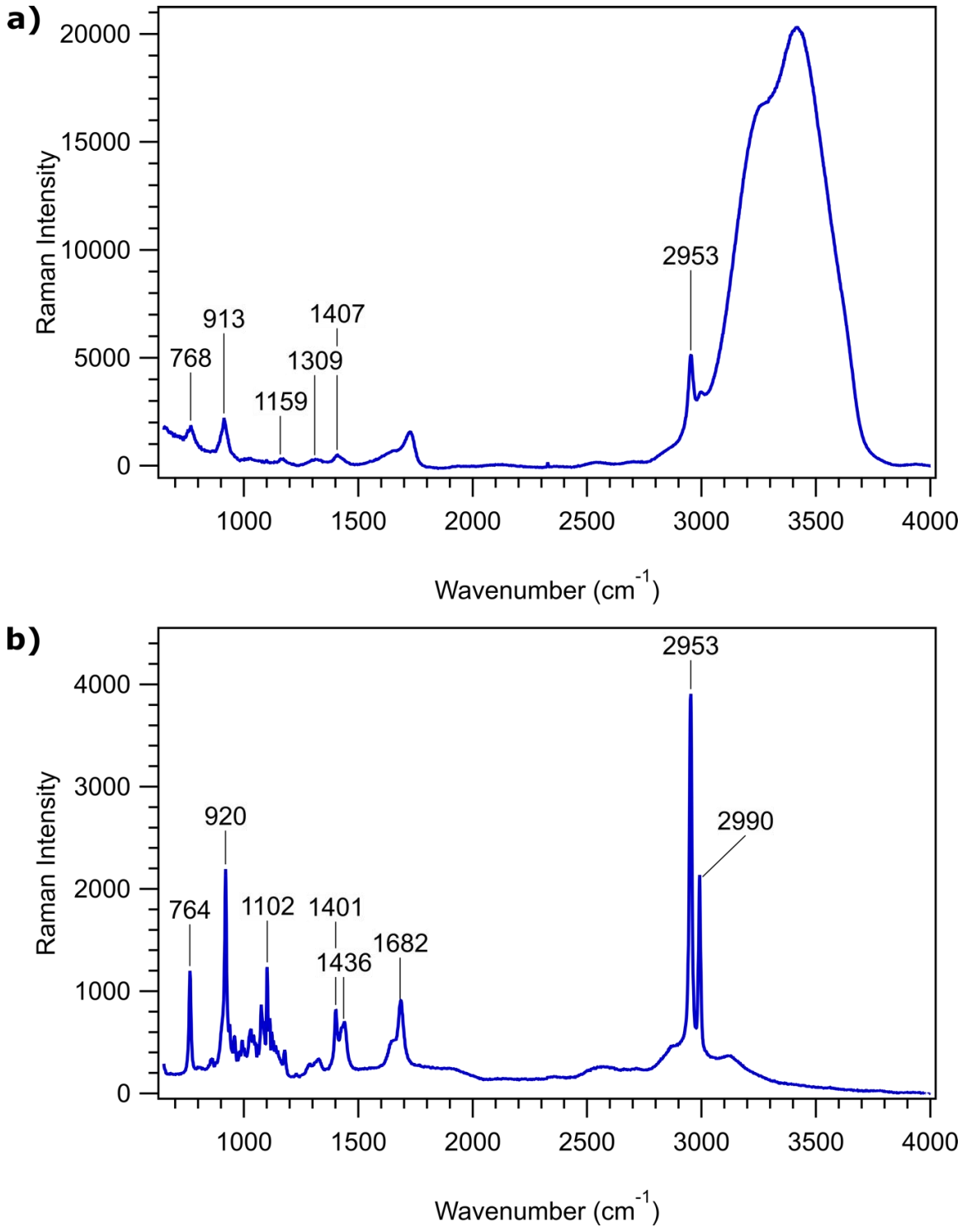

Figure A.23: Confocal Raman spectra of malonic acid, $CH_2(COOH)_2$, in a) solution phase (1 M, pH unadjusted) and b) solid/crystalline phase.

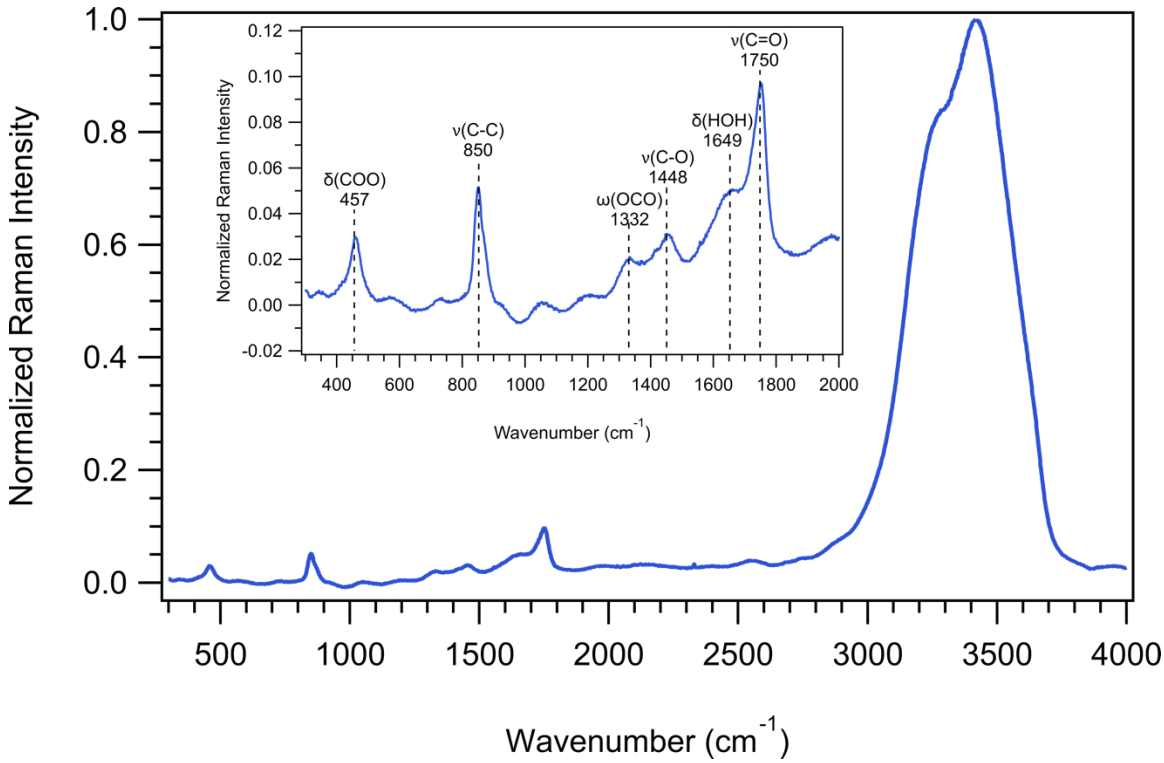

Figure A.24: Confocal Raman spectrum of oxalic acid, $C_2H_2O_4$, (1 M). Inset shows the spectrum in the 300-2000 cm^{-1} range.

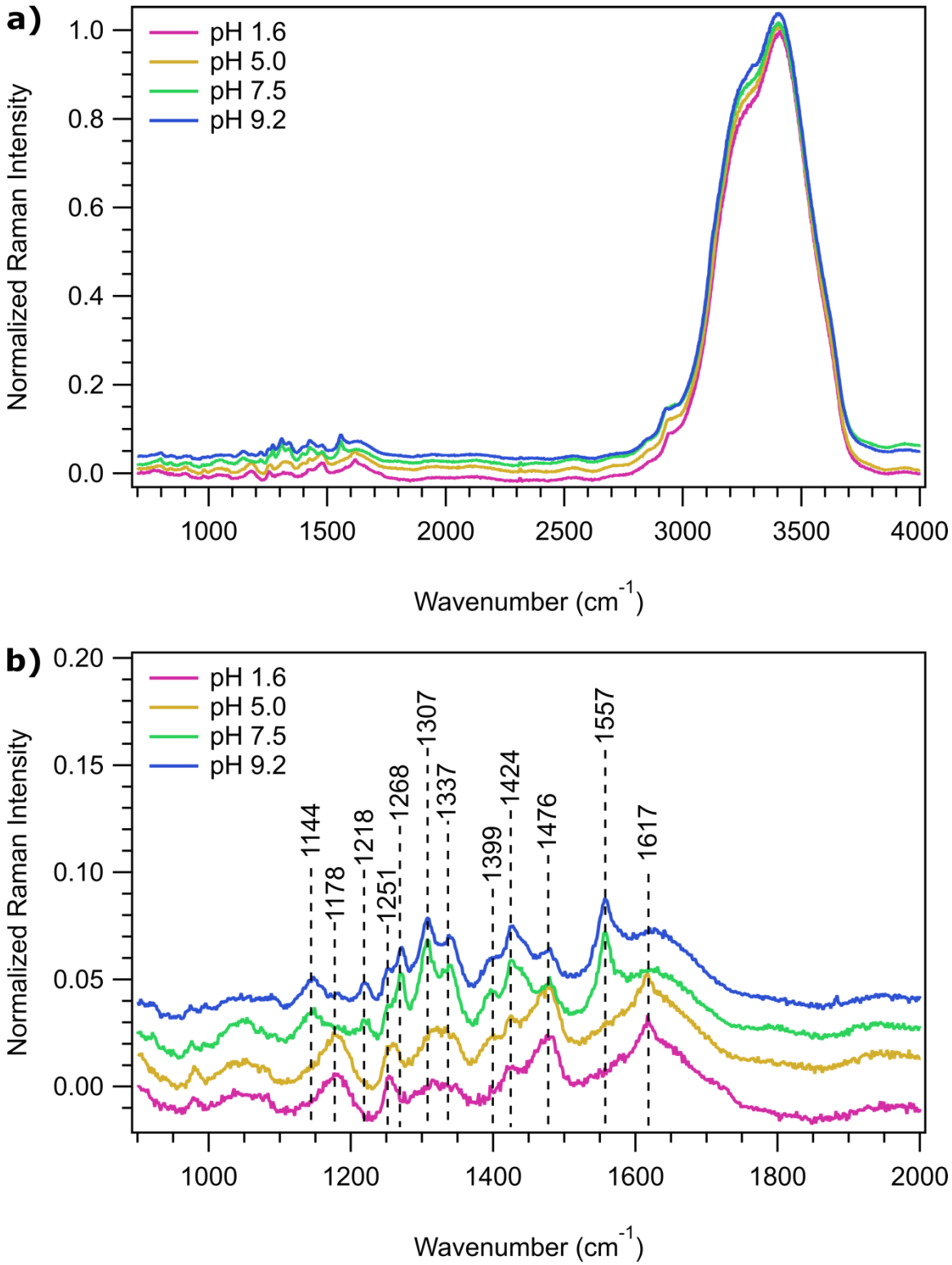

Figure: A.25 Confocal Raman spectra of L-histidine (0.25 M) as a function of pH over a) full spectral range and b) in the 900-2000 cm^{-1} range.

7.11. AOT cavity enhanced Raman spectra

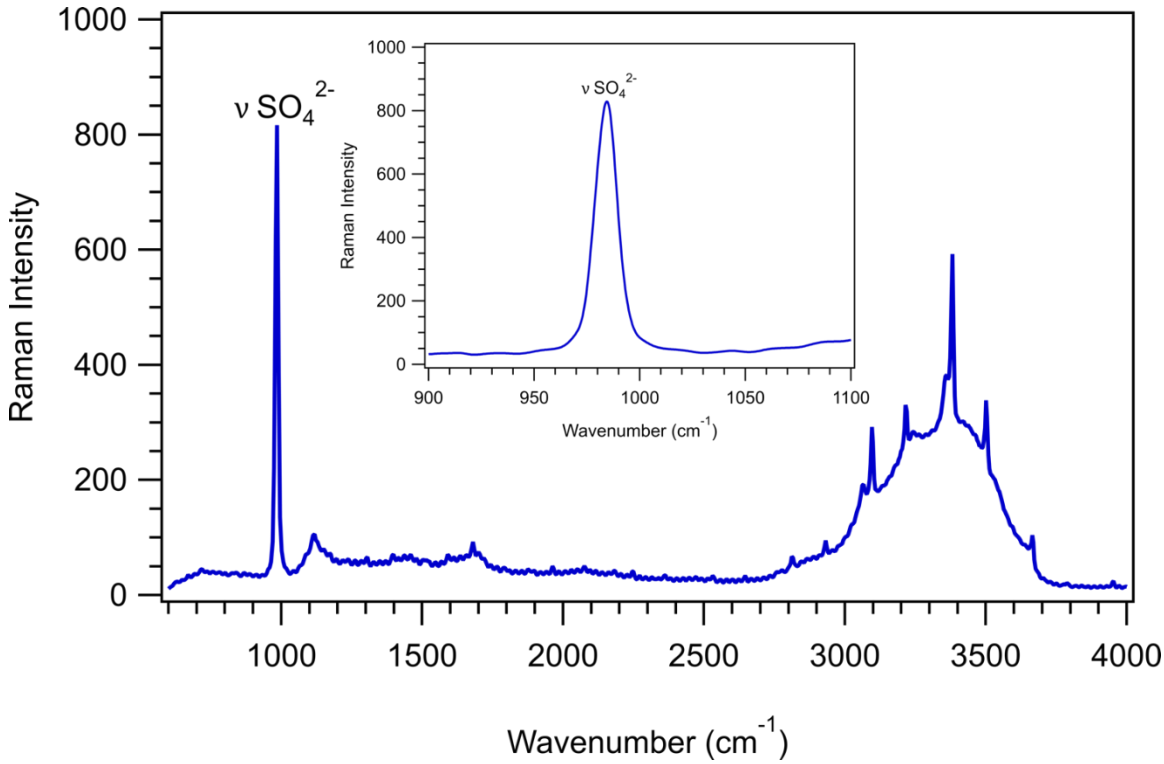

Figure A.26: Cavity enhanced Raman spectrum of a trapped 1 M ammonium sulfate, $(NH_4)_2SO_4$, (1 M, pH unadjusted) droplet. Inset shows the spectrum in the 900-1200 cm^{-1} range highlighting the sulfate stretching mode near 985 cm^{-1}.

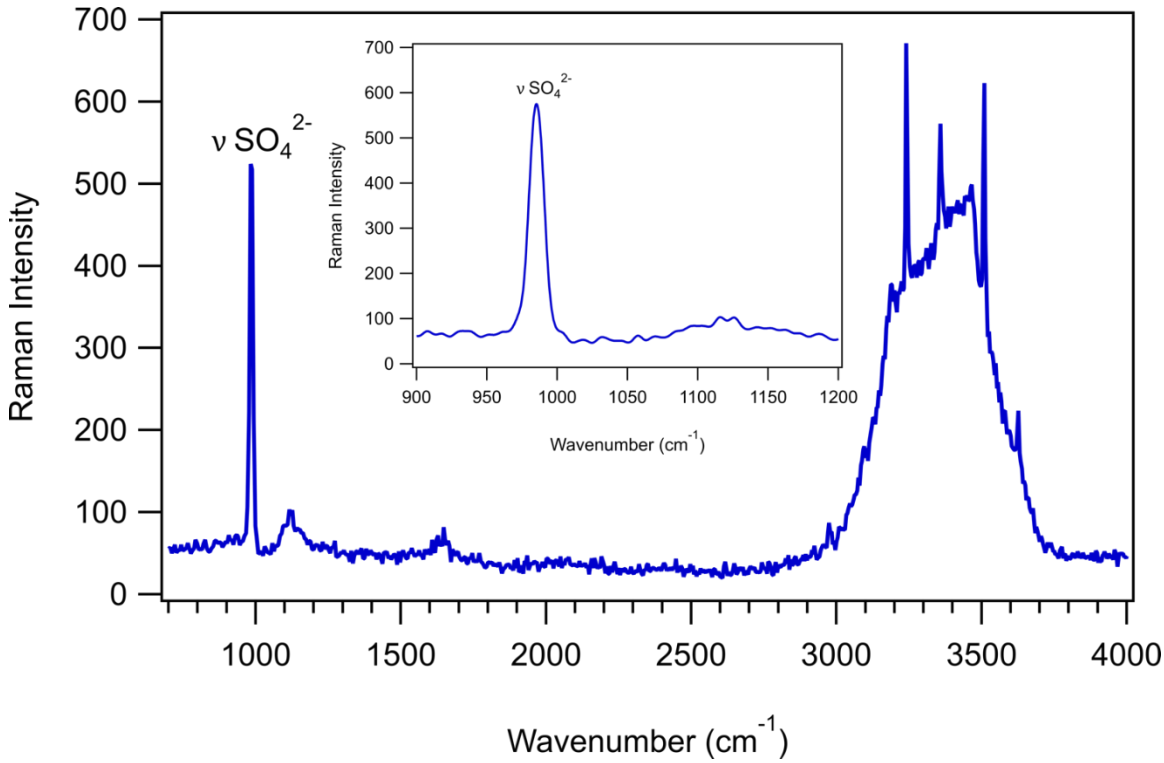

Figure A.27: Cavity enhanced Raman spectrum of a trapped sodium sulfate, Na_2SO_4, (1 M, pH unadjusted) droplet. Inset shows the spectrum in the 900-1200 cm^{-1} range highlighting the sulfate stretching mode near 985 cm^{-1}.

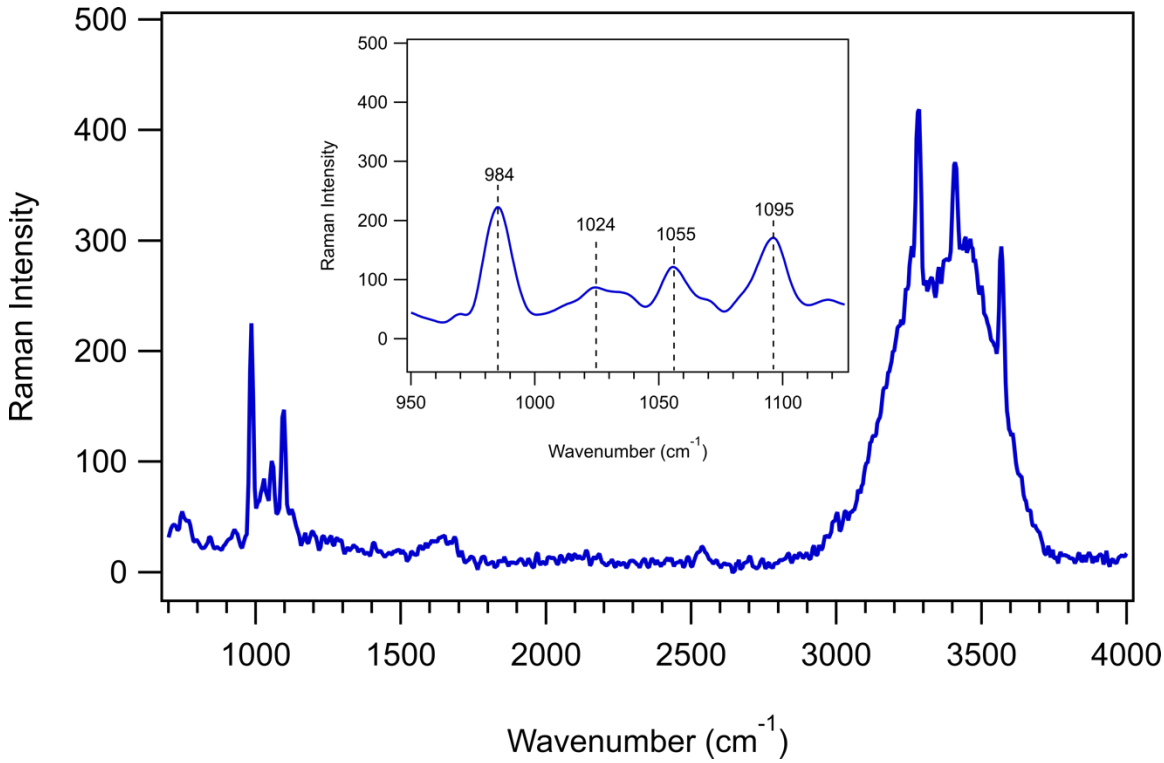

Figure A.28: Cavity enhanced Raman spectrum of a trapped sodium metabisulfite, $Na_2S_2O_5$, (1 M, pH unadjusted) droplet. Inset shows the spectrum in the 950-1125 cm^{-1} range.

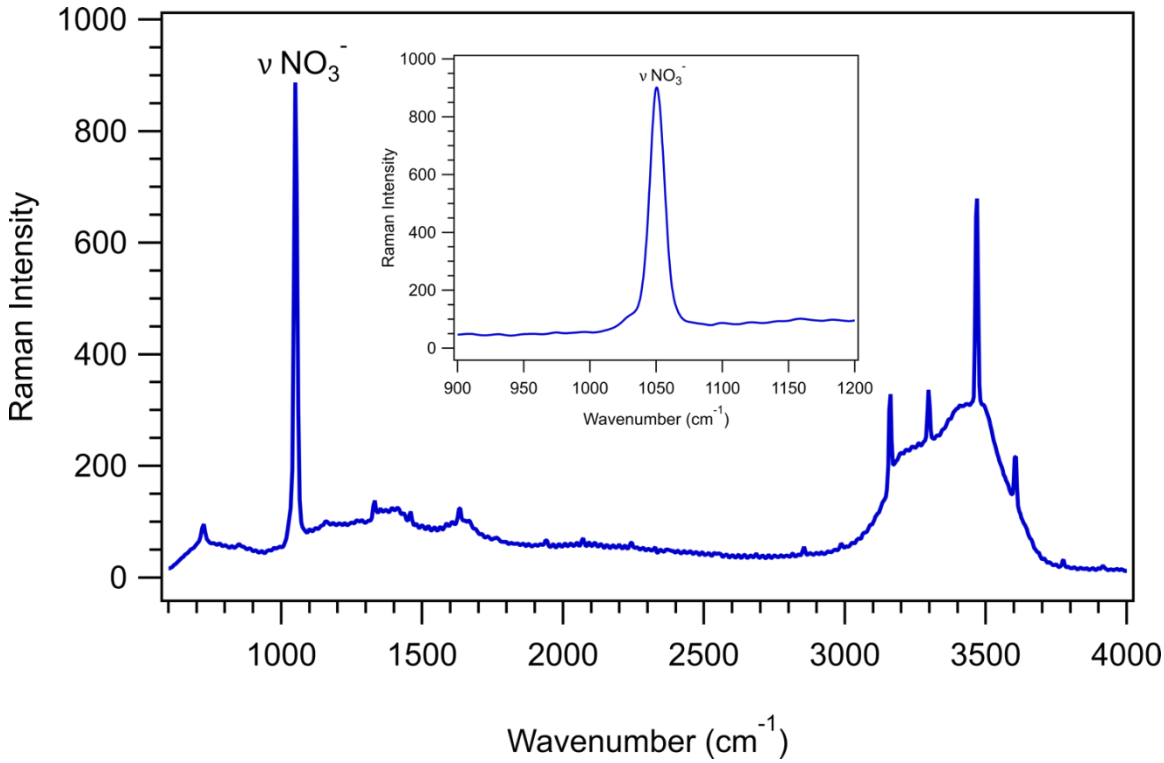

Figure A.29: Cavity enhanced Raman spectrum of a trapped sodium nitrate, $NaNO_3$, (1 M, pH unadjusted) droplet. Inset shows the spectrum in the 900-1200 cm^{-1} range highlighting the nitrate stretching mode.

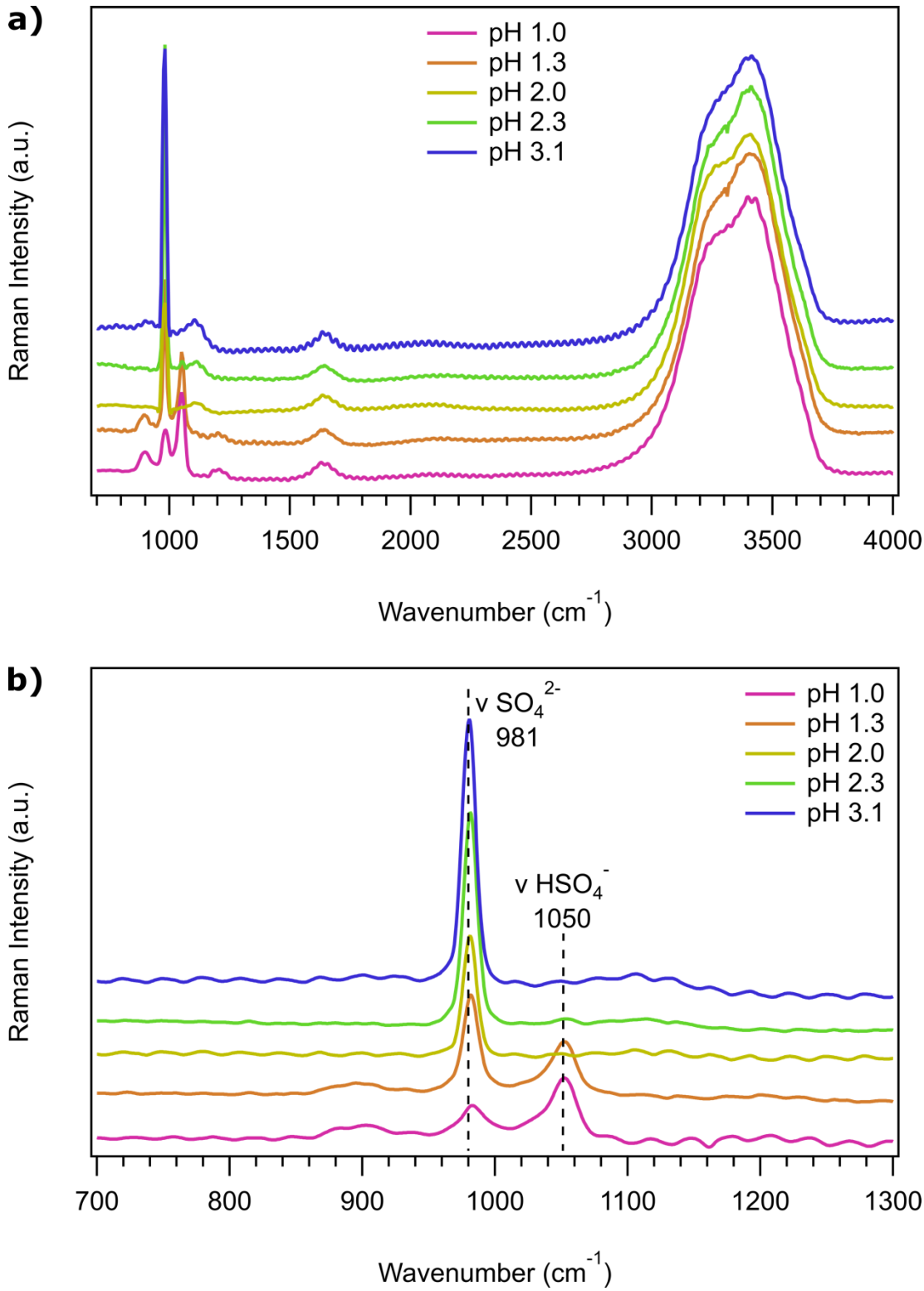

Figure A.30: Cavity enhanced Raman spectra of a trapped sulfuric acid, H_2SO_4, (0.5 M) droplet as a function of pH over a) full spectral range and b) in the 700-1300 cm^{-1} range.

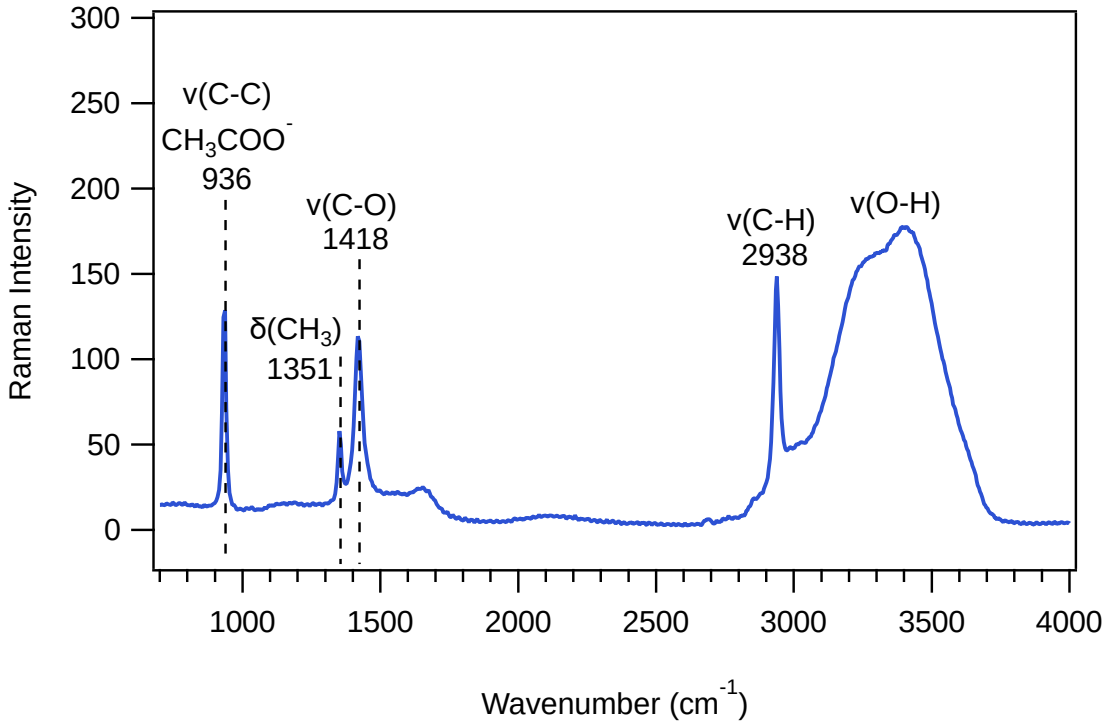

Figure A.31: Cavity enhanced Raman spectrum of a trapped sodium acetate, CH_3COONa, droplet (1 M, pH 9).

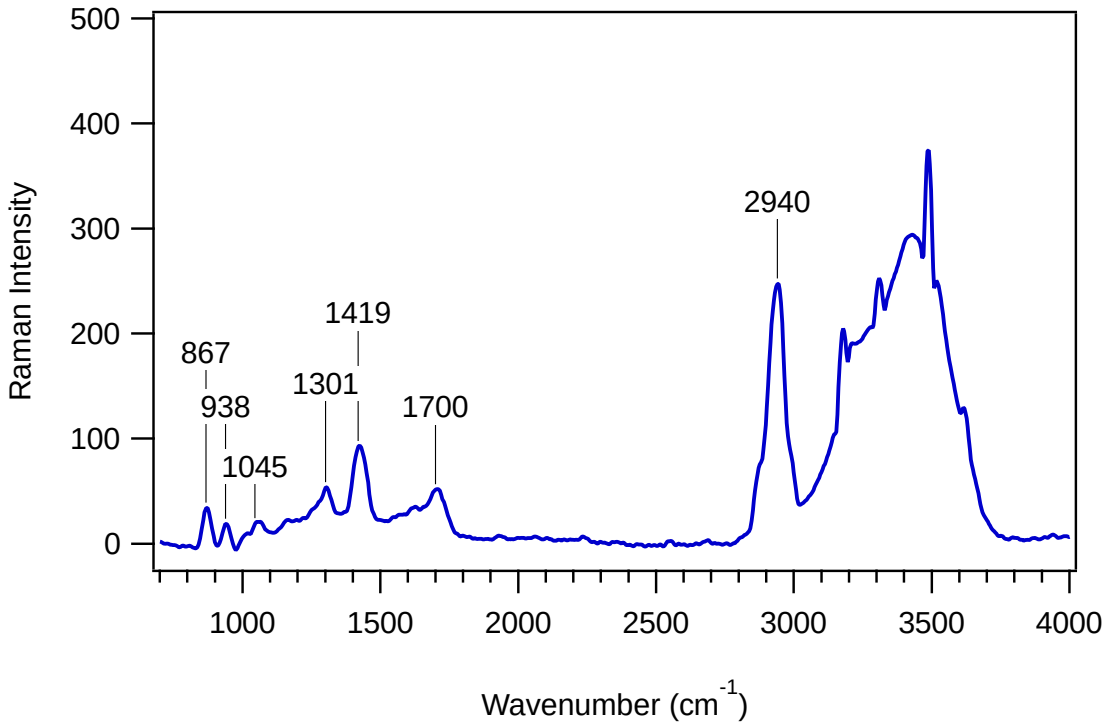

Figure A.32: Cavity enhanced Raman spectrum of a trapped glutaric acid, $C_3H_6(COOH)_2$, (1 M, pH unadjusted) droplet.

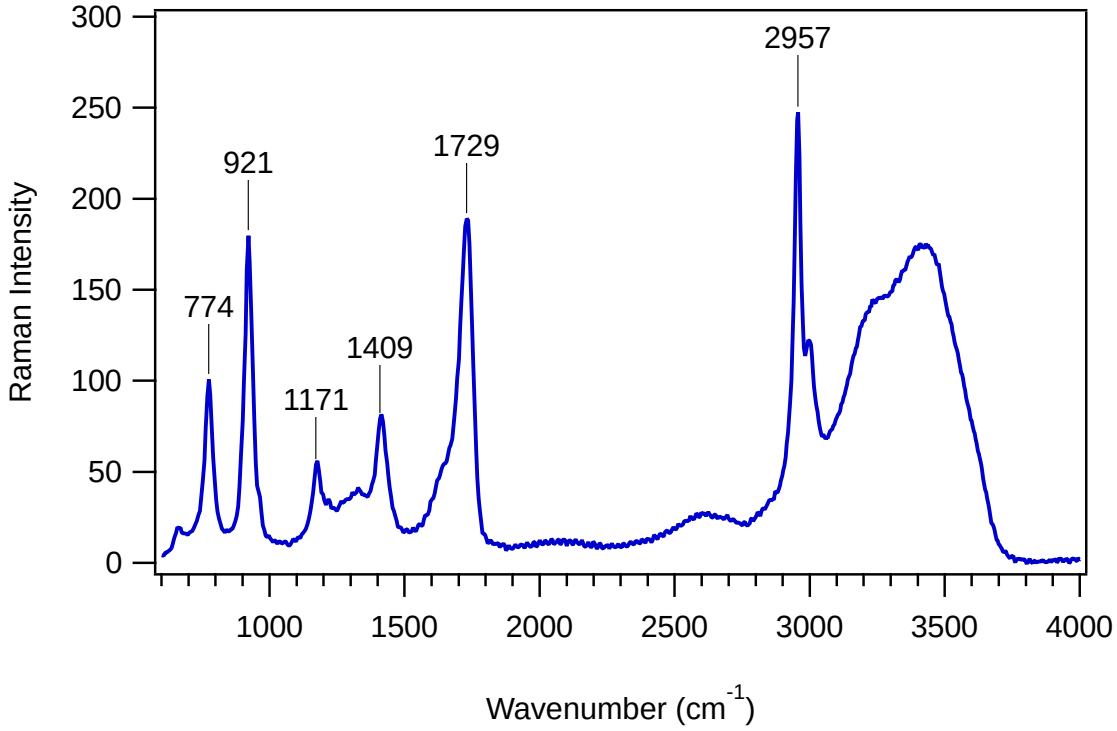

Figure A.33: Cavity enhanced Raman spectrum of a trapped malonic acid, $CH_2(COOH)_2$, (1 M, pH unadjusted) droplet.

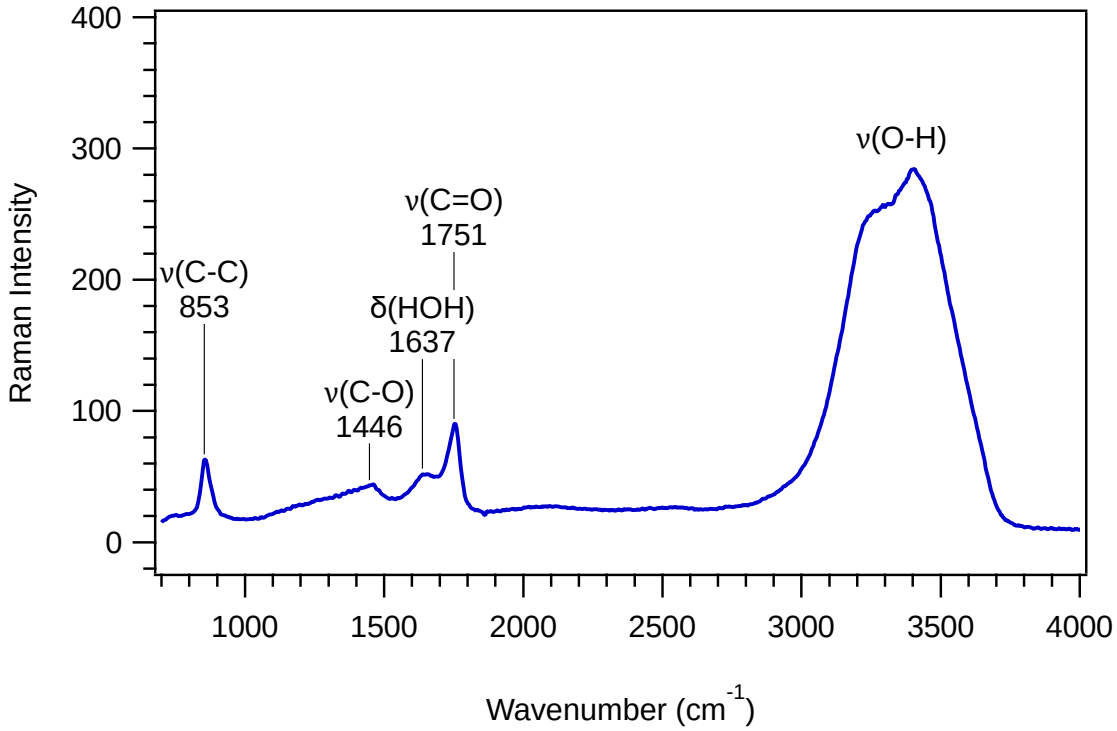

Figure A.34: Cavity enhanced Raman spectrum of a trapped oxalic acid, $C_2H_2O_4$, (1 M, pH unadjusted) droplet.

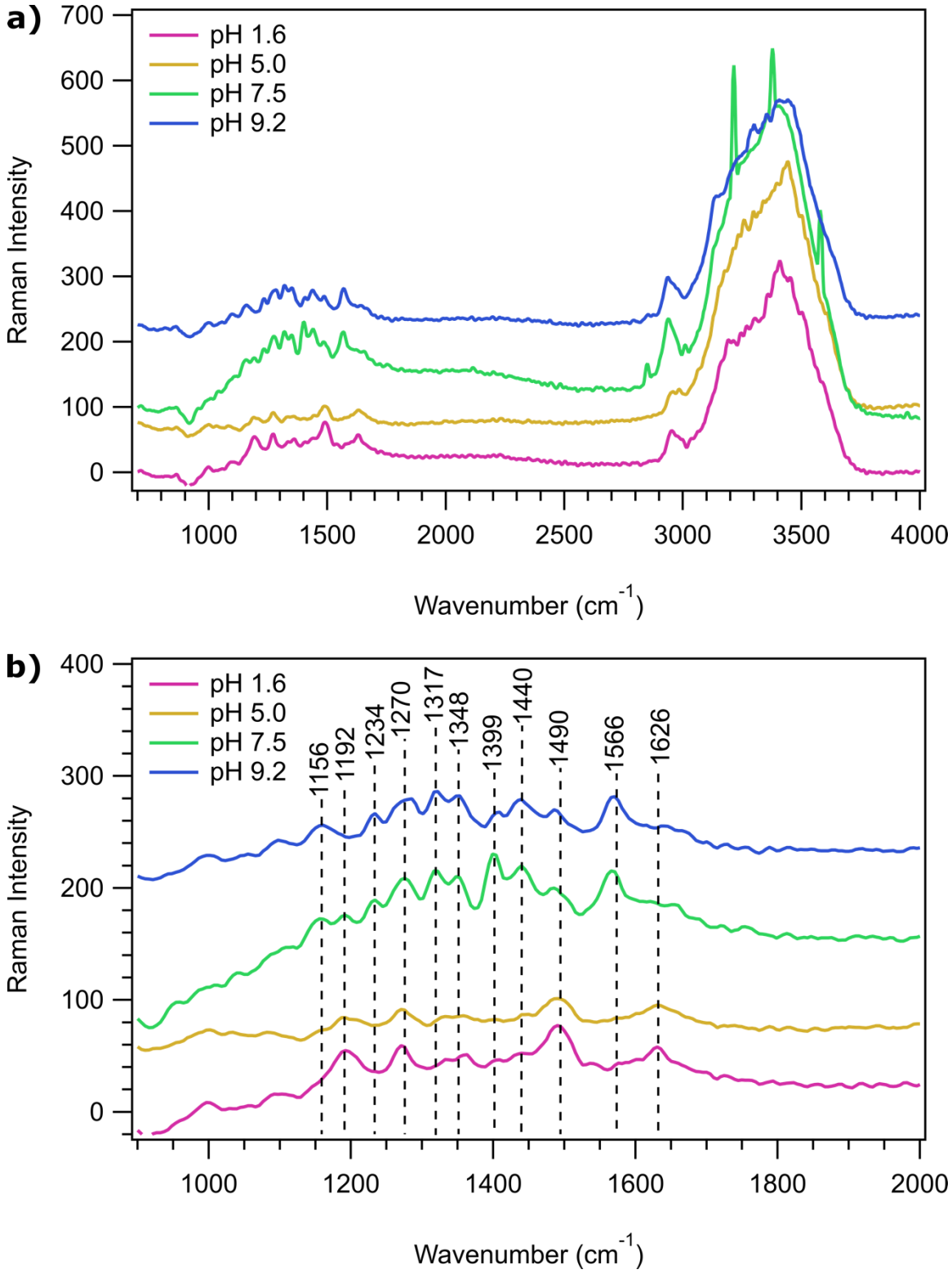

Figure A.35: Cavity enhanced Raman spectra of L-histidine (0.25 M) as a function of pH over a) full spectral range and b) in the 900-2000 cm^{-1} range.